Optimization of dynamic behaviour of advanced active structures

Čakmak, Damjan

Doctoral thesis / Disertacija

2020

Degree Grantor / Ustanova koja je dodijelila akademski / stručni stupanj: **University of Zagreb, Faculty of Mechanical Engineering and Naval Architecture / Sveučilište u Zagrebu, Fakultet strojarstva i brodogradnje**

Permanent link / Trajna poveznica: https://urn.nsk.hr/urn:nbn:hr:235:044764

Rights / Prava: In copyright/Zaštićeno autorskim pravom.

Download date / Datum preuzimanja: **2024-08-17**

University of Zagreb

Faculty of Mechanical Engineering and Naval Architecture

Damjan Čakmak

Optimization of dynamic behaviour of advanced active structures

DOCTORAL DISSERTATION

Zagreb, 2020

University of Zagreb

Faculty of Mechanical Engineering and Naval Architecture

Damjan Čakmak

Optimization of dynamic behaviour of advanced active structures

DOCTORAL DISSERTATION

Supervisor: Dr. Neven Alujević, Assistant Professor

Zagreb, 2020

Sveučilište u Zagrebu
Fakultet strojarstva i brodogradnje

Damjan Čakmak

Optimizacija dinamičkoga ponašanja naprednih aktivnih konstrukcija

DOKTORSKI RAD

Zagreb, 2020.

Sveučilište u Zagrebu
Fakultet strojarstva i brodogradnje

Damjan Čakmak

Optimizacija dinamičkoga ponašanja naprednih aktivnih konstrukcija

DOKTORSKI RAD

Mentor: Doc. dr. sc. Neven Alujević

Zagreb, 2020.

Bibliography data

Scientific area:	Technical Sciences
Scientific field:	Mechanical Engineering
Institution:	Faculty of Mechanical Engineering and Naval Architecture
Thesis supervisor:	Dr. Neven Alujević, Assistant Professor
Number of pages:	140
Number of figures:	22
Number of tables:	6
Number of references:	126
Date of public defence:	Thursday, 30 January 2020

Thesis committee:

Dr. Marko Jokić, Assistant Professor, Chairman of the Thesis Committee

Dr. Hinko Wolf, Full Professor, Member of the Thesis Committee

Dr. Željan Lozina, Full Professor, External member of the Thesis Committee

Archive:	Faculty of Mechanical Engineering and Naval Architecture

Acknowledgements

First and foremost, I would like to express my sincere gratitude to Thesis supervisor, Assistant Professor Neven Alujević for his guidance and advisory through the course of creating this work, and for introducing me to a new world of inerters and active control. His deep engagement and eternal pursuit for excellence led me to numerous fruitful discoveries and successful completion of this scientific trip to the unknown. I am also immensely grateful for the given opportunity of being taught my first steps in Maple symbolic programming, conducting the systematic research, and philosophy of writing scientific papers.

Moreover, I would like to give my deepest thanks to Head of the Chair of Applied Dynamics, committee member, and associate, Professor Hinko Wolf for his selfless help, unconditional trust and utmost patience. His much appreciated advice always kept me focused to the task and gently pushed me to give more. Much of this work is influenced by Professor Wolf's long-lasting impact.

I would also like to give my deep appreciation to Committee members: Assistant Professors Marko Jokić, and Professor Željan Lozina for their valuable time, input and comments regarding the improvement of the thesis quality.

Moreover, I am indebted greatly to Academician Ivo Senjanović for taking me under his fruitful scientific wings and providing invaluable advice when moving parts got stuck. Researching and making new breakthroughs together brought me great joy and immanently changed my perspectives towards scientific community. Consequently, I learned it can be truly enjoyable and fun! This engagement, besides the main research tied to thesis, yielded with interesting scientific discoveries regarding dynamics of thin-walled pre-stressed shell structures, and taught me so much in the process. It also broadened my horizons with respect to countless possibilities of finite element modelling, and consequently influenced some branches of this research. I truly wish that our past, current and future investigations will provide for long lasting legacy. In that sense, I would also like to thank my co-authors, Assistant Professors Ivan Ćatipović and Nikola Vladimir from Department of Naval Architecture, for our long-term successful collaboration.

Next, special thanks are reserved for Professor Damir Semenski. Our combined discussions and counselling about mechanics, everyday life, astrology, and Rock 'N' Roll significantly influenced my further research and life interests alike. Furthermore, Professor

Željko Božić helped me greatly with introduction to scientific conferencing. Our time spent together had a large impact on devoting parts of this thesis to vibration fatigue problems which yielded a highly productive ongoing scientific collaboration.

My especially deep gratefulness is owed to Head of the office of the Department of Applied Mechanics, Begzada Pinjić who constantly provided a much needed moral support and made my working days at the university a pleasurable experience indeed. Begi, thanks to you, when I am at work, I do always feel like I am at home!

I am deeply thankful for finding the truest of friends among the staff of FAMENA, namely Assistant Professor Zvonimir Tomičević; and Research Assistants Mihael Cindori, and Robert Surma. You all remind me what was it like when we were children, everything around us was so much simpler, and friends were indeed for life.

I also thank my dear friend Research Assistant Dr. Jasna Leder, friend and co-author, Research Assistant Ivan Trapić; and work colleague and friend from Chair of Applied Dynamics, Bruno Dogančić. Your ongoing support and effort is deeply appreciated!

Special thanks goes to Professional advisor for postgraduate studies Zvonka Fofić, who made this confusing trip through doctoral studies a lightweight breeze. Our witty conversations always kept us on the bright side of life!

Very important thanks go to my exceptional students and ex-students: Ana Vrgoč, Petra Adamović, Stjepan Orešković, and Andrija Zaplatić, who later became my friends and colleagues. Your fresh bright ideas, youthful playfulness and general positive attitude towards world around us provided me with a much needed nod to the past and strengthened the faith in the future. You also constantly remind me that both learning and teaching process cycle never ends. Only by chance and synchronicity, Ana's work in final stages of her Master's Thesis temporally coincided with the final touches of this Dissertation where topic of broadband spectral fatigue was extensively discussed among us. This also greatly influenced and inspired my plans for future research.

I cannot express enough of my gratitude to my closest family for their unconditional love and inexhaustible support throughout all these years: my mother Sanja, step father and amigo Mario, mother in law and lioness Andrea, grandfather Emil, grandmother Dana and uncle Dubravko. Without your everlasting love and support, none of this would have been even remotely possible. Dudo, my *compadre*, I wish you could see me now!

My eternal love and friendship goes to my life-partner in crime Hanna, for tolerating me, inspiring me and amazing me all these years. We have been through so much together and the world is still beneath our cloud!

I would also like to thank the rest of the entire Chair of Technical Mechanics staff, for the picturesque working atmosphere throughout all these years! Thank you all!

Immanent gratitude is owed to *Mgła* and *Summoning* for providing inspirational transcendent soundscapes during writing and finalizing of Dissertation.

I dedicate this work to my beloved grandmother and brightest star Danica.

Zagreb, January 2020

Table of Contents

List of Figures

List of Tables

Nomenclature

Latin nomenclature

Label	SI Unit	Description
A_i	–	denominator coefficient
b	kg	inertance
B	–	Basquin's (fatigue) exponent
B_i	–	numerator coefficient
c	$\mathrm{N\,s\,m^{-1}}$ ($\mathrm{kg\,s^{-1}}$)	axial viscous damping/dashpot coefficient
C	F	electric capacitance
$\mathbf{C}$	$\mathrm{N\,s\,m^{-1}}$ ($\mathrm{kg\,s^{-1}}$)	axial viscous damping matrix
$C = D/d$	–	spring index
D	m	helical spring mean coil diameter
d	m	helical spring wire diameter
e	–	base of natural logarithm (e $\cong$ 2.718281)
E_k	J ($\mathrm{kg\,m^2\,s^{-2}}$)	kinetic energy
E	Pa ($\mathrm{N\,m^{-2}}$)	Young's modulus (of elasticity)
E	V	electric voltage
$\mathbf{F}$	N ($\mathrm{kg\,m\,s^{-2}}$)	excitation force column vector
$F(t)$	N ($\mathrm{kg\,m\,s^{-2}}$)	excitation force
F_0	N ($\mathrm{kg\,m\,s^{-2}}$)	force amplitude
f_n	Hz ($\mathrm{s^{-1}}$)	fundamental natural frequency
g	$\mathrm{m\,s^{-2}}$	acceleration of Earth's gravity ($g \cong 9,80665$ m/s^2)
g	$\mathrm{N\,s\,m^{-1}}$ ($\mathrm{kg\,s^{-1}}$)	active feedback gain
G	Pa ($\mathrm{N\,m^{-2}}$)	shear modulus
h	m	spring height
H_2	–	*H*-two norm
H_∞	–	*H*-infinity norm
H_i	$\mathrm{m\,s^{-1}\,N^{-1}}$	complex transfer mobility
i	–	transmission/gear ratio (of the rack and pinion inerter)
i	–	imaginary unit (i $= \sqrt{-1}$)
I	A	electric current
$\Im$	–	imaginary part
$I_{x,y,z}$	$\mathrm{m^4}$	axial moment of inertia around x,y,z axes
J_O	$\mathrm{kg\,m^2}$	mass moment of inertia
k	$\mathrm{N\,m^{-1}}$	axial spring stiffness
$\mathbf{K}$	$\mathrm{N\,m^{-1}}$	axial stiffness matrix
K_δ	–	helical spring deflection correction factor
K_τ	–	helical spring (shear) stress correction factor

l	m	spring pitch
L	H	electric inductance
L	m	spring wire total length
m	kg	mass
$\mathbf{M}$	kg	mass matrix
M_0	–	absolute magnification factor
$M_{0,\mathrm{rel}}$	–	relative magnification factor
n	–	number of active coils in the spring
N_f	–	number of cycles to fatigue failure
p	$\mathrm{m\,rev^{-1}}$	ball-screw pitch
r	m	radius
R	Ω	electric resistance
$\Re$	–	real part
S'_f	$\mathrm{Pa\,(N\,m^{-2})}$	fatigue strength coefficient
S_a	$\mathrm{Pa\,(N\,m^{-2})}$	high cycle fatigue stress amplitude
t	s	time
T	s	period
u_0	m	kinematic excitation displacement amplitude
x	m	displacement
$\mathbf{x}$	m	displacement column vector
X	–	dimensionless displacement
$\dot{x}, v$	$\mathrm{m\,s^{-1}}$	velocity
$\dot{\mathbf{x}}$	$\mathrm{m\,s^{-1}}$	velocity column vector
$\ddot{x}, a$	$\mathrm{m\,s^{-2}}$	acceleration
$\ddot{\mathbf{x}}$	$\mathrm{m\,s^{-2}}$	acceleration column vector

Greek nomenclature

Label	**SI unit**	**Description**
$\alpha = (\Omega_2/\Omega_1)^{1/2}$	–	squared natural frequency ratio
$\beta = (\Omega_3/\Omega_1)^{1/2}$	–	squared natural frequency ratio
γ	rad	phase angle
δ	m	deflection
$\zeta = c/c_\mathrm{cr}$	–	modal damping ratio
$\eta = \Omega/\omega_n$	–	dimensionless circular frequency
$\eta_{1,2,3}$	–	damping ratios
λ	–	dimensionless feedback gain
μ_1	–	mass ratio
μ_2	–	dimensionless inertance

v	–	Poisson's ratio
π	–	Ludolf's number ($\pi \cong 3{,}14159$)
σ	Pa (N m^{-2})	normal stress
σ_{eqv}	Pa (N m^{-2})	equivalent stress
τ	Pa (N m^{-2})	shear stress
φ	rad	rotation
ω	rad s^{-1}	yngular velocity
Ω	rad s^{-1}	excitation circular frequency
Ω_1	rad s^{-1}	natural frequency of the uncoupled source body
Ω_2	rad s^{-1}	natural frequency of the coupled receiving body
Ω_3	rad s^{-1}	natural frequency of the uncoupled receiving body
Ω_a	rad s^{-1}	artificial locking frequency
Ω_A	rad s^{-1}	anti-resonant frequency
$\omega_n = f_n/(2\pi)$	rad s^{-1}	fundamental natural circular frequency

List of Abbreviations

Label	Full meaning
1D, 2D, 3D	one-dimensional, two-dimensional, three-dimensional
1DOF	one degree of freedom
2DOF	two degrees of freedom
A	anti-resonance, artificial
A/G	Ancker and Goodier
ACT	actuator
BC	boundary condition
BMM	big mass method
BS	British standard
C	curvature
C/T	Castigliano/Timoshenko
CR	critical
D	denominator
DAVI	dynamic anti-resonant vibration isolator
DCF	displacement correction factor
DIN	*Deutsches Institut für Normung* (Germ.)
DOF	degree of freedom
DVA	dynamic vibration absorber
DVF	direct velocity feedback
EOM	equations of motion
EQV	equivalent
ERS-TMDI	electromagnetic resonant shunt tuned mass-damper-inerter
E-TID	electrically synthesized tuned inerter damper
F	fatigue/failure
FEM	finite element method
FFT	fast Fourier transform
FRF	frequency response function
HCF	high cycle fatigue
HIISDS	hydraulically interconnected inerter-spring-damper suspension
HMH	Huber-Mises-Hencky
IDS	inerter-damper-spring
IDVA	inerter–based dynamic vibration absorber
LIM	limit
LMM	large mass method
LTI	linear and time-invariant
MDOF	multiple degrees of freedom
MDS	mass-damper-spring

N	natural, numerator
NOM	nominal
OPT	optimal
PSD	power spectral density
RB	receiving body
REL	relative
RES	resonant
RMS	root mean square
RP	reference point
SB	source body
SCF	stress correction factor
SDOF	single degree of freedom
SSP	semi–submersible platform
T	transposed
T/C	Timoshenko/Cowper
TF	transfer function
THP	tuned heave plate
THPI	tuned heave plate inerter
TIBD	tuned inerter–based damper
TID	tuned inerter damper
TMD	tuned mass–damper
TMDI	tuned mass–damper–inerter

Abstract

The subject of this research is the improvement of the dynamic behaviour of structures using passive and active approaches to vibration control by using inerters. Inerter is a relatively new element in the theory of mechanical networks. It is a mechanical device that generates force proportional to the relative acceleration between its terminals. The use of inerters is still relatively unexplored and offers many new possibilities of reducing unwanted vibration effects, which is of particular importance in the resonant working conditions of the structure. In the first part of the thesis, passive linear dynamic systems are considered. In the second part, the passive systems are enhanced by the active control. Stability analysis of the active systems is performed. In addition to the parameters that ensure stable operation of the system, the optimization of vibration behaviour of active structures is carried out. The main optimization criterion used is the minimization of the specific kinetic energy of system vibration in a broad frequency band. Throughout the work, analytical and numerical methods are combined, depending on the complexity of the considered system. The achieved results are compared through discussion on the usefulness of the active control and inerter implementation, depending on the system considered. The motivation for the work are synergistic effects regarding the utilization of inerters in parallel with active control systems. The result of the research is a development of new methods for passive and active vibration control. Furthermore, it is shown that employing the inerter in isolation systems can yield with substantial improvements in fatigue life of isolator coupling components, i.e. springs. Novel cylindrical helical spring stress and displacement correction factors are proposed.

Keywords: *Vibration Isolation ; Inerter ; Active Vibration Control ; Direct Velocity Feedback ; Stability of Active Control Systems ; Optimization of Vibration Control Systems ; Fatigue Life ; Helical Spring ; Finite Element Method ; H_2 Optimization; Stress Correction Factor ; Displacement Correction Factor*

Sažetak (Abstract in Croatian)

Tema istraživanja vezana je uz poboljšanje dinamičkog ponašanja konstrukcija koristeći pasivni i aktivni pristup redukciji vibracija uz uporabu inertera. Inerter je relativno novi element u teoriji mehaničkih mreža. Radi se o mehaničkom uređaju koji generira silu proporcionalnu relativnom ubrzanju između svojih priključnih točaka. Upotreba inertera je još relativno neistraženo područje koje pruža mnoge nove mogućnosti smanjenja neželjenih efekata vibracija, što je od osobite važnosti u rezonantnom području rada uređaja. U prvom dijelu istraživanja razmatrani su pasivni linearni dinamički sustavi koji su potom unaprijeđeni aktivnim pristupom s povratnim vezama. Provedena je analiza stabilnosti. Uz parametre koji osiguravaju stabilan rad sustava, provedena je optimizacija vibracijskog ponašanja aktivnih konstrukcija. Glavni korišteni kriterij optimizacije je minimizacija specifične kinetičke energije vibracija sustava u širokom pojasu frekvencija. U radu su korištene analitičke i numeričke metode te njihova kombinacija, ovisno o kompleksnosti razmatranog sustava. Postignuti rezultati su međusobno uspoređeni uz diskusiju o nužnosti implementacije automatske regulacije i inertera ovisno o razmatranom sustavu. Motivacija za rad su sinergijski efekti koji proizlaze iz upotrebe inertera u sprezi s automatskom regulacijom. Rezultat istraživanja je razvoj novih metoda za automatsku regulaciju vibracija. Nadalje, pokazano je da korištenje inertera u izolacijskim sustavima može rezultirati značajnim poboljšanjima vijeka trajanja dijelova izolatora, t.j. opruga. Predloženi su novi korekcijski faktori za naprezanje i pomak cilindrične zavojne opruge.

Ključne riječi: *izolacija vibracija ; inerter ; aktivna kontrola vibracija ; povratna veza po brzini vibracija ; stabilnost aktivnih sustava ; optimizacija dinamičkih sustava ; zamor ; zavojna opruga ; metoda konačnih elemenata ; H_2 optimizacija ; korekcijski faktor naprezanja ; korekcijski faktor pomaka*

Extended Abstract

Inerter is an idealized element in discrete mechanical networks which resists relative acceleration across its two terminals [1]. The coefficient of this resistance is called inertance and is measured in kilograms [2]. An appealing property of inerters is that they can be designed and realized in practice having their inertance significantly larger than their mass [1]. This feature is potentially very useful, so that many recent investigations are focused on the realization and use of inerters for suppressing mechanical vibrations [3].

The concept of "relative mass" has been considered by Schönfeld [4] in connection with developing mechanical–electrical analogies. Schönfeld mentioned the possibility of a relative mechanical inertia and gave a rudimentary scheme of a physical realization of the concept. Smith and Wang [2] developed this idea further by investigating how to design such a device in practice and pointed out a number of peculiarities that the new element brings into a mechanical network. The authors instilled that inerter is the analogue of the capacitor element in electrical networks [2]. Therefore, adding the inerter to classical dampers and springs fills an empty niche enabling a complete synthesis of passive mechanical networks and complete analogy between mechanical and electrical networks [3].

Smith and Wang designed their inerter using a plunger sliding in a cylinder which drives a flywheel through a rack, pinion and gears [2]. Another way of realization of the inerter is through an electromagnetic transducer, i.e. coil and magnet [5]. An electrical circuit of certain impedance can be connected at the terminals of the electromagnetic transducer, which consists of a capacitor coupled in series with resistor and coil in a parallel connection. If the total shunt impedance is properly tuned, then the whole electromechanical network theoretically behaves exactly as if it incorporated an ideal inerter mounted in series with a parallel spring-damper pair. A problem in this realisation is that voice coils are characterised by an inherent electric resistance of the wire in the coil. As a result, unrealistically large scale electromagnetic transducers would be needed to overcome this resistance and synthesize a usable inerter by means of entirely passive electrical shunt circuits. This can be overcome by actively compensating for the coil resistance. In this context, self-powered configurations employing a simultaneous active control and energy harvesting have been considered to synthesize mechatronic inerters [5]. Another type of mechatronic inerter utilizes a rotary DC motor shunted with an appropriate electrical circuit [6]. An inertance-like behaviour can also be accomplished through a scheme in which hydraulic fluid is accelerated [7]. In [8], inerter

realization which uses fluid is achieved with a piston which pushes the fluid through a helical channel.

Inerters can be very useful in vibration absorber systems [9]. Performance of vibration absorbers, especially Tuned Mass Dampers (TMDs) is known to very much depend on the proof mass added to a primary structure to reduce its vibration [10]. As this mass is added to structures exclusively to control their vibrations, it is penalized in lightweight automotive and aerospace applications [11]. In this context the use of inerter elements can be interesting given the fact that their inertance can be significantly larger than their mass [2]. Consequently a number of new concepts have arisen. These include tuned inerter-damper (TID) [12], tuned mass–damper–inerter (TMDI) [13],[14], and inerter–based dynamic vibration absorber (IDVA) [15]. Various applications have been considered using tuned inerter dampers including vibration reduction of cables in cable-stayed bridges [12],[16].

Dynamic vibration absorbers can be made active by using inertial actuators with a velocity or velocity and displacement feedback control scheme. Inertial actuators are typically designed with a low mounted natural frequency in order to widen the range of frequencies where they can efficiently actuate. However, the low natural frequency is usually associated with increased static sags. This limits the applicability of inertial actuators in presence of constant accelerations (i.e. Earth's gravitational acceleration *g*, acceleration of aircraft while manoeuvring, or centrifugal accelerations in rotating structures [17]).

Zilletti [18] investigated an active vibration absorber system in which the inerter is attached in parallel with the suspension spring, damper and the actuator. The author has shown that with such a design it is possible to reduce the natural frequency of the actuator without increasing the proof mass or reducing the suspension stiffness. He considered only an idealized inerter element, which neglects the inertia, stiffness and damping of the gearing mechanism. However, Kras and Gardonio [19] studied the effective weight and dynamic effects of an inerter element composed by a single flywheel which is either pinned or hinged to the base mass or to the proof mass of the actuator.

Inerters can also be very useful in vibration isolation systems [2]. In this sense, authors [20] focused their efforts on improving passive vehicle suspension systems by using inerter. Investigations also include optimizing driving comfort for car driver and passengers by using inerter [21]. The literature also provides information on the use of inerter for semi-active car suspension systems [22], as well as the use of semi-active inerters within the semi-

active suspensions [23]. Further applications of inerters include vibration isolation in civil engineering structures, such as multi-storey buildings under earthquake base excitation [24]. In vibration isolation problems it is often necessary to tune the impedance of the isolator elements based on some optimization criteria. This can be done by either minimizing maxima of the response (minimax or H_∞ optimization), or by minimizing the energy in the response signals (H_2 optimization) [25].

I.   Methods of Research

In this work, the problem of active vibration isolation with velocity feedback loop is considered. With velocity feedback loop it is possible to add active damping to the system and thus reduce the resonant system response. Since it is an active approach, a special attention should be paid to the system stability [26],[27]. It is examined, by using simplified models, whether using an inerter enables efficient active vibration isolation in group of mechanical systems in which active vibration isolation is otherwise difficult to accomplish. This group of systems has been referred to as sub-critical group of systems [26]. Subcritical systems are those that have the fundamental natural frequency of a body that is to be protected from vibrations, greater than the fundamental natural frequency of the body that is the source of vibrations. In such problems, it is examined whether using an inerter can stabilize the otherwise unstable feedback loop and thus enable improved performance of the active vibration isolation system. Along with the active system, a passive isolator scheme with and without inerter is proposed and analyzed in order to determine the benchmark for active isolators that are investigated in the later stages.

In each system, either active or passive, adjustable parameters are tuned to minimize the kinetic energy of the body that is to be protected from vibrations. The broadband dynamic excitation of the source body is assumed. Preliminary research results showed that by careful selection of passive elements such as inerters, dampers and elastic elements within the active mechanical system, substantially improved performance of the isolator can be achieved in terms of reducing the kinetic energy of the protected body. Regarding the active system stability, it is necessary to define the limits of the feedback gain beyond which the system can become unstable [26],[27]. Routh-Hurwitz's stability criterion is used to determine these stability limits [27]. In the control systems theory, Routh-Hurwitz's criterion is a standard mathematical test which enables algebraically determining the necessary and sufficient conditions for the stability of the dynamic system. With this method the stability of a simple

system, with limited number of degrees of freedom can be determined analytically, without the need for numerical incremental and iterative methods. Therefore, the application of Routh-Hurwitz's criterion is preferable for this research.

This is because the described method is applied to a simple two degrees of freedom (2DOF) system, so conclusions are based on analytically derived expressions. Such a simplified system can be considered as a reduced model of potentially more complex structures. The analytical results regarding the stability and performance of the active control are therefore used to make conclusions usable in a wide range of possible applications, which implies a greater generality of the obtained results. The problem analysis is performed in the frequency domain, where the square of the absolute value of the velocity, which is proportional to kinetic energy of the system, is used as the quality measure of the system isolation and hence as the optimization criterion. Some of the methods used in this investigation are the direct inversion of the system dynamic stiffness matrix, and the mode decomposition method. It is investigated how the implementation of the inerter in the isolator affects the system natural frequencies and the associated mode shapes. The viscous damping model is used with discrete (lumped parameter) models. When using the mode decomposition method, modal damping ratios are used [27]. In the case of complex model geometries, the finite element method (FEM) is used [27]-[30]. The finite elements are verified on simple examples that can be solved by analytical means to test the suitability of elements for solving the considered linear, time-invariant (LTI) dynamic problems. The way of simulating the dynamics of an ideal inerter within a FEM environment is determined, analogously to ideal spring or viscous damper.

The work examines whether the performance of the base passive isolator that does not use the inerter can be improved by adding the inerter in parallel to the isolator spring and the damper. As mentioned earlier, two fundamental groups of problems are discussed: subcritical and supercritical [26]. It is tested for each group in particular:

- stability of the feedback loop,

- the performance of the active vibration isolation system.

It is investigated whether the vibration isolation system performance increases with the increase of the feedback gain. It is also investigated whether the vibration isolation effect is achieved in a broadband frequency range [26]. It is studied how coupling of the inerter in parallel to the damper and the spring in the isolator affects the performance and stability of

active and passive vibration isolation systems. In order to enable a wider and more general application of the results, non-dimensional parameters to describe the dynamic model are defined.

An objective conclusion is reached for which systems it is recommended to use the inerter, active isolation, or their combination within the isolator. The results obtained are systematically compared.

II.   Research Objectives

Main research objectives are:

- performance analysis of passive systems for the isolation of broadband vibrations by using an inerter

- optimization of passive vibration isolation systems by using an inerter,

- stability and performance analysis of active systems for the isolation of broadband vibrations by using an inerter,

- optimization of active vibration isolation systems by using an inerter.

III.   Hypotheses of Research

Main research hypotheses are:

- the performance of the base passive vibration isolator that does not use an inerter can be improved by adding the inerter in parallel with the isolator spring and damper,

- the stability of the system for active vibration isolation can be improved by using the inerter of certain inertance,

- the performance of the active vibration isolator can be improved by using the inerter, so that it is possible to achieve active vibration isolation in the wider frequency range.

IV.   Scientific Contribution

Main scientific contribution of this dissertation is comprised of:

- a new method for improving the performance of passive isolators of broadband vibrations by using an inerter,

- a new method for improving the stability and performance of active isolators of broadband vibrations by using an inerter.

Prošireni sažetak (Extended Abstract in Croatian)

Inerter je idealizirani element u diskretnim mehaničkim mrežama koji razvija silu proporcionalnu relativnom ubrzanju između svojih dviju priključnih točaka [1]. Koeficijent proporcionalnosti naziva se inertancijom i mjeri se u kilogramima [2]. Inerteri se mogu konstruirati tako da im je inertancija znatno veća od mase [1]. Ovo svojstvo je potencijalno vrlo korisno, pa već postoje suvremena istraživanja fokusirana na realizaciju i upotrebu inertera za suzbijanje mehaničkih vibracija [3].

Schönfeld [4] je razmatrao koncept "relativne mase" razvijajući analogije između mehaničkih i električnih mreža. Spomenuo je mogućnost relativne mehaničke inercije i predložio osnovnu shemu konstrukcije takvog koncepta. Smith i Wang [2] razvijali su dalje tu ideju istražujući kako konstruirati takav uređaj u praksi te ukazali na brojne osobitosti koje novi element unosi u mehaničku mrežu. Autori su utvrdili da je inerter u mehaničkim mrežama analogan kondenzatoru u električnim mrežama [2]. Prema tome, dodavanje inertera klasičnim masama, prigušivačima i oprugama ispunjava praznu nišu i omogućuje potpunu sintezu pasivnih mehaničkih mreža, kao i potpunu analogiju između mehaničkih i električnih mreža [3].

Smith i Wang oblikovali su svoj inerter pomoću klipa koji klizi u cilindru i pogoni zamašnjak preko zupčaste letve i zupčanika [2]. Drugi način realizacije inertera je putem elektromagnetskog pretvornika, tj. zavojnice i magneta [5]. Na priključne točke elektromagnetskog pretvornika može se spojiti električni krug određene impedancije, koji se sastoji od kondenzatora povezanog u seriji s paralelnim spojem otpornika i zavojnice. Ako se ukupna impedancija dodanog električnog kruga pravilno ugodi, moguće je postići da se spregnuta elektromehanička mreža ponaša kao da je idealni inerter ugrađen u seriju s paralelnim spojem opruge i prigušivača. Problem u ovoj izvedbi je da zavojnicu karakterizira inherentan električni otpor žice zavoja. Kao rezultat toga, nerealistično veliki elektromagnetski pretvarači bi bili potrebni za svladavanje tog otpora i sintezu primjenjivog inertera pomoću potpuno pasivnih električnih krugova. To se može prevladati aktivnim kompenziranjem otpora zavojnice. U tom kontekstu, u literaturi su razmatrane i samo-napajajuće konfiguracije koje koriste istodobno i automatsku regulaciju i rekuperaciju energije kako bi sintetizirale mehatroničke inertere [5]. Još jedan način realizacije mehatroničkog inertera koristi elektromotor premošćen odgovarajućim električnim krugom [6]. Ponašanje slično inertanciji također se može postići preko sheme u kojoj se hidraulična

tekućina ubrzava [7]. U [8], izvedba inertera koji koristi fluid ostvarena je klipom koji potiskuje fluid kroz spiralni kanal.

Inerteri mogu biti vrlo korisni u sustavima dinamičkih prigušivača vibracija [9]. Poznato je da učinkovitost ugođenih dinamičkih prigušivača vibracija (eng. Tuned Mass Dampers, TMDs), bitno ovisi o masi ovješenoj na primarnu konstrukciju kako bi se smanjile vibracije [10]. Budući da se ta masa dodaje ukupnoj masi konstrukcije isključivo u svrhu smanjenja vibracija, maksimalna dopuštena dodana masa je vrlo ograničena u automobilskim i zrakoplovnim konstrukcijama [11]. U tom kontekstu upotreba inertera može biti zanimljiva s obzirom na činjenicu da njihova inertancija može biti znatno veća od njihove mase [2]. Kao posljedica toga, pojavili su se brojni novi koncepti. To uključuje ugođeni inerter-prigušivač [12] (eng. Tuned Inerter-Damper, TID), ugođeni maseni inerter-prigušivač [13],[14] (eng. Mass-Damper-Inerter, TMDI) i dinamički prigušivač vibracija temeljen na inerteru [15] (eng. Inerter–Based Dynamic Vibration Absorber, IDVA). Razmatrane su i razne primjene korištenja ugođenih inerterskih prigušivača za smanjenje vibracija čeličnih užadi u visećim mostovima [12],[16].

Dinamički prigušivači vibracija mogu se aktivirati korištenjem inercijskih aktuatora s regulacijskom shemom uz povratne veze samo po brzini vibracija ili i po brzini i po pomaku. Inercijski aktuatori obično su konstruirani tako da imaju nisku vlastitu frekvenciju kako bi se proširio raspon frekvencija unutar kojeg mogu efikasno pobuđivati vibracije konstrukcije na koju su pričvršćeni. Međutim, niska prirodna frekvencija obično je povezana s povećanim statičkim pomacima. To ograničava primjenjivost inercijskih aktuatora u slučaju konstantnih ubrzanja (tj. ubrzanje Zemljine sile teže *g*, ubrzanje zrakoplova pri manevriranju, ili centrifugalna ubrzanja u rotirajućim konstrukcijama [17]).

Zilletti [18] je istražio aktivni sustav prigušivača vibracija u kojemu je inerter pričvršćen paralelno s ovjesnom oprugom, prigušivačem i aktuatorom sile. Autor je pokazao da je takvom konstrukcijom moguće smanjiti prirodnu frekvenciju aktuatora bez povećanja dodatne mase, ili smanjenja krutosti ovjesa. Razmatrao je samo idealizirani inerter koji zanemaruje inerciju, krutost i prigušenje zupčanog mehanizma. Međutim, Kras i Gardonio [19] su proučavali i efektivnu težinu te dinamičke efekte inertera sastavljenog od jednog zamašnjaka koji je zglobno pričvršćen na osnovnu masu ili na dodanu masu aktuatora.

Inerteri mogu biti vrlo korisni i u sustavima izolacije vibracija [2]. U tom smislu, autori [20] su se usredotočili na poboljšanje pasivnog sustava ovjesa vozila pomoću inertera.

Istraživanja uključuju i optimizaciju ugodnosti vožnje vozača i putnika automobila korištenjem inertera [21]. U literaturi se mogu pronaći i podaci o korištenju ineretera za semi-aktivne sustave ovjesa automobila [22], kao i korištenje semi-aktivnih inertera u sklopu semi-aktivnih ovjesa [23]. Daljnje primjene inertera uključuju izolaciju vibracija u građevinarstvu, primjerice izolaciju vibracija višekatne zgrade u slučaju potresa [24]. Kod problema izolacije vibracija često je potrebno podešavati impedanciju elemenata izolatora na temelju nekih kriterija optimizacije. To se može postići bilo minimiziranjem maksimuma odziva (H_∞ optimizacija), ili minimiziranjem energije signala odziva (H_2 optimizacija) [25].

I.　　Metode istraživanja

U ovom radu je razmatran problem aktivne izolacije vibracija povratnom vezom po brzini vibracija. Povratnim vezama po brzini vibracija moguće je dodavati prigušenje u sustav i tako smanjiti odziv sustava u rezonanciji. U slučaju aktivnog pristupa, potrebno je posebno voditi računa o stabilnosti sustava [26],[27]. Ispitano je mogu li se uporabom inertera poboljšati stabilnost i učinkovitost takvog aktivnog sustava u određenim situacijama. Na pojednostavljenom modelu je ispitano omogućuje li upotreba inertera efikasnu aktivnu izolaciju vibracija u grupi mehaničkih sustava u kojima se inače aktivna izolacija vibracija teško ostvaruje. Ova grupa sustava naziva se pod-kritična grupa sustava [26]. Podkritični sustavi su oni koji imaju fundamentalnu prirodnu frekvenciju tijela kojeg se želi zaštititi od vibracija višu od fundamentalne prirodne frekvencije tijela koje je izvorište vibracija. U takvim problemima, ispitano je može li se korištenjem inertera stabilizirati inače nestabilna povratna veza i tako omogućiti poboljšana učinkovitost sustava za aktivnu izolaciju vibracija. Uz aktivni sustav, predložena je i analizirana i pasivna izolatorska shema sa i bez inertera, kako bi se utvrdila referentna učinkovitost (eng. *benchmark*) za procjenu učinkovitosti aktivnih izolatora koji su kasnije istraživani u radu.

U svakom sustavu, bilo aktivnom, bilo pasivnom, prilagodljivi parametri su ugađani tako da se minimizira kinetička energija tijela kojeg se štiti od vibracija. Pritom je pretpostavljena širokopojasna dinamička uzbuda tijela koje je izvorište vibracija. Preliminarni rezultati istraživanja pokazali su da se pažljivim odabirom pasivnih elemenata kao npr. inerteri, prigušivači i elastični elementi, unutar aktivnog mehaničkog sustava mogu postići bitno poboljšane dinamičke karakteristike sustava u smislu smanjenja štetnih vibracija. U slučaju automatske regulacije dinamičkih sustava, potrebno je obratiti posebnu pažnju na stabilnost sustava. U tu svrhu je nužno definirati granice izvan kojih sustav može postati

nestabilan [26],[27]. Za određivanje parametara stabilnosti aktivnog sustava korišten je Routh-Hurwitzov kriterij stabilnosti [27]. U teoriji regulacijskih sustava, Routh-Hurwitzov kriterij je standardni matematički test kojim je moguće algebarski odrediti nužne te dovoljne uvjete stabilnosti dinamičkog sustava. Postupak određivanja parametara stabilnog sustava ovim kriterijem je potpuno analitički i linearan, bez potrebe za korištenjem numeričkih inkrementalno-iterativnih metoda, ako se radi o relativno jednostavnim sustavima s malim brojem stupnjeva slobode.

Budući da je opisana metoda primijenjena na jednostavnom sustavu s dva stupnja slobode, zaključci se mogu temeljiti na analitički izvedenim izrazima. Takav pojednostavljeni sustav može se smatrati reduciranim modelom potencijalno složenijih konstrukcija. Analitičke metode su korištene zato da se zaključci mogu upotrijebiti u širokom spektru mogućih primjena, pa su dobiveni rezultati općenitiji. Analiza problema je izvršena u frekvencijskoj domeni, gdje je kvadrat apsolutne vrijednosti brzine, veličine proporcionalne kinetičkoj energiji sustava, korišten kao mjera kvalitete izolacije sustava te stoga kao i kriterij optimizacije. Neke od metoda koje su korištene u radu su direktna inverzija matrice krutosti dinamičkog sustava, te metoda modalne dekompozicije. Ispitano je kako implementacija inertera u izolatoru utječe na vlastite frekvencije i pripadajuće forme vibriranja sustava. Korišten je model viskoznog prigušenja sustava, u diskretnom tj. koncentriranom obliku, dok je u slučaju primjene metode modalne dekompozicije korišteno modalno prigušenje [27]. U slučaju geometrije modela kompleksnijih oblika, korištena je i metoda konačnih elemenata (MKE) [27]-[30]. Korišteni konačni elementi su verificirani na jednostavnijim primjerima koje je moguće riješiti analitičkim putem u svrhu ispitivanja prikladnosti elemenata za rješavanje navedene klase linearnih, vremenski invarijantnih dinamičkih problema. Istražena je mogućnost implementacije idealnog inertera unutar metode konačnih elemenata, analogno idealnoj opruzi ili viskoznom prigušivaču.

U radu je ispitano da li se učinkovitost temeljnog pasivnog izolatora koji ne koristi inerter može poboljšati dodavanjem inertera paralelno izolatorskoj opruzi i prigušivaču. Što se tiče aktivnih sustava za izolaciju vibracija, razmatrane su dvije temeljne grupe problema: podkritična i nadkritična [26]. Ispitano je za svaku grupu posebno:

- stabilnost povratne veze,

- učinkovitost aktivnog sustava za izolaciju vibracija.

Ispitano je raste li s porastom pojačanja u povratnoj vezi učinkovitost sustava za izolaciju vibracija. Također, istraženo je postiže li se efekt izolacije vibracija u širokom spektru frekvencija [26]. Analiziran je utjecaj priključenja inertera, paralelno prigušivaču i opruzi u izolatoru, na učinkovitost i stabilnost aktivnih sustava za izolaciju vibracija. Radi šire i općenitije primjene rezultata, u radu su definirani bezdimenzijski parametri kojima je opisan dinamički model razmatranog sustava.

Na temelju provedenih istraživanja, izveden je objektivni zaključak za koje grupe sustava se u izolatoru preporuča upotreba inertera, aktivne izolacije, ili pak njihova kombinacija. Dobiveni rezultati su sistematski prikazani, sa svrhom objektivnije međusobne usporedbe.

II.   Ciljevi istraživanja

Glavni ciljevi istraživanja su:

- analiza učinkovitosti pasivnih sustava za izolaciju širokopojasnih vibracija koji koriste inertere,

- optimizacija pasivnih sustava za izolaciju vibracija upotrebom inertera,

- analiza stabilnosti i učinkovitosti aktivnih sustava za izolaciju širokopojasnih vibracija koji koriste inertere,

- optimizacija aktivnih sustava za izolaciju vibracija upotrebom inertera.

III.   Hipoteze istraživanja

Glavne hipoteze istraživanja su:

- učinkovitost temeljnog pasivnog izolatora vibracija koji ne koristi inerter može se poboljšati dodavanjem inertera paralelno s izolatorskom oprugom i prigušivačem,

- stabilnost sustava za aktivnu izolaciju vibracija moguće je poboljšati upotrebom inertera određene inertancije,

- učinkovitost aktivnog izolatora vibracija moguće je poboljšati upotrebom inertera, pa je tako moguće ostvariti aktivnu izolaciju vibracija u širem području frekvencija.

IV. Znanstveni doprinos

Glavni znanstveni doprinos ove disertacije sastoji se od:

- nove metode za poboljšanje učinkovitosti pasivnih izolatora širokopojasnih vibracija upotrebom inertera,

- nove metode za poboljšanje stabilnosti i učinkovitosti aktivnih izolatora širokopojasnih vibracija upotrebom inertera.

1.   Introduction

Vibration is a phenomenon where oscillations occur about a point of static equilibrium. The vibrations may be of periodic nature, e.g. the motion of a pendulum, or completely random, e.g. the movement of a vehicle on a rough road. Vibrations may be of advantageous nature, e.g. the motion of a tuning fork, strings on a guitar, or the cone of a loudspeaker. However, in many cases, vibrations are harmful and undesirable. Numerous sources of vibration can be found in an industrial environment and real engineering applications, e.g.: impact processes such as pile driving, pressing and blasting; rotating or reciprocating machinery such as motors, engines and compressors; transportation vehicles such as cars, trucks, trains, and aircraft; and either laminar or turbulent flow of fluids [31]. The presence of vibration may lead to wear of bearings, initiation of cracks, yielding of bolts and fasteners, various structural and mechanical failures, or frequent and expensive maintenance of machines [32]. The exposure of humans to vibration may lead to pain, discomfort, reduced working efficiency and compromised safety. Vibration can be eliminated on the basis of theoretical analysis. However, the manufacturing costs involved in eliminating the vibration may become too high. Hence, a designer must compromise between an acceptable amount of vibration and a reasonable manufacturing cost. In some cases, such as rotating machinery, the excitation or shaking force is inherent in the machine, or working environment. Even a relatively small excitation force can cause an undesirably large response near resonance, which is especially evident in inherently lightly damped systems [27],[33],[34]. In these cases, the magnitude of the response can be significantly reduced by the use of isolators and auxiliary mass absorbers. Hence, various techniques of vibration control methods may be employed for elimination or reduction of vibration.

1.1.   Vibration Control

Reduction of structural vibrations can be achieved in a number of different ways, depending on the class of problem considered. The most common ways are: stiffening, damping and isolation [27]. Stiffening consists of shifting the resonant frequency of the structure above the excitation frequency band. Moreover, damping employs reducing the resonant peaks response by dissipating the vibration energy. Finally, isolation implies preventing the propagation of disturbance forces to sensitive parts of the systems.

Vibration isolation is a procedure by which the undesirable effects of vibration are reduced. An object, e.g. a piece of equipment, is isolated from the source of vibrations, or the

other way around, a vibration source is isolated from the rest of the structure. Fundamentally, the procedure involves insertion of a flexible structural member (i.e. isolator which may include rubber pads or mechanical springs) between the sensitive equipment, or payload, that needs to be protected from vibrations, and the source of vibration [35]. A reduction in the dynamic response of the system is then achieved under specified conditions of vibration excitation. An isolation system is defined as either active or passive, depending on whether external power is required for the isolator to perform its function, or not [27],[31],[34]. A passive isolator consists of a resilient member (which provides stiffness) and an energy dissipater (which provides damping). Examples of passive isolators include metal springs, pneumatic springs, and elastomeric (rubber) springs. An active isolator is comprised of a servomechanism with a sensor, signal processor, and actuator interconnected by a feedback loop [27],[31],[35]. Vibration isolation is commonly used in two main types of problems. In the first type, the foundation or supporting base of a vibrating machine is protected against unbalanced dynamic forces. In the second type, the system (i.e. receiving body [26]) is protected against the motion of its foundation or base, or from any type of general disturbance force [27]. Structures subjected to ground motion by earthquakes or other excitations, e.g. explosions or dynamic action of machinery, are examples in which support motions may have to be considered in the analysis of dynamic response [28]. The first type of isolation is used when a mass (or a machine) is subjected to a force or excitation, e.g. oscillatory forces from an engine in a car which can propagate into the supporting structure [27]. Furthermore, in forging and stamping presses, large impulsive forces act on the object to be formed or stamped [31]. These impacts are transmitted to the base or foundation of the forging or stamping machine, which can damage not only the base or foundation but also the surrounding or nearby structures and machines. They can also cause discomfort to human operators in the vicinity of these machines. Similarly, in the case of reciprocating and rotating machines, the inherent unbalanced forces are transmitted to the base or foundation of the machine. In such cases, the force transmitted to the base varies harmonically, and the resulting stresses in the foundation bolts also vary harmonically, which might lead to fatigue failure [32]. Even if the force transmitted is not harmonic in nature, its magnitude must be limited to safe permissible values. In these applications, an isolator can be inserted (in the form of stiffness and/or damping) between the mass being subjected to force or excitation and the base or foundation to reduce the force transmitted to the base or foundation. This is called force isolation [31]. In many applications, the isolator is also intended to reduce the vibratory motion of the mass under the applied force (as in the case of forging or stamping machines).

Thus, both force and displacement transmissibility become important for this type of isolators. The second type of isolation is used when a mass is to be protected against the motion or excitation of its base or foundation, e.g. passenger seated in a moving car or airplane [36]. When the base is subjected to vibration, the connected mass will experience not only a displacement but also a force. The displacement of the mass is generally expected to be smaller than the displacement of the base [27]. For example, a delicate instrument or equipment is to be protected from the motion of its container or package (as when the vehicle carrying the package experiences stochastic vibration while moving on a rough road). The force transmitted to the mass also needs to be reduced. For example, the package or container is to be designed properly to avoid transmission of large forces to the delicate instrument inside to avoid damage. In such cases, an isolator (which provides stiffness and/or damping) can be inserted between the base being subjected to force or excitation and the mass to reduce the motion and/or force transmitted to the mass. Hence, both displacement isolation and force isolation become pertinent in such cases. It must be noted that the effectiveness of an isolator depends on the nature of the force or excitation. For example, an isolator designed to reduce the force transmitted to the base or foundation due to impact forces of forging or stamping may be neither suitable nor effective if the disturbance is a harmonic unbalanced force. Similarly, an isolator designed to handle harmonic excitation at a particular frequency may not be effective for other frequencies or other types of excitation such as step-type excitation.

The vibration absorber, also called dynamic vibration absorber (DVA) [31], or vibration neutralizer, is a mechanical device used to reduce or eliminate unwanted vibration of a harmonically excited system. It consists of another mass and stiffness attached to the main (or original) mass that needs to be protected from vibration. Thus, the main mass and the attached absorber mass constitute 2DOF system. The vibration absorber system consequently possesses two new fundamental natural frequencies. Thus, the stiffness of the absorber should be appropriately chosen in order to yield with an effective dynamic absorber system. The vibration absorber is commonly used in the machinery that operates at constant (rotational) speed, because the vibration absorber is tuned to one particular frequency and is effective only over a narrow band of frequencies [18]. Common applications of the vibration absorber include reciprocating tools, such as sanders, saws, compactors, engines, motors, and pumps [31]. In these systems, the vibration absorber helps balance the reciprocating forces as it counteracts the forces yielding from the rotating imbalance. Without a vibration absorber, the unbalanced reciprocating forces might make the device impossible to physically hold or

effectively control. Appropriate application of DVA may reduce the possibility that a resonance condition will occur. Properly implemented, a dynamic absorber will neutralize the undesirable vibration, which would otherwise reduce service life or cause mechanical damage. Vibration absorbers are also used on high-voltage transmission lines. In this case, the dynamic vibration absorbers, in the form of dumbbell-shaped devices are hung from transmission lines to mitigate the fatigue effects [32] of wind-induced vibration. In such cases, the vibration of the machine or system can be reduced by using a vibration neutralizer or DVA, which is simply another spring-mass system. The dynamic vibration absorber is designed in such way that the anti-resonant frequency of the resulting system coincides with the excitation frequency. Dynamic absorbers may differ from tuned mass dampers (TMD) [33] in the sense that dynamic absorbers do not generally require any damping in order to function satisfactorily. However, damping can be additionally introduced to increase the range of frequencies for which the dynamic absorber is effective [33]. If damping is removed from TMD, it deteriorates to DVA.

Fundamental difference between isolation and absorption problems is demonstrated in Figure 1.1a) and b) respectively. For the both cases a) and b), the system setup and its loading are the same. Primary body, or source body, i.e. mass m_1 is coupled to ground by dashpot c_1 and spring k_1. Secondary body, or receiving body, i.e. mass m_2 is coupled to receiving body by dashpot c_2 and spring k_2. Primary force $F_1(t)$ acts on a source body, i.e. mass m_1. In case the motion of a receiving body, i.e. mass m_2, is of concern, this becomes an isolation problem. In case the motion of a source body, i.e. mass m_1 is of concern, this turns into an absorption problem and mass m_2 becomes an inherent part of the absorber.
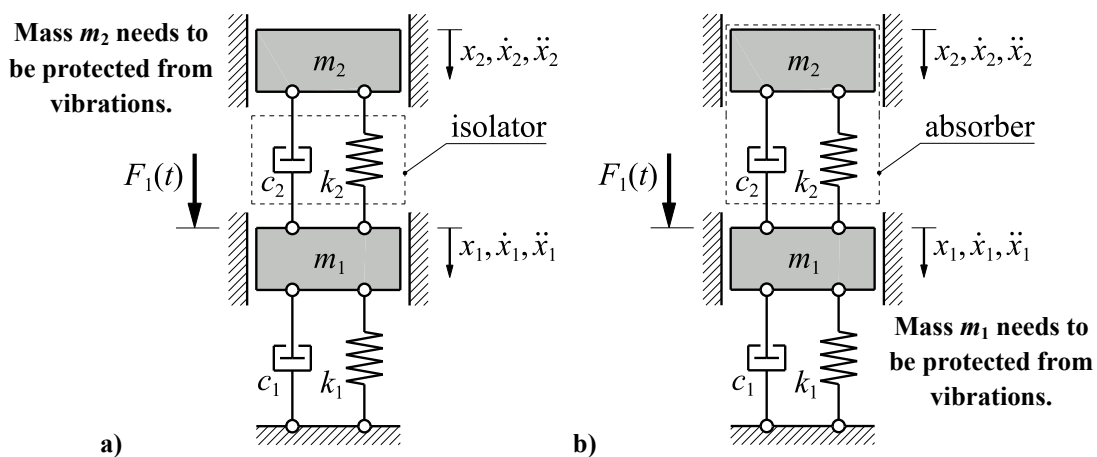

Figure 1.1.   Analogy of 2DOF vibration systems: a) isolation problem, b) absorption problem

In case the structure is made active through the use of actuators and sensors connected by a feedback loop, the main advantage of active control may be exploited [33]. This main advantage is to reduce the sensitivity of the output to the disturbance input. Depending on the circumstances, active structures may be cheaper or lighter than passive structures of comparable performances; or they may demonstrate the performance that no passive structure could offer [27]. As technology rapidly develops and with the introduced availability of low-cost electronic components, it is likely that there will be a growing number of applications where active solutions and applications will become cheaper than the passive ones, for the same or better level of performance. However, it should not be readily concluded that active approach will always be better compared to passive approach and that a control system can substantially compensate for a poor or inadequate design of a structure [27],[34]. In most cases, an initially poor design will remain that way, whether inherently active or passive. Consequently, an active solution should normally be considered only after all other passive means and possibilities have been exhausted [35]. It must be accented that feedback control can compensate for external disturbances only in a limited frequency band that is called the bandwidth of the control system. Outside the bandwidth, the disturbances may even be amplified by the control system, i.e. control spillover [27] may occur.

The disturbance may be either deterministic, such as the unbalance of a motor, or random as in a passenger car riding on a rough road [33]. There are two different approaches to disturbance rejection: feedback and feed-forward. For deterministic sources of excitation which can be measured, such as a rotating unbalance, feed-forward control can be very effective. Feed-forward control can also be effective for the control of random disturbances provided that reference signals well-correlated to the disturbance can be obtained. Feedback strategies for active isolation can be used to control both deterministic and random disturbances, and they do not need a direct measurement of the disturbance [27].

The basic principle of feedback control is as follows: the output of the system is compared to the reference input, and the error signal = (reference input − output), is passed into a compensator and applied to the system, along with the disturbance. The design problem consists of finding the appropriate compensator such that the closed loop system is stable and behaves in the appropriate manner [27]. Probably the most common active approach to stabilize a control system is to introduce a feedback loop around the control path [34].

A special case of the feedback principle known as direct velocity feedback (DVF) may be applied for enhancing vibration isolation effect. This is done by feeding back the

absolute velocity of the payload that needs to be isolated from vibration and acting on payload through actuator which exerts force opposite in direction to sensor-measured absolute velocity. In such case, the feedback loop produces the sky-hook active damping effect [26],[27]. This control law is called sky-hook because the actuator control force $F_{act} = -g \cdot v_{payload}$ is similar to that of a viscous damper of a constant gain g (i.e. active feedback gain, in $kg\,s^{-1}$) attached to the isolated payload and a fixed reference terminal (i.e. *hook*) in the sky [37]. In other words, with DVF control law, for a collocated sensor and actuator control system [27], the sensor output (velocity) is multiplied by a control gain g and fed back to the collocated actuator. Hence, the idea behind the sky-hook damper is that the ideal DVF isolator would enforce the payload to maintain a stable posture as if it was suspended by a fixed imaginary hook in the sky [38], unaffected by the disturbance. Since an actual sky-hook is either impractical or impossible to realize in real engineering applications (e.g. vehicle suspension), these type of active isolation systems are in practice based on the described feedback loop. Theoretically, for a case where the coefficient of the damper reaches an infinite value, the payload would be in a state where it is completely fixed to the imaginary hook, thus the payload will not vibrate.

When a signal correlated to the disturbance is available, feed-forward adaptive filtering constitutes an eligible alternative to feedback for disturbance rejection. It was initially developed for noise control, but it is also proven to be efficient for vibration control [27]. This method relies on the availability of a reference signal correlated to the primary disturbance. This signal is passed through an adaptive filter, and the output is then applied to the system. The filter coefficients are adapted in such a way that the error signal is minimized. The goal of this control scheme is to produce a secondary disturbance such that it cancels the effect of the primary disturbance at the location of the error sensor. Furthermore, there is no guarantee that the global response is also reduced at other locations. Unless the response is dominated by a single vibration mode, there are locations in the structure where the response may be amplified. Unlike the active damping approach which can only attenuate the disturbances near the resonances, feed-forward works for any frequency and attempts to cancel the disturbance completely by generating a secondary signal of opposite phase [27].

1.2.   Stability of Dynamic Systems

If dynamic systems are made active, they may become unstable for a certain unfavourable combination of system parameters. Stability is one of the most important

characteristics for any active system [31]. Although many definitions can be given for the term *stability* depending on the kind of system or the point of view, this definition is given with regards to linear and time-invariant (LTI) systems (i.e., systems for which the mass, damping, and stiffness parameters do not change or vary with time). A system is defined to be asymptotically stable (called stable in control literature) if its free-vibration response approaches zero as time approaches infinity. A system is considered to be unstable if its free-vibration response grows without bound (approaches infinity) as time approaches infinity. Finally, a system is said to be stable (also called marginally stable in control literature) if its free-vibration response neither decays nor grows, but remains constant or oscillates as time approaches infinity. It is evident that an unstable system whose free vibration response grows without bounds can cause damage to the system, adjacent property, or even human life.

The most common criteria for determining the stability of dynamic control systems are Routh-Hurwitz [27],[31],[34] criterion, and Nyquist [27],[34] criterion. The Routh–Hurwitz stability criterion is an algebraic test that provides a necessary and sufficient condition for the stability of a LTI control system. The Routh test is an algorithm used to determine whether all the roots of the characteristic polynomial of a closed-loop linear system have negative real parts. Hurwitz test consists of arranging the coefficients of the polynomial into a square Hurwitz matrix, and investigating whether the polynomial is stable if and only if the sequence of determinants of its principal sub-matrices are all positive. Hurwitz criterion becomes computationally inefficient and cumbersome for large degree polynomials. The Nyquist stability criterion is a graphical technique for determining the stability of a dynamical system. It only considers the Nyquist plot of the open-loop systems, thus it can be applied without explicitly computing the poles and zeros of either the closed-loop or open-loop system. The Nyquist criterion is utilized in electronics and control system engineering, as well as other areas for designing and analyzing systems with feedback. Analogue to Hurwitz test, Nyquist test is also restricted to LTI systems exclusively.

1.3.   Optimization of Dynamic Systems: H_2 and H_∞ Criteria

Using a passively tuned dynamic vibration absorber (DVA) is one way to suppress random vibration in mechanical and civil structures [39]. The traditional damped dynamic vibration absorber (DVA) or tuned mass damper (TMD) is an auxiliary mass–spring system with a damper added between the absorber mass and the primary mass. Its basic function is to limit the vibration amplitude of the primary mass [40]. Passive tuned vibration absorbers were

proposed by Frahm in 1911 [41] and have been widely used to control structural vibrations ever since [18].

In 1928, Ormondroyd and Den Hartog reported that the damping of the DVA had an optimum value for the minimization of the amplitude response of the SDOF system at resonance [39],[40]. This optimization criterion is now known as H_∞ optimization. The fixed-points theory of Den Hartog [42] is commonly used for the determination of the optimum tuning frequency and damping ratios of the DVA attached to a SDOF vibrating system.

On the other hand, H_2 optimization of the vibration absorber has the objective function of minimizing the mean vibration energy of the primary structure under white noise excitation. To extend the application of the DVA, in 1963, Crandall and Mark [43] proposed another optimization principle of the damped DVA. They utilized the objective function of minimizing the mean vibration energy, i.e. the mean square motion of the primary structure under white noise excitation of the PSD excitation [39] over the entire frequency range. Authors found the optimized tuning frequency and damping ratios for the SDOF system, which is now called H_2 optimization [44]-[47] of dynamic vibration absorber. The exact solution of the H_2 optimization for the traditional DVA attached to an undamped primary system was derived by Warburton [48].

The H_2 and H_∞ optimization criteria are normally considered if the vibrating system is subjected to random excitation such as wind loading [40]. Cheung and Wong derived the H_∞ and H_2 optimum parameters of the traditional DVA for suppressing vibrations in plates [39]. Studies which incorporate H_2 optimization usually employ the minimization of specific kinetic energy (i.e. vibration velocity amplitudes) [44],[45]. However, studies dealing with minimization of displacement amplitudes can also be found in the literature [46],[47].

1.4. Inerter Concept and its Applications

Inerter is a novel mechanical element in the theory of mechanical networks. Its proposal is attributed to Professor Malcolm C. Smith from Cambridge University. From Smith's seminal paper [1], it is defined as "a mechanical two-terminal, one-port device with the property that the equal and opposite force applied at the terminals is proportional to the relative acceleration between the terminals". The constitutive relation and the kinetic energy E_k stored by the inerter respectively are given with relations

$$F_{\text{inerter}} = b(\dot{v}_1 - \dot{v}_2) = b(a_1 - a_2), \quad E_{k,\text{inerter}} = \frac{b}{2}(v_1 - v_2)^2, \qquad (1.1a,b)$$

where constant *b* is called the *inertance* with the SI units in kilograms, and v_1 and v_2 are velocities. Relations from Eq. (1.1) are related to inerter scheme denoted in Figure 1.2.
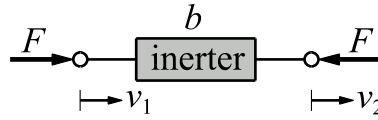

Figure 1.2.   Inerter scheme and its working principle

Various researchers used different symbols and schemes for inerter representations. Most common schematics are denoted in Table 1.1 and tied to corresponding references. It seems that simple rectangle, analogue to Figure 1.2, is the most common inerter representation, as it is conceived in Smith's original paper [1]. "Held" rectangle is also used [18] in order to imply *relative* acceleration between the terminals. Rotating flywheel is another convenient inerter representation and it implies its possible physical realization [19].
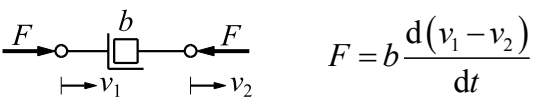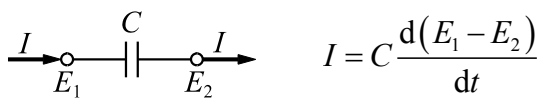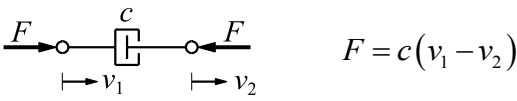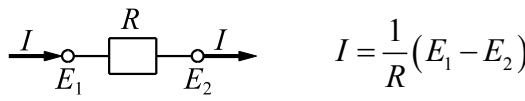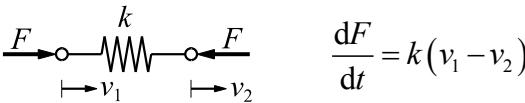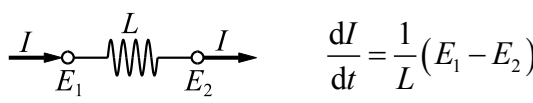
Table 1.1.   Different schematics for ideal inerter depiction

Type	Rectangle	"Held" rectangle	Rotating flywheel
Scheme			
Literature	[1]-[3],[5],[7],[9],[12]-[15]	[18]	[19],[49]-[52]

The main motivation for proposing the inerter was the incompleteness of the force/electrical current analogy between mechanical and electrical systems [1]. It is known that mechanical and electrical networks operate with similar dynamics. The force *F* and velocity *v* in mechanical systems can be analogized to the current *I* and voltage *E* in the electrical systems, respectively [53]. Hence, the spring and damper in mechanical systems can be analogized to the inductor and resistor in electrical systems, respectively. However, a mechanical device truly analogue to the capacitor in electrical systems was missing. Historically, the mass is seen as the mechanical element corresponding to the capacitor in electrical systems [2]. However, from Newton's Second Law, the acceleration of the mass is relative to a fixed point in the inertial frame. This means the one terminal of the mass is the ground and the other terminal is the centre of the mass. Hence, the mass cannot be considered as a genuine two-terminal device. The electrical element that corresponds to the mass is actually a *grounded* capacitor, which is a particular analogy valid only for this specific case. Due to this restriction between force/current analogy, the inerter has been proposed. From the definition of inerter, it can be noted that inerter is a genuine two-terminal device which has similar dynamics to the capacitor. By proposing inerter, the force/current analogy is completed, and the spring-damper-inerter mechanical networks can be directly represented as

inductor-resistor-capacitor electrical networks [1]. The correspondence analogy that includes the inerter is shown in Table 1.2, which is adopted and modified from [1]-[3],[53]-[55]. It should be accented that although inerter is initially motivated by the force/current analogy, its properties are not purely dependent on this analogy. Consequently, inerter possesses some unique functions for mechanical systems, e.g. providing large apparent mass without actually increasing the mass of the structure [56], and representing the mechanical equivalent of the springs as an energy-storing element [53], noted in Eq. (1.1b).

Table 1.2. Analogy between mechanical and electrical networks

Mechanical	Electrical
inerter with inertance *b*, kg	**capacitor with capacitance *C*, F**
$F = b\dfrac{\mathrm{d}(v_1 - v_2)}{\mathrm{d}t}$	$I = C\dfrac{\mathrm{d}(E_1 - E_2)}{\mathrm{d}t}$
damper with damping coefficient *c*, N s m⁻¹	**resistor with resistance *R*, Ω**
$F = c(v_1 - v_2)$	$I = \dfrac{1}{R}(E_1 - E_2)$
spring with stiffness *k*, N m⁻¹	**inductor with inductance *L*, H**
$\dfrac{\mathrm{d}F}{\mathrm{d}t} = k(v_1 - v_2)$	$\dfrac{\mathrm{d}I}{\mathrm{d}t} = \dfrac{1}{L}(E_1 - E_2)$

The introduction of inerter provides a truly novel mechanical concept. The equally important issue is how to construct a real mechanical structure or device possessing the same or at least similar properties with the definition and concept of inerter. The procedure of constructing a physical embodiment of inerter is referred to as *realization*. Up to present, there are mainly three types of realizations of inerter [53]. These are the rack and pinion inerter [1]-[3],[57], the ball-screw inerter [3],[51],[57]-[60] and the hydraulic/fluid inerter [7],[8],[61]. Fundamental schematics of the rack and pinion, and ball-screw embodiments of the inerter are denoted in Figure 1.3a) and b) respectively.
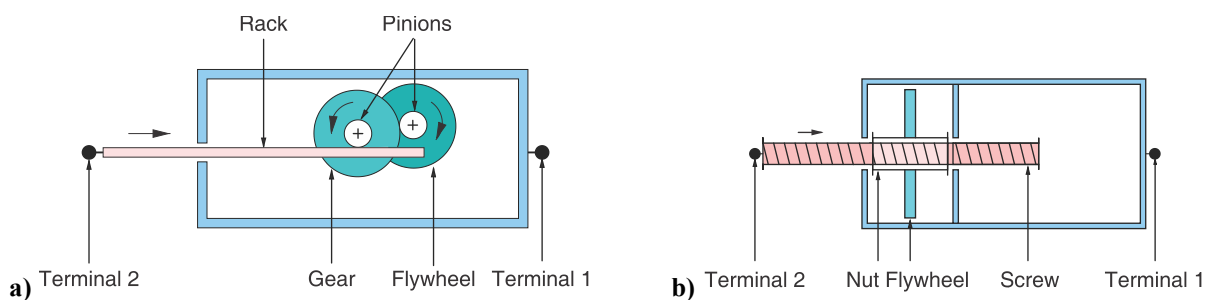
Figure 1.3. Simple schematics of the inerter [3],[57]: a) rack and pinion inerter, b) ball-screw inerter

Figure 1.4 shows the more detailed schematic (a) and prototype physical embodiment (b) of a rack/pinion type inerter from Figure 1.3a). In this inerter, a plunger slides into a cylinder which drives a flywheel through a system of rack/pinion and gears [1].
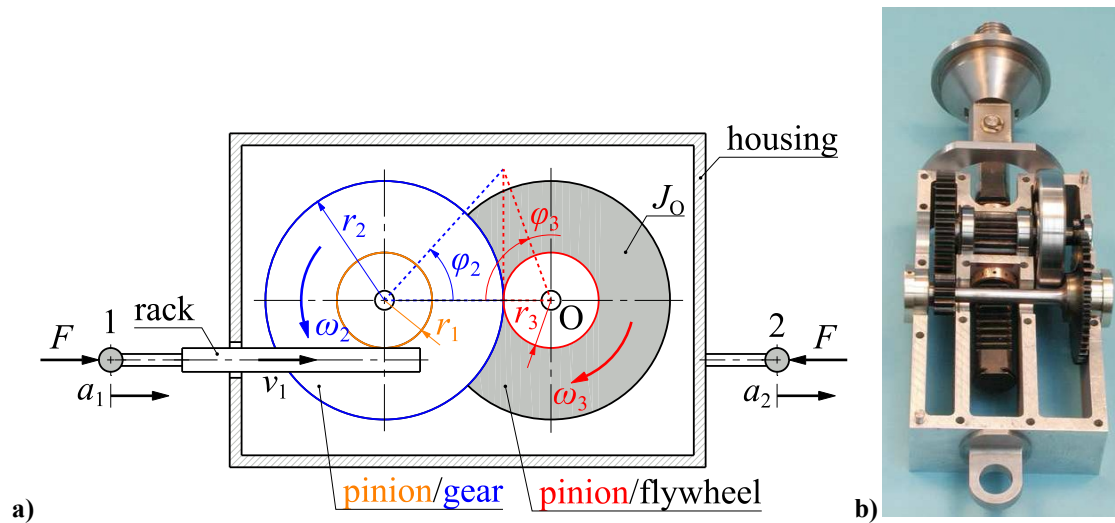
Figure 1.4. **Rack and pinion inerter: a) detailed schematic, b) mechanical prototype [2],[57]**

By assuming the ideal inerter performance and thus neglecting the masses of the housing, the plunger, the rack/pinion couple and finally the gears; the inertance b of assembly from Figure 1.4, and its dynamic can be respectively approximated as

$$b = \left(\frac{r_2}{r_1}\right)^2 \frac{J_O}{r_3^2} = i^2 \frac{J_O}{r_3^2}, \quad F = b(a_1 - a_2), \qquad (1.2a,b)$$

where r_1 and r_3 are pinions radii, r_2 is gear radius, J_O is flywheel mass moment of inertia, and $i = r_2/r_1$ is the gear ratio. Moreover, considering the structure of Eq. (1.2a), denominators r_1 and r_3 should be as small as possible, and numerators r_2 and J_O should be as large as possible, in order to approach the ideal inerter concept in a quadratic manner.

A physical embodiment of a rack and pinion inerter shown in Figure 1.4b) is manufactured at the Cambridge University Engineering Department. The total mass of the mechanism is ~3.5 kg, while the realized inertance is ~725 kg [53].

Furthermore, Figure 1.5a) presents schematic of inerter b combined with dashpot c and springs k and k_1, while Figure 1.5b) denotes its mechanical prototype realization [2],[3]. Rack and pinion type inerter from Figure 1.4b) is employed into this assembly.
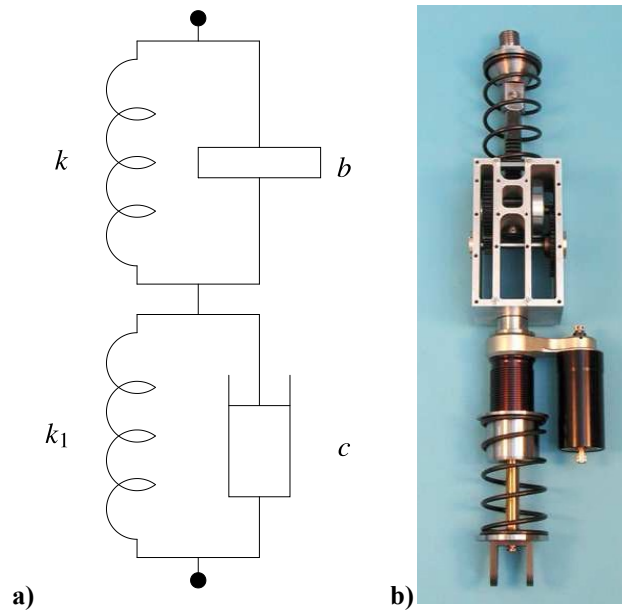
Figure 1.5.   **Inerter in series with damper and combined with centring springs in parallel [2],[3]: a) circuit diagram, b) mechanical assembly prototype with rack and pinion inerter**

The rack and pinion inerter can bear large loads [2],[3],[53]. Consequently, a relatively large inertance can be realized. However, the inherent stick/slip friction [19] and the backlash/clearances between the gears may significantly increase the nonlinearities of the inerter or add damping. Various effects of inerter nonlinearities are thoroughly discussed in [58],[60],[62]-[66]. A possible viable solution is to replace the rack and pinion driving motion by a ball-screw type, shown in Figure 1.3b). Thus, the second generation of the mechanical inerter, namely the ball-screw inerter, was proposed [3]. Compared with the rack/pinion inerter, the friction is greatly reduced in a ball-screw type inerter, and the detrimental backlash can be eliminated by pre-loading [53]. Figure 1.6a) presents more detailed scheme from concept in Figure 1.3b), while Figure 1.6b) and Figure 1.7 show a prototype manufactured at the Cambridge University Engineering Department. The actual mass of the prototype device is just ~1 kg, while the practically realized inertance is ~180 kg [53].
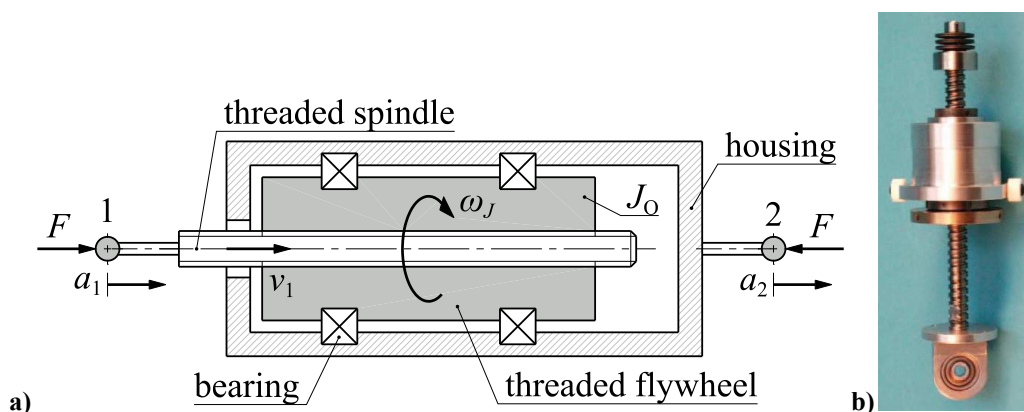
Figure 1.6.   **Ball-screw inerter: a) detailed schematic, b) mechanical prototype [3]**

Similar to the rack/pinion inerter, the inertance of the ball-screw inerter can be represented as the product of a transmission ratio and the flywheel's moment of inertia

$$b = \left(\frac{2\pi}{p} \right)^2 J_O = i^2 J_O,$$ (1.3)

where p is the screw/thread pitch (SI units of m/rev), term $2\pi/p$ is the transmission ratio of the ball-screw, and J_O is flywheel mass moment of inertia. Mass of the device is disregarded.
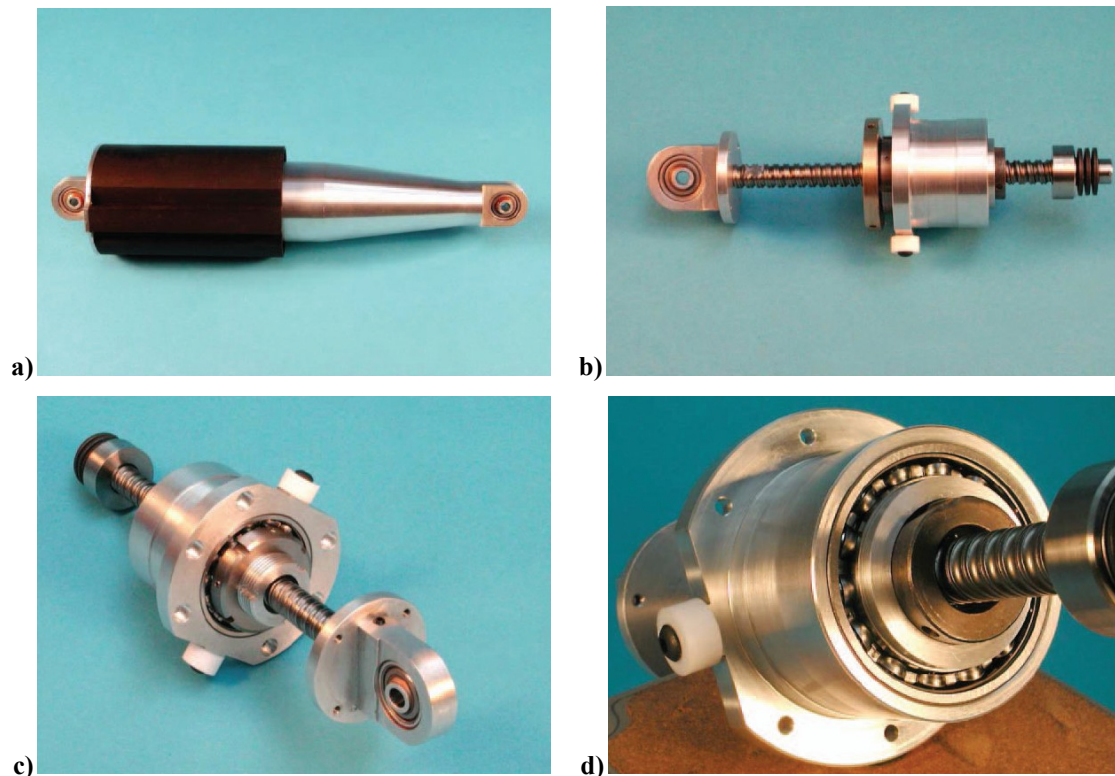
Figure 1.7. **Ball-screw inerter made at Cambridge University Engineering Department; mass ≈ 1 kg, adjustable inertance ≈ 60–240 kg [3]: a) complete inerter with outer case, b) ball-screw, nut and flywheel, c) flywheel removed, d) thrust bearing**

Third type of flywheel-based inerter is the hydraulic inerter. It was proposed, realized and experimentally validated in [7], where the hydraulic transmission motion is employed. Device was assembled from a hydraulic cylinder, motor and helical pipes. The dynamic of an ideal hydraulic inerter was derived. On the basis of the obtained results, authors reported that the proposed hydraulic inerter is shown to be effective.

In summary, the fundamental working principle and a common feature of the flywheel-based inerters is converting the linear motion into rotational motion and vice versa, and storing kinetic energy into a flywheel by using its rotary inertia. A flywheel is driven by a transmission structure (the rack/pinion, the ball-screw, and the hydraulic type), and the moment of inertia of the flywheel is magnified by the transmission mechanism to realize the

effect of the inertance. The relative acceleration between two terminals creates a force in the opposite direction of the motion, which is proportional to the inertance constant. Hence, there are two main requirements for the flywheel-based inerter transmission mechanism. The first one is the ability to transform the linear motion into rotary motion. The second one is the ability of magnifying the inertia of the flywheel, commonly through gear ratio or transmission ratio.

Inerter has been successfully applied in Formula One racing car suspensions [3]. This yielded significant performance gains in handling and grip. At the 2005 Spanish Grand Prix, McLaren team achieved a victory on the first racing deployment of the inerter. During that time, to keep the technology secret from its competitors, a smart decoy or code-name "*J*-damper" was invented for the inerter. At the time of introduction, there was much speculation about what the *J*-damper actually was. The Cambridge and Formula One connection was finally revealed in 2008 and it was then confirmed that *J*-damper is in fact – an inerter [3]. One can insinuate that cleverly chosen prefix "*J*" probably stands for standard mass moment of inertia SI nomenclature. Moreover, "damper" is just a misleading title, as inerter does not dissipate energy, but analog to electrical capacitor – it rather stores and releases it. Nowadays, the inerter has been embraced and employed by other Formula One teams [3]. From the mechanical control point of view, the introduction of inerter provides an extra parameter compared with the traditional mass-damper-spring (MDS) mechanical systems [53]. This potentially enables that the performance of the inerter-damper-spring (IDS) mechanical networks is always superior or at least equivalent to traditional damper-spring networks. In case this does not hold, or performance benefits due to inerter influence are negligible, the inerter may be removed in order to simplify the inerter-damper-spring networks into the damper-spring networks. It is well documented that inerter can provide significant performance improvements for various mechanical systems [53], including vehicle suspensions [1], landing gears [67],[68], wind turbines [69],[70], bridge vibration control systems [71], storage tanks [72], tall multi-storey buildings [24],[73], cables [74], energy harvesters [5],[75], and general vibration control (i.e. absorber/isolator) systems [76]-[84].

Vehicle suspensions are essential parts of a vehicle, determining the overall performance of a vehicle, which is also one of the main application fields of inerter. This is evident in numerous inerter-related suspension performance benefits reported by various researchers [2],[21]-[23],[38],[54],[58]-[60],[64],[85]-[95]. In Smith and Wang [2], the performances of six inerter-based networks applied as suspension struts were evaluated and

compared with the traditional spring-damper strut. It was reported that more than 10% improvements can be obtained by using inerter, in terms of the ride comfort and handling performance measures. With regard to previously introduced skyhook concept [27], Hu et al. [88] investigated the comfort-oriented vehicle suspension design problem by using a skyhook inerter configuration. The logical basis of the skyhook inerter is to use a grounded inerter to virtually increase the sprung mass of a vehicle, as it is analytically demonstrated that increasing the sprung (i.e. suspended car body) mass can always improve the ride comfort performance. Since it requires a fixed inertia reference which may be impossible to achieve in practice, the skyhook inerter can be implemented by active means. To approximate the skyhook inerter configuration, active inerters are hence employed. Analogue to Brzeski et al. who proposed inerter which enables change of inertance [13],[14], Authors Li et al. [91] studied the suspension performances with an adaptive inerter under the assumption that the inertance may be adjusted in real-time. A quarter-car model with an inerter installed in parallel with a spring and a damper was considered. Benefits were reported when compared to non-adjustable inerter configuration. Innovative concepts such as "on-off" switchable inerters [93] as components of vehicle suspensions and their performance benefits were also studied.

Additionally, the interest in passive network synthesis has also been revitalized since inerter introduction [53]. Due to the completeness of the mechanical-electrical analogy, advanced supplements to existing vibration control concepts are reported. These are: tuned inerter damper (TID) [12],[96], enhanced type of traditional tuned mass–damper (TMD) [97] to tuned mass–damper–inerter (TMDI) [13],[14],[75],[98]-[103], tuned inerter-based damper (TIBD) [104], and inerter–based dynamic vibration absorber (IDVA) [15]. Concepts which incorporate mechatronic inerter embodiment were also proposed, e.g. electrically synthesized tuned inerter damper (E-TID) [5] and electromagnetic resonant shunt tuned mass-damper-inerter (ERS-TMDI) [46]. A new hydraulically interconnected inerter-spring-damper suspension (HIISDS) [105] was developed to compensate for traditional passive suspension limitations, such as the imbalance of ride performance and handling stability. In [106], a novel inerter-based control system, namely a tuned heave plate inerter (THPI), is proposed for control of semi-submersible platforms (SSP) heave vibrations. In this system, an inerter device is added to the THP to further improve the performance of conventional THP. A novel waterwheel inerter was developed to realize the suggested device. The analytical results showed that THPI is more effective to mitigate the heave motion of SSP compared to the

conventional methods, and the novel waterwheel inerter is capable of generating a large apparent mass by using a relatively small corresponding waterwheel.

Since the inerter may generate a large apparent mass, Chen et al. [56] investigated the influence of inerter on natural frequencies of dynamic system. Authors have shown that the natural frequencies of a discrete parameter mechanical system with an inerter can always be diminished by increasing the inertance value. This suggested that the employment of an inerter in an active vibration absorber could be used to improve its control stability by lowering the resonance frequency of the device without softening the coupling spring [18]. The influence of inerter on natural frequencies was further studied by Hu et al. [107]. Authors investigated the problem of natural frequency assignment for mass-chain systems with inerters. It was reported that mass-chain systems with inerters may have multiple natural frequencies, which is different from conventional mass-chain systems (without inerters) whose natural frequencies are always simple. Furthermore, Suciu and Tsuji [108] investigated the influence of inertance on the amplitude of vibration, phase angle, natural frequency, damping ratio, and logarithmic decrement of one degree of freedom (1DOF) vibration system equipped with inerter of variable inertance. Authors noted that the inerter decreases the natural frequency of the undamped system and also of the damped system if the damping ratio is below ~0.707. On the other hand, the inerter increases the natural frequency of the damped system if the damping ratio exceeds ~0.707.

It is well known that DVA produces an anti-resonant frequency [27]. This phenomenon is more prominent if the damping in the system is low. By choosing the stiffness and the mass of a single degree of freedom (SDOF) DVA accordingly, one can place anti-resonance (i.e. zero) at any chosen frequency [27]. However, as noted before, the DVA also adds another DOF and consequent resonant frequency (i.e. pole) to the system [27]. Moreover, there is an alternative method to generate anti-resonant frequencies in a system by *inertial coupling* [109]. Vibration isolators that utilize inertial coupling to generate anti-resonant frequencies were first developed in the 1960s by researchers in the aerospace industry. The development of a novel kind of vibration isolator was pursued due to strict requirements on stiffness and mass of the isolators used in the aerospace industry [109]. This new system was invented and proposed by Flannelly [110], and called "Dynamic Anti-resonant Vibration Isolator" (DAVI). DAVI utilizes a levered mass–spring combination to generate an anti-resonant frequency in the system. Anti-resonance occurs when the inertial force generated by the levered mass completely cancels the spring force. If damping in the

system is negligible, the effect becomes more prominent. This phenomenon occurs at a particular frequency, which depends on the added mass of the isolator, the lever ratio and the spring stiffness. Unlike DVA which produces an additional DOF, DAVI is implemented strictly on the load path. Thus, rigidly coupled motion occurs and the number of DOF in the system is not increased. When DAVI is introduced in a SDOF system, inertial forces generated by the levered mass increase the effective/apparent mass of the system. Thus, the resonant frequency decreases and the isolator is capable of operating in a lower-frequency range. Applications of DAVI in the aerospace industry can be found in the literature [110]. For example, Rivin [35] reported that the rectilinear motion of a primary structure can be transformed into rotary motion by a flywheel and a ball-screw, which can also be used to generate the desired inertial forces to generate a zero in the system. The rotational analogue of the leverage mechanism of Flannelly [110] is the low helix angle of the ball-screw. Consequently, both Rivin and Flannelly concepts yield inerter-like behaviour similar to one introduced by Smith [1] and Smith and Wang [2]. Historically, Flannelly (1967) concept [110] thus predate by far the first inerter embodiment conceived and realized by Smith (2002) [1]. Moreover, Rivin (2003) concept [35] predates the ball-screw inerter conceived and realized by Chen et al. (2009) [3]. The first noted concept of "relative mass" in the literature can be attributed to Schönfeld [4] (1954).

1.5.   Vibration Fatigue

Mechanical vibrations can span displacement amplitudes from meters in civil engineering practical situations, to nano-meters in precision engineering applications. Vibrations detrimental effects on dynamic systems and structures may be of various natures, where failure is one of the most important ones [27]. Vibration-induced structural failure may occur due to excessive stress/strain during transient or steady-state events (e.g. building response to earthquake loading), by instability due to particular operating conditions (e.g. bridge flutter under wind excitation, reported in Tacoma Narrows bridge catastrophe during wind-induced vibration [31]), or simply by fatigue (e.g. flexible mechanical parts in operating machines). The engineering structure or machine component exposed to vibration can fail because of material fatigue resulting from the cyclic variation of the induced stress/strain. Whenever the frequency of external excitation coincides with a natural frequency of machine or mechanical structure, there may appear a phenomenon known as resonance which could lead to additional excessive deflections and may result with eventual catastrophic failure [31].

Any periodic function can be decomposed into Fourier series and presented as a summation of finite number of sinusoidal waves with multiple frequencies and different amplitudes and phase angles. In stochastic processes, the phase angles are of random nature [32]. Since the phase angles do not contribute to energy, the power spectral density (PSD) function alone is ordinarily used. PSD is obtained by taking the squared modulus of the Fast Fourier Transform (FFT). PSD of a random signal $x(t)$ gives a measure of the speed with which the signal changes in the frequency domain [31]. The FFT outputs a complex number given with respect to frequency, however only the amplitude of each sine wave is retained in a PSD. All phase information is consequently discarded. Operating with a PSD proves to be rather beneficial when working with complicated and computationally expensive FEM models. Hence, the calculation of the frequency response functions (FRFs) is convenient and much faster than a long-term transient dynamic analysis in the time domain [32]. When loading conditions are prescribed in the form of PSD which is defined in a frequency domain, structural response of systems can be computed by using the transfer function (TF), i.e. FRF of target systems and PSD of excitation loads.

A spring is a type of mechanical link, which is in most applications ideally assumed to possess negligible mass and damping [31]. It is one of the most important fundamental mechanical components found in many practical applications [111]. The most common type of spring is the helical-coil spring used in retractable pens and pencils, staplers, and suspensions of cars, freight trucks and other vehicles. Springs in the vibration isolation systems are subjected to random dynamic loads during service. The crack may initiate and eventually propagate at a stress concentration location of the spring, leading to a potentially catastrophic fatigue failure, especially evident in case of resonant conditions. In order to evaluate the vibration induced fatigue in the spring, it is necessary to designate stiffness, stress and damping parameters of the dynamic system. The springs must expectedly withstand relatively long exploitation period. Thus, appropriate high cycle fatigue (HCF) [32] calculation method (above ~10^3 life cycles) is usually used for evaluating fatigue-life. Biaxial shear-governed fatigue life criterion is commonly utilized for spring fatigue estimation where most stressed region is normally located at the inner side of the helix [111]. Multiple stress correction factors for helical spring are proposed in the literature which account for influence of this highly stressed region [111]-[113]. Moreover, an unresolved discussion is noted in the literature [111] whether using the aforementioned stress correction factor may yield with overly conservative fatigue life estimation.

1.6.   Dissertation Structure Overview

This thesis is structured according to Scandinavian PhD model (a.k.a. *multi-paper*, i.e. *collection-of-papers* PhD model).

With regard to previously presented literature overview, the primary aim of dissertation is to study and determine performance benefits of inerter in general LTI passive and active vibration isolation systems. Moreover, the stability of special class of vibration isolation systems known as sub-critical systems [26] is investigated. These systems can be described as systems that have the uncoupled fundamental natural frequency of a body that is to be protected from vibrations (i.e. receiving body), larger than the uncoupled fundamental natural frequency of the body that is the source of vibrations (i.e. source body). It is determined whether using an inerter can stabilize the otherwise conditionally stable feedback loop and enable improved performance of the active vibration isolation system. Investigation is enriched by studying vibration fatigue induced effects in coupling components and isolator components of the receiving body, i.e. cylindrical coil spring. Inerter influence in prolonging fatigue life of dynamic systems' deformable components, i.e. springs, is determined. Broadband H_2 optimization criterion is employed where possible. Additionally, helical spring stress and stiffness analytical expressions are investigated. Finally, novel expressions which improve the accuracy of standard stress and stiffness expressions for helical springs are proposed. Study is verified by performing accompanying numerous parametric finite element based-calculations and comparing the results to ones obtained analytically.

Chapter 2 provides detailed discussion on applied methods and obtained results. First subchapter serves as an introductory paragraph and sets the framework for further conducted research. Each adjacent subchapter is dedicated to providing point to point review, recapitulation and additional information on its corresponding published paper.

In Chapter 3, unified conclusions of dissertation are given. Various general inerter benefits are emphasized for numerous vibration isolation applications.

According to Scandinavian model, CC/SCI scientific papers attached at the end serve as an obligatory Appendix and provide for core substance and basis of this dissertation.

2.   Discussion on Methods and Results

This chapter is comprised of the topics which directly correspond to published papers which are attached at the end of this dissertation:

- Fundamental Mathematical Model for Broadband Optimization of the Vibration Isolation (Introductory Paragraph),

- Performance and Stability of Inerter-Based Passive and Active Isolator Systems (Paper 1),

- Enhancing the Vibration Induced Fatigue Life of Helical Spring due to Inerter in the Isolator (Paper 2),

- Comparison of Different H_2 Optimization Criteria With Regard to Vibration Fatigue and Numerical Verification (Paper 3),

- Inerter Benefits in Kinematically Excited Systems and Isolator Helical Spring Novel Stress and Correction Factors (Paper 4).

Supplementary material with regard to conducted research and some findings omitted in published papers due to their length are also provided. Some of the material is reproduced from author's own published papers tied to this Dissertation.

2.1.   Mathematical Model of the Vibration Isolation Problem

Figure 2.1 shows general multi-degree of freedom (MDOF) axial vibration system under excitation. The number of DOFs is n.

Mass m_1 is coupled to the lower fixed reference through dashpot c_1 and spring k_1. Mass m_n is coupled to the upper fixed reference through dashpot c_{n+1} and spring k_{n+1}. Every mass is interconnected to its adjacent mass by dashpot c_n and spring k_n. General random forcing $F_n(t)$ acts upon each mass.
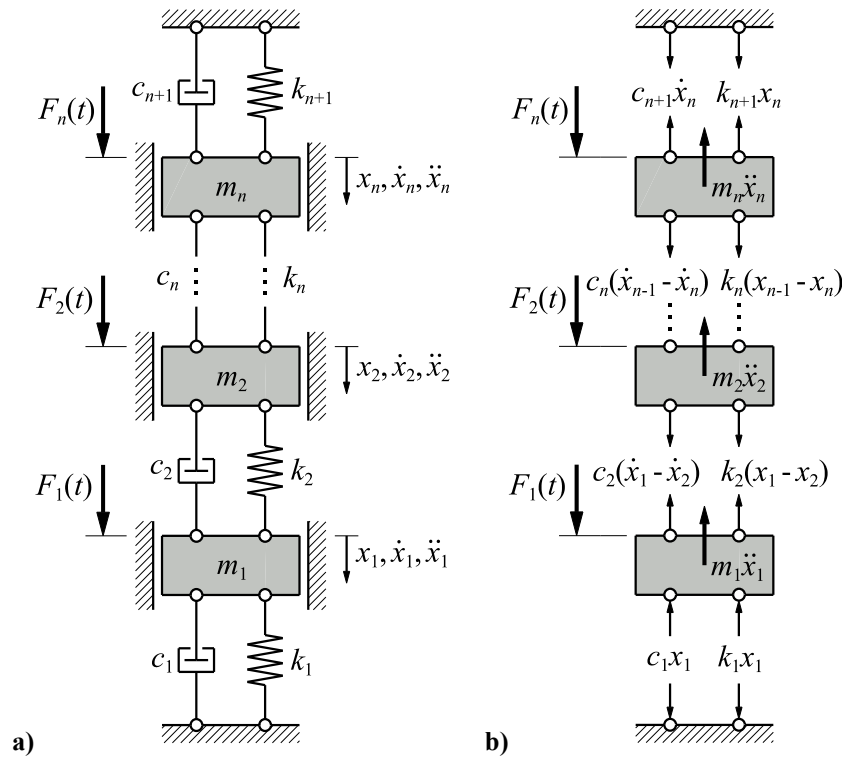
Figure 2.1.   **MDOF discrete vibration system: a) scheme, b) free-body diagram, $x_n < x_{n+1}$**

The equations of motion (EOM) [27],[31] for the MDOF vibration system in Figure 2.1 can be written in the matrix form as

$$\mathbf{M}\ddot{\mathbf{x}}(t) + \mathbf{C}\dot{\mathbf{x}}(t) + \mathbf{K}\mathbf{x}(t) = \mathbf{F}(t), \tag{2.1}$$

where $\mathbf{M}$ is the global mass matrix, $\mathbf{C}$ is the global damping matrix, $\mathbf{K}$ is the global stiffness matrix and $\mathbf{F}(t)$ is the excitation column force vector. Displacement of the masses $m_1 - m_n$ from static equilibrium, velocity and acceleration vectors are denoted by $\mathbf{x}(t)$, $\dot{\mathbf{x}}(t)$ and $\ddot{\mathbf{x}}(t)$ respectively. Global matrices and vectors from Eq. (2.1) are defined with

$$\mathbf{M} = \begin{bmatrix} m_1 & 0 & \cdots & 0 & 0 \\ 0 & m_2 & \cdots & 0 & 0 \\ \vdots & \vdots & \ddots & \vdots & \vdots \\ & & \cdots & m_{n-1} & 0 \\ \text{Sym.} & & \cdots & 0 & m_n \end{bmatrix}, \tag{2.2}$$

$$\mathbf{C} = \begin{bmatrix} c_1 + c_2 & -c_2 & \cdots & 0 & 0 \\ -c_2 & c_2 + c_3 & \cdots & 0 & 0 \\ \vdots & \vdots & \ddots & \vdots & \vdots \\ & & \cdots & c_{n-1} + c_n & -c_n \\ \text{Sym.} & & \cdots & -c_n & c_n + c_{n+1} \end{bmatrix}, \tag{2.3}$$

$$\mathbf{K} = \begin{bmatrix} k_1 + k_2 & -k_2 & \cdots & 0 & 0 \\ -k_2 & k_2 + k_3 & \cdots & 0 & 0 \\ \vdots & \vdots & \ddots & \vdots & \vdots \\ & & \cdots & k_{n-1} + k_n & -k_n \\ \text{Sym.} & & \cdots & -k_n & k_n + k_{n+1} \end{bmatrix}, \tag{2.4}$$

$$\mathbf{x} = \begin{bmatrix} x_1(t) \\ x_2(t) \\ \vdots \\ x_n(t) \end{bmatrix}, \quad \mathbf{F} = \begin{bmatrix} F_1(t) \\ F_2(t) \\ \vdots \\ F_n(t) \end{bmatrix}, \tag{2.5a,b}$$

where the parameters and functions in the matrices and vectors are denoted in Figure 2.1.

By assuming simple harmonic excitation and expressing the excitation and the steady-state response in the complex form $\mathbf{F}(t) = \mathbf{F}_0 e^{i\Omega t}$ and $\mathbf{x}(t) = \mathbf{x}_0 e^{i\Omega t}$, where $i = \sqrt{-1}$, and Ω is the circular excitation frequency, the direct solution of Eq. (2.1) can be written as

$$\mathbf{x}_0(\Omega) = \begin{bmatrix} x_{01} & x_{02} & \cdots & x_{0n} \end{bmatrix}^{\mathrm{T}} = \left[(i\Omega)^2 \mathbf{M} + i\Omega \mathbf{C} + \mathbf{K} \right]^{-1} \mathbf{F}, \tag{2.6}$$

where terms inside the square bracket denote dynamic stiffness matrix and $\mathbf{x}_0(\Omega)$ is the complex displacement amplitude column vector.

In this study, reduced or simplified vibration model that can be handled analytically is analyzed. The number of degrees of freedom is set to $n = 2$. Moreover, the force acting upon DOF1 is assumed to be random and broadband having a flat PSD equal to unity over all frequencies. The system from Figure 2.1 is now reduced to simple source/receiving body 2DOF configuration as discussed in e.g. [26],[27]. The assembly of m_1, c_1 and k_1 is further referred to as the *source body* and the assembly of m_2, c_3 and k_3 is further referred to as the *receiving body*. This approximation may represent a simplified reduced-order model of a system of a more complex nature which includes distributed mass, stiffness and damping parameters [26]. Furthermore, the damping of the source and receiving bodies is assumed to be fairly light, thus the effects of the source mass m_1 and the receiving mass m_2 dampers are further neglected, i.e. $c_1 \approx c_3 \approx 0$. This allows for relatively simple and transparent analytical solution without numerical approximation.

Adopting the previous simplifications and multiplying the Eq. (2.6) with the term $(i\Omega)$ yields with the complex velocity amplitudes expression

$$\dot{\mathbf{x}}_0(\Omega) = \begin{bmatrix} \dot{x}_{01} & \dot{x}_{02} \end{bmatrix}^{\mathrm{T}} = i\Omega \mathbf{x}_0(\Omega). \tag{2.7}$$

Considering the vibration isolation problem, the complex velocity amplitude $\dot{x}_{02}$, i.e. the transfer mobility function $H_i(\Omega)$, i.e. the mean square response [32] of mass m_2 from Eq. (2.7) can be written as

$$H_i(\Omega) \equiv \frac{\dot{x}_{02}(\Omega)}{F_{01}} = \frac{B_0 + (\mathrm{i}\Omega)B_1 + (\mathrm{i}\Omega)^2 B_2 + \cdots + (\mathrm{i}\Omega)^{i-1} B_{i-1}}{A_0 + (\mathrm{i}\Omega)A_1 + (\mathrm{i}\Omega)^2 A_2 + \cdots + (\mathrm{i}\Omega)^i A_i},$$ (2.8)

where $i = 4$, and coefficients $A_0 - A_4$ and $B_0 - B_3$ with respect to Eq. (2.8) are given by

$$
\begin{aligned}
A_0 &= (k_2 + k_3)k_1 + k_2 k_3 & B_0 &= 0 \\
A_1 &= c_2(k_1 + k_3) & B_1 &= k_2 \\
A_2 &= (m_2 + b_2)k_1 + (m_1 + m_2)k_2 + (m_1 + b_2)k_3, & B_2 &= c_2. \\
A_3 &= c_2(m_1 + m_2) & B_3 &= b_2 \\
A_4 &= (m_2 + b_2)m_1 + b_2 m_2
\end{aligned}
$$ (2.9a-i)

According to [43] and [48], H_2 norm i.e. specific kinetic energy (per unit mass and per unit excitation spectral force) of the vibration system at hand can be written as

$$I_i = \int_{-\infty}^{\infty} |H_i(\Omega)|^2 \, \mathrm{d}\Omega.$$ (2.10)

Closed form solutions of integral from Eq. (2.10) were derived by James et al. [114] for the degree of polynomial from Eq. (2.8) up to $i = 7$, and summarized in the book by Newland [115]. According to [115], the system whose mean square response is calculated must be a stable system. Otherwise, the obtained mean square response and consequent integrated results hold no physical value. In a passive system, no instability may occur whatsoever. In an active system, the stability must be checked pre-hand. Since the system under consideration is at the moment passive, the explicit solution to the integral from Eq. (2.10) [115] unambiguously writes as

$$\frac{I_4}{\pi} = \frac{A_0 B_3^2 (A_0 A_3 - A_1 A_2) + A_0 A_1 A_4 (2B_1 B_3 - B_2^2) - A_0 A_3 A_4 (B_1^2 - 2B_0 B_2) + A_4 B_0^2 (A_1 A_4 - A_2 A_3)}{A_0 A_4 (A_0 A_3^2 + A_1^2 A_4 - A_1 A_2 A_3)},$$ (2.11)

The effectiveness of vibration isolation is further studied by minimizing the resulting H_2 norm scalar value I_4 from Eq. (2.10), i.e. (2.11). Mathematically, this now becomes a problem of minimization over multiple variables, i.e. specifically isolator parameters.

2.2.   Optimization and Stability of Inerter-Based Isolator Systems

The analyzed vibration isolation system is shown in Figure 2.2. The system consists of a source/receiving body setup. It is analogue to a previously discussed simple system, enhanced with the addition of a passive inerter of inertance b_2 and a direct velocity feedback i.e. skyhook damping in the isolator. The skyhook damping scheme is comprised of an actuator, a velocity sensor, and a feedback loop. The actuator is mounted in parallel with the spring, dashpot and inerter. Ideal sensor-actuator transducers are assumed. The actuator force $F_{actuator}$, from Figure 2.2b), is thus given by

$$F_{actuator} = -g\dot{x}_2, \tag{2.12}$$

where g is the feedback gain. The primary force F_1 acts on the source body. The goal of the study is to minimize vibrations of receiving body, i.e. mass m_2. This is done by optimally tuning the parameters of active vibration isolation system, i.e. c_2, k_2, b_2 and g.
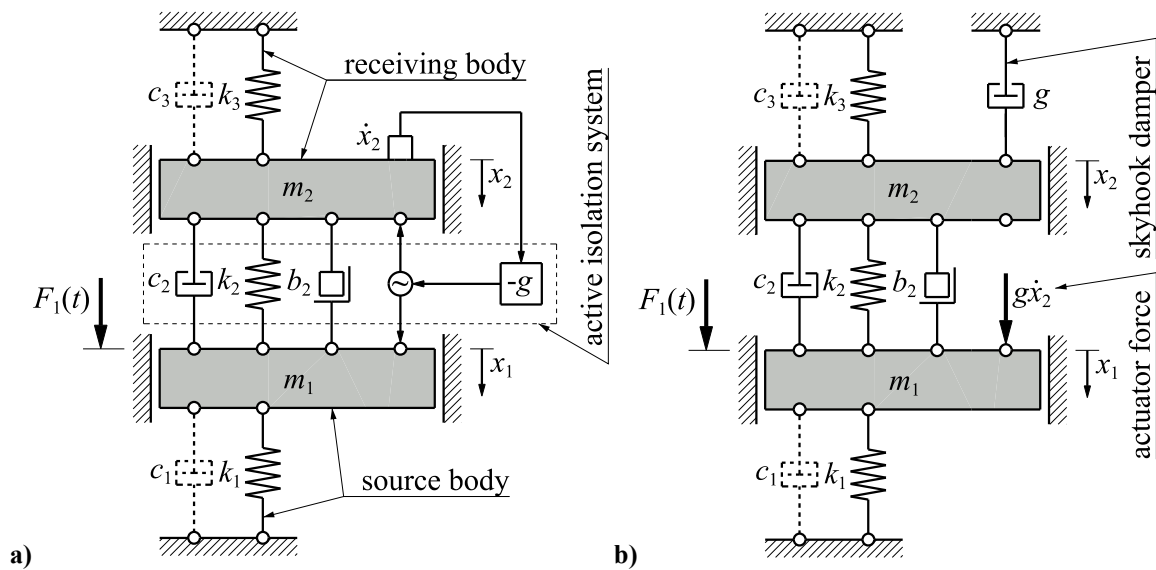
Figure 2.2.   **2DOF active vibration isolation system: a) scheme, b) analogue skyhook scheme**

The EOM for the system from Figure 2.2 are given by

$$
\begin{aligned}
\left(m_1 + b_2\right)\ddot{x}_1 - b_2\ddot{x}_2 + \left(c_1 + c_2\right)\dot{x}_1 - \left(c_2 + g\right)\dot{x}_2 + \left(k_1 + k_2\right)x_1 - k_2 x_2 = F_1 \\
-b_2\ddot{x}_1 + \left(m_2 + b_2\right)\ddot{x}_2 - c_2\dot{x}_1 + \left(c_2 + c_3 + g\right)\dot{x}_2 - k_2 x_1 + \left(k_2 + k_3\right)x_2 = 0
\end{aligned}
\tag{2.13a,b}
$$

The steady state solution of Eqs. (2.13) can be obtained analogue to Eq. (2.6), where corresponding matrices and vectors are

$$
\mathbf{M} = \begin{bmatrix} m_1 + b_2 & -b_2 \\ -b_2 & m_2 + b_2 \end{bmatrix}, \quad
\mathbf{C} = \begin{bmatrix} c_1 + c_2 & -c_2 - g \\ -c_2 & c_2 + c_3 + g \end{bmatrix}, \quad
\mathbf{K} = \begin{bmatrix} k_1 + k_2 & -k_2 \\ -k_2 & k_2 + k_3 \end{bmatrix}. \tag{2.14a-c}
$$

$$\mathbf{x} = \begin{bmatrix} x_1(t) \\ x_2(t) \end{bmatrix}, \quad \mathbf{F} = \begin{bmatrix} F_1(t) \\ 0 \end{bmatrix}. \tag{2.15a,b}$$

It can be noted that mass matrix $\mathbf{M}$ from Eq. (2.14a) is no longer purely diagonal due to the inerter influence, however it is still symmetric. Furthermore, damping matrix $\mathbf{C}$ from Eq. (2.14b) is no longer symmetric due to the skyhook damping scheme. Moreover, the corresponding undamped eigenvalue problem [31] from Eqs. (2.14a,c) is formulated as

$$\left[\mathbf{K} - \left(\omega_{n1,2} \right)^2 \mathbf{M} \right] \mathbf{x}(t) = 0. \tag{2.16}$$

For a more general approach, the following dimensionless coefficients are introduced

$$\alpha = \left(\frac{\Omega_2}{\Omega_1} \right)^2, \quad \beta = \left(\frac{\Omega_3}{\Omega_1} \right)^2, \quad \eta_2 = \frac{c_2}{2\sqrt{m_1 k_1}}, \quad \lambda = \frac{g}{c_2}, \quad \mu_1 = \frac{m_2}{m_1}, \quad \mu_2 = \frac{b_2}{m_2}. \tag{2.17a-f}$$

where α and β are squared natural frequency ratios, η_2 is the damping ratio, λ is the feedback gain normalised with respect to the passive damping dashpot coefficient c_2, and μ_1 and μ_2 are the mass and inertance ratios respectively. Furthermore, Ω_1 is the undamped natural frequency of the uncoupled source body Ω_1 (as if the source body was uncoupled from receiving body by removing spring k_2 and dashpot c_2), Ω_3 is the undamped natural frequency of the uncoupled receiving body (as if the receiving body was uncoupled from source body by removing spring k_2 and dashpot c_2), and Ω_2 is the natural frequency of the receiving body as if it was attached to a fixed reference base by the spring of stiffness k_2 only. These three natural frequencies Ω_1, Ω_2 and Ω_3 are defined as

$$\Omega_1 = \sqrt{\frac{k_1}{m_1}}, \quad \Omega_2 = \sqrt{\frac{k_2}{m_2}}, \quad \Omega_3 = \sqrt{\frac{k_3}{m_2}}. \tag{2.18a-c}$$

For special case when either k_2 or c_2 is set very high compared to the rest of the system damping and stiffness parameters, there may occur an artificial resonance Ω_a of the system with the isolator effectively locked. Consequently, masses m_1 and m_2 vibrate together in phase with equal displacements. This resonant frequency is given by the expression

$$\Omega_{a,lim} = \lim_{c_2, k_2 \to \infty} \Omega_a = \sqrt{\frac{k_1 + k_3}{m_1 + m_2}}. \tag{2.19}$$

Preliminary simulations for the system at hand are performed in the time domain by numerically solving the Eqs. (2.13). The primary forcing is defined as a harmonic sine function where $F_1(t) = F_0 \sin(\Omega t)$. The fixed parameters for all simulations are chosen as follows: $\alpha = 2$, $\beta = 2$ and $\mu_1 = 1$, while isolator passive damping, inertance and active damping

are varied. Dimensionless excitation circular frequency is defined as $\Omega/\omega_{n1} = 1$, where undamped resonance is implied. Also, the response of the system to resonant frequency excitation from Eq. (2.19) is studied in one case where $\Omega/\Omega_a = 1$. Since $\beta > 1$, system is inherently subcritical and consequently only conditionally stable if employing skyhook damping scheme [26]. All initial conditions for simulations are set to zero, i.e. for $t_0 = 0$, $x_1(t_0) = 0$, $x_2(t_0) = 0$, $v_1(t_0) = 0$, $v_2(t_0) = 0$. Dimensionless displacements of masses m_1 and m_2 are defined as $X_{1,2}(t) = x_{1,2}(t)x_{1st}^{-1}$, where x_{1st} is the quasi-static displacement of mass m_1 under constant force magnitude F_{01}, i.e. when inertial and damping effects are neglected. Dimensionless time is defined as $T = t\Omega(2\pi)^{-1}$, thus abscissa serves as a vibration period counter. Twenty periods are considered in each simulation in order to observe the trends of the responses for a sufficiently long time period.

Figure 2.3 shows the simulated transient response of analyzed 2DOF passive system, i.e. skyhook damper λ is switched off and inertance μ_2 is set to zero. In Figure 2.3a), the undamped resonant response is considered, i.e. $\eta_2 = 0$ for $\Omega/\omega_{n1} = 1$. In Figure 2.3b), highly damped response is considered for locked isolator damper i.e. $\eta_2 = 25$ for $\Omega/\Omega_a = 1$.
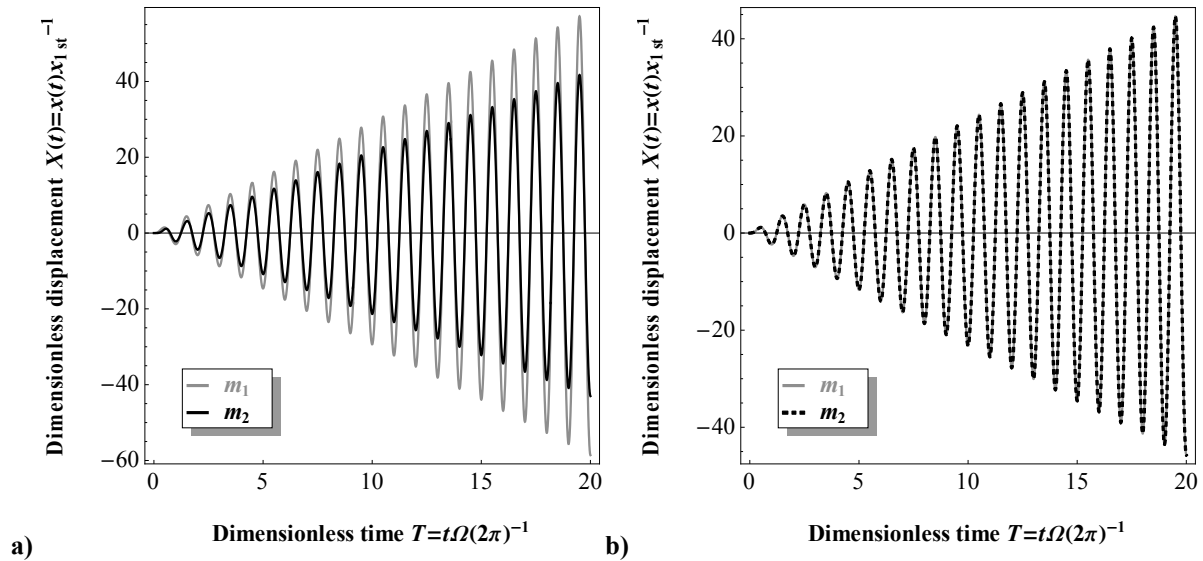
Figure 2.3.   **Transient response of 2DOF system, $\mu_2 = 0$, $\lambda = 0$: a) $\eta_2 = 0$, $\Omega = \omega_{n1}$, b) $\eta_2 = 25$, $\Omega = \Omega_a$**

In both cases, the amplitude of the dimensionless response increases linearly with time. As time reaches infinity, dimensionless responses also tend to infinity. Moreover, the resonant frequency Ω_a from Eq. (2.19) is clearly demonstrated in Figure 2.3b) as dimensionless responses almost completely overlap and relation $X_1(m_1) \approx X_2(m_2)$ holds, where

$$\eta_{2\infty} = \lim_{\eta_2 \to \infty} \eta_2, \quad T_\infty = \lim_{T \to \infty} T \quad \Rightarrow \quad X_1\left(\eta_{2\infty}, T_\infty\right) = X_2\left(\eta_{2\infty}, T_\infty\right) = \infty. \quad \text{(2.20a-c)}$$

Thus, there must exist an optimal damping value η_{2opt} in between those two extreme values, which can prevent observed uncontrolled response. Furthermore, more moderate damping is introduced where $\eta_2 = 0.25$. Dimensionless excitation frequency is defined as $\Omega/\omega_{n1} = 1$ in all adjacent simulations. Figure 2.4a) shows the resonant transient response of the lightly damped passive system. Active damping λ is still switched off. It can be seen that the amplitude of the response converges to steady state as time tends to infinity. Figure 2.4b) introduces active skyhook damping with a dimensionless feedback gain of $\lambda = 2$ which reveals unstable system response with flutter [31] instability. This demonstrates the inherent conditional stability of the subcritical class of vibration systems. Inertance is still $\mu_2 = 0$ for both simulations denoted in Figure 2.4.
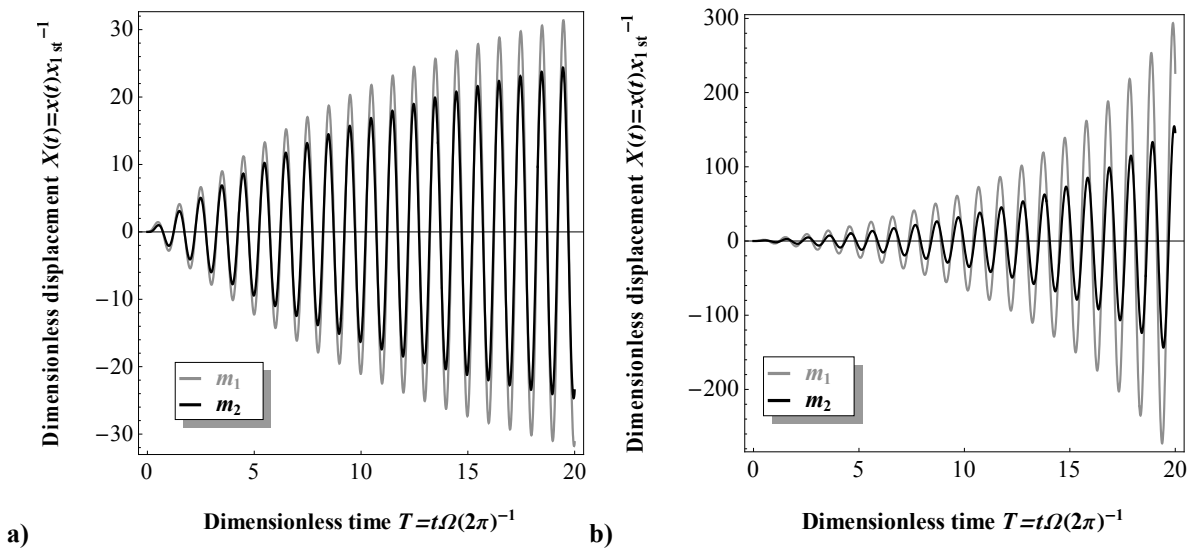
Figure 2.4.　　　**Transient response of 2DOF system, $\mu_2 = 0$, $\eta_2 = 0.25$, $\Omega = \omega_{n1}$: a) $\lambda = 0$, b) $\lambda = 2$**

Finally, inerter μ_2 is introduced in the isolation system. Skyhook damping coefficient is kept at the beforehand adopted fixed value of $\lambda = 2$. The accompanying responses are shown in Figure 2.5. A relatively small inertance $\mu_2 = 1$ is utilized for simulation results depicted in Figure 2.5a). Although flutter instability is apparently still present with this setup, response is clearly reduced when compared directly to response in Figure 2.4b). When even larger inertance ratio $\mu_2 = 4$ is employed in Figure 2.5b), a drastic reduction of both responses is observed compared to Figure 2.3, Figure 2.4 and Figure 2.5a). Most importantly, a steady state stable response is finally achieved in active isolation system, by the inerter-governed influence.

a)   **b)**
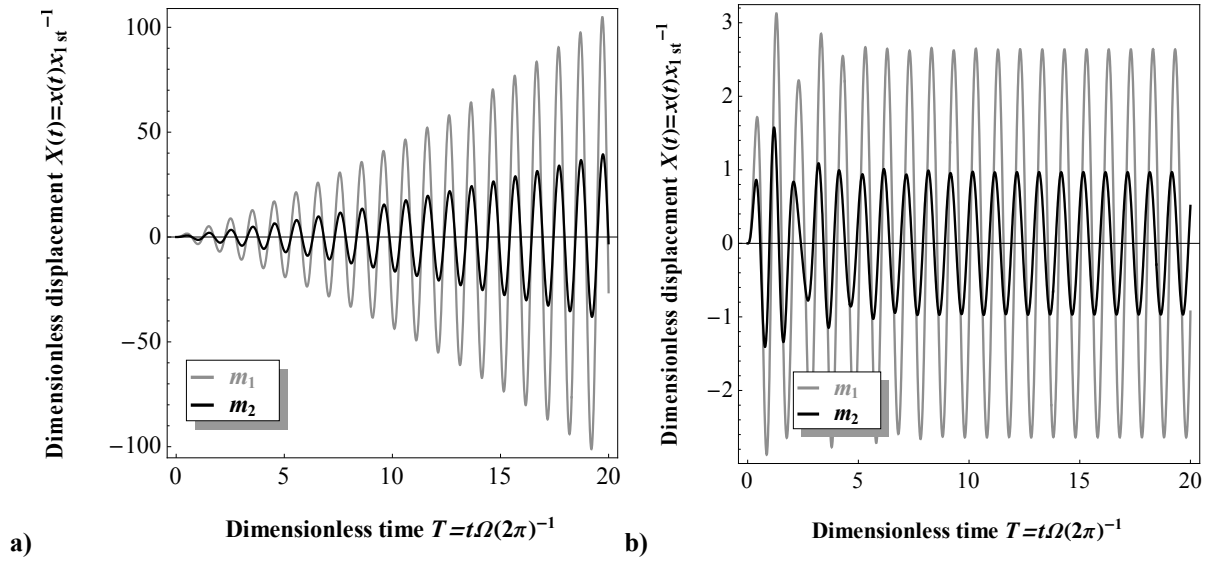
Figure 2.5.   Transient response of 2DOF system, $\eta_2 = 0.25$, $\lambda = 2$, $\Omega = \omega_{n1}$: a) $\mu_2 = 1$, b) $\mu_2 = 4$

For the passive system without inerter, the minimum specific kinetic energy of the system $I_{4\min}$ is studied by considering steady-state velocity of mass m_2 in the form implied by Eq. (2.7). It may be obtained from Eqs. (2.13-2.15), (2.17) and (2.18) by utilizing Eqs. (2.8-2.9) and (2.11), and minimizing with respect to dimensionless passive damping η_2. Optimum damping may be written in dimensional and dimensionless forms respectively as

$$c_{2\text{opt1}} = k_2 \sqrt{\frac{m_1 + m_2}{k_1 + k_3}}, \quad \eta_{2\text{opt1}} = \frac{\alpha\mu_1}{2}\sqrt{\frac{1+\mu_1}{1+\beta\mu_1}}. \tag{2.21a,b}$$

From Eqs. (2.21), accompanying specific kinetic energy expressions can thus be written in corresponding dimensional and dimensionless forms respectively with

$$\frac{I_{4\min(\text{dimensional})}}{2\pi} = k_2 \frac{\sqrt{(m_1 + m_2)(k_1 + k_3)}}{(m_2 k_1 - m_1 k_3)^2}, \quad \frac{I_{4\min(\text{dimensionless})}}{2\pi} = \alpha \frac{\sqrt{(\beta\mu_1 + 1)(\mu_1 + 1)}}{\mu_1(\beta - 1)^2}. \tag{2.22a,b}$$

By studying the structure of Eqs. (2.22), two main conclusions are drawn.

Firstly, it is observed that the optimum specific kinetic energy index $I_{4\min}$ is directly proportional to the isolator spring stiffness k_2 and corresponding squared natural frequency ratio α, which is effectively a dimensionless measure of spring stiffness. This implies using the compliant spring for better isolation effect. Albeit, decreasing spring stiffness k_2 may results in an overly large static or stationary deflections to which there is a practical limit in real engineering situations due to e.g. Earth's gravity g. Trivial mathematical solution is to set $k_2 = 0$ and completely decouple the source/receiving body systems, however this is neither viable, nor a physical course of action. Thus, opposing requirements dictate the choice of stiffness of the spring k_2. Consequently, isolator spring stiffness cannot be unambiguously

optimized and for this case, it is considered as a fixed value. Furthermore, since Den Hartog fixed-points theory [39] H_∞ type optimization generally considers tuning the isolator damping and stiffness simultaneously [42], it is not applicable to its full potential for this class of isolation problems due to previously discussed isolator spring stiffness-governed inherent static sag requirements. Nevertheless, damping can be tuned according to either H_2, or H_∞ criteria with regard to fixed given stiffness k_2.

Secondly, in Eq. (2.22b) can be noted that if the squared natural frequency ratio β tends to unity, I_{4min} tends to infinity since denominator tends to zero. This is the case in which the uncoupled natural frequency of the source body tends to the uncoupled natural frequency of the receiving body, i.e. $\Omega_1 \approx \Omega_3$. Hence, for a successful vibration isolation effect, the system should be detuned in such way that $\Omega_1 \neq \Omega_3$.

Specific kinetic energy of the system is further studied by incorporating the inerter in the isolator. It is found that mass m_2 may achieve even lower state of kinetic energy when an inerter is employed in the isolator. Parameters of the corresponding optimal passive damping c_{2opt2}, i.e. η_{2opt2}, and the optimum inertance b_{2opt}, i.e. μ_{2opt} are obtained analytically in a closed form by further minimizing the kinetic energy of the system. However, the obtained closed-form analytical expressions are of substantial length and cannot be denoted explicitly as in e.g. Eq. (2.21). Furthermore, the stability problem is considered by employing the Routh-Hurwitz method. Active control gain λ and inertance μ_2 in the isolator are taken into account. The chart of Hurwitz coefficients with respect to Eqs. (2.13) and (2.14-2.15) is given in Table 2.1. It is irrelevant which DOF is taken into account since Hurwitz criterion considers characteristic equation of the closed loop, i.e. denominator of the TF which is one and the same for all DOFs. The influence of inerter on active isolator stability is studied.

Table 2.1. **Hurwitz coefficients chart for $i = 4$**

H_{i-3}	A_3	A_1		
H_{i-2}	A_4	A_2	A_0	
H_{i-1}		A_3	A_1	
H_i		A_4	A_2	A_0

It is found that for subcritical systems where the fundamental natural frequency of the receiving body is larger than that of the source body, the use of inerter characterised by simple inequality relation $\mu_2 > \alpha$ improves the stability by virtually turning a subcritical active vibration isolation problem into a supercritical one. This allows for unconditionally stable system and theoretically unlimited amounts of applicable feedback gain λ.

2.3.   Enhancing the Fatigue Life of Helical Spring due to Inerter

In this chapter, previously conducted investigation is expanded. The vibration induced fatigue effects of coupling spring in the receiving body due to broadband frequency excitation are additionally introduced and considered. The studied problem is represented by a discrete parameter model shown in Figure 2.6a). The model is similar to one from Figure 2.2a), however skyhook damping scheme is not considered herein. It is assumed that the critical component concerning fatigue is a helical spring of stiffness k_3, Figure 2.6b). Parameters of the considered spring are as follows: E is (Young) modulus of elasticity, v is Poisson's ratio, S'_f is fatigue strength coefficient, and "B" is Basquin's exponent, i.e. fatigue strength exponent [32] denoted in capital letter in order not to be mixed up with inertance coefficient "b". Number of active coils is denoted as n ($n = 2$ in Figure 2.6b) and h is spring total height where $h = n \cdot l$, and l is the spring pitch. Diameters D and d are mean coil and wire diameters respectively, and $C = D/d$ is defined as spring index [116]. Recommended physical values of spring index C for practical engineering purposes lie between $C = 4 - 12$ [116]. Angle α represents the pitch angle which can be calculated according to expression $\alpha = \arctan[l(\pi D)^{-1}]$. Moreover, total length of the spring wire is designated with L.
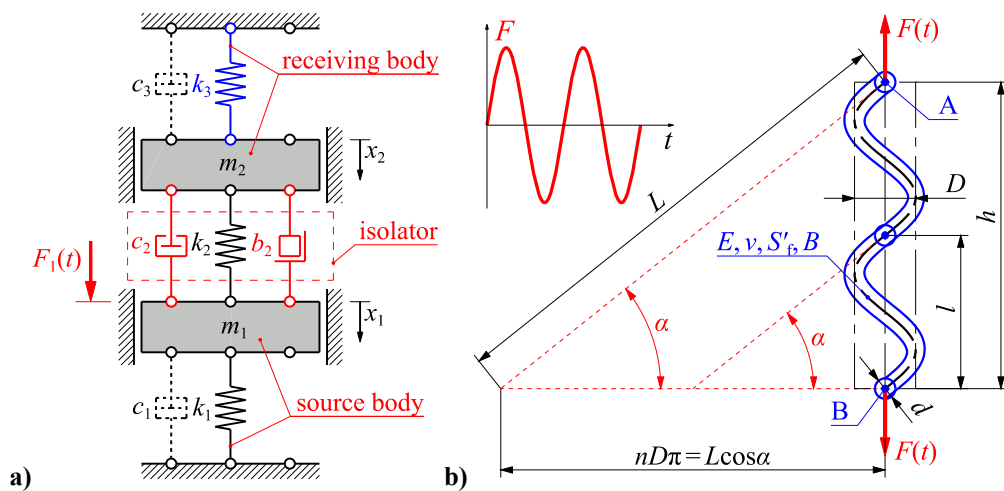
Figure 2.6.   **a) 2DOF linear discrete vibration isolation system, b) helical spring k_3 properties**

Cylindrical helical spring is usually for simplicity viewed as a thin/slender, curved rod/beam subjected to torsion load [111]-[113],[116]. In that case, only nominal values are considered, e.g.: nominal spring stiffness k_{nom}, nominal spring deflection δ_{nom}, and nominal spring shear stress τ_{nom}. Consequently, only torsion shear is taken into account. Hence, direct shear, curvature, and pitch angle effects are neglected. If spring geometry deviates from simple curved rod assumption, additional correction factors K_δ (displacement correction factor, DCF) and K_τ (stress correction factor, SCF) need to be applied for more accurate

displacement and shear stress calculation, where relations $\delta_{max} = K_\delta \delta_{nom}$ and $\tau_{max} = K_\tau \tau_{nom}$ now hold. Figure 2.7 schematically shows circular cross-section of the spring with its related stress components and its corresponding cumulative shear stress τ correction. Shift of the helical spring neutral line consequently results with maximum shear stress τ_{max} appearing at the point closest to spring axis x, Figure 2.7c).
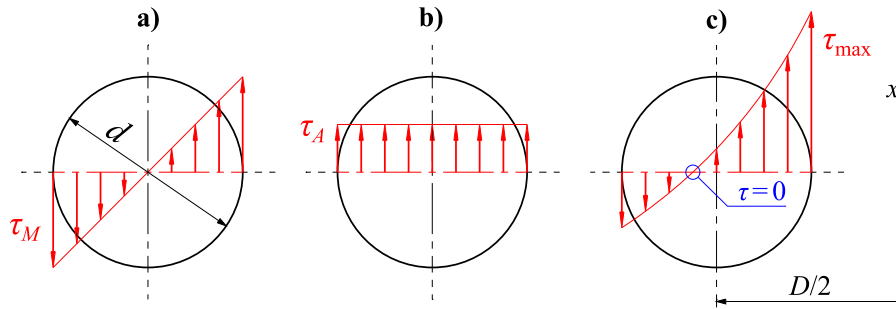
Figure 2.7. Spring shear stresses: a) torsion shear τ_M, b) transverse/direct shear τ_A, c) combined torsion and direct shear with additional curvature "c" and pitch angle α effects $\tau_{max} = \tau_M + \tau_A + \tau_c + \tau_\alpha$

Multiple expressions for correcting deflection and stress are reported in the referent literature [111]-[113]. Some of these expressions are summed up in Table 2.2.

Table 2.2. Expressions for stress correction factors K_τ and deflection correction factors K_δ

Author/Standard	Stress correction factor K_τ	Deflection correction factor K_δ
Strength of Materials		
Wahl, DIN 13906	$\dfrac{4C-1}{4C-4} + \dfrac{k_w}{C} = \dfrac{4C-1}{4C-4} + \dfrac{1+2\nu}{2(1+\nu)C}$	-
Röver	$\cos(\alpha)\left[\dfrac{C}{C-\cos^2(\alpha)} + \dfrac{1+\sin^2(\alpha)}{4C}\right]$	-
Wood	$\dfrac{C}{C-1} + \dfrac{1}{2C}$	$\dfrac{2C^2+C-1}{2C^2}$
Honegger	$\cos(\alpha)\left[\dfrac{C}{C-\cos^2(\alpha)} + \dfrac{0.615}{C}\right]$	$\dfrac{2C^2-\cos^4(\alpha)}{2C^2\cos^5(\alpha)}$
Timoshenko/Cowper	-	$1 + \dfrac{7+6\nu}{12C^2(1+\nu)}$
Elasticity Theory		
Göhner, DIN 2089	$1 + \dfrac{5}{4C} + \dfrac{7}{8C^2} + \dfrac{1}{C^3}$	$\cos(\alpha) + \dfrac{3\cos^5(\alpha)}{16(C^2-1)} + \dfrac{\sin(\alpha)\tan(\alpha)}{1+\nu}$
Ancker and Goodier	$1 + \dfrac{5}{4C} + \dfrac{7}{8C^2} + \dfrac{1}{2}\tan^2(\alpha)$	$1 - \dfrac{3}{16C^2} + \dfrac{3+\nu}{2(1+\nu)}\tan^2(\alpha)$
Castigliano/Timoshenko	-	$\dfrac{(16C^2-13)\cos(\alpha)}{16(C^2-1)} + \dfrac{\sin(\alpha)\tan(\alpha)}{1+\nu}$
Approximate/Empirical relation		
Bergsträsser, DIN 13906	$\dfrac{C+0.5+\sin^2(\alpha)}{C-0.75+1.51\sin^2(\alpha)}$	-
Sopwith, BS 1726	$\dfrac{C+0.2}{C-1}$	-
Strain Energy (Castigliano's) Method		
Shigley	-	$1 + \dfrac{1}{2C^2}$
Dym	-	$\left(1+\dfrac{1}{2C^2}\right)\cos(\alpha) + \left(1+\dfrac{1}{4C^2}\right)\dfrac{\tan(\alpha)\sin(\alpha)}{(1+\nu)}$

Certain expressions in Table 2.2 (i.e. Wahl, Röver, Wood, Honegger, Göhner, Ancker and Goodier, Bergsträsser, and Sopwith) are adopted from [113]. Further added are strain energy based relations by Shigley [116] and Dym [117]. Göhner stress correction factor was previously included in older, now defunct DIN 2089 (Germ. Deutsches Institut für Normung) [118],[119]. Currently valid DIN 13906 standard includes Wahl [111] and Bergsträsser stress correction factors [120],[121]. Sopwith stress correction factor was previously used as a part of BS 1726 (British Standard) [122].

Two additional expressions are also presented in Table 2.2, denoted with darker (gray) background. The first one is Castigliano/Timoshenko (C/T) deflection correction which was originally derived by Timoshenko [123] based on Castigliano's method, theory of elasticity and Göhner's displacement correction. C/T correction is presented here in a more convenient and compatible dimensionless form with regard to other authors' expressions. The second one is novel Timoshenko/Cowper (T/C) displacement correction factor based on thick Timoshenko shear beam. It is derived and proposed in the scope of this dissertation. Correction factor is comprised of Timoshenko beam theory [124] enriched with Cowper shear correction for circular cross-section [125]. All of the expressions from Table 2.2 are denoted in Figure 2.8a) and b) for mutual visual comparison. Acronym A/G implies Ancker and Goodier [112] stress and deflection correction factors.

a)   b)
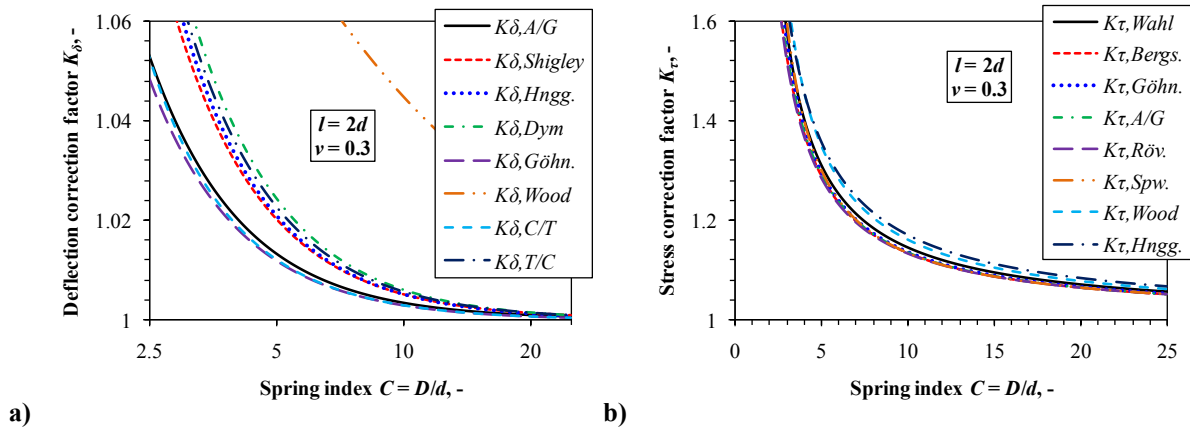
Figure 2.8.   **Different correction factors for $v = 0.3$: a) deflection correction K_δ, b) stress correction K_τ**

By assuming Basquin's HCF equation [32], adopting appropriate SCF and DCF, and finally considering von Mises distortion energy criterion for biaxial shear-governed proportional fatigue loading, following simple relation is obtained for spring fatigue life

$$N_\mathrm{f} = \left(\frac{S_\mathrm{a}}{S'_\mathrm{f}}\right)^{\frac{1}{B}} \Rightarrow N_\mathrm{f}(\varOmega) = \left[\sqrt{3}\,\frac{K_\tau}{K_\delta}\,\frac{G}{C^2 n\pi d}\,\frac{|x_{02}(\varOmega)|}{S'_\mathrm{f}}\right]^{\frac{1}{B}}, \qquad (2.23\mathrm{a,b})$$

where S_a denotes fully reversed fatigue stress amplitude herein equal to modulus of equivalent complex stress amplitude $|\sigma_{0eqv}|$, and $G = E[2(1+v)]^{-1}$ is the shear modulus. Eq. (2.23b) is obtained by relating the spring life $N_f(\Omega)$ in the frequency domain to absolute displacement amplitudes $|x_{02}|$ of mass m_2. The relation is valid for the cases when one terminal of the spring is immovable. In case both terminals are movable, e.g. in case of base excitation, the term x_{02} should be swapped with the relative displacement amplitude, i.e. $x_{02,rel}$. From minimization of specific kinetic energy in the inerter-based system, following expression for optimal damping is obtained in dimensional form

$$c_2\left(b_2 \neq 0\right) = \sqrt{\frac{m_1 + m_2}{k_1 + k_3} k_2^{\,2} - 2b_2 k_2 + \frac{m_1 k_3^{\,2} + m_2 k_1^{\,2} + b_2 \left(k_1 + k_3\right)^2}{\left(k_1 + k_3\right)\left[m_1\left(b_2 + m_2\right) + b_2 m_2\right]} b_2^{\,2}}, \qquad (2.24)$$

where by setting $b_2 = 0$, one obtains previously obtained Eq. (2.21a), i.e. optimum damping c_{opt} for the system without inerter. In order to parametrically evaluate the proposed procedure, example parameters for the system from Figure 2.6a) are given in Table 2.3.

Table 2.3.   Example 2DOF vibration isolation system parameters

m_1, kg	m_2, kg	k_1, N/mm	k_2, N/mm	k_3, N/mm	F_0, kN
m_0	$2 \cdot m_0$	k_0	$k_0/10$	k_0	1

Mass is adopted as $m_0 = 100$ kg and spring stiffness k_0 is determined with respect to scheme from Figure 2.6b) and corresponding Table 2.4. Optimized inertance and damping parameters are determined from Eq. (2.24). Adopted correction factors from Table 2.2 are A/G for DCF, and Wahl for SCF.

Table 2.4.   Example helical spring of stiffness k_0 geometric and material properties

D, mm	d, mm	n, -	l, mm	E, MPa	v, -	S'_f, MPa	B, -
50	17	1	$2 \cdot d$	200 000	0.3	925	-0.1

In order to demonstrate the principle of similitude between displacement amplitudes of mass m_2 and corresponding spring k_3 inverse number of cycles to fatigue failure N_f^{-1}, broadband frequency response for both quantities is shown side-by-side in Figure 2.9a) and b) respectively. For additional reference, case with optimum inertance $b_2 = b_{opt}$ is also plotted for zero damping i.e. $c_2 = c_0 = 0$. The improvement in the number of cycles to failure N_f is evident at most frequencies when using the optimum damping c_{opt} in comparison to low damping $c_{sub} = c_{opt}/100$, or high damping $c_{sup} = 100 \cdot c_{opt}$. Additionally, a significant further improvement in the fatigue life N_f is observed at most frequencies, in case where the optimum inerter b_{opt} is implemented in combination with the optimum damper c_{opt2}. Anti-resonance phenomenon at

frequency Ω_A is observed for the case with the optimum inerter b_{opt} and without damping ($c_2 = 0$), which specifically demonstrates inerter b_2 influence. Contrary to that, if using very large damping in the isolator, *i.e.* $c_{sup} = 100 \cdot c_{opt}$, new resonance Ω_a from Eq. (2.19) is observed, as two masses m_1 and m_2 vibrate together in phase with equal displacements, velocities, and accelerations, acting as a quasi-rigid body.
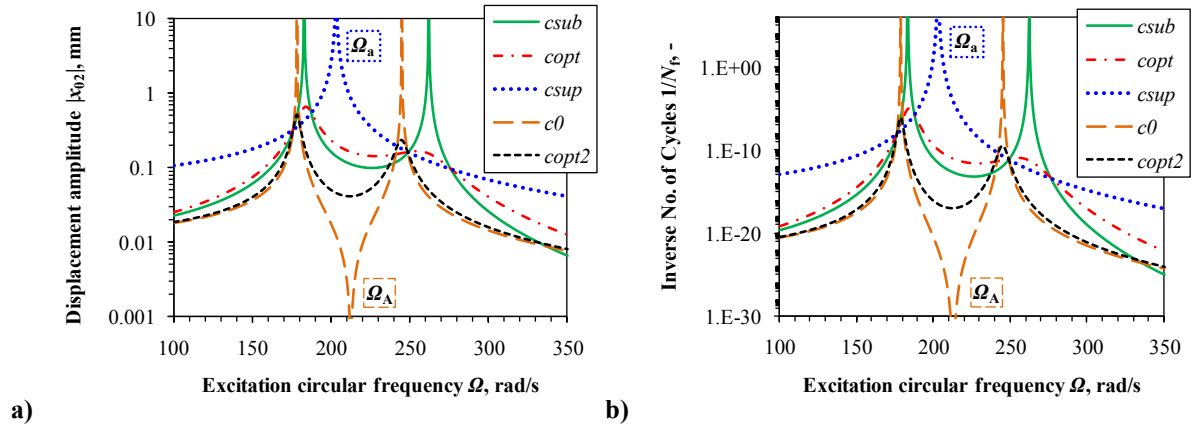
Figure 2.9.　　　2DOF FRFs: a) displacement amplitude $|x_{02}|$, b) spring k_3 inverse No. of cycles N_f^{-1}

Anti-resonant frequency Ω_A for undamped response from Figure 2.9 is obtained as

$$\Omega_A = \sqrt{\frac{k_2}{b_2}}. \tag{2.25}$$

In the next chapter, which corresponds to directly succeeding Paper 3, different optimization criterion is utilized and compared to current optimized results.

2.4.　Comparison of Different H_2 Optimization Criteria and Numerical Verification

Passive isolation control model from previous chapter is adopted. The same inerter-based vibration model as in Figure 2.6a) is considered. Procedure is verified through comparison with numerical solutions. Direct dynamic method is employed in *Abaqus* [28], and complex stress field is imported into *Fe-Safe* [30] in order to numerically evaluate spring fatigue life in the frequency domain. Furthermore, ideal flywheel-based inerter is implemented into *Abaqus* by using native **Equation* functionality where FE relative nodal displacements are tied to rotation of the fictitious discrete flywheel. Smith's rack and pinion inerter analogy is employed. Analytical and numerical results are compared where very good agreement is observed between the two approaches to problem.

Previously derived Timoshenko/Cowper beam based deflection correction solution (Table 2.2) agrees excellently with FEM beam-based solution [28],[29]. However, these two concurrent solutions are completely divergent when compared to theory of elasticity based A/G [112] correction and complementary FEM 3D continuum-based solutions [28],[29]. Thus, Timoshenko beam-based solution shouldn't be used when thick springs with small index C are considered. Moreover, Wahl stress correction seems to agree the best with FEM 3D continuum-based solutions [28],[29] compared to other expressions from Table 2.2 and Figure 2.8, especially when Poisson's ratio $v \approx 0.3$ is considered. However, the accuracy of Wahl's approximation for larger spring pitch angles is yet to be determined.

For alternative approach with regard to previous chapter, more general H_2 optimization criterion which considers complex displacement amplitudes x_{02} is now taken into account. By minimizing the closed form integral solution from Eq. (2.11), the following expressions are obtained for optimum damping c_{opt2} and optimum inertance b_{opt} respectively, regarding inerter-based vibration isolation system

$$c_{opt2}\left[\mathcal{H}_2\left(x_0\right)\right] = \frac{k_2\left|k_1 m_2 - m_1 k_3\right|}{\sqrt{\left[\left(k_2 + k_3\right)k_1 + k_2 k_3\right]\left(m_1 + m_2\right)\left(k_1 + k_3\right)}}, \quad b_{opt}\left[\mathcal{H}_2\left(x_0\right)\right] = \frac{k_2\left(m_1 + m_2\right)}{k_1 + k_3}. \quad (2.26a,b)$$

If inerter is not considered, optimum damping c_{opt} is given by

$$c_{opt(b_2=0)}\left[\mathcal{H}_2\left(x_0\right)\right] = k_2 \frac{\sqrt{\left(m_1 + m_2\right)^2 k_2 + k_1 m_2^2 + k_3 m_1^2}}{\sqrt{\left[\left(k_2 + k_3\right)k_1 + k_2 k_3\right]\left(m_1 + m_2\right)}}. \quad (2.27)$$

Optimization results are summarized in Figure 2.10. Curves $c_{opt}(v_0)$ and $c_{opt2}(v_0)$ directly correspond to curves c_{opt} and c_{opt2} from Figure 2.9 since exactly the same parameters from Table 2.3 and Table 2.4 are utilized. It may be concluded that displacement-based optimization criterion $H_2(x_0)$ yields general further improvement compared to velocity-based, i.e. specific kinetic energy minimization criterion $H_2(v_0)$ demonstrated in previous chapter. This is true for the test cases with and without inerter. Moreover, improvements are much more pronounced for the displacement-based optimization compared to velocity-based optimization when utilizing combined optimum damping c_{opt2} and inertance b_{opt}. For the velocity based-optimization, over 1 million cycles are achieved. However, for herein proposed displacement- (i.e. fatigue-) based optimization, over 3.5 times more cycles are achieved. Thus, for shown family of vibration isolation systems it is justifiable to include inerter in the isolator and perform displacement-based optimization analysis if stress of coupling elastic components is of crucial importance.
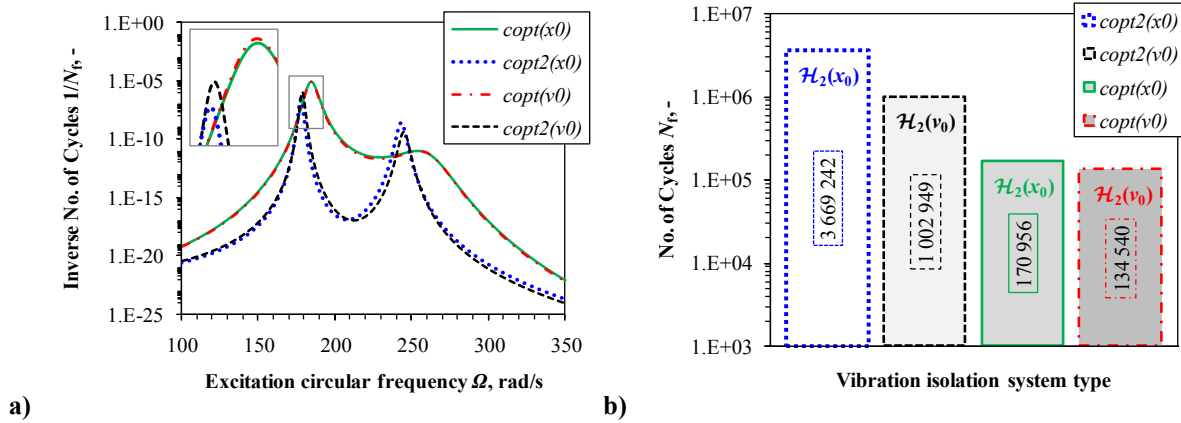
Figure 2.10.   **Spring k_3 number of cycles to fatigue failure $N_f(k_3)$: a) $1/N_f(\Omega)$ FRFs, b) $N_f(\omega_{n1})$**

The question of determining the more accurate spring deflection and stress correction factors is addressed in the next chapter.

2.5.   Isolator Helical Spring Novel Stress and Correction Factors

In this final chapter, which directly corresponds to published paper 4, the vibration fatigue induced effects in the isolator helical spring are considered. Previously expressed concerns regarding general accuracy of adopted A/G [112] and Wahl [111] correction factors respectively are addressed. Both absolute and relative displacements are analyzed. Generally, the stresses in engineering structures are always proportional to relative displacements. Thus, relative displacement is adopted as relevant criterion regarding corresponding fatigue analyses. Simple 1DOF vibration isolation problem is revisited by additionally adopting the relative mass concept. Leverage based isolation system originally conceived by Flannelly [110] and discussed in [109] is considered herein in order to obtain inertance-like effect analogous to one described by Smith [1] in his rack/pinion concept.

Proposed simple 1DOF inerter-based isolator is depicted in Figure 2.11a), and its corresponding free-body scheme counterpart is given in Figure 2.11b).
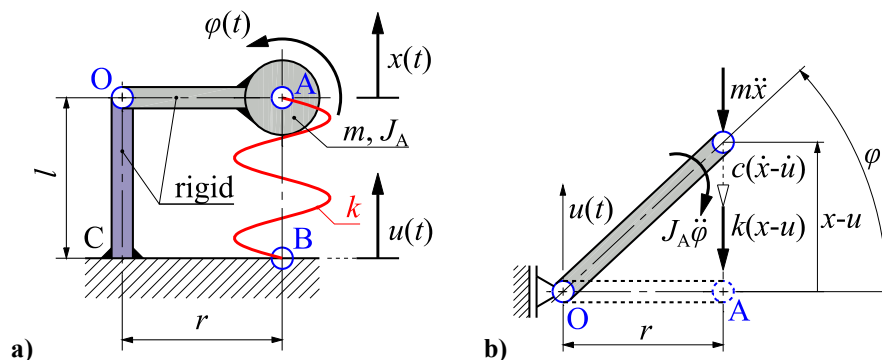
Figure 2.11.   **1DOF inerter-based vibration isolator: a) scheme, b) free-body diagram, $x > u$**

The EOM for the dynamic system at hand may be written as

$$\sum M_{\mathrm{O}} = 0 \quad \Rightarrow \quad m\ddot{x}r + J_{\mathrm{A}}\ddot{\varphi} + c(\dot{x} - \dot{u})r + k(x - u)r = 0, \tag{2.28}$$

where J_{A} is flywheel mass moment of inertia. Small vibration rotation amplitudes are assumed where $\sin(\varphi) \approx \varphi$, and $\cos(\varphi) \approx 1$. By adopting expression $J_{\mathrm{A}} = r^2 b$ and kinematic relation $(x - u) \equiv x_{\mathrm{rel}} = r\varphi$, and dividing by rotation radius r, Eq. (2.28) morphs into translational dynamic force equilibrium

$$m\ddot{x} + b(\ddot{x} - \ddot{u}) + c(\dot{x} - \dot{u}) + k(x - u) = 0. \tag{2.29}$$

Hence, this simple rotational/translational system exhibits inerter-like behaviour whose inertance is given by $b = J_{\mathrm{A}}/r^2$. Kinematic complex broadband excitation is assumed in the form $u(t) = u_0 \mathrm{e}^{\mathrm{i}\Omega t}$, where u_0 is the ground displacement complex amplitude, "e" is the base of the natural logarithm, imaginary number $\mathrm{i} = \sqrt{-1}$, Ω is the excitation circular frequency and t is the time. Furthermore, the solution of Eq. (2.29) is assumed as $x(t) = x_0 \mathrm{e}^{\mathrm{i}\Omega t}$ where x_0 is the complex displacement amplitude of mass m. Separating the response and excitation variables yields with the dynamic forces equilibrium, and consequent absolute (*i.e.* x_0/u_0) and relative (*i.e.* $x_{0,\mathrm{rel}}/u_0$) steady-state complex solutions of Eq. (2.28), which respectively write as

$$(m+b)\ddot{x} + c\dot{x} + kx = b\ddot{u} + c\dot{u} + ku \quad \Rightarrow \quad \frac{x_0}{u_0} = \frac{(\mathrm{i}\Omega)^2 b + \mathrm{i}\Omega c + k}{(\mathrm{i}\Omega)^2 (m+b) + \mathrm{i}\Omega c + k}, \quad \frac{x_{0,\mathrm{rel}}}{u_0} = \frac{x_0 - u_0}{u_0}. \tag{2.30a-c}$$

Steady-state complex dynamic forces amplitude F_0 equilibrium which yields from Eq. (2.30a,b) is visually represented in Figure 2.12a). Complex plane real and imaginary axes are denoted by symbols $\Re$ and $\Im$ respectively.

It is implied from Eq. (2.30c) and corresponding complex displacement amplitudes vector representation in Figure 2.12b) that relative displacement $x_{\mathrm{rel}}(t) = x(t) - u(t)$ (*i.e.* relative displacement complex amplitude $x_{0,\mathrm{rel}} = x_0 - u_0$) directly corresponds to spring k stress. In return, spring stress is inversely and non-linearly proportional to number of cycles to fatigue failure N_{f}, analogue to results reported in previous chapters.

Angles γ, α and β from Figure 2.12 represent phase angles/differences [31] between vectors of complex force amplitudes and complex displacement amplitudes respectively.
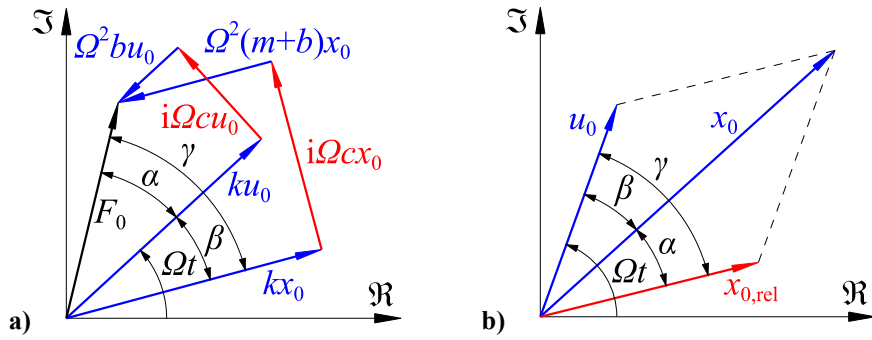
Figure 2.12.   **Vectors of forces and displacements in the complex plane: a) complex force amplitudes, b) complex displacement amplitudes**

For a more general approach, the following parameters are introduced

$$m_{\text{eqv}} = m + b, \quad \omega_n = \sqrt{\frac{k}{m_{\text{eqv}}}} \quad \Rightarrow \quad \eta = \frac{\Omega}{\omega_n}, \quad \zeta = \frac{c}{c_{\text{cr}}} = \frac{c}{2\sqrt{m_{\text{eqv}}k}}, \quad \mu = \frac{b}{m}, \quad (2.31\text{a-e})$$

where $\eta = \Omega/\omega_n$ is dimensionless excitation frequency, Ω is circular excitation frequency and $\omega_n = (k/m_{\text{eqv}})^{1/2}$ is a fundamental natural frequency of the system, conveniently scaled with respect to system equivalent mass $m_{\text{eqv}} = m + b$. Since inertance b algebraically contributes to equivalent, *i.e.* apparent mass m_{eqv}, this effect yields with diminishing of fundamental natural frequency ω_n. Furthermore, $\zeta = c/[2(m_{\text{eqv}}k)^{1/2}]$ is dimensionless damping ratio, *i.e.* proportional [31] or modal [27]-[29] damping as a fraction of critical damping, and $c_{\text{cr}} = 2(m_{\text{eqv}}k)^{1/2}$ is critical damping. Finally, dimensionless inertance ratio is designated as $\mu = b/m$. Relative displacement amplitude $|x_{0,\text{rel}}| = |x_0 - u_0|$ is further denoted through convenient relative magnification factor $M_{0,\text{rel}}$ with respect to Eqs. (2.30-2.31). Absolute magnification factor $M_0 = |x_0/u_0|$ from Eq. (2.30b) and corresponding relative magnification factor $M_{0,\text{rel}} = |x_0/u_0 - 1|$ from Eq. (2.30c) can now be written as dimensionless frequency η-dependent scalars as

$$M_0(\eta) = \left|\frac{x_0}{u_0}\right| = \left|1 + \frac{\eta^2}{(1 + 2i\eta\zeta - \eta^2)(1 + \mu)}\right|, \quad M_{0,\text{rel}}(\eta) = \left|\frac{x_{0,\text{rel}}}{u_0}\right| = \left|\frac{x_0 - u_0}{u_0}\right| = \left|\frac{\eta^2}{(1 + 2i\eta\zeta - \eta^2)(1 + \mu)}\right|. \quad (2.32\text{a,b})$$

By employing complex expansion of the simplified expression from Eq. (2.32a), absolute magnification factor M_0 can also be conveniently written in a more compact form as

$$M_0(\eta) = \sqrt{\frac{\mathfrak{R}_{\text{N}}^2 + \mathfrak{I}_{\text{N}}^2}{\mathfrak{R}_{\text{D}}^2 + \mathfrak{I}_{\text{D}}^2}}, \quad (2.33)$$

where squared coefficients under the square root of Eq. (2.33) are real $\mathfrak{R}_{\text{N}}$ and imaginary $\mathfrak{I}_{\text{N}}$ components of numerator and real $\mathfrak{R}_{\text{D}}$ and imaginary $\mathfrak{I}_{\text{D}}$ components of denominator respectively. These coefficients with respect to expanded Eq. (2.32a) and corresponding compact Eq. (2.33) are written as

$$\Re_{\mathrm{N}} = 1 + \mu\left(1 - \eta^2\right), \quad \Im_{\mathrm{N}} = 2\zeta\eta\left(1 + \mu\right), \quad \Re_{\mathrm{D}} = \left(1 - \eta^2\right)\left(1 + \mu\right), \quad \Im_{\mathrm{D}} = \Im_{\mathrm{N}} = 2\zeta\eta\left(1 + \mu\right). \quad (2.34\text{a-d})$$

It can be observed from Eqs. (2.34b,d) that imaginary components of numerator and denominator are equal. Coefficients from Eq. (2.34a-d) are used to define the phase angles γ and α, with regard to Figure 2.12, which can be written as

$$\gamma(\eta) = \arctan\left(\frac{\Im_{\mathrm{D}}}{\Re_{\mathrm{D}}}\right) = \arctan\left(\frac{2\zeta\eta}{1 - \eta^2}\right), \quad \alpha(\eta) = \arctan\left(\frac{\Im_{\mathrm{N}}}{\Re_{\mathrm{N}}}\right) = \arctan\left[\frac{2\zeta\eta\left(1 + \mu\right)}{1 + \mu\left(1 - \eta^2\right)}\right]. \quad (2.35\text{a,b})$$

Finally, from Eqs. (2.35) total phase angle β can be written as

$$\beta(\eta) = \gamma - \alpha. \quad (2.36)$$

where β is essentially an argument of Eq. (2.32a), *i.e.* Eq. (2.30b), by considering complex plane scheme denoted in Figure 2.12. Moreover, the phase angles γ, α and β are herein defined as positive values.

Parametric plots for magnification factor M_0 are shown in Figure 2.13 for various combinations of ζ and μ. In Figure 2.13a), inertance ratio $\mu = 1$ is fixed, while damping ratio ζ is varied. Anti-resonance effect [109],[110] is observed when combined with a very small damping ratio, and it is represented by a vertical dashed line. Such effect is an evident consequence of inerter impact. The obtained effect is somewhat lost when damping increases. By viewing the influence of varying damping ζ, it can be observed that there exists a fixed point in Figure 2.13a) represented by a circle marker where all FRFs cross and magnification factor value is $M_0 = 1$, regardless of damping. Furthermore, by inspecting Figure 2.13b) it can be noted that changing the inertance ratio μ while fixing damping ratio ζ influences dimensionless anti-resonance position which in return diminishes and tends closer to resonant dimensionless frequency, *i.e.* $\eta = 1$. Moreover, larger inertance ratio μ seemingly also beneficially influences the response near resonance, *i.e.* reduces it. Additionally, for system without inerter, *i.e.* when $\mu = 0$, the response at higher frequencies shows standard roll-off behaviour where magnification factor M_0 tends to zero when dimensionless frequency η tends to infinity [31]. However, by employing the inerter, beneficiary effect of lower displacement amplitudes on higher frequencies (*i.e.* for $\eta \gg 1$) is apparently permanently lost when $\mu \neq 0$. When η tends to infinity, response $M_{0\infty}$ (*i.e.* magnification factor when $\eta \to \infty$) asymptotically tends to constant value denoted by horizontal dashed line in Figure 2.13a). It can additionally be observed in Figure 2.13b) that $M_{0\infty}$ value tends to higher values for rising dimensionless inertance μ, which is considered to be a non-desired and impairing effect. Thus, low-

frequency applications may be suitable for inerter implementations in this context, as discussed by Yilmaz and Kikuchi [109].
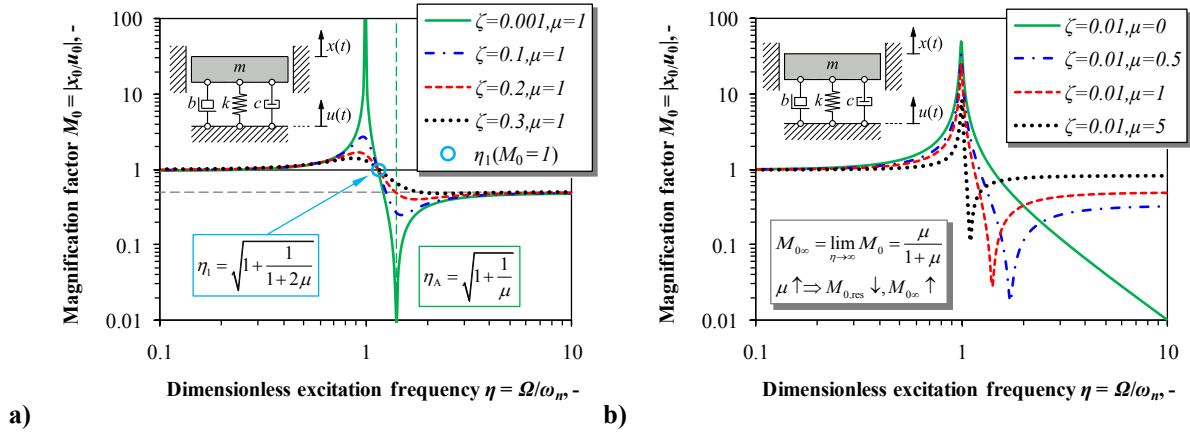

Figure 2.13.   Absolute magnification factor M_0 by varying: a) damping ratio ζ ($\mu = 1$), b) inertance ratio μ ($\zeta = 0.01$)

The value of dimensionless frequency where all FRFs cross can be obtained by setting $M_0 = 1$ in either Eq. (2.32a), or (2.33) and solving for $\eta = \eta_1$. The undamped anti-resonance dimensionless frequency η_A can be obtained by setting $M_0 = 0$ and $\zeta = 0$ in either Eqs. (2.32a), or (2.33), and solving for η. These two expressions can be respectively written as

$$\eta_1 \equiv \eta\left(M_0 = 1\right) = \sqrt{1 + \frac{1}{1 + 2\mu}}, \quad \eta_A \equiv \eta\left(M_0 = 0, \zeta = 0\right) = \sqrt{1 + \frac{1}{\mu}}. \qquad (2.37a,b)$$

By setting $\mu = 0$ in Eq. (2.37a), η_1 converges to common value where $\eta_1 = \sqrt{2}$ [31]. Moreover, by setting $\mu = 0$ in Eq. (2.37b), η_A tends to ∞, which is in accordance with $M_0 \rightarrow 0$ when $\eta \rightarrow \infty$ [31] (solid M_0 line in Figure 2.13b). Two extreme conditions are considered next. In order to obtain the value of $M_{0\infty}$, symbolic limit analysis is performed on Eq. (2.33). Furthermore, magnification factor for resonant conditions $M_{0,res}$ is determined by setting $\eta = 1$ in Eq. (2.33). These two relations can be respectively written as

$$M_{0\infty} = \lim_{\eta \to \infty} M_0 = \frac{\mu}{1 + \mu}, \quad M_{0,res} \equiv M_0\left(\eta = 1\right) = \sqrt{1 + \frac{1}{\left[2\zeta\left(1 + \mu\right)\right]^2}}. \qquad (2.38a,b)$$

By further performing limit analysis on Eq. (2.38a) for $\mu \rightarrow \infty$, magnification factor becomes $M_{0\infty} = 1$ for the entire frequency range $\eta \in [0, \infty]$, including resonance and anti-resonance conditions. This is due to the fact that anti-resonance effect eventually completely cancels out resonance effect since limit value for η_A from Eq. (2.37b) asymptotically tends to $\eta_{A\infty} = 1$ for $\mu \rightarrow \infty$. Hence, isolator effectively locks and the whole system moves as a rigid body where motion is exclusively governed by base excitation. This effect benefits the

resonant conditions. However, it yields with severe degradation of magnification factor M_0 at frequencies higher than anti-resonance, *i.e.* when $\eta > \eta_A$. Thus, there is an inherent trade-off between improved performance near resonant conditions and degraded performance at higher frequencies that needs to be considered when setting μ. Consequently, inertance ratio μ cannot be optimized and its appropriate value depends solely on loading conditions. This is also evident since employing the inerter in the isolator yields with straight line FRFs after anti-resonant dimensionless frequency η_A, Figure 2.13. Nevertheless, inertance can be set in order to desirably tune the value of undamped fundamental natural frequency ω_n from Eq. (2.31b), or to influence the position of the dimensionless anti-resonant frequency η_A from Eq. (2.37b).

Figure 2.14. denotes phase angles γ, α and β from Eqs. (2.35,2.36). Figure 2.14a) presents phase angles of standard isolation system without inerter [31], while Figure 2.14b) denotes phase angles with inerter present. As phase angle γ from Eq. (2.35a) does not include inertance coefficient μ, plots for γ (solid lines in Figure 2.14) are identical in both Figure 2.14a) and b). However, as phase angle α from Eq. (2.35b) includes dimensionless inertance μ; plots for α (dash-dotted lines in Figure 2.14) are noticeably different. This is already hinted in Figure 2.12a). Since phase angle $\beta = \gamma - \alpha$ in Eq. (2.36) depends on both angles simultaneously, it is also inherently influenced by this relation.
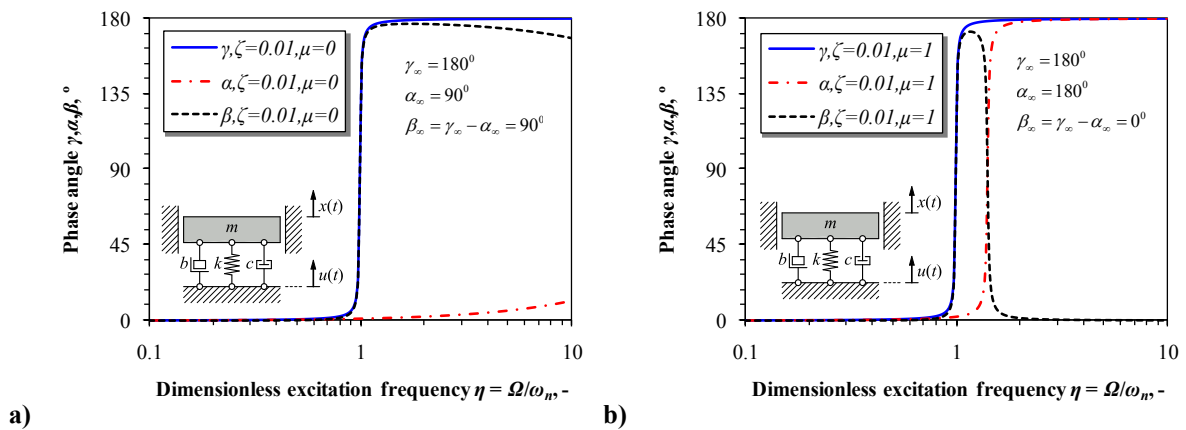
Figure 2.14. **Phase angle γ, α, β, $\zeta = 0.01$: a) inertance ratio $\mu = 0$, b) inertance ratio $\mu = 1$**

Phase lag [27],[31] occurs for $\eta > 1$ (+180° lag for $\zeta = 0$), while novel anti-resonance inerter-based isolator effect additionally introduces phase lead for $\eta > \eta_A$ and seemingly shifts phase back to 0°. Hence, additional limit analysis for Eq. (2.36) is performed which yields with summarized expressions

$$\beta_\infty = \lim_{\eta \to \infty} \beta \left(\mu = 0 \right) = 90°, \quad \beta_\infty = \lim_{\eta \to \infty} \beta \left(\mu \neq 0 \right) = 0°. \tag{2.39a,b}$$

Thus, it can be recapitulated that standard 1DOF isolator phase angle β_∞ consistently tends to 90° without inerter [31]. However, β_∞ tends to 0° with inerter of any positive arbitrary inertance ratio μ value present in the system. Furthermore, parametric plots for phase angle β from Eq. (2.36) are shown in Figure 2.15 for various combinations of ζ and μ. Equal ζ and μ parameters are used as in Figure 2.13a) and b). It is observed that rate of asymptotical convergence to $\beta_\infty = 0°$ depends on both damping and inertance effects simultaneously. The larger the dimensionless damping ζ is, the rate of convergence is slower, see Figure 2.15a). Contrary to that, the larger the inertance ratio μ is, the rate of convergence to zero after resonance is faster, since phase lead occurs immediately after post-resonant phase lag for rising dimensionless inertance, i.e. $\mu\uparrow$, as shown in Figure 2.15b) with dotted line.

a)   b)
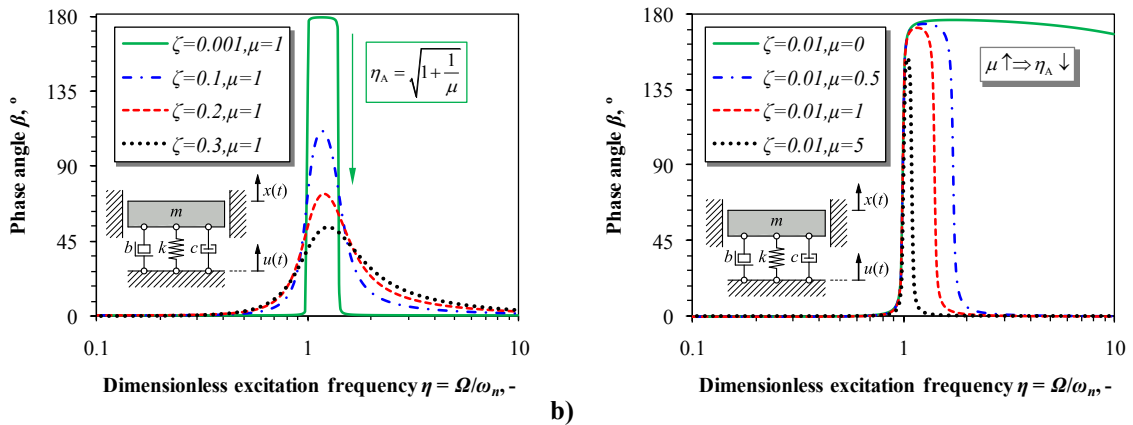
Figure 2.15.   **Phase angle $\beta \angle (x_0/u_0)$ by varying: a) damping ratio ζ ($\mu = 1$), b) inertance ratio μ ($\zeta = 0.01$)**

Relative displacement amplitude $|x_{0,\text{rel}}|$ and corresponding relative magnification factor $M_{0,\text{rel}}$ respectively are considered with regard to scheme from Figure 2.12b). Besides Eq. (2.30c) and Eq. (2.32b), these quantities can also be expressed by using vector addition/subtraction cosine rule (*i.e.* by Pythagorean Theorem) with relations

$$|x_{0,\text{rel}}| = \sqrt{|x_0|^2 + |u_0|^2 - 2|x_0 u_0|\cos(\beta)}, \quad M_{0,\text{rel}} = \left|\frac{x_{0,\text{rel}}}{u_0}\right| = \sqrt{\left|\frac{x_0}{u_0}\right|^2 + 1 - 2\left|\frac{x_0}{u_0}\right|\cos(\beta)}. \quad (2.40\text{a,b})$$

In conclusion, reported anti-resonant frequency η_A value is always higher than resonant dimensionless frequency value (*i.e.* unity). Additionally, the improvements for absolute magnification factor M_0 are evident up to near-resonant and anti-resonant frequencies $0 < \eta \leq \eta_\text{A}$ due to installation of an inerter. However, an inherent trade-off and consequent degradation is observed for frequencies beyond anti-resonance where $\eta \gg \eta_\text{A}$. Furthermore, the improvements are evident for relative magnification factor $M_{0,\text{rel}}$ at all frequencies $0 < \eta \leq \infty$ due to addition of an inerter. This is evident from structure of Eq. (2.32b) and corresponding limit analysis for increasing dimensionless inertance μ value where

$$\lim_{\mu \to \infty} M_{0,\text{rel}} = 0. \tag{2.41}$$

These generalized findings are summarized through following relations

$$\eta_{\text{A}}\left(\mu \in [0,\infty\rangle\right) > 1, \quad \mu \uparrow \Rightarrow M_0\left(\eta \in \langle 0, \sim \eta_{\text{A}}]\right) \downarrow, \quad \mu \uparrow \Rightarrow M_{0,\text{rel}}\left(\eta \in \langle 0, \infty]\right) \downarrow. \tag{2.42a-c}$$

Furthermore, novel spring stress and displacement correction factors are proposed. These approximate expressions explicitly write as

$$K_{\tau,A/G,i} = \overbrace{1.005}^{\text{emp. corr.}} + \frac{5}{4C} + \overbrace{\frac{8}{7C^2}}^{\text{math. corr.}} + \overbrace{\frac{1+2\nu}{2(1+\nu)}}^{\text{Wahl/Timo. corr.}} \tan^2(\alpha), \quad K_{\delta,A/G,i} = 1 - \frac{3}{16C^2} + \overbrace{\frac{3.185 + \nu}{2(1+\nu)}}^{\text{emp. corr.}} \tan^2(\alpha). \tag{2.43a,b}$$

Proposed correction factors from Eq. (2.43) are compatible with original approximate A/G [112] and Wahl/Timoshenko [111] corrections when pitch angle is rather small and Poisson's ratio $\nu \approx 0.3$. However, it is shown through performed detailed parametric FEM analyses that proposed corrections may capture thick spring (i.e. small spring index C), large pitch angle α, and arbitrary Poisson's ratio ($\nu = 0 - 0.5$) effects simultaneously.

By considering relative magnification factor $M_{0,\text{rel}}$ from Eq. (2.32b) and modifying the Eq. (2.23b) to take into account relative displacement amplitudes $x_{0,\text{rel}}$, following relation is obtained for assessing the spring fatigue life in resonant conditions

$$N_{\text{f,res}}\left(\Omega = \omega_n\right) = \left[\sqrt{3}\,\frac{K_\tau}{K_\delta}\,\frac{G}{C^2 n \pi d}\,\frac{|u_0|}{2\zeta(1+\mu)S'_{\text{f}}} \right]^{\frac{1}{B}}. \tag{2.44}$$

Novel spring correction factors from Eqs. (2.43) are readily incorporated into Eq. (2.44). In order to verify analytical findings, FEM is utilized next. Both direct stiffness method and analogue mode superposition method are employed. Due to limitations of numerical implementation of mode superposition when considering kinematic excitation, approximate big mass method (BMM) [28] or large mass method (LMM) [126] is used.

It is shown that all derived expressions match FEM results very well. When stress and deflection correction is omitted, i.e. for simpler isolator model considered, the differences in results between analytical and numerical method are negligible.

3.   Conclusions and Future Work

3.1.   Conclusions

In this research, novel inerter-based passive and active vibration isolation systems are presented. Benchmark isolators not employing and employing the inerter are investigated. The methodology is studied on a simple one degree and two degrees of freedom systems so that general conclusions can be drawn based on analytically derived expressions. The systems are classified as the source/receiving body types. Source body implies the part of the structure that is excited by vibrations, i.e. the source of vibrations. Receiving body includes the part of the structure that needs to be protected from vibrations. In one degree of freedom systems, broadband frequency kinematic excitation is considered. In two degrees of freedom systems, broadband force excitation is considered. These simplified systems can be considered as reduced order models of potentially more advanced and complex structures. The frequency averaged kinetic energy of the receiving body, i.e. broadband velocity amplitudes are used as the measure for vibration isolation quality. Moreover, general H_2 optimization which utilizes broadband displacement amplitudes is used as an alternative optimization metric for fair benchmark comparison. Vibration fatigue related optimization is tied to corresponding displacement based optimization. It is determined that H_∞ optimization criterion is not suitable for solving this class of vibration isolation problems, thus it is not utilized. This is due to the real physical constraints which govern the stiffness of the isolator spring in the system and hence limit the applicability of the method. In active systems, which utilize direct velocity feedback, also called the skyhook damping, Hurwitz analytical criterion is used for stability assessment. Analytically obtained expressions are verified via numerical simulations, most notably finite element method. Direct and mode superposition methods are used. Ideal inerter concept is successfully implemented into finite element-based linear dynamic models.

It is shown throughout the investigation that the vibration isolation performance of the fundamental passive isolator not employing the inerter can be improved by adding the inerter in parallel with the isolator spring and damper. This improvement is especially evident if the source and receiving bodies have similar uncoupled natural frequencies. If these frequencies are theoretically exactly the same, the isolator locks and its function is immanently deteriorated. This is called the critical system. For such cases, isolator parameters become irrelevant as system is inherently poorly designed. Thus, such setup should be avoided beforehand, in the initial stages of dynamic system design. By investigating the

stability of the active control when no inerter is used, two fundamental families of vibration isolation problems are defined. The first family (i.e. supercritical systems) is characterised by the natural frequency of the uncoupled source body larger than the natural frequency of the uncoupled receiving body. For this type of systems, any physically available feedback gain can be utilized without compromising the stability of the feedback control system. This results in a prominent broadband vibration isolation effect where theoretically unlimited amounts of feedback gain may be set. The second family of systems (i.e. subcritical systems) is characterised with the natural frequency of the uncoupled source body being smaller than the natural frequency of the uncoupled receiving body. The range of stable feedback gains is here limited which results in poor vibration isolation performance due to conditionally limited feedback gain. However with the inclusion of the inerter, broadband active vibration isolation can also be achieved in the subcritical family of systems. Adding the inerter into the isolator effectively generates effect that stabilises the control loop unconditionally, hence arbitrarily large feedback gains may be utilized for active vibration control. Consequently, improved stability margin is achieved for subcritical type of vibration isolation systems.

Furthermore, it is shown that employing the inerter in isolation systems can yield with substantial improvements in fatigue life of isolator coupling components, i.e. springs. With regard to vibration fatigue and corresponding dynamically loaded structural elements, novel improved analytical expressions for cylindrical helical spring stress and deflection correction are proposed. Novel helical spring stress and correction factors are proposed in order to be able to analytically assess the dynamic properties of the structures and its deformable elements' corresponding fatigue life. Consistency of novel correction factors with original correction factors from literature is reported. The influence of pitch angle and Poisson's ratio on deflection and stress field is determined. It is noted that arising spring pitch angle significantly influences spring stress and stiffness and thus shouldn't be neglected. Novel correction factors, based on the performed finite element method analysis in the scope of this investigation, outperform correction factors available in the current literature for arbitrary physical value of spring index, pitch angle and Poisson's ratio. This accuracy improvement is especially evident when large spring pitch angle effects are addressed. Moreover, proposed spring correction factors could potentially be used for design of the helical springs which consider homogenous materials other than steel.

The result of the research is a development of new method for passive and active vibration control. Main research findings can be summarized through following conclusions:

- The performance of the basic passive vibration isolator that does not use an inerter is improved by adding the inerter of specific optimized inertance in parallel with the isolator spring and damper. Optimized inertance is obtained in closed-form.

- The stability and corresponding performance of the system for active vibration isolation is improved by using the inerter of large enough inertance. This yields with potential opportunity to theoretically achieve unconditionally stable active vibration isolation in the wider frequency range. Necessary inertance is obtained in closed-form.

- Employing the inerter in the isolator can substantially prolong and enhance the fatigue life of dynamically loaded structures. Inerter-related improvements are especially evident in resonant working conditions, particularly when only small inherent damping is present in the system.

Thus, a new method for improving and enhancing the performance of both passive and active isolators in broadband frequency range by using inerters is developed in the scope of this work. Cumulative contribution of this work is accomplished by linking the inerter benefits to control theory and vibration-induced fatigue. The method proposed in this investigation could potentially find usage in assessing harmful vibrations, appropriately optimizing dynamic systems, and consequently preventing excessive oscillations and corresponding damage in general isolators and suspensions. Simplified analytical assessments may be performed in conjunction with computationally more expensive finite element method calculations. Obtained results could be used as indicators for conducting full-field experimental measurements.

Moreover, numerous potential real engineering applications for inerter may be observed, e.g.: automotive, aerospace, building construction etc. Inerter revitalized possibilities for additional applications in various passive and active isolator systems, most notably vehicle suspensions. Due to relative ease of implementation and low expense of manufacturing, the inerter-based devices will expectedly become standard suspension elements in Formula 1 racing in the near future. Presumably, it is only a question of imminent time before inerters appear in commercial vehicles' suspensions readily available to the common population.

3.2.   Future Work

This theoretical investigation opened many new possibilities for further inerter implementation in vide variety of real engineering applications and left some open questions for future research.

Firstly, simple experimental validation of obtained results may be performed as a direct extension of performed work. Full-field experimental measurements should confirm the influence of inerter in the isolator of subcritical system on stability of active control when using skyhook active damping scheme. Moreover, experimental measurements of cylindrical springs in both static and dynamic test environment could be performed to determine the correctness and accuracy of proposed correction factors, most notably when larger spring pitch angles are addressed. Materials other than steel may be considered. Additional effects, e.g. strain rate and mean static pre-stress could be studied.

Purely spectral fatigue probabilistic type of optimization, which takes into account random power spectral density broadband frequency excitation, may be performed in the future. This would yield with more realistic evaluation of deformable parts' durability in suspensions, or general isolator components.

In order to try to overcome the deficiencies of mechanical inerters (i.e. stick/slip and backlash/clearances-induced nonlinearities), inerter may by synthesized by mechatronic means, e.g. by using an active system which comprises of set of sensors and actuators and mimics the relative mass concept. Direct acceleration feedback, in contrast to direct velocity feedback may be utilized. Future theoretical and experimental study could adopt and investigate this approach.

Furthermore, in order to complete the investigations of sub/super-critical systems employing inerters, skyhook scheme with inerter in supercritical systems will be investigated. Different parallel/series setup of isolator components will be studied, with the aim of retaining the achieved benefits of current setup. Also, the influence of real, non-idealized inerter added mass on stability and performance of subcritical systems is yet to be determined.

Literature

[1]　　Smith, M.C., Synthesis of mechanical networks: The inerter, IEEE Transactions on Automatic Control 47(10) (2002) 1648–1662.

[2]　　Smith, M.C., Wang, F.-C., Performance Benefits in Passive Vehicle Suspensions Employing Inerters, Vehicle System Dynamics 42(4) (2004) 235–257.

[3]　　Chen, M.Z.Q., Papageorgiou, C., Scheibe, F., Wang, F.-C., Smith, M.C., The missing mechanical circuit element, IEEE Circuits and Systems Magazine 9(1) (2009) 10–26.

[4]　　Schönfeld, J.C., Analogy of hydraulic, mechanical, acoustic and electrical systems, Applied Scientific Research, Section B 3(1) (1954) 417–450.

[5]　　Gonzalez-Buelga, A., Clare, L.R., Neild, S.A., Jiang, J.Z., Inman, D.J., An electromagnetic inerter-based vibration suppression device, Smart Materials and Structures 24(5) (2015) 1–10.

[6]　　Li, D., Liu, Y.-Z., Designing and Simulating a Mechatronic Inerter, Applied Mechanics and Materials 620 (2014) 28–32.

[7]　　Wang, F.-C., Hong, M-F., Lin, T.-C., Designing and testing a hydraulic inerter, Proceedings of the Institution of Mechanical Engineers, Part C, Journal of Mechanical Engineering Science 225(1) (2010) 66–72.

[8]　　Swift, S.J., Smith, M.C., Glover, A.R., Papageorgiou, C., Gartner, B., Houghton, N.E., Design and modelling of a fluid inerter, International Journal of Control 86(11) (2013) 2035–2051.

[9]　　Brzeski, P., Pavlovskaia, E., Kapitaniak, T., Perlikowski, P., The application of inerter in tuned mass absorber, International Journal of Non-Linear Mechanics 70 (2015) 20–29.

[10]　Bein, T., Mayer, D., Bös, J., Recent solutions for noise & vibration control in vehicles, 41st International Congress and Exposition on Noise Control Engineering 2012, INTER-NOISE 2012 5 (2012) 3759–3771.

[11]　Bein, T., Bös, J., Herold, S., Mayer, D., Melz, T., Thomaier, M., Smart interfaces and semi-active vibration absorber for noise reduction in vehicle structures, Aerospace Science and Technology 12(1) (2008) 62–73.

[12]　Lazar, I.F., Neild, S.A., Wagg, D.J., Vibration suppression of cables using tuned inerter dampers, Engineering Structures 122 (2016) 62–71.

[13]   Brzeski, P., Kapitaniak, T., Perlikowski, P., Novel type of tuned mass damper with inerter which enables change of inertance, Journal of Sound and Vibration 349 (2015) 56–66.

[14]   Brzeski, P., Lazarek, M., Perlikowski, P., Experimental study of the novel tuned mass damper with inerter which enables changes of inertance, Journal of Sound and Vibration 404 (2017) 47–57.

[15]   Hu, Y., Chen, M.Z.Q., Performance evaluation for inerter-based dynamic vibration absorbers, International Journal of Mechanical Sciences 99 (2015) 297–307.

[16]   Shi, X., Zhu, S., Dynamic characteristics of stay cables with inerter dampers, Journal of Sound and Vibration 423 (2018) 287–305.

[17]   Zhao, G., Alujević, N., Depraetere, B., Pinte, G., Swevers, J., Sas, P., Experimental study on active structural acoustic control of rotating machinery using rotating piezo-based inertial actuators, Journal of Sound and Vibration 348 (2015) 15–30.

[18]   Zilletti, M., Feedback control unit with an inerter proof-mass electrodynamic actuator, Journal of Sound and Vibration 369 (2016) 16–28.

[19]   Kras, A., Gardonio, P., Velocity feedback control with a flywheel proof mass actuator, Journal of Sound and Vibration 402 (2017) 31–50.

[20]   Chen, M.Z.Q., Wang, K., Zou, Y., Lam, J., Realization of a Special Class of Admittances with One Damper and One Inerter for Mechanical Control, IEEE Transactions on Automatic Control 58(7) (2013) 1841–1846.

[21]   Kuznetsov, A., Mammadov, M., Sultan, I., Hajilarov, E., Optimization of improved suspension system with inerter device of the quarter-car model in vibration analysis, Archive of Applied Mechanics 81(10) (2011) 1427–1437.

[22]   Chen, M.Z.Q., Hu, Y., Li, C., Chen, G., Performance Benefits of Using Inerter in Semiactive Suspensions, IEEE Transactions on Control Systems Technology 23(4) (2015) 1571–1577.

[23]   Chen, M.Z.Q., Hu, Y., Li, C., Chen, G., Application of Semi-Active Inerter in Semi-Active Suspensions Via Force Tracking, ASME Journal of Vibration and Acoustics 138(4) (2016) 041014-1–041014-11.

[24]   Lazar, I.F., Neild, S.A., Wagg, D.J., Using an inerter-based device for structural vibration suppression, Earthquake Engineering & Structural Dynamics 43(8) (2014) 1129–1147.

[25]   Hu, Y., Chen, M.Z.Q., Shu, Z., Huang, L., Analysis and optimisation for inerter-based isolators via fixed-point theory and algebraic solution, Journal of Sound and Vibration 346 (2015) 17–36.

[26]   Alujević, N., Wolf, H., Gardonio, P., Tomac, I., Stability and performance limits for active vibration isolation using blended velocity feedback, Journal of Sound and Vibration 330(21) (2011) 4981–4997.

[27]   Preumont, A., Vibration Control of Active Structures, An Introduction, Fourth Edition, Solid Mechanics and Its Applications Volume 246, Springer International Publishing, AG, 2018.

[28]   Dassault Systèmes, Abaqus 6.9 User's guide and theoretical manual, Hibbitt, Karlsson & Sorensen, Inc., 2009.

[29]   Dassault Systèmes, Catia V5R19 Documentation: Finite Element Reference Guide, 2007.

[30]   Safe Technology, Fe-Safe 6 User Manual, 2011.

[31]   Rao, S.S., Mechanical Vibrations, Sixth Edition in SI Units, Global Edition, Pearson, London, 2017.

[32]   Bishop, N.W.M., Sherratt, F., Finite Element Based Fatigue Calculations, NAFEMS Ltd, Farnham, 2000.

[33]   Elias, S., Matsagar, V., Research developments in vibration control of structures using passive tuned mass dampers, Annual Reviews in Control 44 (2017) 129-156.

[34]   Hagedorn, P., Spelsberg-Korspeter, G. (Eds.), Active and Passive Vibration Control of Structures, CISM International Centre for Mechanical Sciences 558, Springer-Verlag, Wien, 2014.

[35]   Rivin, E.I., Passive Vibration Isolation, ASME Press, New York, 2003.

[36]   Karnopp, D.C., Trikha, A.K., Comparative Study of Optimization Techniques for Shock and Vibration Isolation, ASME Journal of Engineering for Industry 91(4) (1969) 1128–1132.

[37]   Kaplow, C.E., Velman, J.R., Active Local Vibration Isolation Applied to a Flexible Space Telescope, Journal of Guidance Control and Dynamics 3(3) (1980) 227–233.

[38]   Zhang, X.-J., Ahmadianb, M., Guoa, K.-H., On the benefits of semi-active suspensions with inerters, Shock and Vibration 19(3) (2012) 257–272.

[39]   Cheung, Y.L., Wong, W.O., H∞ and H2 optimizations of a dynamic vibration absorber for suppressing vibrations in plates, Journal of Sound and Vibration 320(1–2) (2009) 29-42.

[40]   Cheung, Y.L., Wong, W.O., H2 optimization of a non-traditional dynamic vibration absorber for vibration control of structures under random force excitation, Journal of Sound and Vibration 330(6) (2011) 1039–1044.

[41]   Frahm, H., Device for damping vibrations of bodies, U.S. Patent, 989,958 (1911) 3576–3580.

[42]   Den Hartog, J.P., Mechanical Vibrations, Dover Publications Inc., New York, 1985.

[43]   Crandall, S.H., Mark, W.D., Random Vibration in Mechanical Systems, Academic Press, New York, 1963.

[44]   Alujević, N., Zhao, G., Depraetere, B., Sas, P., Pluymers, B., Desmet, W., H2 optimal vibration control using inertial actuators and a comparison with tuned mass dampers, Journal of Sound and Vibration 333(18) (2014) 4073–4083.

[45]   Zhao, G., Alujević, N., Depraetere, B., Sas, P., Dynamic analysis and H2 optimisation of a piezo-based tuned vibration absorber, Journal of Intelligent Material Systems and Structures 26(15) (2014) 1995–2010.

[46]   Sun, H., Luo, Y., Xiuyong, W., Zuo, L., Seismic control of a SDOF structure through electromagnetic resonant shunt tuned mass-damper-inerter and the exact H2 optimal solutions, Journal of Vibroengineering 19(3) (2017) 2063–2079.

[47]   Cheung, Y.L., Wong, W.O., Cheng, L., Optimization of a hybrid vibration absorber for vibration control of structures under random force excitation, Journal of Sound and Vibration 332(3) (2013) 494–509.

[48]   Warburton, G.B., Optimum Absorber Parameters for Various Combinations of Response and Excitation Parameters, Earthquake Engineering and Structural Dynamics 10(3) (1982) 381–401.

[49]   Høgsberg, J., Vibration control by piezoelectric proof-mass absorber with resistive-inductive shunt, Mechanics of Advanced Materials and Structures (2019) 1–13.

[50]   Pan, C., Zhang, R., Design of structure with inerter system based on stochastic response mitigation ratio, Structural Control and Health Monitoring 25(6) (2018) 1–21.

[51]   Wen, H., Guo, J., Li, Y., Liu, Y., The transmissibility of a vibration isolation system with ball-screw inerter based on complex mas, Journal of Low Frequency Noise, Vibration and Active Control 35 (2018) 1–12.

[52]   Barredo, E., Blanco, A., Colín, J., Penagos, V.M., Abúndez, A., Vela, L.G., Meza, V., Cruz, R.H., Mayén, J., Closed-form solutions for the optimal design of inerter-

based dynamic vibration absorbers, International Journal of Mechanical Sciences 144 (2018) 41–53.

[53]   Chen, M.Z.Q., Hu, Y., Inerter and Its Application in Vibration Control Systems, Springer Verlag, Singapore, Beijing, 2019.

[54]   Chen, M.Z.Q., Hu, Y., Wang, F.-C., Passive Mechanical Control With a Special Class of Positive Real Controllers: Application to Passive Vehicle Suspensions, ASME Journal of Dynamic Systems, Measurement, and Control 137(12) (2015) 121013-1–121013-11.

[55]   Evangelou, S., Limebeer, D.J.N., Sharp, R.S., Smith, M.C., Mechanical Steering Compensators for High-Performance Motorcycles, ASME Journal of Applied Mechanics 74(2) (2007) 332–346.

[56]   Chen, M.Z.Q., Hu, Y., Huang, L., Chen, G., Influence of inerter on natural frequencies of vibration systems, Journal of Sound and Vibration 333(7) (2014) 1874–1887.

[57]   Papageorgiou, C., Houghton, N.E., Smith, M.C., Experimental Testing and Analysis of Inerter Devices, ASME Journal of Dynamic Systems Measurement and Control 131(1) (2009) 011001-1–011001-11.

[58]   Sun, X.Q., Chen, L., Wang, S.H., Zhang, X.L., Yang, X.F., Performance investigation of vehicle suspension system with nonlinear ball-screw inerter, International Journal of Automotive Technology 17(3) (2016) 399–408.

[59]   Wang, F.-C., Chan, H.-A., Vehicle suspensions with a mechatronic network strut, Vehicle System Dynamics 49(5) (2011) 811–830.

[60]   Wang, F.-C., Su, W.-J., Impact of inerter nonlinearities on vehicle suspension control, Vehicle System Dynamics: International Journal of Vehicle Mechanics and Mobility 46(7) (2008) 575–595.

[61]   Liu, X., Jiang, J.Z., Titurus, B., Harrison, A., Model identification methodology for fluid-based inerters, Mechanical Systems and Signal Processing 106 (2018) 479–494.

[62]   Brzeski, P., Perlikowski, P., Effects of play and inerter nonlinearities on the performance of tuned mass damper, Nonlinear Dynamics 88(2) (2017) 1027–1041.

[63]   Moraes, F.H., Silveira, M., Gonçalves, P.J., On the dynamics of a vibration isolator with geometrically nonlinear inerter, Nonlinear Dynamics 93(3) (2018) 1–16.

[64]   Soong, M.F., Ramli, R., Mahadi, W.N.L., Ride Evaluation of Vehicle Suspension Employing Non-Linear Inerter, Applied Mechanics and Materials 471 (2013) 9–13.

[65]   Zhang, X.-L., Gao, Q., Nie, J., The mem-inerter: A new mechanical element with memory, Advances in Mechanical Engineering 10(6) (2018) 1–13.

[66]   Zhang, Z., Lu, Z.-Q., Ding, H., Chen, L.-Q., An inertial nonlinear energy sink, Journal of Sound and Vibration 450 (2019) 199–213.

[67]   Li, Y., Jiang, J.Z., Neild, S.A., Inerter-Based Configurations for Main-Landing-Gear Shimmy Suppression, Journal of Aircraft 54(2) (2017) 684–693.

[68]   Li, Y., Jiang, J.Z., Neild, S.A., Wang, H., Optimal Inerter-Based Shock–Strut Configurations for Landing-Gear Touchdown Performance, Journal of Aircraft 54(5) (2017) 1901–1909.

[69]   Hu, Y., Wang, J., Chen, M.Z.Q., Li, Z., Sun, Y., Load mitigation for a barge-type floating offshore wind turbine via inerter-based passive structural control, Engineering Structures 177 (2018) 198–209.

[70]   Zhang, R., Zhao, Z., Dai, K., Seismic response mitigation of a wind turbine tower using a tuned parallel inerter mass system, Engineering Structures 180 (2019) 29–39.

[71]   Xu, K., Bi, K., Han, Q., Li, X., Du, X., Using tuned mass damper inerter to mitigate vortex-induced vibration of long-span bridges: Analytical study, Engineering Structures 182 (2019) 101–111.

[72]   Zhang, R., Zhao, Z., Pan, C., Influence of mechanical layout of inerter systems on seismic mitigation of storage tanks, Soil Dynamics and Earthquake Engineering 114 (2018) 639–649.

[73]   Zhang, S.Y., Jiang, J.Z., Neild, S., Optimal configurations for a linear vibration suppression device in a multi-storey building, Structural Control and Health Monitoring 24(3) (2016) 1–17.

[74]   Sun, L., Hong, D., Chen, L., Cables interconnected with tuned inerter damper for vibration mitigation, Engineering Structures 151 (2017) 57–67.

[75]   Marian, L., Giaralis, A., The tuned mass-damper-inerter for harmonic vibrations suppression, attached mass reduction, and energy harvesting, Smart structures and systems 19(6) (2017) 665–678.

[76]   Chen, M.Z.Q., Wang, K., Zou, Y., Chen, G., Realization of Three-port Spring Networks with Inerter for Effective Mechanical Control, IEEE Transactions on Automatic Control 60(10) (2015) 2722–2727.

[77]   Hu, Y., Chen, M.Z.Q., Xu, S., Liu, Y., Semiactive Inerter and Its Application in Adaptive Tuned Vibration Absorbers, IEEE Transactions on Control Systems Technology 25(1) (2017) 294–300.

[78]   Jin, X., Chen, M.Z.Q., Huang, Z., Minimization of the beam response using inerter-based passive vibration control configurations, International Journal of Mechanical Sciences 119 (2016) 80–87.

[79]   Siami, A., Karimi, H.R., Cigada, A., Zappa, E., Sabbioni, E., Parameter optimization of an inerter-based isolator for passive vibration control of Michelangelo's Rondanini Pietà, Mechanical Systems and Signal Processing 98 (2018) 667–683.

[80]   Wang, Y., Wang, R.-C., Meng, H.-D., Analysis and comparison of the dynamic performance of one-stage inerter-based and linear vibration isolators, International Journal of Applied Mechanics 10(1) (2018) 1–36.

[81]   Masri, S.F., Caffrey, J.P., Transient Response of a SDOF System With an Inerter to Nonstationary Stochastic Excitation, ASME Journal of Applied Mechanics 84(4) (2017) 041005-1–041005-10.

[82]   Wang, F.-C., Wu, S.-Y., Vibration control of an optical table employing mechatronic inerter networks, Journal of Vibration and Control 22(1) (2016) 224–234.

[83]   Basili, M., De Angelis, M., Pietrosanti, D., Modal analysis and dynamic response of two adjacent single-degree-of-freedom systems linked by spring-dashpot-inerter elements, Engineering Structures 174 (2018) 736–752.

[84]   Pan, C., Zhang, R., Luo, H., Li, C., Shen, H., Demand-based optimal design of oscillator with parallel-layout viscous inerter damper, Structural Control and Health Monitoring 25(1) (2017) 1–15.

[85]   Chen, H.-J., Su, W.-J., Wang, F.-C., Modeling and analyses of a connected multi-car train system employing the inerter, Advances in Mechanical Engineering 9(8) (2017) 1–13.

[86]   Chen, L., Liu, C., Liu, W., Nie, J., Shen, Y., Chen, G., Network synthesis and parameter optimization for vehicle suspension with inerter, Advances in Mechanical Engineering 9(1) (2017) 1–7.

[87]   Hu, Y., Chen, M.Z.Q., Shu, Z., Passive vehicle suspensions employing inerters with multiple performance requirements, Journal of Sound and Vibration 333(8) (2014) 2212–2225.

[88]   Hu, Y., Chen, M.Z.Q., Sun, Y., Comfort-oriented vehicle suspension design with skyhook inerter configuration, Journal of Sound and Vibration 405 (2017) 34–47.

[89]   Hu, Y., Wang, K., Chen, Y., Chen, M.Z.Q., Inerter-based semi-active suspensions with low-order mechanical admittance via network synthesis, Transactions of the Institute of Measurement and Control (2018) 1–13.

[90] Jiang, J.Z., Matamoros-Sanchez, A.Z., Goodall, R.M., Smith, M.C., Passive suspensions incorporating inerters for railway vehicles, Vehicle System Dynamics: International Journal of Vehicle Mechanics and Mobility 50(1) (2012) 263–276.

[91] Li, P., Lam, J., Cheung, K.C., Control of vehicle suspension using an adaptive inerter, Proceedings of the Institution of Mechanical Engineers, Part D, Journal of Automobile Engineering 229(14) (2015) 1934–1943.

[92] Shen, Y., Chen, L., Yang, X., Shi, D., Yang, J., Improved design of dynamic vibration absorber by using the inerter and its application in vehicle suspension, Journal of Sound and Vibration 361 (2016) 148–158.

[93] Soong, M.F., Ramli, R., Mahadi, W.N.L., Saifizul, A., Ride improvement of vehicle suspensions with switchable inerter based on force cancellation strategy, Journal of Vibroengineering 19(2) (2017) 1260–1272.

[94] Soong, M.F., Ramli, R., Wan Mahadi, W.N.L., Vehicle suspensions with parallel inerter: effectiveness in improving vibration isolation, Journal of Vibroengineering 16(1) (2014) 256–265.

[95] Tran, T.-T., Hasegawa, H., Advanced Passive Suspension with Inerter Devices and Optimization Design for Vehicle Oscillation, International Journal of Mechanical Engineering and Robotics Research 4(4) (2015) 354–360.

[96] De Domenico, D., Impollonia, N., Ricciardi, G., Soil-dependent optimum design of a new passive vibration control system combining seismic base isolation with tuned inerter damper, Soil Dynamics and Earthquake Engineering 105 (2018) 37–53.

[97] Gonzalez-Buelga, A., Clare, L.R., Cammarano, A., Neild, S.A., Burrow, S.G., Inman, D.J., An optimised tuned mass damper/harvester device, Structural Control and Health Monitoring 21(8) (2014) 1154–1169.

[98] Ruiz, R., Taflanidis, A.A., Giaralis, A., Lopez-Garcia, D., Risk-informed optimization of the tuned mass-damper-inerter (TMDI) for the seismic protection of multi-storey building structures, Engineering Structures 177 (2018) 836–850.

[99] De Domenico, D., Ricciardi, G., An enhanced base isolation system equipped with optimal tuned mass damper inerter (TMDI), Earthquake Engineering & Structural Dynamics (2017) 1–24.

[100] Giaralis, A., Petrini, F., Wind-Induced Vibration Mitigation in Tall Buildings Using the Tuned Mass-Damper-Inerter, ASCE Journal of Structural Engineering 143(9) (2017) 04017127-1–04017127-11.

[101] Lazarek, M., Brzeski, P., Perlikowski, P., Design and identification of parameters of tuned mass damper with inerter which enables changes of inertance, Mechanism and Machine Theory 119 (2018) 161–173.

[102] Marian, L., Giaralis, A., Optimal design of a novel tuned mass-damper–inerter (TMDI) passive vibration control configuration for stochastically support-excited structural systems, Probabilistic Engineering Mechanics 38 (2014) 156–164.

[103] Pietrosanti, D., De Angelis, M., Basili, M., Optimal design and performance evaluation of systems with Tuned Mass Damper Inerter (TMDI), Earthquake Engineering & Structural Dynamics 46(8) (2017) 1367–1388.

[104] Wen, Y., Chen, Z., Hua, X., Design and Evaluation of Tuned Inerter-Based Dampers for the Seismic Control of MDOF Structures, ASCE Journal of Structural Engineering 143(4) (2017) 04016207-1–04016207-11.

[105] Wang, R., Ye, Q., Sun, Z., Zhou, W., Cao, Y., Chen, L., A study of the hydraulically interconnected inerter, Mechanics Based Design of Structures and Machines 45(4) (2017) 415–429.

[106] Ma, R., Bi, K., Hao, H., Mitigation of heave response of semi-submersible platform (SSP) using tuned heave plate inerter (THPI), Engineering Structures 177 (2018) 357–373.

[107] Hu, Y., Chen, M.Z.Q., Smith, M.C., Natural frequency assignment for mass-chain systems with inerters, Mechanical Systems and Signal Processing 108 (2018) 126–139.

[108] Suciu, B., Tsuji, Y., Theoretical Investigation on the Dynamic Characteristics of One Degree of Freedom Vibration System Equipped with Inerter of Variable Inertance, International Journal of Mechanical, Aerospace, Industrial, Mechatronic and Manufacturing Engineering 11(3) (2017) 448–456.

[109] Yilmaz, C., Kikuchi, N., Analysis and design of passive band-stop filter-type vibration isolators for low-frequency applications, Journal of Sound and Vibration 291(3-5) (2006) 1004–1028.

[110] Flannelly, W.G., Dynamic antiresonant vibration isolator, U.S. Patent No. 3,322,379, 1967.

[111] Wahl, A.M., Mechanical Springs, First Edition, Penton Pub. Co., Cleveland, 1944.

[112] Ancker, C.J.Jr., Goodier, J.N., Pitch and Curvature Correction for Helical Springs, ASME Journal of Applied Mechanics 25(4) (1958) 466–470.

[113]   Research Committee on the Analysis of Helical Spring, Report of Research Committee on the Analysis of Helical Spring, Transactions of Japan Society of Spring Engineers 2004(49) (2004) 35–75.

[114]   James, H.M., Nichols, N.B., Phillips, R.S., Theory Of Servomechanisms, MIT Radiation Laboratory series, Vol. 25, First Edition, McGraw-Hill Book Company, Inc., New York, 1947.

[115]   Newland, D.E., An Introduction to Random Vibrations, Spectral & Wavelet Analysis, Third Edition, Dover Publications, New York, 2005.

[116]   Budynas R.G., Nisbett J.K., Shigley's Mechanical Engineering Design, 10th Edition. McGraw-Hill, New York, 2015.

[117]   Dym, C.L., Consistent derivations of spring rates for helical springs, ASME Journal of Mechanical Design 131(7) (2009) 1–5.

[118]   DIN EN 2089-1-1963-01, Helical springs made from round wire and rod - Calculation and design of Compression springs, 1963.

[119]   DIN EN 2089-1-1963-02, Helical springs made from round wire and rod - Calculation and design of Tension springs, 1963.

[120]   DIN EN 13906-1, Cylindrical helical springs made from round wire and bar - Calculation and design - Part 1: Compression springs, Beuth Verlag, Berlin, 2002.

[121]   DIN EN 13906-2, Cylindrical helical springs made from round wire and bar - Calculation and design - Part 2: Extension springs, Beuth Verlag, Berlin, 2002.

[122]   Hearn, E.J., Mechanics of Materials, Volume 1, An Introduction to the Mechanics of Elastic and Plastic Deformation of Solids and Structural Materials, Third Edition, Butterworth-Heinemann, Oxford, 1997.

[123]   Timoshenko S.P., Strength of Materials, Part II, Advanced Theory and Problems, Second Edition, D. Van Nostrand. Company, Inc., New York, 1940.

[124]   Timoshenko, S.P., Goodier, J.N., Theory of Elasticity, Second Edition, McGraw-Hill Book Co., New York, 1951.

[125]   Cowper, G.R., The Shear Coefficients in Timoshenko's Beam Theory, ASME Journal of Applied Mechanics 33(2) (1966) 335–340.

[126]   Kim, Y.-W., Jhung, M.J., A study on large mass method for dynamic problem of multiple degree-of-freedom system excited by ground acceleration time history, Journal of Mechanical Science and Technology 28(1) (2014) 25–41.

Curriculum Vitae

Damjan Čakmak was born on August 14, 1979 in Makarska, Croatia. In 1997, he finished high School Classics-Program Secondary School (Klasična Gimnazija), in Zagreb and started his studies at the Faculty of Mechanical Engineering and Naval Architecture (FAMENA), University of Zagreb. From 1999-2009 he worked on implementing information and communication technologies at the companies Novointel d.o.o. and «Nenem» d.o.o. In 2010 he continued studies at FAMENA which he finished in 2015 with honours. Since 2015, he has been employed at the Faculty of Mechanical Engineering and Naval Architecture, University of Zagreb, at the Department of Applied Mechanics, Chair of Applied Dynamics as a teaching assistant and a PhD student. He is involved in the teaching of graduate study courses Mechanics II (Cro. *Mehanika II*) and Theory of Vibrations (Cro. *Teorija Vibracija*). During PhD studies, he authored or co-authored 10 Current Contents (CC) published scientific papers in renowned journals, one scientific paper indexed in Scopus database and 4 scientific conference papers with international peer-review. He holds ACA (Avaya Certified Associate) + ACS (Avaya Certified Specialist) industrial certificates for telecommunications. He plays electric and acoustic guitar and has issued several music albums under Aquarius Records record publisher, Zagreb.

List of Publications

CROSBI: https://tinyurl.com/y2auuszr, **GoogleScholar**: https://tinyurl.com/yy9cbxoo

Declaration: Parts of the work presented in this Dissertation have been published in some of the articles listed below.

List of CC Scientific Journal Papers:

- Čakmak, D., Tomičević, Z., Wolf, H., Božić, Ž., Semenski, D., Trapić, I., *Vibration fatigue study of the helical spring in the base-excited inerter-based isolation system*, Engineering Failure Analysis 103 (2019) 44–56.

- Senjanović, I., Alujević, N., Ćatipović, I., Čakmak, D., Vladimir, N., Cho, D.-S., *Buckling analysis of toroidal shell by Rayleigh-Ritz method*, ASME Journal of Pressure Vessel Technology 141(4) (2019) 041204-1–041204-14.

- Senjanović, I., Čakmak, D., Alujević, N., Ćatipović, I., Vladimir, N., Cho, D.-S., *Pressure and rotation induced tensional forces of toroidal shell and their influence on natural vibrations*, Mechanics Research Communications 96 (2019) 1–6.

- Senjanović, I., Ćatipović, I., Alujević, N., Čakmak, D., Vladimir, N., *A finite strip for the vibration analysis of rotating toroidal shell under internal pressure*, ASME Journal of Vibration and Acoustics 141(2) (2019) 021013-1–021013-17.

- Alujević, N., Čakmak, D., Wolf, H., Jokić, M., *Passive and active vibration isolation systems using inerter*, Journal of Sound and Vibration 418 (2018) 163–183.

- Čakmak, D., Tomičević, Z., Wolf, H., Božić, Ž., *H_2 optimization and numerical study of inerter-based vibration isolation system helical spring fatigue life*, Archive of Applied Mechanics 89(7) (2019) 1221–1242.

- Čakmak, D., Wolf, H., Božić, Ž., Jokić, M., *Optimization of an inerter-based vibration isolation system and helical spring fatigue life assessment*, Archive of Applied Mechanics 89(5) (2019) 859–872.

- Senjanović, I., Alujević, N., Ćatipović, I., Čakmak, D., Vladimir, N., *Vibration analysis of rotating toroidal shell by the Rayleigh-Ritz method and Fourier series*, Engineering Structures 173 (2018) 870–891.

- Senjanović, I., Ćatipović, I., Alujević, N., Čakmak, D., Vladimir, N., *Free in-plane and out-of-plane vibrations of rotating thin ring based on the toroidal shell theory*, Archives of Mechanics 70(5) (2018) 429–455.

- Senjanović, I., Ćatipović, I., Alujević, N., Vladimir, N., Čakmak, D., *A finite strip for the vibration analysis of rotating cylindrical shells*, Thin-Walled Structures 122 (2018) 158–172.

List of Scientific Journal Papers in Other Databases (Scopus):

- Senjanović, I., Alujević, N., Ćatipović, I., Čakmak, D., Vladimir, N., Lozina, Ž., Some dilemmas in energy approach to vibration and stability analysis of pressurized and rotating toroidal shells, International Journal for Engineering Modelling 32(1) (2019) 59–76.

List of International Scientific Conference Papers:

- Čakmak, D., Božić, Ž., Wolf, H., Tomičević, Z., *Vibration and Fatigue Study of an Inerter-Based Isolation System*, 2nd International Conference on Structural Integrity and Durability 2018 Conference Proceedings, ICSID2018 Dubrovnik (2018) 1–5.

- Alujević, N., Čakmak, D., Wolf, H., Jokić, M., *An inerter-based active vibration isolation system*, Proceedings of the International Conference on Engineering Vibration (ICoEV 2017) - MATEC Web of Conferences 148 (2018) 11001.

- Senjanović, I., Ćatipović, I., Alujević, N., Vladimir, N., Čakmak, D., *Sophisticated finite strip for vibration analysis of a rotating cylindrical shell*, Proceedings of the International Conference on Engineering Vibration (ICoEV 2017) - MATEC Web of Conferences 148 (2018) 07001.

- Čakmak, D., Božić, Ž., Wolf, H., Alujević, N., *Simultaneous Vibration and Fatigue Optimization of an Inerter-based Vibration Isolation System*, International Conference on Structural Integrity and Durability 2017 Conference Proceedings, ICSID2017 Dubrovnik (2017) 1–7.

Summary of Scientific Papers

This chapter provides the summary and scientific contribution of published papers which are directly related to this dissertation. All of the presented papers are self-contained and tied through common topic: either active or passive vibration isolation control by employing inerter. Preformed investigations are primarily of theoretical nature and include finite element method-based analysis for verification purposes. Ideal inerter concept is implemented in finite element based-solution. Paper 1 lays the foundation of the dissertation and determines the main framework of the conducted investigation. Inerter and active skyhook damping control is introduced. All of the hypotheses of the research are proven and main scientific contributions are given within this manuscript. Minimization of specific kinetic energy is adopted as optimization criterion and Hurwitz criterion is used as stability metric. The contribution of this paper is recognized through citation in the first comprehensive introduction to the inerter textbook [53] authored by one of the leading inerter pioneers Chen and Hu. Furthermore, papers 2 and 3 serve as directly tied investigations and continuation of paper 1. Vibration fatigue of the receiving body helical spring is introduced and discussed. Finite element method is employed. Dynamic system comprised of inerter-based isolator similar to that from paper 1 is analyzed, however exclusively passive control is considered. More general H_2 (displacement) optimization criterion is used in conjunction with minimization of specific kinetic energy in order to evaluate fatigue-related benefits due to inerter in the isolator. Final paper 4 considers exclusively the fatigue in the inerter-based isolator helical spring and studies the inerter influence through detailed parametric analyses. Omitted parts of the paper which consider absolute displacement amplitudes are additionally included in this thesis in full. Simple physical realization of leverage type inerter is proposed. Additionally, improved helical spring stress and displacement corrections are proposed and verified. Papers are listed in chronological order of publishing.

Authorship contributions: The specific contributions made by each author is indicated in the appropriate category with each authors' name initials followed by their surnames.

Paper 1

In this paper, an inerter-based source body/receiving body two degrees of freedom vibration isolation system is investigated. Ideal passive inerter is utilized. Passive and active isolation schemes are considered. Active system employs direct velocity feedback. Performance and stability of the system are studied for the active and passive schemes. Broadband frequency excitation is presumed. Direct dynamic stiffness method is employed.

Scientific contribution of the paper is given as follows. It is reported that passive isolation systems employing inerters always outperform isolation systems not employing inerters according to broadband H_2 norm optimization criterion. Specific kinetic energy of the system, which is proportional to receiving body broadband velocity amplitudes, is taken into account. Furthermore, the influence of inerter on the stability of the active system is analyzed, and the performance benefits of using an inerter in subcritical systems were noted. It is shown that inerter of certain inertance can stabilize feedback loop and ensure stable skyhook damping. Inertance necessary for obtaining stable system with theoretically unlimited feedback gain is defined through simple analytical expression. All solutions are obtained in the closed form. Finally, analytical solutions are verified through parametric numerical simulations, where it was shown that derived expressions are approximately valid for more complex isolation systems with inherent damping present.

Study conception and design: N. Alujević, D. Čakmak, H. Wolf and M. Jokić

Acquisition of data: D. Čakmak and N. Alujević

Analysis and/or interpretation of data: N. Alujević and D. Čakmak

Drafting of the manuscript: N. Alujević and D. Čakmak

Critical revision: N. Alujević, D. Čakmak, H. Wolf and M. Jokić

Approval of the version of the manuscript to be published: N. Alujević, D. Čakmak, H. Wolf and M. Jokić

Paper 2

In this paper, the fatigue of coupling helical spring of receiving body in an inerter-based two degrees of freedom vibration isolation system is investigated. Passive isolation scheme is considered. The minimization of the specific kinetic energy of the system is used as an optimization criterion, with regard to previous work. Broadband frequency excitation is assumed. High cycle fatigue criterion for coupling spring is utilized through Basquin's equation. Approximate spring displacement and stress correction factors from referent literature are considered for vibration fatigue. The stresses in the spring are obtained through relating them with absolute displacements of the corresponding receiving body.

Scientific contribution of the paper is given as follows. Novel, Timoshenko thick beam-based spring displacement correction factor utilizing Cowper shear correction is derived analytically. Timoshenko-based displacement correction matches satisfyingly well with established correction factors from referent literature. It is demonstrated that velocity-based optimization yields with significant improvements in receiving body coupling helical spring fatigue life. Simple expression for assessment of receiving body coupling spring fatigue life for arbitrary excitation frequency is given in closed form. Expression embodies discussed displacement and stress correction factors, and applied inertance. Chosen correction factors are Ancker and Goodier for displacement, and Wahl for stress. Analogue to previous results, isolator systems which incorporate inerter outperform systems without inerter. Improvements are reported in specific kinetic energy index and fatigue life simultaneously.

Study conception and design: D. Čakmak, H. Wolf and Ž. Božić

Acquisition of data: D. Čakmak

Analysis and/or interpretation of data: D. Čakmak, H. Wolf and Ž. Božić

Drafting of the manuscript: D. Čakmak

Critical revision: D. Čakmak, H. Wolf, Ž. Božić and M. Jokić

Approval of the version of the manuscript to be published: D. Čakmak, H. Wolf, Ž. Božić and M. Jokić

Paper 3

In this paper, the fatigue of coupling helical spring of receiving body in an inerter-based two degrees of freedom vibration isolation system is further studied as a direct chronological continuation of previously published work form Paper 2. Exclusively passive isolation control scheme is again considered. General H_2 norm optimization is utilized where both displacement and velocity amplitudes are used as separate criterion. Results are mutually contrasted with special accent on fatigue life enhancement. Finite element method in software suite *Abaqus* combined with *Fe-Safe* for vibration induced fatigue assessment is employed with purpose of results verification.

Scientific contribution of the paper is given as follows. Previously derived Timoshenko-based displacement correction factor is verified against finite element method results. Although results match almost perfectly with finite element beam-based solution, they are completely divergent compared to finite element continuum-based solution and theory of elasticity-based Ancker and Goodier solution. Thus, although apparently correctly derived, Timoshenko-based displacement correction is disregarded according to results reported in this study. Furthermore, it is reported that displacement-based optimization criterion outperforms velocity-based optimization criterion when considering fatigue life exclusively as a metric. Inerter-based displacement optimization criterion yields with optimum performance compared to other schemes. Previously derived simple expression for fatigue life assessment is verified against finite element method. Although utilized correction factors from referent literature are approximate, very good agreement between analytical and numerical results is observed. Optimization process and entire dynamic procedure, including fatigue life assessment, is further verified against numerical solution through simplified model which is not incorporating correction factors. In this case, almost perfect match up of the results is achieved. Ideal inerter concept is successfully incorporated into finite element-based solution by using *Abaqus* native **Equation* functionality. Novel anti-resonance effects of the receiving body are observed in numerical solution due to inerter implementation.

Study conception and design: D. Čakmak, Z. Tomičević, H. Wolf and Ž. Božić

Acquisition of data: D. Čakmak

Analysis and/or interpretation of data: D. Čakmak, Z. Tomičević, H. Wolf and Ž. Božić

Drafting of the manuscript: D. Čakmak and Z. Tomičević

Critical revision: D. Čakmak, Z. Tomičević, H. Wolf and Ž. Božić

Approval of the version of the manuscript to be published: D. Čakmak, Z. Tomičević, H. Wolf and Ž. Božić

Paper 4

Čakmak, D., Tomičević, Z., Wolf, H., Božić, Ž., Semenski, D., Trapić, I., *Vibration fatigue study of the helical spring in the base-excited inerter-based isolation system*, Engineering Failure Analysis 103 (2019) 44–56., DOI: https://doi.org/10.1016/j.engfailanal.2019.04.064

In this paper, the fatigue of coupling helical spring of receiving body in an inerter-based one degree of freedom vibration isolation system is studied as a continuation of previously published work. Contrasting previous studies which incorporate force excitation, broadband base kinematic excitation is assumed herein. Relative displacements, which are directly proportional to stresses in the isolator spring, are considered. Influence of inerter on relative displacements is studied in the broad frequency range. Parametric analysis is performed. Due to nature of dynamic system, it cannot be optimized. However, it can be tuned according to desired criterion. Modal and direct dynamic methods are considered. Approximate, but accurate big/large mass method is utilized for numerical modal analysis.

Scientific contribution of the paper is given as follows. Beneficial influence of inerter on relative displacements and directly related isolator spring stresses is observed in broad frequency range. Reduction of vibration amplitudes is especially evident in resonant conditions due to beneficial inerter influence. This is especially important when considering lightly damped systems which may act as a band-pass filter under random excitation. Hence, fundamental natural frequency expectedly always tends to get excited. Furthermore, novel helical spring displacement and stress correction factors are derived in closed form by using combined theory of elasticity, strength of materials and numerical solutions. It is shown that proposed correction factors are more accurate than the most accurate correction factor from referent literature, i.e. Ancker and Goodier, and Wahl. Accuracy improvement is most evident when large spring pitch angles are considered. Moreover, novel correction factors incorporate the influence of spring pitch, spring index and material Poisson's ratio simultaneously. Thus

they can be used for analytically assessing the spring stress and displacement in materials other than regular steel. Entire proposed closed form dynamic procedure is verified via finite elements-based fatigue calculations in *Abaqus* and *Fe-Safe*. Given procedure can be utilized for simple analytical vibration fatigue assessment of springs in suspensions or any general isolator system incorporating inerters.

Study conception and design: D. Čakmak, Z. Tomičević, H. Wolf, Ž. Božić, D. Semenski and I. Trapić

Acquisition of data: D. Čakmak

Analysis and/or interpretation of data: D. Čakmak, Z. Tomičević, H. Wolf, Ž. Božić, D. Semenski and I. Trapić

Drafting of the manuscript: D. Čakmak and Z. Tomičević

Critical revision: D. Čakmak, Z. Tomičević, H. Wolf, Ž. Božić, D. Semenski and I. Trapić

Approval of the version of the manuscript to be published: D. Čakmak, Z. Tomičević, H. Wolf, Ž. Božić, D. Semenski and I. Trapić

Paper 1, https://doi.org/10.1016/j.jsv.2017.12.031

Passive and active vibration isolation systems using inerter

N. Alujević, D. Čakmak*, H. Wolf, M. Jokić

Faculty of Mechanical Engineering and Naval Architecture, University of Zagreb, Ivana Lučića 5, 10 000 Zagreb, Croatia

ARTICLE INFO

ABSTRACT

This paper presents a theoretical study on passive and active vibration isolation schemes using inerter elements in a two degree of freedom (DOF) mechanical system. The aim of the work is to discuss basic capabilities and limitations of the vibration control systems at hand using simple and physically transparent models. Broad frequency band dynamic excitation of the source DOF is assumed. The purpose of the isolator system is to prevent vibration transmission to the receiving DOF. The frequency averaged kinetic energy of the receiving mass is used as the metric for vibration isolation quality. It is shown that the use of inerter element in the passive vibration isolation scheme can enhance the isolation effect. In the active case, a feedback disturbance rejection scheme is considered. Here, the error signal is the receiving body absolute velocity which is directly fed to a reactive force actuator between the source and the receiving bodies. In such a scheme, the so-called subcritical vibration isolation problems exist. These problems are characterised by the uncoupled natural frequency of the receiving body larger than the uncoupled natural frequency of the source body. In subcritical vibration isolation problems, the performance of the active control is limited by poor stability margins. This is because the stable feedback gain is restricted in a narrow range between a minimum and a maximum. However, with the inclusion of an inerter in the isolator, one of the two stability margins can be opened. This enables large, theoretically unlimited negative feedback gains and large active damping of the receiving body vibration. A simple expression for the required inertance is derived.

© 2017 Elsevier Ltd. All rights reserved.

1. Introduction

Inerter is a one port element in mechanical networks which resists relative acceleration across its two terminals [1,2]. The coefficient of this resistance is called inertance and is measured in kilograms. An appealing property of inerters is that they can be designed and realised in practice having their inertance significantly larger than their mass [1,2]. This opens many interesting possibilities so that many authors reported on how to design and use inerters to suppress mechanical vibrations [1–23].

The concept of "relative mass" has been considered in the past in connection with mechanical–electrical analogies by Schönfeld [24]. He mentioned the possibility of a two-terminal mechanical inertance and gave a rudimentary scheme of a physical realisation of the concept. Smith [1], and Smith and Wang [2] developed this idea by investigating how to design such a device in practice and pointed out a number of peculiarities that the new element brings into a mechanical network. The

* Corresponding author.
   E-mail address: damjan.cakmak@fsb.hr (D. Čakmak).

authors described the characteristic phase lead property which cannot be achieved with conventional passive struts consisting of springs and dampers only, and instilled that inerter is the analogue of the capacitor element in electrical networks [2]. Therefore, adding the inerter to classical dampers and springs fills an empty niche enabling a complete synthesis of passive mechanical networks [2–4,24].

Smith and Wang designed their inerter using a plunger sliding in a cylinder which drives a flywheel through a rack, pinion and gears [2]. In this design the inertance can be set by the choosing the gear ratio. Such a realisation should be viewed as approximating its mathematical ideal in a similar way that real springs, dampers, capacitors, etc. approximate their mathematical ideals [2]. In other words, effects such as friction, stick-slip of the gear pairs, or the elasticity of the gears and connecting rods are inevitably present in gear-train based inerter constructions. Other physical realisations of inerters have been proposed as well. For example, an electromagnetic transducer (voice coil, linear motor) can be shunted with an electrical impedance consisting of a capacitance connected in series to a parallel resistance-inductance pair. If the total shunt impedance is properly tuned, then the whole electromechanical network theoretically behaves exactly as if it incorporated an ideal inerter mounted in series with a parallel spring damper-pair [6]. A problem in this realisation is that voice coils are characterised by an inherent electric resistance of the wire in the coil. This resistance causes the dimensionless electromechanical coupling coefficient of the transducer to downscale rather unfavourably [25–27]. As a result, unrealistically large scale electromagnetic transducers would be needed to synthesize a usable inerter by means of entirely passive electrical shunt circuits. This can be overcome by actively compensating for the coil resistance [6]. A number of "negative impedance" electrical circuit designs comprising operational amplifiers, which could be used for this purpose can be found in Ref. [28]. However, such an approach is active which on one hand requires energy and on the other a careful regard of the stability and robustness of the system. For these reasons, self-powered configurations employing a simultaneous active control and energy harvesting have been considered to synthesize mechatronic inerters [6]. Another type of mechatronic inerter utilises a rotary DC motor shunted with an appropriate electrical circuit [7]. This is in order to supplement the mechanical inertance associated with the rotor moment of inertia with additional electrically synthesised inertance [7]. An inertance-like behaviour can also be accomplished through a scheme in which hydraulic fluid is accelerated [8,9]. This can be achieved with a piston which pushes the fluid through a helical channel [9]. This design involves relatively large parasitic damping so that the device is best modelled by considering a nonlinear damper in parallel to the idealised inerter [9].

Inerters can be very useful in vibration isolation systems. In this sense, many authors focused their efforts on improving vehicle suspension systems using inerters [2,10–13]. Further applications of inerters include vibration isolation in civil engineering structures, such as multi-storey buildings under earthquake base excitation [14]. In vibration isolation problems it is often necessary to tune the impedance of the isolator elements based on some optimisation criteria. This can be done by either minimising maxima of the response (minimax or H_∞ optimisation), or by minimising the energy in the response signals (H_2 optimisation) [15].

Inerters can also be very useful in vibration absorber systems. Performance of vibration absorbers, especially Tuned Mass Dampers (TMDs) is known to very much depend on the proof mass added to a primary structure to reduce its vibration. This mass is added to structures exclusively to control their vibrations, so it is penalised in lightweight automotive and aerospace applications [16,17]. In this context the use of inerter elements can be interesting given the fact that their inertance can be significantly larger than their mass. Consequently a number of new concepts have arisen. These include tuned inerter damper (TID), tuned mass–damper–inerter (TMDI), and inerter–based dynamic vibration absorber (IDVA) [18–22]. In these systems the working frequency of the absorber can be tuned by changing the inertance. In particular, it can be reduced without increasing the physical mass of the vibration absorber while preserving the static stiffness of the absorber suspension spring. Various applications have been considered using tuned inerter dampers including vibration reduction of cables in cable-stayed bridges [18,19].

Dynamic vibration absorbers can be made active. Active vibration absorbers can be realised using inertial actuators with a velocity or velocity + displacement feedback control scheme [29–36]. Normally, inertial actuators must be designed with a low mounted natural frequency [29–36]. This requires either large inertial mass or soft suspension stiffness. Both is hard to realise in practice since the mass must not be too large as this would add too much weight to the structure, and the stiffness cannot be too small due to large sags in case of constant accelerations (gravity, vehicle manoeuvring). The low natural frequency also limits the applicability of inertial actuators in cases of structures rotating at a high speed which exposes co-rotating actuators to large centrifugal forces [37–39].

Considering now the use of inerters in active vibration absorber systems, Zilletti investigated a system in which the inerter is attached in parallel with the suspension spring, damper, and the actuator [23]. The author has shown that in this way it is possible to reduce the blocked natural frequency of the actuator without adding to the actual proof mass, apart from the relatively small mass added by the inerter construction. This approach has been shown not only to increase the range of frequencies where the active control can be achieved, but also to improve the stability and the robustness of the active control scheme which uses the inertial actuator to develop the control force [23]. Zilletti considered only an idealised inerter element, which neglects the inertial, stiffness and damping effects of the gearing mechanism that converts axial relative motion at the terminals of the inerter into angular motion of the inerter wheels. However, Kras and Gardonio considered the effective weight and dynamics effects of an inerter element composed by a single flywheel which is either pinned or hinged to the base mass or to the proof mass of the actuator [40].

In this paper an active vibration isolation problem is considered. It is shown that the use of inerter can significantly improve the stability and performance of the active vibration isolation system in certain situations. In particular, it is shown

analytically on a simplified model problem that the use of inerter enables successful active vibration isolation in a family of mechanical systems that are otherwise difficult to control. This family of system has been referred to as subcritical 2 DOF systems. Subcritical systems are those characterised by the natural frequency of the receiving body larger than the natural frequency of the source body. In such vibration isolation problems the use of inerter is shown to stabilise the feedback loop and therefore to enable a remarkable active vibration isolation effect. In addition to the active vibration isolation system, several inerter-based and inerter-free passive isolator schemes are proposed and analysed, with the aim of establishing fair benchmarks for the evaluation of the performance of the active isolators studied later in the paper.

The paper is structured into six sections. In the second section, the physical and mathematical models are presented and the model problem is postulated. In section 3 a benchmark passive vibration isolation scheme not employing the inerter is discussed. In section 4 a benchmark passive vibration isolation scheme employing the inerter is analysed. Finally, in section 5 a comprehensive stability and performance analysis of the active vibration isolation scheme is given. This analysis indicates the subcritical family of vibration isolation systems that requires the use of inerters in the isolator to have stable and performant active vibration isolator. In order to ensure a fair comparison among all active and passive configurations, the performance of the vibration isolation is measured through a unified criterion which is the mean kinetic energy of the receiving body. In each system, either active of passive, tuneable parameters are adjusted in order to minimise the kinetic energy of the receiving body per unit, spectrally white, dynamic excitation of the source body.

2. Mathematical model

In this section the mathematical model of an inerter-based active vibration isolation system is formulated. As shown in Fig. 1. the problem studied is represented by a lumped parameter two degree of freedom (DOF) mechanical system. The system consists of two masses m_1 and m_2 coupled by a spring k_2, a viscous damper c_2 and an inerter of inertance b_2. The inerter produces a force proportional to the relative acceleration between masses m_1 and m_2. The two masses are attached to fixed reference bases via the two mounting springs k_1 and k_3. The lower mass m_1 is excited by the disturbance force F_1. It is assumed that the force F_1 has characteristics of an ideal white noise and that the power spectral density (PSD) of the force equals one over all frequencies.

In this study the purpose of the vibration isolation system is to reduce vibrations of mass m_2 which are due to the forcing F_1 acting on the mass m_1. Therefore, a structure approximated by the mass m_1 and spring k_1 is referred to as the source body, and a structure characterised by the mass m_2 and stiffness k_3 is referred to as the receiving body (Fig. 1.).

Such lumped parameter approximation may be representative of a system of more complicated nature, incorporating structures with distributed mass and stiffness parameters. For example, the modal mass and stiffness of the fundamental mode of a flexible rectangular source panel can be represented through the mass m_1 and stiffness k_1. Similarly, the mass m_2 and stiffness k_3 can represent the modal mass and stiffness corresponding to the fundamental mode of a flexible radiating panel. Finally, the stiffness k_2 between the two masses could represent a coupling impedance associated with the breathing mode of an air cavity between the two panels. In such a way the simplified 2 DOF model could be used to describe the low-frequency dynamic behaviour of acoustically coupled double panels as discussed in, for example [41]. Other systems may also be representable by the general configuration shown in Fig. 1 [29,42–44]. In case a more detailed and accurate analysis is required, attention should be paid to the influence of higher order residual modes, see for example [45].
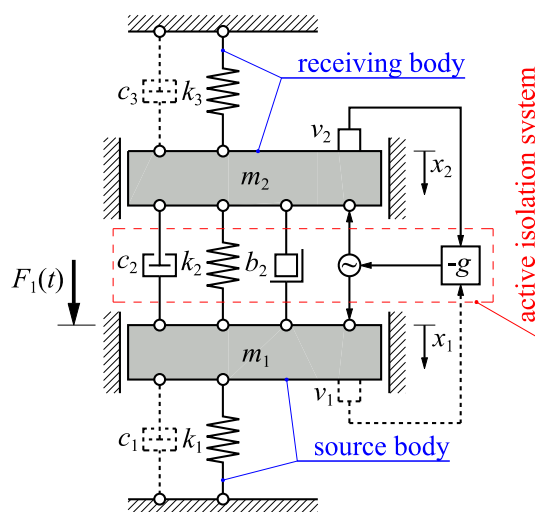

Fig. 1. The two degree of freedom active vibration isolation system.

The active part of the vibration isolation system is realised through a skyhook damping unit [44], [46]. The skyhook damper consists of a reactive actuator, a velocity sensor, and a feedback loop between the output of the sensor and the input to the actuator. The actuator is mounted in parallel with the passive part of the isolation system (spring, dashpot and inerter) with its terminals also attached to the two masses (Fig. 1.). The velocity sensor is mounted onto mass m_2 in order to realise a disturbance rejection control scheme. In this scheme the actuator is driven with a signal proportional to the negative absolute velocity of the receiving body amplified by a constant control gain g. Idealised sensor-actuator transducers are assumed. Thus the feedback gain g has physical dimension of Ns/m and could be referred to as the active damping coefficient. Practical velocity sensors are normally realised using standard accelerometers with time-integrated outputs. The cut-off frequency of the integration circuit is usually chosen low, so that in the frequency range between the cut-off frequency of the integrator and the blocked natural frequency of the accelerometer, the time-integrated output of the accelerometer is proportional to velocity [25,29,31,32]. An advanced MEMS velocity sensor with internal velocity feedback has been proposed in Ref. [47].

The actuator force F_A is given by

$$F_A = -g\dot{x}_2. \tag{1}$$

The equations of motion are

$$
\begin{aligned}
(m_1 + b_2)\ddot{x}_1 - b_2\ddot{x}_2 + (c_1 + c_2)\dot{x}_1 - (c_2 + g)\dot{x}_2 + (k_1 + k_2)x_1 - k_2 x_2 &= F_1 \\
-b_2\ddot{x}_1 + (m_2 + b_2)\ddot{x}_2 - c_2\dot{x}_1 + (c_2 + c_3 + g)\dot{x}_2 - k_2 x_1 + (k_2 + k_3)x_2 &= 0.
\end{aligned} \tag{2a,b}
$$

The equations of motion Eq. (2a,b) can be written in the matrix form as

$$\mathbf{M}\ddot{\mathbf{x}} + \mathbf{C}\dot{\mathbf{x}} + \mathbf{K}\mathbf{x} = \mathbf{F}, \tag{3}$$

where $\mathbf{M}$ is the mass matrix, $\mathbf{K}$ is the stiffness matrix, $\mathbf{C}$ is the damping matrix, $\mathbf{x}(t)$, $\dot{\mathbf{x}}(t)$ and $\ddot{\mathbf{x}}(t)$ are the displacement, velocity and acceleration column vectors respectively, and $\mathbf{F}(t)$ is excitation column vector. These matrices/vectors are given by the following expressions

$$\mathbf{M} = \begin{bmatrix} m_1 + b_2 & -b_2 \\ -b_2 & m_2 + b_2 \end{bmatrix}, \quad \mathbf{C} = \begin{bmatrix} c_1 + c_2 & -c_2 - g \\ -c_2 & c_2 + c_3 + g \end{bmatrix}, \quad \mathbf{K} = \begin{bmatrix} k_1 + k_2 & -k_2 \\ -k_2 & k_2 + k_3 \end{bmatrix}, \tag{4a -c}$$

$$\mathbf{x} = \begin{bmatrix} x_1(t) \\ x_2(t) \end{bmatrix}, \quad \mathbf{F} = \begin{bmatrix} F_1(t) \\ 0 \end{bmatrix}, \tag{5a -b}$$

where the parameters/functions in the matrices/vectors are as indicated in Fig. 1. Note that the gain g generates diagonally asymmetric active damping terms in the system damping matrix $\mathbf{C}$. Throughout this study, the damping of the source and receiving structures is assumed to be light. Thus the effects of dampers between the source mass m_1 and the ground and between the receiving mass m_2 and the ground are neglected *i.e.* $c_1 \approx c_3 \approx 0$. This enables significantly less complex mathematical derivations in the forthcoming parts of the study. Furthermore it leads to a more transparent model regarding the physics governing the system dynamical behaviour. Nevertheless, the main results are cross-checked with results using a full damping model where the influence of dampers c_1 and c_3 is not neglected. These results with the full damping model can be found in Appendix of the paper.

Assuming a simple harmonic excitation and expressing the excitation and the steady-state response in the exponential form $\mathbf{F}(t) = \widehat{\mathbf{F}}e^{j\omega t}$ and $\mathbf{x} = \widehat{\mathbf{x}}e^{j\omega t}$, where $j = \sqrt{-1}$, Eq. (3) can be written as

$$\mathbf{S}(j\omega)\mathbf{x}(j\omega) = \mathbf{F}(j\omega), \tag{6}$$

where $\mathbf{S}(j\omega)$ is the dynamic stiffness matrix with the following form

$$\mathbf{S}(j\omega) = -\omega^2\mathbf{M} + j\omega\mathbf{C} + \mathbf{K}. \tag{7}$$

Solution of Eq. (6) can be obtained by inversion of the dynamic stiffness matrix $\mathbf{S}(j\omega)$ as

$$\mathbf{x}(j\omega) = \mathbf{S}^{-1}(j\omega)\mathbf{F}(j\omega). \tag{8}$$

Differentiating Eq. (8) in order to obtain velocities results in expression

$$\dot{\mathbf{x}}(j\omega) = \mathbf{Y}(j\omega)\mathbf{F}(j\omega), \tag{9}$$

where $\dot{\mathbf{x}}(j\omega) = j\omega\mathbf{x}(j\omega)$ is the velocity vector and $\mathbf{Y}(j\omega) = j\omega\mathbf{S}^{-1}(j\omega)$ is the mobility matrix representing four frequency response functions (FRFs) between velocities and forces. By taking $\mathbf{M}$, $\mathbf{K}$ and $\mathbf{C}$ matrices from Eq. (4a−c), the steady-state complex response can be expressed in terms of the two driving points and two transfer mobilities as

$$Y_{11}(j\omega) = \frac{(j\omega)^3(m_2 + b_2) + (j\omega)^2(c_2 + g) + (j\omega)(k_2 + k_3)}{(j\omega)^4[(b_2 + m_2)m_1 + b_2 m_2] + (j\omega)^3[(c_2 + g)m_1 + c_2 m_2] + (j\omega)^2[(m_2 + b_2)k_1 + (m_1 + m_2)k_2 + (m_1 + b_2)k_3] + (j\omega)[(c_2 + g)k_1 + c_2 k_3] + (k_2 + k_3)k_1 + k_2 k_3},$$ (10a)

$$Y_{12}(j\omega) = \frac{(j\omega)^3 b_2 + (j\omega)^2(c_2 + g) + (j\omega)k_2}{(j\omega)^4[(b_2 + m_2)m_1 + b_2 m_2] + (j\omega)^3[(c_2 + g)m_1 + c_2 m_2] + (j\omega)^2[(m_2 + b_2)k_1 + (m_1 + m_2)k_2 + (m_1 + b_2)k_3] + (j\omega)[(c_2 + g)k_1 + c_2 k_3] + (k_2 + k_3)k_1 + k_2 k_3}.$$ (10b)

$$Y_{21}(j\omega) = \frac{(j\omega)^3 b_2 + (j\omega)^2 c_2 + (j\omega)k_2}{(j\omega)^4[(b_2 + m_2)m_1 + b_2 m_2] + (j\omega)^3[(c_2 + g)m_1 + c_2 m_2] + (j\omega)^2[(m_2 + b_2)k_1 + (m_1 + m_2)k_2 + (m_1 + b_2)k_3] + (j\omega)[(c_2 + g)k_1 + c_2 k_3] + (k_2 + k_3)k_1 + k_2 k_3},$$ (10c)

$$Y_{22}(j\omega) = \frac{(j\omega)^3(m_1 + b_2) + (j\omega)^2 c_2 + (j\omega)(k_1 + k_2)}{(j\omega)^4[(b_2 + m_2)m_1 + b_2 m_2] + (j\omega)^3[(c_2 + g)m_1 + c_2 m_2] + (j\omega)^2[(m_2 + b_2)k_1 + (m_1 + m_2)k_2 + (m_1 + b_2)k_3] + (j\omega)[(c_2 + g)k_1 + c_2 k_3] + (k_2 + k_3)k_1 + k_2 k_3},$$ (10d)

where $Y_{ij} = \dot{x}_i/F_j$ is a mobility function of the system, representing a velocity of the mass i due to a unit force at the mass j. If $i = j$ then the corresponding FRF is referred to as a driving point mobility, otherwise it is a referred to as a transfer mobility.

The transfer mobility Y_{21}, representing the velocity response of the receiving body per unit forcing of the source body, is used to assess the quality of the vibration isolation throughout this paper. With the aim of more general approach, mobility Y_{21} in Eq. (10c) can be expressed in the following dimensionless form

$$\Upsilon_{21}(j\varOmega) = \frac{B_0 + (j\varOmega)B_1 + (j\varOmega)^2 B_2 + (j\varOmega)^3 B_3}{A_0 + (j\varOmega)A_1 + (j\varOmega)^2 A_2 + (j\varOmega)^3 A_3 + (j\varOmega)^4 A_4},$$ (11)

where coefficients $A_0 \ldots A_4$ and $B_0 \cdots B_3$ are given by

$$
\begin{aligned}
A_0 &= \mu_1(\alpha\beta\mu_1 + \alpha + \beta) & B_0 &= 0 \\
A_1 &= 2\eta_2(\beta\mu_1 + \lambda + 1) & B_1 &= \alpha\mu_1 \\
A_2 &= \mu_1(\alpha\mu_1 + \beta\mu_1\mu_2 + \alpha + \beta + \mu_2 + 1) & B_2 &= 2\eta_2 \\
A_3 &= 2\eta_2(\mu_1 + \lambda + 1) & B_3 &= \mu_1\mu_2 \\
A_4 &= \mu_1(\mu_1\mu_2 + \mu_2 + 1)
\end{aligned}
$$ (12a −i)

where

$$\alpha = \left(\frac{\varOmega_2}{\varOmega_1}\right)^2, \quad \beta = \left(\frac{\varOmega_3}{\varOmega_1}\right)^2, \quad \eta_2 = \frac{c_2}{2\sqrt{m_1 k_1}}, \quad \lambda = \frac{g}{c_2}, \quad \mu_1 = \frac{m_2}{m_1}, \quad \mu_2 = \frac{b_2}{m_2}, \quad \varOmega = \frac{\omega}{\varOmega_1},$$ (13a −g)

and $\Upsilon_{21} = m_1\varOmega_1 Y_{21}$ is now the dimensionless transfer mobility. Throughout the rest of the paper, it is assumed that m_1 and $\varOmega_1$ are constant values, used for scaling the transfer mobility function Y_{21} to convenient dimensionless form.

In Eq. (13a−g), α and β are squared natural frequency ratios, η_2 is the damping ratio, λ is the feedback gain normalised with respect to the passive damping coefficient, and μ_1 and μ_2 are the mass and inertance ratios respectively. Furthermore, $\varOmega$ is dimensionless circular frequency normalised with respect to the natural frequency of the uncoupled source body $\varOmega_1$ (as if the source body was uncoupled by removing spring k_2), $\varOmega_3$ is the natural frequency of the uncoupled receiving body (as if the receiving body was uncoupled by removing spring k_2), and $\varOmega_2$ is the natural frequency of the receiving body as if it was attached to a fixed reference base through the spring of stiffness k_2 only. The three natural frequencies $\varOmega_1 \ldots \varOmega_3$ are thus

$$\varOmega_1 = \sqrt{\frac{k_1}{m_1}}, \quad \varOmega_2 = \sqrt{\frac{k_2}{m_2}}, \quad \varOmega_3 = \sqrt{\frac{k_3}{m_2}}.$$ (14a −c)

Given that the excitation force F_1 with unit PSD has been assumed, the specific kinetic energy of the receiving body (per unit mass, per unit excitation force) can be calculated as

$$I_k = \int\limits_{-\infty}^{\infty} |\Upsilon_{21}(\mathrm{j}\Omega)|^2 \mathrm{d}\Omega, \tag{15}$$

according to the Parseval's identity. The specific kinetic energy index I_k is used throughout this study as a measure of the performance of broad frequency band vibration isolation. The objective is to minimise this quantity of all vibration isolation systems analysed in the paper.

The specific kinetic energy index in Eq. (15) can according to [48] be calculated as

$$I_k = \pi \frac{A_0 B_3^2 (A_0 A_3 - A_1 A_2) + A_0 A_1 A_4 \left(2 B_1 B_3 - B_2^2\right) - A_0 A_3 A_4 \left(B_1^2 - 2 B_0 B_2\right) + A_4 B_0^2 (A_1 A_4 - A_2 A_3)}{A_0 A_4 \left(A_0 A_3^2 + A_1^2 A_4 - A_1 A_2 A_3\right)}. \tag{16}$$

Substituting coefficients $A_0 \dots A_4$ and $B_0 \cdots B_3$ from Eq. (12) into Eq. (16) yields

$$I_k = 2\pi \frac{\begin{pmatrix} 1/4\mu_2(\mu_2\beta - \alpha)^2\mu_1^4 + 1/4(\mu_2\beta - \alpha)\left[(\lambda + 2)\mu_2^2 + (\beta - \alpha\lambda - 2\alpha)\mu_2 - \alpha\right]\mu_1^3 + \\ + \left\{ \begin{array}{l} 1/4(1 + \lambda)\mu_2^3 - 1/2(-1/2 + \alpha)(\lambda + 1)\mu_2^2 + \\ + \left[\left(1/4\alpha^2 - 1/2\alpha\right)\lambda + \beta\eta_2^2 + 1/4\alpha^2 - 1/2\alpha\right]\mu_2 + 1/4\alpha^2(\lambda + 1) \end{array} \right\}\mu_1^2 + \\ + [(1 + \beta + \lambda)\mu_2 + \beta]\eta_2^2\mu_1 + \eta_2^2(1 + \mu_2)(\lambda + 1) \end{pmatrix}}{\eta_2(1 + \mu_2 + \mu_2\mu_1)(\beta - 1)[\lambda(\mu_2\beta - \alpha)\mu_1 + (\lambda + 1)(\lambda\mu_2 - \alpha\lambda + \beta - 1)]\mu_1^2} \tag{17}$$

In the remaining parts of the paper, four types of vibration transmission control are studied and compared with respect to their performance in minimising the kinetic energy index I_k. These are: passive control without inerter, passive control with inerter, active control without inerter and active control with inerter.

3. Passive control without inerter

In this section the effectiveness of a passive vibration isolation system without inerter is analysed as a fundamental benchmark. In this case, the dimensionless feedback gain λ (corresponding to the dimensional feedback gain g) and the dimensionless inerter ratio μ_2 (corresponding to the inertance b_2) equal zero. The transfer mobility (Eq. (11)), and the kinetic energy index (Eq. (17)) now reduce to

$$\Upsilon_{21}(\mathrm{j}\Omega) = \frac{2(\mathrm{j}\Omega)^2\eta_2 + (\mathrm{j}\Omega)\alpha\mu_1}{(\mathrm{j}\Omega)^4\mu_1 + 2\eta_2(\mu_1 + 1)(\mathrm{j}\Omega)^3 + \mu_1[\alpha(\mu_1 + 1) + \beta + 1](\mathrm{j}\Omega)^2 + 2\eta_2(1 + \beta\mu_1)(\mathrm{j}\Omega) + \mu_1[\alpha(\beta\mu_1 + 1) + \beta]}, \tag{18}$$

$$I_k = \pi \frac{\alpha^2\mu_1^2(\mu_1 + 1) + 4\eta_2^2(\beta\mu_1 + 1)}{2\mu_1^2\eta_2^2(\beta - 1)^2}. \tag{19}$$

The effectiveness of such simple passive isolator is first studied by varying the damping ratio η_2 of an example system. Parameters that characterise the example system are $\alpha = 2$, $\beta = 5$ and $\mu_1 = 1/2$. The modulus of the transfer mobility $|\Upsilon_{21}|$ is shown in Fig. 2(a) for three values of the passive damping ratio η_2: a relatively small one (solid line), medium (dashed line) and large damping ratio (dash-dotted line).

In case with a small damping ratio, velocity amplitudes are very large when the system is excited near either of the two natural frequencies (at dimensionless frequencies of about 1.25 and 2.75). As the damping increases, the amplitudes at these frequencies decrease. If a very large damping ratio is used, it generates a new resonance condition, at a dimensionless frequency of about 1.55. This is because for such a large damping coefficient, the dashpot between the two masses effectively locks, and two masses m_1 and m_2 vibrate together in phase, appearing to be tied rigidly. In fact, when the damping ratio η_2 tends to infinity, vibration amplitude at this new resonance frequency also tends to infinity since no additional damping exists in the system, (*i.e.* undamped source and receiving structures are assumed, $c_1 = c_3 = 0$). A situation with light, non-zero damping c_1 and c_3 is illustrated and discussed in the Appendix. The new, artificial natural frequency approaches

$$\Omega_{na} = \frac{\omega_{na}}{\Omega_1} = \sqrt{\frac{1 + \beta\mu_1}{1 + \mu_1}}, \tag{20}$$

indicating that the system now behaves like a 1 DOF system having a natural frequency $\omega_n = \sqrt{k/m}$ where $k = k_1 + k_3$ and $m = m_1 + m_2$. It can be seen in Fig. 2(a) that there are four frequencies at which the mobility amplitude $|\Upsilon_{21}(\mathrm{j}\Omega)|$ is
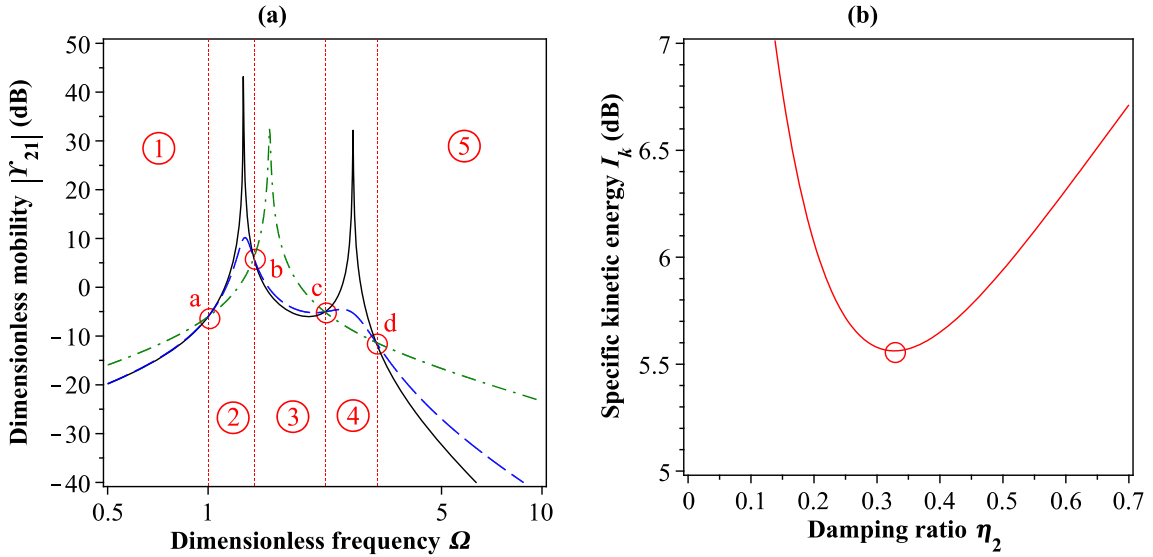
Fig. 2. Isolation system performance without inerter b_2 ($\mu_2 = 0$): (a) Transfer mobility function $|Y_{21}(j\Omega)|$, $\eta_2 = \eta_{2opt1}/100$ (solid line), $\eta_2 = \eta_{2opt1}$ (dashed line), $\eta_2 = 100\eta_{2opt1}$ (dash-dotted line), (b) Specific kinetic energy index I_k.

independent of the damping ratio η_2. By requiring that derivative with respect to η_2 of the modulus of the mobility $Y_{21}(j\Omega)$ in Eq. (16) vanishes, the following four frequencies are obtained

$$\Omega_a = 1, \quad \Omega_c = \sqrt{\beta}$$

$$\Omega_{b,d}^2 = \frac{1}{2} \mp \left[(2 + 2\mu_1)\alpha + 1 + \beta + \sqrt{4(\mu_1 + 1)^2\alpha^2 - 4(\mu_1 - 1)(\beta - 1)\alpha + (\beta - 1)^2} \right]. \tag{21a-d}$$

where $|Y_{21}(j\Omega)|$ is invariant with respect to the isolator damping. The four circles in Fig. 2(a) denote these frequencies and the corresponding moduli of the dimensionless transfer mobility. According to Eq. (21a–d) and Fig. 2(a), the entire frequency band can be divided into five ranges with respect to how vibration transmission measured through $|Y_{21}(j\Omega)|$ depends on the damping ratio. As shown in Table 1. in Ranges 2 and 4 (near resonances), an increase in the damping ratio causes a decrease in the vibration transmission, but in Ranges 1, 3 and 5, the effect of increased damping is opposite. Indices a, b, c and d from Table 1 are chosen in such way that relation $\Omega_a < \Omega_b < \Omega_c < \Omega_d$ holds for $\beta > 1$, whereas for $\beta < 1$, Ω_a and Ω_c now switch places.

Therefore the impact of the passive damping ratio η_2 at various frequency ranges is inconsistent. It is thus interesting to see how the receiving body specific kinetic energy index I_k, being a frequency averaged quantity, varies with the damping ratio. This variation is plotted in Fig. 2(b). It can be seen that it has a minimum as denoted by the circle. It can be shown that this minimum is achieved for

$$\eta_{2opt1} = \frac{\alpha\mu_1}{2} \sqrt{\frac{1 + \mu_1}{1 + \beta\mu_1}}, \tag{22}$$

where η_{2opt1} is the optimal passive damping ratio. The corresponding minimum specific kinetic energy is

$$I_{kmin} = 2\pi \frac{\alpha\sqrt{(\beta\mu_1 + 1)(\mu_1 + 1)}}{\mu_1(\beta - 1)^2}. \tag{23}$$

In fact, the frequency response curve indicated by the dashed line in Fig. 2(a) corresponds to the optimal damping ratio η_{2opt1} calculated according to Eq. (22). The remaining two lines are with a light damping $\eta_{2opt1}/100$ (solid) and a very large damping $100\eta_{2opt1}$ (dash-dotted). Thus the optimum damping ratio is a result of a trade-off between damping down the

Table 1
Dimensionless circular frequency Ω key ranges.

Range 1	Range 2	Range 3	Range 4	Range 5
$\Omega \in \langle 0, \Omega_a \rangle$	$\Omega \in \langle \Omega_a, \Omega_b \rangle$	$\Omega \in \langle \Omega_b, \Omega_c \rangle$	$\Omega \in \langle \Omega_c, \Omega_d \rangle$	$\Omega > \Omega_d$
$\eta \uparrow \Rightarrow |Y_{21}(j\Omega)| \uparrow$	$\eta \uparrow \Rightarrow |Y_{21}(j\Omega)| \downarrow$	$\eta \uparrow \Rightarrow |Y_{21}(j\Omega)| \uparrow$	$\eta \uparrow \Rightarrow |Y_{21}(j\Omega)| \downarrow$	$\eta \uparrow \Rightarrow |Y_{21}(j\Omega)| \uparrow$

vibration transmission around the two resonances (Ranges 2 and 4) without excessively increasing vibration transmission in the remaining three frequency ranges (Ranges 1, 3 and 5).

By examining Eq. (23) it can be seen that the optimum specific kinetic energy $I_{k\min}$ is proportional to the squared natural frequency ratio α, which is effectively a dimensionless measure of the isolator spring stiffness k_2. Therefore the softer the isolator spring stiffness, the better is the vibration isolation effect. However, decreasing spring stiffness k_2 normally results in large static deflections to which there is a limit in real engineering situations. In other words, opposing requirements dictate the choice of stiffness of the spring k_2. On the other hand, in Eq. (23) can be seen that if the squared natural frequency ratio β tends to unity, I_k tends to infinity. This is the situation in which the uncoupled natural frequency of the source body tends to the uncoupled natural frequency of the receiving body ($\Omega_1 = \Omega_3$). Therefore, for a good vibration isolation effect, the system should be detuned in such way that $\Omega_3 \gg \Omega_1$.

In conclusion, the study of the benchmark passive isolation scheme in this section indicates that it is possible to optimise vibration isolation effects by optimising the isolator damping. However, the vibration isolation capability of such a scheme becomes very limited if $\Omega_1 \approx \Omega_3$. In the following section it is discussed how these limitations can be relaxed by incorporating the inerter in the isolator construction.

4. Passive control with inerter

With the inclusion of an inerter, the frequency response functions (FRF) between the receiving body motions and the source body excitation becomes characterised by an anti-resonance. This is illustrated in Fig. 3(a) which shows the amplitude of the dimensionless transfer mobility $|Y_{21}(j\Omega)|$ of an example system characterised by $\alpha = 2$, $\beta = 5$, $\mu_1 = 1/2$.

Therefore, the system is the same as in the previous section, except that an inerter of dimensionless inertance $\mu_2 \approx 0.692$ is now attached to the system according to the scheme in Fig. 1. The value of $\mu_2 \approx 0.692$ is chosen because it is, as shown later in the paper, the optimum inertance. Active control is still switched off ($\lambda = 0$). It should be noted that normally FRFs between two different locations (*i.e.* between two different degrees of freedom) of a linear mechanical system are characterised by at least two consecutive resonances without an anti-resonance between them, as the case is in Fig. 2(a). Anti-resonance between all consecutive resonances can only be expected with driving point FRFs. The use of inerter changes this situation. In fact, a transfer FRF can become qualitatively similar to a typical driving point FRF, as shown in Fig. 3(a). By inspecting the numerator in Eq. (10c), it can be seen that incorporating the inerter into the isolator places the anti-resonance at the frequency $\omega_A = \sqrt{k_2/b_2}$, or in the dimensionless form (Eqs. (11–13))

$$\Omega_A = \sqrt{\frac{\alpha}{\mu_2}}, \tag{24}$$

where index "A" denotes "anti-resonance". Thus the location of this anti-resonance is not restricted to the frequency range between the two resonances. Instead the new zero can be freely placed in the entire frequency range assuming that the inerter with an appropriate inertance can be realised in practice. This is illustrated in Fig. 3(b). The properties of the system in Fig. 3(b) are still the same ($\alpha = 2$, $\beta = 5$, $\mu_1 = 1/2$), except that the inertance ratio μ_2 is varied in the range from $\alpha/(2\beta)$ to 2α. In
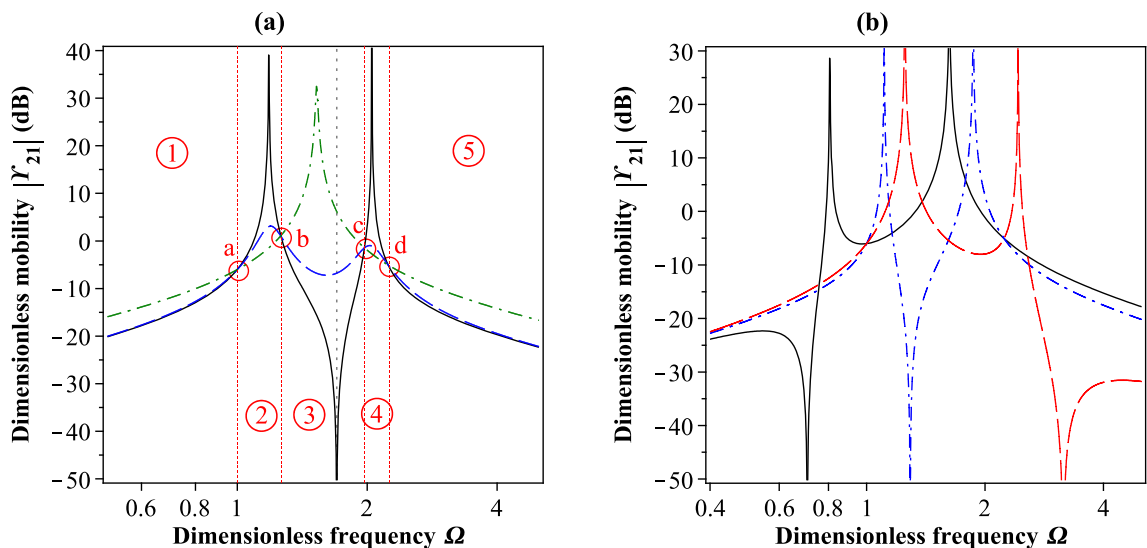

Fig. 3. Transfer mobility function $|Y_{21}(j\Omega)|$: (a) $\eta_2 = 0$ (solid line), $\eta_2 = \eta_{2\text{opt2}}$ (dashed line), $\eta_2 = 100\eta_{2\text{opt2}}$ (dash-dotted line), (b) $\eta_2 = 0$: $\mu_2 > \alpha$ (solid line), $\alpha/\beta < \mu_2 < \alpha$ (dash-dotted line), $\mu_2 < \alpha/\beta$ (dashed line).

fact, it can be shown that for $\beta > 1$, if the inertance ratio μ_2 is larger than the frequency ratio α, then the anti-resonance is positioned below the first resonance. If the inertance ratio is between α and α/β, then the anti-resonance is between the two resonances. Finally, if the inertance ratio μ_2 is smaller than α/β, then the anti-resonance is above the second resonance. This can be shown to be exactly valid for an entirely undamped system with $\eta_2 = 0$, and approximately valid for lightly damped systems (see Appendix to the paper). However, for $\beta < 1$ and if the inertance ratio μ_2 is smaller than the frequency ratio α, then it can be shown that anti-resonance is positioned above the second resonance and if the inertance ratio μ_2 is larger than α/β, then the anti-resonance is below the first resonance. This free choice of the anti-resonance opens possibilities to control "tonal" vibration transmission due to simple harmonic excitation. In this case, a lightly damped isolator would be necessary for a maximised performance which is perhaps similar to how vibration neutralisers (lightly damped, single frequency tuned vibration absorbers) are designed [49,50].

However, in this study the focus is put onto a broadband, white noise dynamic excitation of the source body. It is shown next that the kinetic energy index of the receiving body I_k has a minimum with respect to both damping ratio η_2 and inertance ratio μ_2. Differentiating Eq. (17) with respect to η_2 yields

$$\frac{\partial I_k}{\partial \eta} = 4\pi \left\{ \begin{array}{c} -1/4\mu_2(\mu_2\beta - \alpha)^2\mu_1^4 - 1/4(\mu_2\beta - \alpha)\left[2\mu_2^2 + (\beta - 2\alpha)\mu_2 - \alpha\right]\mu_1^3 + \\ +\left[-1/4\mu_2^3 + (1/2\alpha - 1/4)\mu_2^2 + \left(\eta_2^2\beta - 1/4\alpha^2 + 1/2\alpha\right)\mu_2 - 1/4\alpha^2\right]\mu_1^2 + \\ +[(1 + \beta)\mu_2 + \beta]\eta_2^2\mu_1 + \eta_2^2(1 + \mu_2) \end{array} \right\}. \tag{25}$$

By equalling Eq. (25) to zero and solving for η_2, one obtains

$$\eta_2 = \frac{\mu_1}{2} \frac{\sqrt{\begin{array}{c}(1 + \beta\mu_1)^2\mu_2^3 + \left[-2(\mu_1 + 1)(1 + \beta\mu_1)\alpha + 1 + \mu_1\beta^2\right]\mu_2^2 - \\ -2\alpha\left[-1/2(\mu_1 + 1)^2\alpha + \beta\mu_1 + 1\right]\mu_2 + \alpha^2(\mu_1 + 1)\end{array}}}{\sqrt{(1 + \mu_2 + \mu_1\mu_2)(1 + \beta\mu_1)}}, \tag{26}$$

where η_2 is now the optimal damping ratio for a given inertance ratio μ_2. By substituting Eq. (26) into Eq. (17), differentiating with respect to μ_2, equalling with zero and solving for μ_2, optimal inertance ratio parameter μ_{2opt} may be obtained which subsequently yields an expression for a minimum specific kinetic energy I_k. However, explicit expressions for μ_{2opt}, η_{2opt2} and I_{kopt2} are omitted in this paper because they are rather involved and cannot be clearly interpreted. Nevertheless, Fig. 4(a) shows that the frequency averaged kinetic energy index of the receiving body has a minimum at $\eta_2 = \eta_{2opt2}$ and $\mu_2 = \mu_{2opt}$. The example system considered is still characterised by $\alpha = 2$, $\beta = 5$ and $\mu_1 = 1/2$. The optimum values for this system are $\eta_{2opt2} \approx 0.162$ and $\mu_{2opt} \approx 0.692$. The minimum position for I_k is denoted by the circle whereas the optimum damping ratio η_2 as a function of the inertance ratio μ_2 (Eq. (26)) is illustrated using the dashed line. Considering now again Fig. 3(a), the effects of varying the damping ratio η_2 are similar to the case without inerter. With light damping, the receiving body response is large around the two resonances, and with a damping coefficient too large, a new lightly damped resonance occurs as with
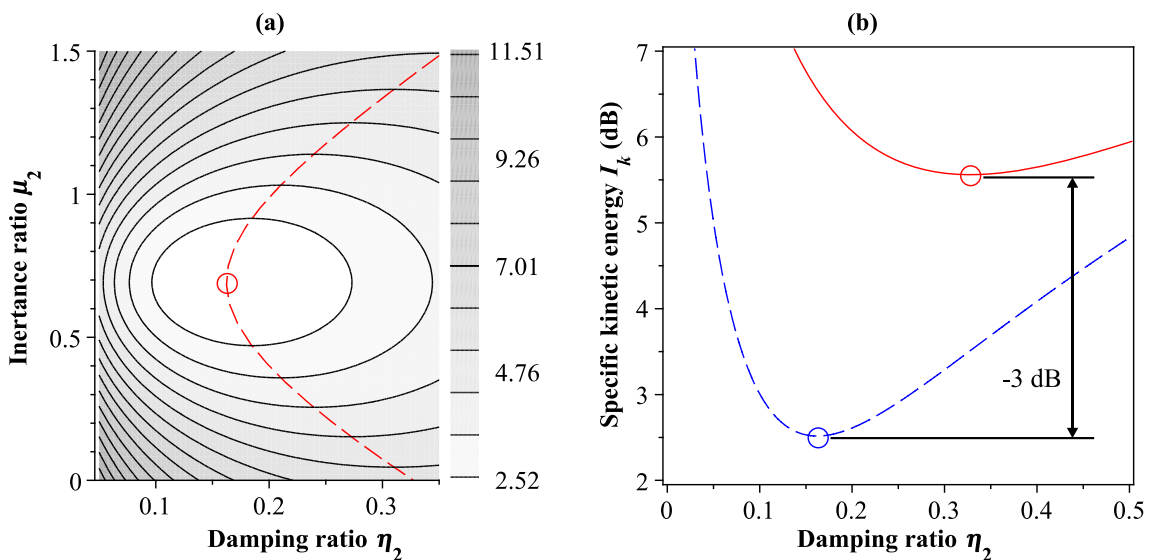

Fig. 4. Isolation system performance with inerter b_2 ($\mu_2 = \mu_{2opt}$): (a) specific kinetic energy index I_k as a function of η_2 and μ_2, (b) specific kinetic energy index I_k: comparison of the cases with and without inerter; $\mu_2 = 0$ (solid line), $\mu_2 = \mu_{2opt}$ (dashed line).

the case in previous section with no inerter. However, under the optimal setting, the vibration velocity amplitude is further reduced in comparison to the case without inerter ($\mu_2 = 0$). This is due to the anti-resonance phenomenon which is a special case of inerter influence and otherwise cannot be obtained by combining only elements of classical mass-damper-spring (MDS) system if the scheme shown in Fig. 1 is followed. Similar to the case without inerter, it can be seen in Fig. 3(b) that there are four frequencies where the dimensionless transfer mobility amplitudes $|Y_{12}(j\Omega)|$ are independent of damping ratio η_2. The four circles in Fig. 3(a) denote these frequencies and the corresponding dimensionless mobility amplitudes $|Y_{21}(j\Omega)|$. They can be calculated as

$$\Omega_a = 1, \quad \Omega_d = \sqrt{\beta}$$

$$\Omega_{b,c} = \frac{\sqrt{2(1 + 2\mu_2 + 2\mu_2\mu_1)\left(\mp\sqrt{\begin{array}{c} 1 + 2\mu_1\mu_2\beta + 2\alpha + \beta + 2\mu_2 + 2\alpha\mu_1 + \\ \overline{4(-\alpha + \mu_2\beta)^2\mu_1^2 + 4(-\alpha + \mu_2\beta)(\beta + 2\mu_2 - 2\alpha - 1)\mu_1 +} \\ +(2\alpha + \beta - 1 - 2\mu_2)^2 \end{array}}\right)}}{2 + 4(\mu_1 + 1)\mu_2}, \tag{27a–d}$$

It can be noted that expressions (27a,b) are identical to (21a,b) for the case without inerter. However, with inerter, the values of $\Omega_{a,b,c,d}$ can now all switch places depending on how the parameters of the system are chosen, except that $\Omega_{b,c}$ from Eq. (27c–d) are always such that inequality $\Omega_b < \Omega_c$ holds.

It is interesting to compare the maximum vibration isolation effect obtained using an optimally tuned damper c_2 without inerter (η_{2opt1}) to that with an optimally tuned damper and inerter pair (μ_{2opt}, η_{2opt2}). This comparison is shown in Fig. 4(b). The plot shows the receiving body specific kinetic energy index I_k as a function of the passive damping ratio η_2 for the two cases. It can be seen that the use of inerter improves the optimised vibration isolation performance by ~3 dB for the case considered. Clearly, this improvement depends on the parameters that characterise the system. Fig. 5 shows the improvement designated in Fig. 4(b) as a function of the system parameters α, β and μ_1.

The parametric study is presented so that the ratio between the optimum kinetic energy index with inerter and the optimum kinetic energy without inerter is shown as a function of the frequency parameter β. In Fig. 5(a) this variation is shown for three different frequency ratios α, and in Fig. 5(b) the variation is shown for three different parameters μ_1. The fixed parameter of the example systems shown in Fig. 5(a) is $\mu_1 = 1/2$, while the fixed parameter of the example systems shown in Fig. 5(b) is $\alpha = 1/2$. It is apparent from the two plots that the best improvements due to the use of the inerter are obtained if the source and receiving bodies have similar uncoupled resonance frequencies, that is if β approaches unity, or $\Omega_1 \approx \Omega_3$. However, these results must be interpreted with care. This is because if the two resonance frequencies are exactly the same, then both configurations with and without inerter are equally ineffective, as shown by the vertical lines in the two plots which tend to 0 dB if β is exactly one. This is due to the fact that $c_1 = c_3 = 0$ is assumed. In Appendix to the paper, a plot analogue to the two plots in Fig. 5 is shown, in which results obtained by considering various levels of passive damping c_1 and
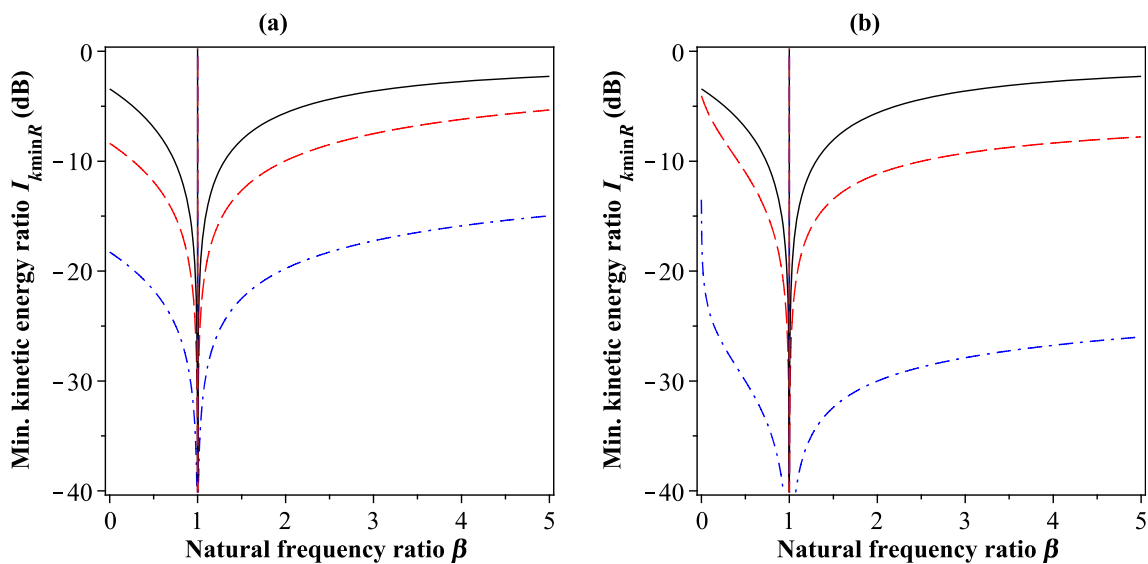

Fig. 5. Minimum specific kinetic energy ratio index I_{kminR}, $\lambda = 0$: (a) $\alpha = 1/2$ (solid line), $\alpha = 10$ (dashed line), $\alpha = 10^3$ (dash-dotted line), (b) $\mu_1 = 1/2$ (solid line), $\mu_1 = 10$ (dashed line), $\mu_1 = 10^3$ (dash-dotted line).

c_3 were considered. The plot in the Appendix indicates that for systems with non-negligible, but still light damping c_1 and/or c_3, the use of inerter gives the best vibration isolation improvement at the frequency ratio β slightly below and slightly above unity. With large damping coefficients c_1 and c_3, the best effects of including the inerter are again observed with $\beta = 1$.

In conclusion, the passive isolator scheme enhanced by incorporating an inerter, exhibits an improved broadband vibration isolation performance in terms of the specific kinetic energy of the receiving body. In the following section it is investigated how much can the vibration isolation performance be further increased by engaging the velocity feedback unit in the isolator scheme shown in Fig. 1.

5. Active control

5.1. Stability in general

With the frequency domain analysis, the stability of active control systems cannot be seen directly from the frequency response of the system. In other words, the model presented in section 2 mathematically allows for calculating frequency response functions using Eq. (10) for both stable and unstable systems. However, such FRFs for unstable systems would be physically meaningless. It is thus necessary to carefully investigate the active control system stability properties before calculating the prospective performance metrics, such as the kinetic energy index given by Eq. (16). It has previously been shown that active vibration isolation systems can exhibit stability problems as discussed in for example [29,43,51,52]. In this subsection, the stability of the feedback control loop is studied with reference to the dimensionless active damping coefficient λ by applying the Routh-Hurwitz [53,54] stability criterion to the characteristic equation of the system. The characteristic equation is the denominator of Eq. (11).

According to the Routh-Hurwitz necessary stability condition and Eq. (12) in order for $A_{1,3} > 0$, it must be

$$\forall \beta < 1 \Rightarrow \lambda > -(\beta \mu_1 + 1) \; \text{ in order for } A1 > 0, \tag{28}$$

$$\forall \beta > 1 \Rightarrow \lambda > -(\mu_1 + 1) \; \text{ in order for } A3 > 0. \tag{29}$$

In other words, if $\beta < 1$ the condition $A_1 > 0$ is a stricter one and if $\beta > 1$, then $A_3 > 0$ is the stricter condition. Considering now the Routh-Hurwitz sufficient condition for stability, it states that all diagonal sub-determinants H_1, H_2 and H_3, as well as the main determinant H_4 of Hurwitz matrix must be positive. The principal determinant H_4 is proportional to the sub-determinant H_3 with an always positive term $\mu_1(\alpha(\beta \mu_1 + 1) + \beta)$ and is thus automatically positive if H_3 is positive. Thus the relevant criteria that must be satisfied simultaneously are Eqs. (28) and (29) plus the following additional ones

$$H_1 > 0 \Rightarrow \lambda + \mu_1 + 1 > 0, \tag{30}$$

$$H_2 > 0 \quad \Rightarrow \quad 2\mu_1\eta_2\{[\mu_1(\mu_2(\beta - 1) + \alpha)\lambda + \alpha + \beta] + \mu_1[1 + \alpha(2 + \mu_1)] + \alpha + \beta\} > 0, \tag{31}$$

$$H_3 > 0 \Rightarrow 4\mu_1^2\eta_2^2(\beta - 1)\left\{(\mu_2 - \alpha)\lambda^2 + [\beta\mu_2(\mu_1 + 1) + \beta - 1 - \alpha(\mu_1 + 1)]\lambda + \beta - 1\right\} > 0. \tag{32}$$

Note that A_1, A_3, H_1 and H_2 are linear functions of the dimensionless feedback gain λ, whereas H_3 is a quadratic function of λ. The quadratic determinant H_3 changes sign at the following values of the feedback gain

$$\lambda_{1,2} = \frac{\mu_2(\beta\mu_1 + 1) - \alpha(\mu_1 + 1) + \beta - 1 \mp \sqrt{(\alpha - \mu_2\beta)^2\mu_1^2 + 2\mu_1(\alpha - \mu_2\beta)(\alpha + 1 - \mu_2 - \beta) + (\alpha - \mu_2 + \beta - 1)^2}}{2(\alpha - \mu_2)}.$$

$$\tag{33a,b}$$

In the forthcoming discussion, it is shown that by ensuring the validity of inequality (32), all other stability conditions are satisfied automatically. In other words, the condition (32) is a *sufficient* stability condition for the problem studied.

5.1.1. Stability without inerter − subcritical and supercritical systems

If the inerter is not used, *i.e.* $\mu_2 = 0$, Eq. (33a,b) can be simplified to

$$\lambda_{1,2} = \frac{\beta - 1 - \alpha(\mu_1 + 1) \mp \sqrt{(1 + \mu_1)^2\alpha^2 - 2(\mu_1 - 1)(\beta - 1)\alpha + (\beta - 1)^2}}{2\alpha}, \tag{34a,b}$$

where λ_1 is the lower value out of two zeros. At this point it is convenient to graphically represent all expressions relevant for the system stability as a function of the dimensionless feedback gain λ. This is done in Fig. 6. Two different cases are presented. Fig. 6(a) shows the case when the squared natural frequency ratio $\beta < 1$ and Fig. 6(b) shows the case with $\beta > 1$. The parameters for an example system shown in Fig. 6(a) are $\alpha = 2$, $\mu_1 = 1/2$, $\eta_2 = 1$ and $\beta_{(a)} = 1/2$, and the parameters for an example
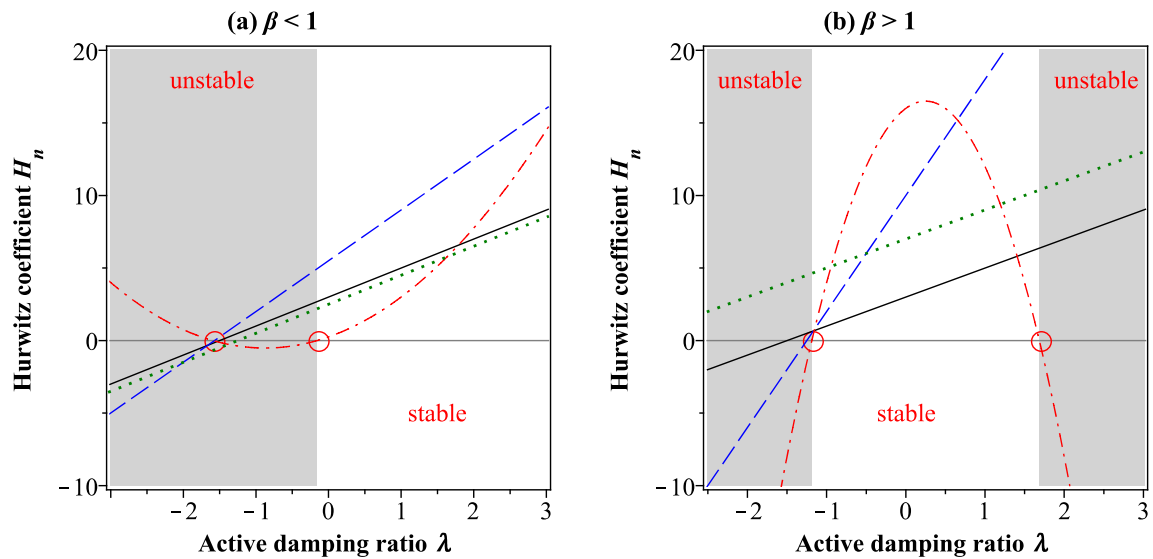
Fig. 6. Dependency of Hurwitz coefficients H_1 (solid line), H_2 (dashed line), H_3 (dash-dotted line) and A_1 (dotted line) magnitude on active damping ratio λ without inerter b_2 ($\mu_2 = 0$): (a) $0 < \beta_{\mathrm{I}} < 1$, (b) $\beta_{\mathrm{II}} > 1$.

system shown in Fig. 6(b) are the same, except $\beta_{(b)} = 5$. The zeros of the 3rd principal diagonal minor H_3 from Eq. (34a,b) are denoted by the two circles. In both plots can be seen that if the principal diagonal minor with the quadratic dependence on the feedback gain is positive, *i.e.* $H_3 > 0$, then all other stability conditions are automatically satisfied. In fact, by closely inspecting Eqs. (28)–(32) it could be deduced that it is generally true that if $H_3 > 0$ then all other conditions, *i.e.* Eqs. (28)–(31), are automatically satisfied and the stability is guaranteed. Thus Eq. (32) represents the strictest stability condition and it becomes sufficient to make sure that $H_3 > 0$ in order to have a stable feedback loop.

Physically this indicates that if the uncoupled natural frequency of the source body is larger than the uncoupled natural frequency of the receiving body, then a negative velocity feedback loop with an arbitrary large feedback gain can be used. As discussed in the forthcoming section 5.2, this is a situation in which very convincing active vibration isolation effects can be achieved that can significantly outperform the two passive vibration isolation schemes discussed in the previous two subsections. On the other hand, in situation in which the uncoupled natural frequency of the source body is smaller than the uncoupled natural frequency of the receiving body, as shown in Fig. 6(b), the range of dimensionless feedback gains is limited between λ_1 and λ_2, according to Eq. (34), and shown in Fig. 6(b). Therefore, the maximum feedback gain is limited by λ_2 above which the second order principal diagonal minor becomes negative with further increasing the feedback gain. This is because the parabola in Fig. 6(b) is oriented downwards whereas the parabola in Fig. 6(a) is oriented upwards. This situation results in limited active vibration control performance as discussed in the forthcoming section 5.2.

In conclusion, it can be stated that all systems representable by the scheme in Fig. 1 can be divided into two families. The first family can be referred to as *supercritical* and it is characterised by $\beta < 1$. The systems belonging to this group allow for the implementation of unconditionally stable active vibration isolation scheme based on the direct feedback of the absolute velocity of the receiving body. The second family is characterised by $\beta > 1$ and it can be referred to as *subcritical*. The systems belonging to this group do not allow for the implementation of unconditionally stable absolute velocity feedback scheme. On the contrary, the feedback loop is conditionally stable with a limited maximum feedback gain.

Practical vibration isolation problems belonging to the supercritical family are the problems of isolating vibrations coming from a flexible base towards sensitive equipment mounted on the base. A practical problem belonging to the subcritical group could be a problem in which running machinery is elastically mounted on the flexible base, for example a punching press. In such case, the broadband vibrations originating from the impact, transmit from the machine to the base. It appears from the above analysis that it would be significantly more difficult to guarantee the stability of the absolute velocity feedback control applied on the latter, subcritical family of vibration isolation problems. Given these difficulties, it is interesting to investigate the effects of the use of an inerter with subcritical systems characterised by $\beta > 1$. This investigation is carried out in the following subsection.

5.1.2. Stability with inerter — stabilising the feedback loop in a subcritical system

If an inerter is used in an isolator of a subcritical system characterised by $\beta > 1$, then interesting effects can be observed with regard to the stability of the feedback loop. By inspecting Eq. (32), it can be seen that the third principal diagonal minor H_3, which is essential for the stability of the active control, has the quadratic coefficient in λ equal to $\mu_2 - \alpha$. This coefficient determines whether the corresponding parabola is pointing upwards or downwards. Given that the term $(\beta - 1)$ multiplying
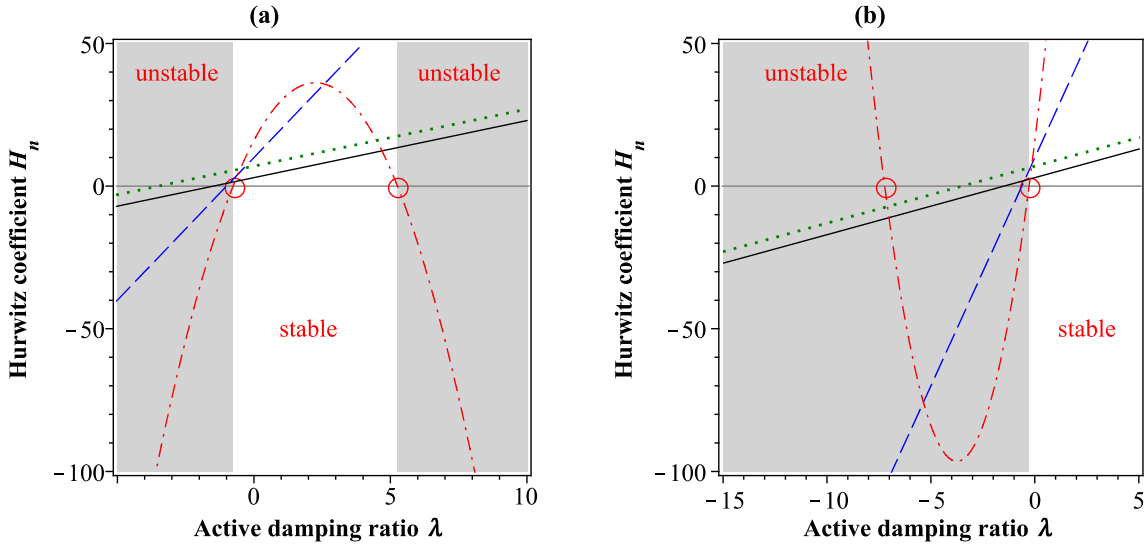
Fig. 7. Dependency of Hurwitz coefficients H_1 (solid line), H_2 (dashed line), H_3 (dash-dotted line) and A_1 (dotted line) magnitude on active damping ratio λ with inerter b_2 ($\mu_2 \neq 0$) and $\beta_{II} > 1$: (a) $\mu_2 < \alpha$, (b) $\mu_2 > \alpha$.

the squared bracket expression is positive with subcritical systems, it turns out that an inerter with dimensionless inertance $\mu_2 > \alpha$ can make the quadratic coefficient of the parabola positive. This in turn results in an upward pointing parabola. Therefore unconditional stability can be achieved also with subcritical systems simply by adding an inerter with $\mu_2 > \alpha$. This is illustrated in Fig. 7(a) which shows all principal diagonal minors calculated according to Eqs. (30)–(32). The system is again characterised by $\alpha = 2$, $\mu_1 = 1/2$, $\eta_2 = 1$ and $\beta = 5$, just like in Fig. 6(b). As shown in Fig. 7(a), with the inclusion of inerter when $\beta_{II} > 1$ and $\mu_{2(a)} = \alpha/2$, the limited stable range of λ between $\lambda_{H1} < \lambda < \lambda_{H2}$, is expanded in comparison with Fig. 6(b). If the inertance is further increased, so that $\mu_2 = 2\alpha$, the system becomes stable for any $\lambda > \lambda_{H2}$, as shown in Fig. 7(b). Therefore, for subcritical systems where the fundamental natural frequency of the receiving body is larger than that of the source body, the use of inerter characterised by $\mu_2 > \alpha$ drastically improves the stability by turning a subcritical active vibration isolation problem into a supercritical one. This is quite essential for the performance of the active vibration isolation, as discussed in the following subsections.

5.2. Performance

5.2.1. Without inerter

The performance of the active control is first studied without the use of inerter, therefore dimensionless parameter μ_2 equals zero. Fig. 8(a) shows the specific kinetic energy index of the receiving body plotted as a function of the passive and active damping ratio. Firstly, a supercritical system is assumed so the frequency ratio β is smaller than one. Fig. 8(a) indicates that as the active damping ratio (the feedback gain) is increased, the kinetic energy index monotonically decreases demonstrating that the desired active vibration isolation effect is achieved. Fig. 8(b) shows the dimensionless transfer mobility function (the velocity of the receiving body per unit forcing of the source body, as a function of frequency) for increasing active damping ratios.

It can be seen that the amplitude of the dimensionless mobility function $|Y_{21}(j\Omega)|$ diminishes in the vicinity of Ω_{n1} and Ω_{n2} which is tied to significant reduction of specific kinetic energy I_k. In addition, no increase of the amplitude of the mobility with an increase in the feedback gain can be seen at any frequency. Thus a true broadband active vibration isolation effect can be achieved. The characteristic parameters of the example system illustrated in Fig. 8(a) are $\alpha = 1/2$, $\beta = 1/2$ and $\mu_1 = 1/2$. Parameters of the example system shown in Fig. 8(b) are the same, except that the damping ratio had to be fixed to $\eta_2 = 0.5\%$. Therefore in such supercritical system, the use of inerter appears to be unnecessary, since the system is stable for any given positive value of λ.

Considering now the subcritical case, where $\beta_{II} > 1$, the system is stable for a limited narrow λ range as already discussed in section 5.1 and as shown in Fig. 6(b). Therefore it is interesting to investigate into performance of the active control for subcritical systems when the stable feedback gain is restricted between the lower and upper margins shown in Fig. 6(b).

The kinetic energy index of the receiving body in this case ($\beta_{II} > 1$) is shown in Fig. 9(a). The parameters of the example system shown in Fig. 9(a) are $\alpha = 1/2$, $\beta = 2$ and $\mu_1 = 1/2$.
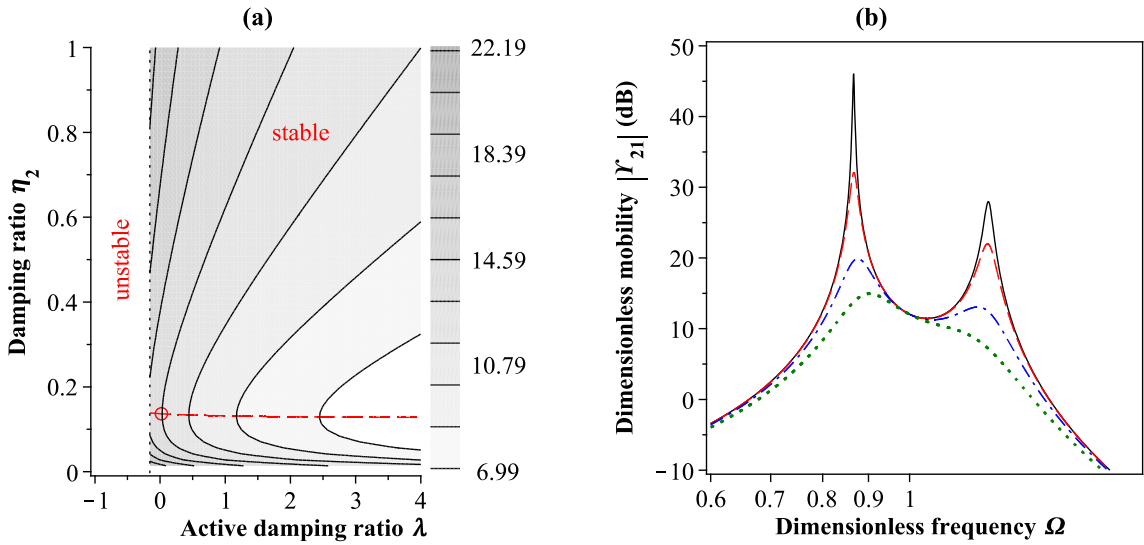
Fig. 8. Isolation system performance without inerter b_2 ($\mu_2 = 0$) and $0 < \beta_I < 1$: (a) Specific kinetic energy index I_k, (b) Transfer mobility function $|Y_{21}(j\Omega)|$, $\lambda = 0$ (solid line), $\lambda = 2$ (dashed line), $\lambda = 10$ (dash-dotted line), $\lambda = 20$ (dotted line).
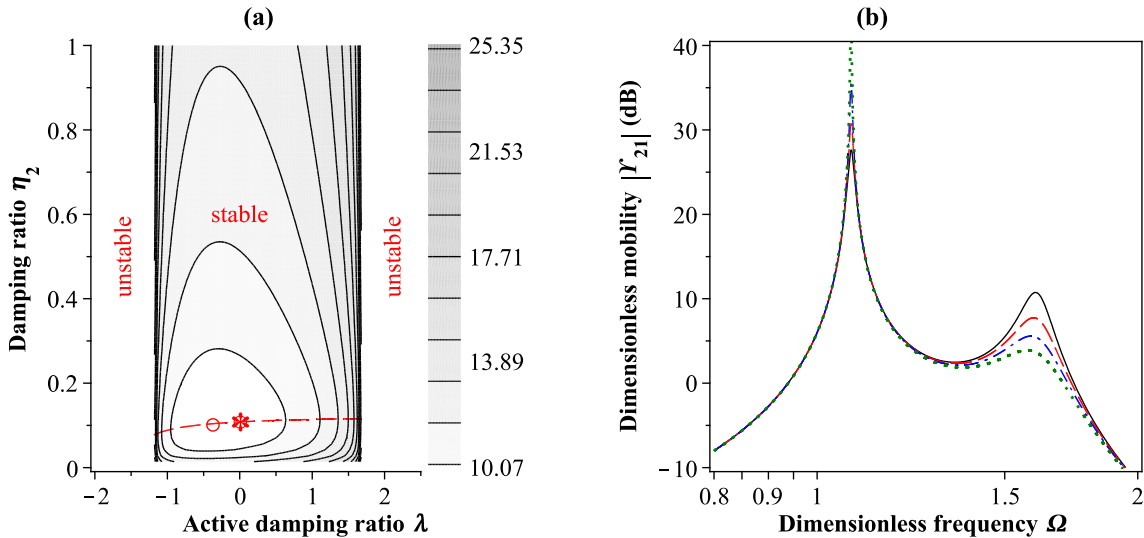

Fig. 9. Isolation system performance without inerter b_2 ($\mu_2 = 0$) and $\beta_{II} > 1$: (a) Specific kinetic energy index I_k, (b) Transfer mobility function $|Y_{21}(j\Omega)|$, $\lambda = 0$ (solid line), $\lambda = 0.5$ (dashed line), $\lambda = 1$ (dash-dotted line), $\lambda = 1.5$ (dotted line).

It can be seen in Fig. 9(a) that there is an optimum combination of the passive and active damping ratios that minimises the kinetic energy index which is marked by the red circle. The optimum passive damping ratio as a function of the active damping ratio is shown by the red dashed line in Fig. 9(a). Similar to Eq. (22), this function is obtained by differentiating Eq. (17) with respect to λ and equalling with zero which yields following relation

$$\eta_{2\text{opt},\lambda} = \frac{\alpha\mu_1}{2} \sqrt{\frac{1 + \mu_1 + \lambda}{1 + \beta\mu_1 + \lambda}}. \tag{35}$$

By comparing it with Eq. (22), it can be observed that λ is now added under the root of both numerator and denominator. If $\lambda = 0$, Eq. (35) reduces to Eq. (22). Eq. (35) is denoted by dashed line in Fig. 9(a). By inserting Eq. (35) into Eq. (17), an expression for minimum specific kinetic energy along the dashed line can be obtained

$$I_{k\text{min}} = 2\pi \frac{\alpha\sqrt{(\beta\mu_1 + \lambda + 1)(\mu_1 + \lambda + 1)}}{\mu_1(\beta - 1)\left[(-1 + \beta - \mu_1\alpha - \alpha)\lambda - 1 + \beta - \alpha\lambda^2\right]}. \tag{36}$$

By differentiating Eq. (36) with respect to λ, equalling with zero and solving for λ, optimal active damping coefficient λ_{opt} is obtained. Inserting both $\eta_{2\text{opt},\lambda}$ from Eq. (35) and λ_{opt} into Eq. (17) yields an expression for minimum specific kinetic energy I_k. However, the relations for λ_{opt}, $\eta_{2\text{opt},\lambda 2}$ and I_k are too cumbersome and not easily interpretable, so they are omitted. Nevertheless the global minimum position for I_k with respect to two variables λ_{opt} and $\eta_{2\text{opt},\lambda 2}$ exists and it is denoted by the circle in contour plot. The asterisk in Fig. 9(a) denotes the minimum kinetic energy index if value of λ is set to zero, which implies the use of optimised passive control. By comparing the surface levels in Fig. 9(a) at the optimum active control (circle) and the optimum passive control (asterisk) it can be seen that the level difference is about one dB. Therefore, the active control can outperform the passive control, but the corresponding improvement in performance is not particularly convincing. It can be concluded that with subcritical system the performance of the active vibration scheme is questionable, since a significantly simpler passive system can achieve nearly the same vibration isolation effect. The reasons for this are further investigated by plotting the dimensionless transfer mobility $|\Upsilon_{21}(j\Omega)|$ as a function of frequency for cases with no control ($\lambda = 0$) and with the active control using increasing active damping ratios (increasing feedback gains) in Fig. 9(b). The parameters for the example system shown in Fig. 9(b) are the same as in Fig. 9(a), except that a fixed passive damping ratio $\eta_2 = 0.02$ is used. It can be seen in Fig. 9(b), that although the amplitude of the dimensionless mobility $|\Upsilon_{21}(j\Omega)|$ reduces in the vicinity of second dimensionless circular frequency Ω_{n2} with rising λ, a significant overshoot can be observed in the vicinity of first dimensionless circular frequency Ω_{n1} for rising λ. Fig. 10(a) shows that for rising λ, the specific kinetic energy I_k also rises significantly until instability occurs. Therefore, using active control without inerter in cases when $\beta_{\text{II}} > 1$ results in generally doubtful performance. Fig. 10(b) shows the comparison between the optimum active vibration isolation and the optimum passive vibration isolation for a subcritical system characterised by $\alpha = 1/2$, $\beta = 2$ and $\mu_1 = 1/2$ in terms of the amplitude of the transfer mobility $|\Upsilon_{21}(j\Omega)|$ plotted as a function of frequency. The same parameters are used in Fig. 10(a) where the passive damping ratio is set to $\eta_2 = 0.02$. The optimised active control results in a slightly lesser kinetic energy index compared to the optimised passive control (Fig. 10(a)), which is obtained by damping down the velocity response around the first natural frequency at the expense of slightly increasing the response around the second natural frequency (Fig. 10(b)). In conclusion, the improvement in the performance due to the use of active control probably does not justify the complexity of the vibration isolation system in subcritical systems.

5.2.2. Comment on the reciprocity principle

So far, it has been shown that all active vibration isolation problems shown in Fig. 1 can be categorised as subcritical or supercritical, depending on the frequency ratio β. The above stability and performance analyses indicate that with supercritical systems, the active vibration isolation based on absolute velocity feedback can be expected to yield very good vibration isolation effects. With subcritical systems this is not the case due to poor stability margins and the consequent unconvincing vibration isolation performance.
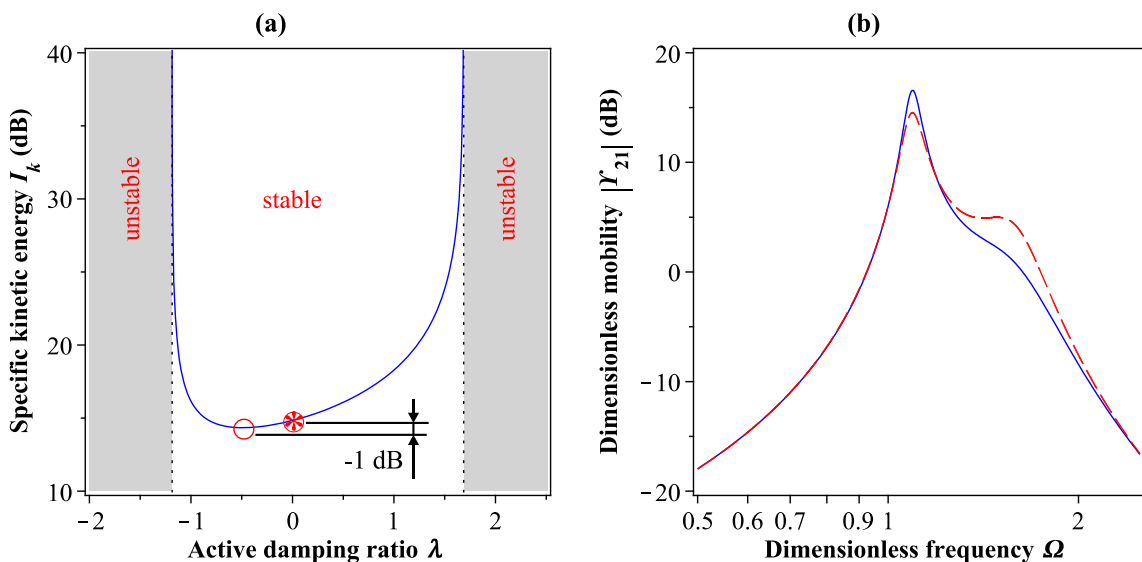

Fig. 10. Isolation system performance without inerter b_2 ($\mu_2 = 0$) and $\beta_{\text{II}} > 1$: (a) Specific kinetic energy index I_k, (b) Transfer mobility function $|\Upsilon_{21}(j\Omega)|$, $\lambda = 0$, $\eta_2 = \eta_{2\text{opt}1}$ (solid line), $\lambda = \lambda_{\text{opt}}$, $\eta_2 = \eta_{2\text{opt},\lambda 2}$ (dashed line).

At this point, it should be noted that this division into supercritical/subcritical systems is based on the assumption that the velocity sensor is mounted on the receiving body. With respect to that, one possible way of turning a subcritical vibration isolation problem into a supercritical one would be to place the sensor on the source body (see Fig. 1. - dashed alternative feedback loop). Then, the body where the sensor is located is characterised by the larger natural frequency than the other body, and the new feedback loop will be stable for an arbitrary large gain implementing a negative velocity feedback since everything else in the system is symmetric. In fact, the transfer mobility $Y_{12}(j\Omega)$, in the case the sensor is located on the source body will be affected by the control loop in the same way the transfer mobility $Y_{21}(j\Omega)$ is affected by the control loop if the sensor is mounted on the receiving body. Similarly, the transfer mobility $Y_{21}(j\Omega)$, in the case the sensor is located on the source body, will be affected by the control loop in the same way $Y_{12}(j\Omega)$ is affected by the control loop if the sensor is mounted on the receiving body. In other words, if the sensor is located on the source body of a system characterised by $\Omega_3 > \Omega_1$ (subcritical), the velocity of the mass m_1 due to the force exciting the mass m_2 should decrease with increasing the feedback gain similarly to what is shown in Fig. 8(b). The question however is what happens with the velocity of the mass m_2 due to forcing at the mass m_1 in such case. According to the reciprocity principle which states that $Y_{21} = Y_{12}$, the velocity of the mass m_2 should monotonically decrease with the increase of the feedback gain and this should provide a simple solution to the vibration isolation problem in subcritical systems.

However, the reciprocity principle does not hold if the system is made active. In other words, $Y_{21} \neq Y_{12}$ if $\lambda \neq 0$ which can be seen by comparing Eqs. (10b) and (10c). Although the two frequency response functions are characterised by the same denominators, they have different numerators. In fact, the two numerators become the same only if the feedback gain is zero. This is a consequence of the diagonally asymmetric damping matrix from Eq. (4b). The disruption of the reciprocity principle is illustrated on an example system in Fig. 11.

The example system parameters are $\alpha = 1$, $\beta = 1/2$, $\mu_1 = 1$ and $\eta_2 = 0.02$. The dimensionless feedback gain λ assumes either a very large ($\lambda = 25$), or zero value ($\lambda = 0$). Fig. 11 shows a clear difference between Y_{21} (dashed line) and Y_{12} (solid line) in case the active damping ratio of $\lambda = 25$ is used. Only if the active damping ratio is set to zero, then the two mobilities become the same as indicated by the red dotted line in Fig. 11.

This prevents a straightforward solution of the subcritical vibration isolation problem by placing the sensor on the source body. Although this would solve the stability problem, it would not improve the isolation performance. This is because, as shown by the solid line, the mobility function Y_{12} becomes characterised by a significant overshot at higher frequencies.

However, as discussed in the forthcoming part of the paper, the use on an inerter in the isolator may be a viable solution to the subcritical vibration isolation problems. It has already been shown in section 5.1.2 that the use of inerter with inertance $\mu_2 > \alpha$ opens one of the two stability margins and enables the use of large, theoretically unlimited feedback gains in subcritical systems. In the following subsection the performance of such an inerter-based active vibration isolation system is discussed, *i.e.* it is shown how such control affects the kinetic energy of the receiving body.
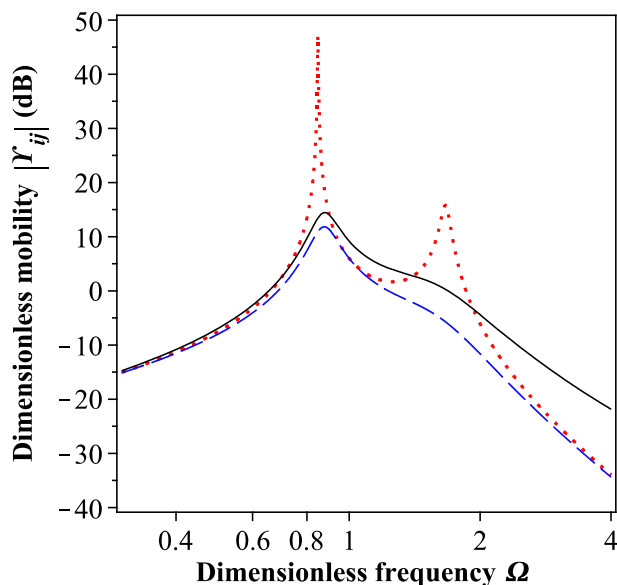

Fig. 11. Disruption of the reciprocity principle, $\mu_2 = 0$, transfer mobility function $|Y_{ij}(j\Omega)|$: $Y_{12} = Y_{21}$, $\lambda = 0$ (dotted line), Y_{12}, $\lambda = 25$ (solid line), Y_{21}, $\lambda = 25$ (dashed line).
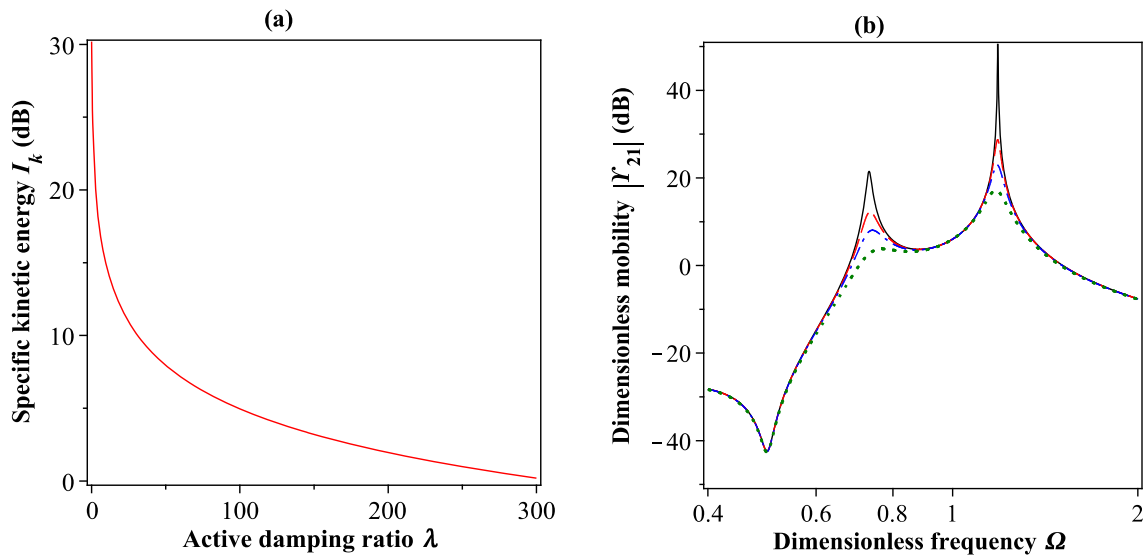
Fig. 12. Isolation system performance with inerter b_2 ($\mu_2 \neq 0$), $\beta_{II} > 1$ and $\mu_2 > \alpha$: (a) Specific kinetic energy index I_k, (b) Transfer mobility function $|Y_{21}(j\Omega)|$, $\lambda = 0$ (solid line), $\lambda = 5$ (dashed line), $\lambda = 10$ (dash-dotted line), $\lambda = 20$ (dotted line).

5.2.3. With inerter

Fig. 12(a) shows the specific kinetic energy I_k plotted as a function of the active damping ratio λ of a subcritical system characterised by $\alpha = 1/2$, $\beta = 2$, $\mu_1 = 1/2$ and $\eta_2 = 0.01$, equipped with an inerter of inertance $\mu_2 = 2$. Therefore an inertance large enough to stabilise the feedback loop is used ($\mu_2 > \alpha$). It can be seen that with an increase in the dimensionless feedback gain λ, the specific kinetic energy index monotonically decreases indicating that the desired vibration isolation effect is accomplished. Fig. 12(b) shows the amplitude of the dimensionless transfer mobility $|Y_{21}(j\Omega)|$ plotted against frequency for increasing feedback gains. Note the anti-resonance effect at frequencies below the first resonance, introduced by inerter. It can be seen that with the increase in the feedback gain, the receiving body response is decreased at both resonance frequencies. The higher the gain, the lower is the velocity response. There can be seen no frequencies at which the increase of the feedback gain causes an increase in the response. Therefore, it can be concluded that the inclusion of the inerter in the active vibration isolation scheme with subcritical problems is essential in establishing stable and efficient active vibration isolation. It should be noted that the inerter can be seen from the control point of view as a relative acceleration feedback. In other words, subtracted outputs of two accelerometers mounted on the receiving and source bodies could theoretically be fed to the reactive actuator in addition to the existing velocity feedback in order to synthesize the inerter element actively. However, such "derivative" active vibration control has never been achieved in practice to the best of authors' knowledge. It appears that the corresponding sensor-actuator frequency response function does not roll-off with frequency which causes very pronounced stability problems associated with high frequency poles, as discussed for example in Ref. [55]. It is therefore very useful in the scheme to include the inerter as a passive element which mimics the effects of a relative acceleration feedback to reactive force actuator.

6. Conclusions

In this paper, a novel, inerter-based active vibration isolation system is presented. Two fundamental passive benchmark isolators are also investigated, one not employing the inerter and the other employing the inerter. The methodology is studied on a simple two degree of freedom system so that many conclusions can be drawn based on analytically derived expressions. Such a simplified system can be seen as a reduced order model of a potentially more complex structure. It is shown in the paper that the vibration isolation performance of the fundamental passive isolator not employing the inerter can be improved by adding the inerter in parallel with the isolator spring and damper. This improvement is particularly significant if the source and receiving bodies have similar uncoupled natural frequencies. By investigating the stability of the active control when no inerter is used, it is found that there are two fundamental families of vibration isolation problems. With the first family (supercritical systems), which is characterised by the natural frequency of the uncoupled source body larger than the natural frequency of the uncoupled receiving body, large feedback gains can be used without compromising the stability of the feedback control system. This results in a convincing broadband vibration isolation effect. With the second family of systems (subcritical systems), the natural frequency of the uncoupled source body is below the natural frequency of the uncoupled receiving body. The range of stable feedback gains is limited which results in poor vibration isolation performance. However

with the inclusion of the inerter, broadband active vibration isolation can also be achieved in the subcritical family of systems. Adding the inerter into the isolator effectively generates a sort of relative acceleration feedback that stabilises the control loop. In fact, it is analytically calculated in the paper that the minimum inertance to stabilise the loop is proportional to the stiffness of the isolator spring and inversely proportional to the squared natural frequency of the source body. It is important to mention that direct acceleration feedback would not be possible in practice due to very pronounced stability problems, therefore the passive element which mimics such feedback is very useful.

Acknowledgements

Appendix A

So far it has been assumed that the passive damping of the source and the receiving body is light to the limit that it becomes negligible and the corresponding damper coefficients c_1 and c_3 were assumed to be zero. In this Appendix, the validity of these assumptions is tested. This is done by plotting some characteristic results in case when the damping co-efficients c_1 and c_3 are set so that the two corresponding damping ratios $\eta_{1,3}$ both equal 1%. The corresponding damping ratios are defined as

$$\eta_1 = \frac{c_1}{2\sqrt{m_1 k_1}}, \quad \eta_3 = \frac{c_3}{2\sqrt{m_2 k_3}}. \tag{37a-b}$$

The first situation that is discussed is with reference to Fig. 2 where the damping coefficients c_1 and c_3 were neglected. In Fig. A1, the plots analogue to those of Fig. 2 are shown with $\eta_1 = \eta_3 = 0.01$.
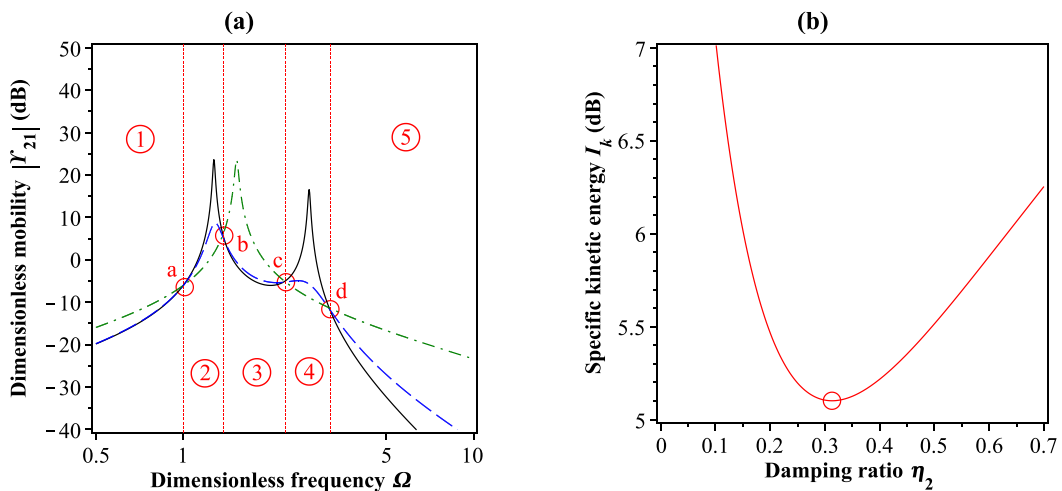

Fig. A1. Isolation system performance without inerter b_2 ($\mu_2 = 0$) for $\eta_1 = \eta_3 = 0.01$: (a) Transfer mobility function $|Y_{21}(j\Omega)|$, $\eta_2 = \eta_{2opt1}/100$ (solid line), $\eta_2 = \eta_{2opt1}$ (dashed line), $\eta_2 = 100\eta_{2opt1}$ (dash-dotted line), (b) Specific kinetic energy index I_k.

All other parameters that characterise the system are the same as in Fig. 2. It can be seen that the qualitative response of the system is the same as that illustrated in Fig. 2. However, quantitatively the minimum kinetic energy in Fig A1(b) is about 1/2 dB lower than in Fig. 2. Also, the corresponding optimum damping ratio η_2 is slightly higher than in the situation illustrated in Fig. 2. Therefore it can be stated that the basic conclusions drawn for undamped source and receiving bodies, are also valid for lightly damped source and receiving bodies. The analytical simplified expressions for the optimum damping of the isolator η_2 and the minimum kinetic energy index are also approximately valid under the assumption of lightly damped source and receiver bodies. Considering now the passive vibration isolation with the use of inerter, Fig. A2 depicts results corresponding to Fig. 3 when the damping $\eta_1 = \eta_3 = 0.01$. Again, all other parameters that characterise the system are the same as in Fig. 2. In Fig. A2. it can be seen that the same qualitative characteristics of the receiving body response are observed with lightly damped source and receiving bodies in case inerters are incorporated in the passive isolator.
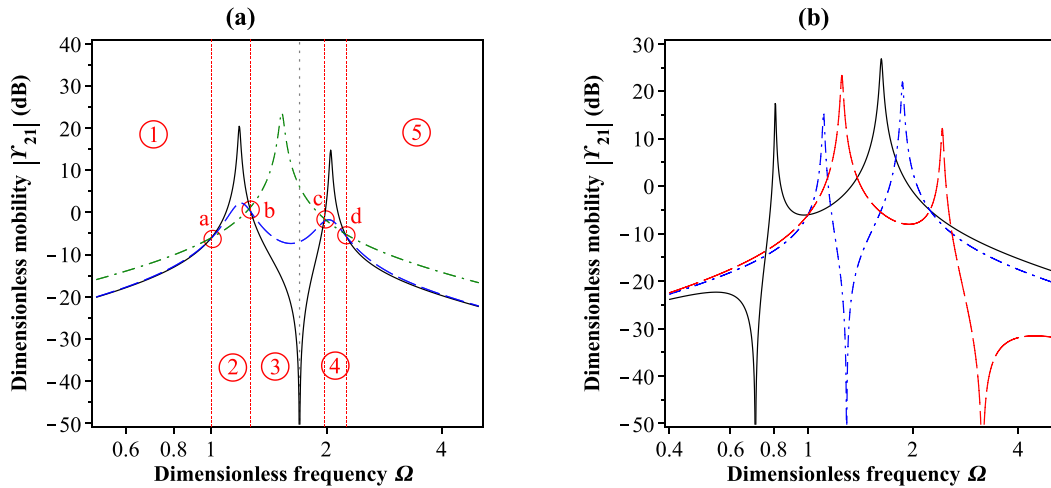
Fig. A2. Transfer mobility function $|Y_{21}(j\Omega)|$ for $\eta_1 = \eta_3 = 0.01$: (a) $\eta_2 = 0$ (solid line), $\eta_2 = \eta_{2opt2}$ (dashed line), $\eta_2 = 100\eta_{2opt2}$ (dash-dotted line), (b) $\eta_2 = 0$: $\mu_2 > \alpha$ (solid line), $\alpha/\beta < \mu_2 < \alpha$ (dash-dotted line), $\mu_2 < \alpha/\beta$ (dashed line).

The following figure, Fig. A3 aims to illustrate the influence of the light damping ratios $\eta_1 = \eta_3 = 0.01$ on the optimum combination of inertance and damping ratio η_2 in Fig. A3(a), and on the improvement of the vibration isolation performance due to the added inerter. It can also be seen in Fig. A3(a) that the optimum combination the inertance ratio μ_2 and damping ratio η_2 is virtually not affected. Fig. A3(b) on the other hand shows that with lightly damped source and the receiving bodies, the kinetic energy of vibration of the receiving body reduces both with and without inerter. The relative improvement due to the inerter however remains to be ~3 dB.
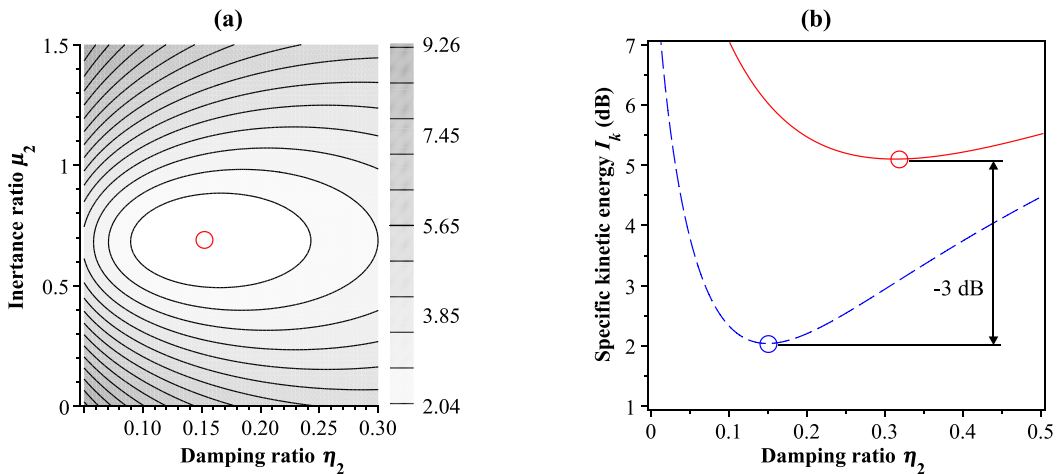
Fig. A3. Isolation system performance for $\eta_1 = \eta_3 = 0.01$: (a) specific kinetic energy index I_k as a function of η_2 and μ_2, (b) specific kinetic energy index I_k: comparison of the cases with and without inerter; $\mu_2 = 0$ (solid line), $\mu_2 = \mu_{2opt}$ (dashed line).

A plot analogue to the two plots in Fig. 5 is shown next in Fig. A4, where results obtained by considering various levels of passive damping c_1 and c_3 are considered. It can be seen that as the damping coefficients c_1 and c_3 (and the corresponding damping ratios η_1 and η_3) are reduced, the plot becomes similar to the plots in Fig. 5. (*i.e.* the red solid line in Fig. A4.). However, as the two damping coefficients approach about 0.1%, the plots cease to resemble those in Fig. 5 which are valid for undamped source and receiving bodies.
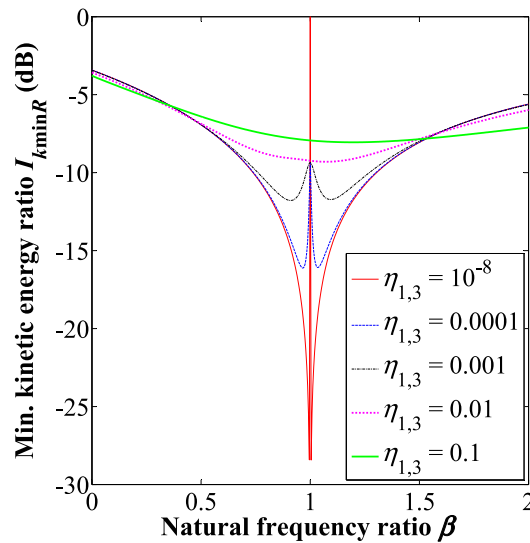
Fig. A4. Minimum specific kinetic energy ratio index I_{kminR}, $\lambda = 0$, $\alpha = 1/2$, $\mu_1 = 1/2$: $\eta_{1,3} = 10^{-8}$ (solid line), $\eta_{1,3} = 0.0001$ (dashed line), $\eta_{1,3} = 0.001$ (dash-dotted line), $\eta_{1,3} = 0.01$ (dotted line), $\eta_{1,3} = 0.1$ (thick solid line).

This is shown by the magenta dotted line and the green thick solid line in Fig. A4. In such cases with low to moderate damping ratios of the two bodies, it appears that the greatest improvement of the vibration isolation performance by adding the inerter in the isolator scheme can be expected with source and receiving bodies having similar uncoupled natural frequencies ($\beta \approx 1$).

References

[1] M.C. Smith, Synthesis of mechanical networks: the inerter, IEEE Trans. Automat. Contr. 47 (2002) 1648–1662.
[2] M.C. Smith, F.C. Wang, Performance benefits in passive vehicle suspensions employing inerters, Veh. Syst. Dyn. 42 (2004) 235–257.
[3] M.Z.Q. Chen, C. Papageorgiou, F. Scheibe, F.-C. Wang, M.C. Smith, The missing mechanical circuit element, IEEE Circ. Syst. Mag. 9 (2009) 10–26.
[4] M.Z.Q. Chen, Y. Hu, L. Huang, G. Chen, Influence of inerter on natural frequencies of vibration systems, J. Sound Vib. 333 (2014) 1874–1887.
[5] M.Z.Q. Chen, K. Wang, Y. Zou, G. Chen, Realization of three-port spring networks with inerter for effective mechanical control, IEEE Trans. Automat. Contr. 60 (2015) 2722–2727.
[6] A. Gonzalez-Buelga, L.R. Clare, S.A. Neild, J.Z. Jiang, D.J. Inman, An electromagnetic inerter-based vibration suppression device, Smart Mater. Struct. 24 (2015) 1–10.
[7] D. Li, Y.-Z. Liu, Designing and simulating a mechatronic inerter, Appl. Mech. Mater. 620 (2014) 28–32.
[8] F.-C. Wang, M.-F. Hong, T.-C. Lin, Designing and testing a hydraulic inerter, Proc. Inst. Mech. Eng. Part C J. Mech. Eng. Sci. 225 (2011) 66–72.
[9] S.J. Swift, M.C. Smith, A.R. Glover, C. Papageorgiou, B. Gartner, N.E. Houghton, Design and modelling of a fluid inerter, Int. J. Contr. Syst. Modell. Feedback Contr. A Special Issue Dedicated to Sir Alistair G.J. MacFarlane 86 (2013) 2035–2051.
[10] M.Z.Q. Chen, Y. Hu, C. Li, G. Chen, Performance benefits of using inerter in semiactive suspensions, IEEE Trans. Contr. Syst. Technol. 23 (2015) 1571–1577.
[11] M.Z.Q. Chen, K. Wang, Y. Zou, J. Lam, Realization of a special class of admittances with one damper and one inerter for mechanical control, IEEE Trans. Automat. Contr. 58 (2013) 1841–1846.
[12] M.Z.Q. Chen, Y. Hu, C. Li, G. Chen, Application of semi-active inerter in semi-active suspensions via force tracking, J. Vib. Acoust. 138 (2016) 1–11.
[13] A. Kuznetsov, M. Mammadov, I. Sultan, E. Hajilarov, Optimization of improved suspension system with inerter device of the quarter-car model in vibration analysis, Arch. Appl. Mech. 81 (2011) 1427–1437.
[14] I.F. Lazar, S.A. Neild, D.J. Wagg, Using an inerter-based device for structural vibration suppression, Earthq. Eng. Struct. Dynam. 43 (2014) 1129–1147.
[15] Y. Hu, M.Z.Q. Chen, Z. Shu, L. Huang, Analysis and optimisation for inerter-based isolators via fixed-point theory and algebraic solution, J. Sound Vib. 346 (2015) 17–36.
[16] T. Bein, D. Mayer, J. Bös, Recent solutions for noise & vibration control in vehicles, in: 41st International Congress and Exposition on Noise Control Engineering 2012, INTER-NOISE 2012 5, 2012, pp. 3759–3771.
[17] T. Bein, J. Bös, S. Herold, D. Mayer, M. Melz, M. Thomaier, Smart interfaces and semi-active vibration absorber for noise reduction in vehicle structures, Aero. Sci. Technol. 12 (2008) 62–73.
[18] I.F. Lazar, S.A. Neild, D.J. Wagg, Performance Analysis of Cables with Attached Tuned-inerter-dampers, in: Conference Proceedings of the Society for Experimental Mechanics Series, vol. 2, 2015, pp. 433–441.
[19] I.F. Lazar, S.A. Neild, D.J. Wagg, Vibration suppression of cables using tuned inerter dampers, Eng. Struct. 122 (2016) 62–71.
[20] P. Brzeski, T. Kapitaniak, P. Perlikowski, Novel type of tuned mass damper with inerter which enables change of inertance, J. Sound Vib. 349 (2015) 56–66.
[21] P. Brzeski, E. Pavlovskaia, T. Kapitaniak, P. Perlikowski, The application of inerter in tuned mass absorber, Int. J. Non Lin. Mech. 70 (2015) 20–29.
[22] Y. Hu, M.Z.Q. Chen, Performance evaluation for inerter-based dynamic vibration absorbers, Int. J. Mech. Sci. 99 (2015) 297–307.
[23] M. Zilletti, Feedback control unit with an inerter proof-mass electrodynamic actuator, J. Sound Vib. 369 (2016) 16–28.
[24] J.C. Schönfeld, Analogy of hydraulic, mechanical, acoustic and electrical systems, Appl. Sci. Res. 3 (1954) 417–450.
[25] P. Gardonio, C. González Díaz, Downscaling of proof mass electrodynamic actuators for decentralized velocity feedback control on a panel, Smart Mater. Struct. 19 (2010) 1–14.
[26] S.J. Elliott, M. Zilletti, Scaling of electromagnetic transducers for shunt damping and energy harvesting, J. Sound Vib. 333 (2014) 2185–2195.
[27] M.J. Brennan, J. Garcia-Bonito, S.J. Elliott, A. David, R.J. Pinnington, Experimental investigation of different actuator technologies for active vibration control, Smart Mater. Struct. 8 (1999) 145–153.

[28] D.H. Sheingold, Impedance and admittance transformations using operational amplifiers, The Lightning Empiricist 12 (1964) 1–8.
[29] S.J. Elliott, M. Serrand, P. Gardonio, Feedback stability limits for active isolation systems with reactive and inertial actuators, J. Vib. Acoust. 123 (2001) 250–261.
[30] J. Høgsberg, M.L. Brodersen, S. Krenk, Resonant passive–active vibration absorber with integrated force feedback control, Smart Mater. Struct. 25 (4) (2016) 1–10.
[31] C. Paulitsch, P. Gardonio, S.J. Elliott, Active vibration control using an inertial actuator with internal damping, J. Acoust. Soc. Am. 119 (2006) 2131–2140.
[32] C.G. Díaz, C. Paulitsch, P. Gardonio, Smart panel with active damping units. Implementation of decentralized control, J. Acoust. Soc. Am. 124 (2008) 898–910.
[33] N. Alujević, G. Zhao, B. Depraetere, P. Sas, B. Pluymers, W. Desmet, H$_2$ optimal vibration control using inertial actuators and a comparison with tuned mass dampers, J. Sound Vib. 333 (2014) 4073–4083.
[34] J. Rohlfing, S.J. Elliott, P. Gardonio, Feedback compensator for control units with proof-mass electrodynamic actuators, J. Sound Vib. 331 (2012) 3437–3450.
[35] M. Zilletti, P. Gardonio, S.J. Elliott, Optimisation of a velocity feedback controller to minimise kinetic energy and maximise power dissipation, J. Sound Vib. 333 (2014) 4405–4414.
[36] Y.L. Cheung, W.O. Wong, L. Cheng, Minimization of the mean square velocity response of dynamic structures using an active-passive dynamic vibration absorber, J. Acoust. Soc. Am. 132 (2012) 197–207.
[37] G. Zhao, N. Alujević, B. Depraetere, G. Pinte, J. Swevers, P. Sas, Experimental study on active structural acoustic control of rotating machinery using rotating piezo-based inertial actuators, J. Sound Vib. 348 (2015) 15–30.
[38] G. Zhao, N. Alujević, B. Depraetere, G. Pinte, P. Sas, Adaptive-passive control of structure-borne noise of rotating machinery using a pair of shunted inertial actuators, J. Intell. Mater. Syst. Struct. 27 (2016) 1584–1599.
[39] G. Zhao, N. Alujević, B. Depraetere, P. Sas, Dynamic analysis and H$_2$ optimisation of a piezo-based tuned vibration absorber, J. Intell. Mater. Syst. Struct. 26 (2015) 1995–2010.
[40] A. Kras, P. Gardonio, Velocity feedback control with a flywheel proof mass actuator, J. Sound Vib. 402 (2017) 31–50.
[41] A. Caiazzo, N. Alujević, B. Pluymers, W. Desmet, Active control of turbulent boundary layer sound transmission into a vehicle interior, J. Phys. Conf. 744 (2016) 012026.
[42] R.M. Chalasani, Ride performance potential of active suspension systems – Part I: simplified analysis based on a quarter-car model, in: ASME Symposium on Simulation and Control of Ground Vehicles and Transportation Systems, AMD-vol. 80, DSC-vol. 2, 1986, pp. 187–204.
[43] A. Preumont, Vibration Control of Active Structures, second ed., Kluwer Academic, London, 2002 (Chapter 6), "Active vibration isolation".
[44] C.E. Kaplow, J.R. Velman, Active local vibration isolation applied to a flexible space telescope, AIAA J. Guid. Contr. 3 (1980) 227–233.
[45] S. Krenk, J. Høgsberg, Tuned resonant mass or inerter-based absorbers: unified calibration with quasi-dynamic flexibility and inertia correction, Proc. R. Soc. A 472 (2185) (2016).
[46] D.C. Karnopp, A.K. Trikha, Comparative study of optimization techniques for shock and vibration isolation, Trans. Am. Soc. Mech. Eng. J. Eng. Ind. Ser. B 91 (1969) 1128–1132.
[47] P. Gardonio, M. Gavagni, A. Bagolini, Seismic velocity sensor with an internal sky-hook damping feedback loop, IEEE Sensor. J. 8 (11) (2008) 1776–1784.
[48] D.E. Newland, An Introduction to Random Vibrations, Spectral & Wavelet Analysis, third ed., Dover Publications Inc, New York, 2005.
[49] E. Rustighi, M.J. Brennan, B.R. Mace, A shape memory alloy adaptive tuned vibration absorber: design and implementation, Smart Mater. Struct. 14 (2005) 19–28.
[50] J.Q. Sun, M.R. Jolly, M.A. Norris, Passive, adaptive and active tuned vibration absorbers—a survey, J. Mech. Des. Trans. Am. Soc. Mech. Eng. 117 (1995) 234–242.
[51] A. Preumont, A. Francois, F. Bossens, A. Abu-Hanieh, Force feedback versus acceleration feedback in active vibration isolation, J. Sound Vib. 257 (2002) 605–613.
[52] N. Alujević, H. Wolf, P. Gardonio, I. Tomac, Stability and performance limits for active vibration isolation using blended velocity feedback, J. Sound Vib. 330 (2011) 4981–4997.
[53] E.J. Routh, A Treatise on the Stability of a Given State of Motion: Particularly Steady Motion, Macmillan and Co., London, 1877.
[54] A. Hurwitz, "Über die Bedingungen, unter welche neine Gleichungnur Wurzelnmit negative reellen Theilenbesitzt" (On the conditions under which an equation has only roots with negative real parts), Math. Ann. 46 (1895) 273–284.
[55] N. Alujević, I. Tomac, P. Gardonio, Tuneable vibration absorber using acceleration and displacement feedback, J. Sound Vib. 331 (2012), 2731–2728.

Paper 2, https://doi.org/10.1007/s00419-018-1447-x

CrossMark

ORIGINAL

D. Čakmak · H. Wolf · Ž. Božić · M. Jokić

Optimization of an inerter-based vibration isolation system and helical spring fatigue life assessment

Abstract This paper presents an analytical analysis and optimization of vibration-induced fatigue in a generalized, linear two-degree-of-freedom inerter-based vibration isolation system. The system consists of a source body and a receiving body, coupled through an isolator. The isolator consists of a spring, a damper, and an inerter. A broadband frequency force excitation of the source body is assumed throughout the investigation. Optimized system, in which the kinetic energy of the receiving body is minimized, is compared with suboptimal systems by contrasting the fatigue life of a receiving body helical spring with several alternative isolator setup cases. The optimization is based on minimizing specific kinetic energy, but it also increases the number of cycles to fatigue failure of the considered helical spring. A significant portion of this improvement is due to the inclusion of an optimally tuned inerter in the isolator. Various helical spring deflection and stress correction factors from referent literature are discussed. Most convenient spring stress and deflection correction factors are adopted and employed in conjunction with pure shear governed proportional stress in the context of high-cycle fatigue.

1 Introduction

Mechanical systems, e.g. car suspension systems [1,2] are often subjected to high dynamic loading during their lifetime. Such service loadings can cause unwanted vibration and premature failure, resulting from destructive fatigue mechanisms [3]. These are especially evident in case of resonant harmonic excitations [1,3]. Heavy-duty springs used in car suspension systems [1,2] are an example where a crack may initiate at a stress concentration location and further propagate, potentially leading to a catastrophic failure [3–5]. Considering vibration fatigue modelling and analysis of helical springs, both stiffness and strength parameters of general vibration system should be determined for adequate mathematical modelling, which can be found in [6–18]. Classical works on strength of materials [19,20], elasticity theory [21] and recent mechanical engineering literature [22,23] touch on the subject of spring durability and spring fatigue. Considering springs as machine elements that need to withstand exceptionally long life, appropriate high-cycle fatigue (HCF) calculation method [23–28] is usually utilized for fatigue lifetime assessment. Extensive studies on the spring fatigue life, particularly for helical springs, have been conducted [28–34].

From related literature [6–11], it can be observed that various stress and deflection correction factors are used for spring strength analysis by different authors. Most often applied stress correction factors are those introduced by Wahl [6,7,10,11,14–17,19–23], Bergsträsser [10,11,14,17,22] and Göhner [7–9,14,17]. For

D. Čakmak (✉) · H. Wolf · Ž. Božić · M. Jokić
University of Zagreb, Faculty of Mechanical Engineering and Naval Architecture, I. Lučića 5, 10000 Zagreb, Croatia
E-mail: damjan.cakmak@fsb.hr
Tel.: +385 1 6168 426

example, German DIN standard on calculation and design of cylindrical helical springs was previously based on Göhner [8,9]; however, it is now based on the Bergsträsser and Wahl [10,11] correction factors. The stress correction factors may significantly influence predicted fatigue lifetime of helical springs. Wahl himself in his work [7] suggests that application of his own stress correction factor may result in over-conservative fatigue life prediction. However, e.g. SAE [15] and Ugural [23] recommend using Wahl's stress correction factor, especially for fatigue analysis. Shigley [22], for instance, recommends the Bergsträsser's correction factor for fatigue lifetime assessment, for engineering simplicity reasons; however, he does not advise against using Wahl.

Regarding helical spring fatigue, Berger and Kaiser [28,29] analysed results of very high-cycle fatigue (VHCF) tests on helical compression springs up to 10^9 cycles, where they observed that cracks tend to occur below the surface beyond 10^7 cycles, which is a practical upper limit for HCF. The authors also mentioned that Göhner and Bergsträsser correction factors could yield too conservative results in a fatigue life assessment, which is in agreement with Wahl [7]. Commonly, fatigue life assessment of mechanical springs is based on fatigue endurance to torsion shear [19–23]. Contrary to that, Del Llano-Vizcaya et al. [30] point out that during fatigue testing of compression springs with large index (coil radius to wire radius ratio), the dominant fatigue cracks are initiated and propagated by variation of the principal tensile stress, rather than by the maximum shear stress. Pyttel et al. [31] used Wahl stress correction factor and finite element method (FEM) for helical spring stress analysis. Rivera et al. [32] also used Wahl stress correction for spring for elevator doors analytical fatigue analysis. On the other hand, Ružička et al. [33] used Göhner [8,9,14] and Ancker & Goodier [12,14] stress correction factor for analytical spring fatigue study and compared it with FEM results. Kamal et al. [34] used FEM for both stress ($S - N$) and strain-life fatigue ($\varepsilon - N$) analysis of helical spring.

Contemporary literature dealing with vibration and dynamic problems tied to fatigue, e.g. [1,3–5] do not yet incorporate the beneficiary usage of inerter [2,35] in a classical mass-damper-spring (MDS) environment. In mechanical networks, inerter is a relatively novel element developed by Smith [2] which produces force proportional to relative acceleration ($a_2 - a_1$) between its terminals, i.e. relation $F_{inrt} = b(a_2 - a_1)$ holds. The coefficient of inerter resistance force F_{inrt} is called *inertance*. It is denoted by label "b" and is measured in kilograms. Ideal inerter can be approximated in the same sense in which mathematical ideals approximate, e.g. springs and viscous dampers. Ideally, it is assumed that its mass is small compared to produced inertance [2]. According to authors' knowledge, no attempt to include the ideal inerter concept in commercial FEM codes is recorded in the literature.

In the presented study, analytical investigation is conducted to model the fatigue load of a helical spring acting as an elastic element in a simple and physically transparent two-degree-of-freedom (2-DOF) inerter-based vibration isolation system. In Sect. 2, analytical mathematical 2-DOF inerter-based vibration isolation system model is established where optimized parameters for both viscous damper and inerter are determined. Minimization of kinetic energy is used as a criterion. In Sect. 3, different dimensionless spring deflection and stress correction factors available from referent literature are discussed, which are later used in the context of analytically determining displacement and stress amplitudes under harmonic force loading. Finally, Sect. 4 presents a benchmark example by utilizing previously adopted optimization model and employing adopted spring correction factors. Benchmark is performed by comparing vibration fatigue study of systems with optimized parameters to sub-par systems. Method for deriving the optimal damping and optimal inertance combined with optimal damping is developed and employed. Göhner-, Castigliano- and Timoshenko-based deflection correction factor is derived in dimensionless form. There is no record in the literature of employing Timoshenko thick beam formulation [19–21] and Cowper shear correction factor [36] for spring deflection correction, which is also investigated in the scope of this paper, where novel deflection correction factor is derived. Analytical expression based on the von Mises criterion [22,27,37] for shear governed biaxial and proportional stress, which explicitly ties vibration displacement amplitudes through Basquin's equation with HCF of helical spring, is derived and given in explicit form.

2 2-DOF inerter-based vibration isolator mathematical model

In this chapter, the generalized analytical mathematical model for discrete 2-DOF inerter-based vibration isolation system is established analytically. The studied problem is represented by a discrete parameter model as shown in Fig. 1a. It is assumed that the critical component concerning fatigue is a helical spring k_3, also shown in Fig. 1b where E is (Young) modulus of elasticity, v is Poisson's factor/ratio, S'_f is fatigue strength coefficient, and "B" is Basquin's exponent, i.e. fatigue strength exponent [24,25] here denoted in capital letter in order not to be confused with inertance "b". Number of active coils is denoted as n ($n = 2$ in Fig. 1b),
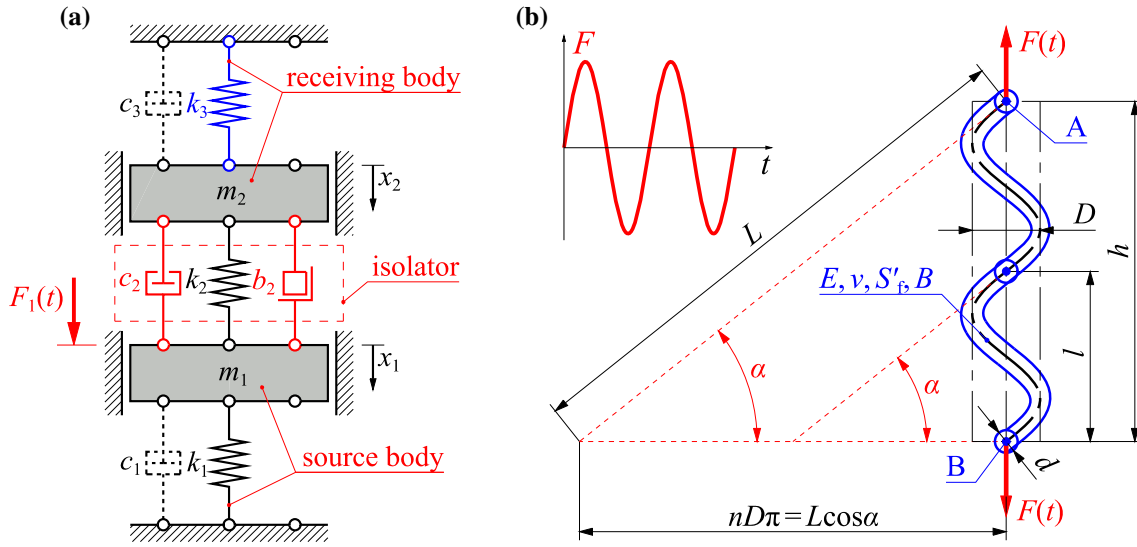
Fig. 1 **a** The 2-DOF linear discrete vibration isolation system, **b** helical spring k_3 properties (colour figure online)

and h is spring length where $h = n \cdot l$. Diameters D and d are large and small spring diameters, respectively, and $C = D/d$ is defined as spring index [7,22,23]. D can also be designated as the mean coil diameter and d as the wire diameter [22]. Recommended values of spring index C for practical purposes lie between $C = 4 - 12$ [22]. Angle α represents the pitch angle which can be calculated according to geometric expression $\alpha = \arctan[l/(\pi D)]$, where l is the spring pitch. For the time being, the spring stress is not considered and spring stiffness is denoted simply as "k_3".

The goal of the vibration-based optimization is to minimize vibrations of the *receiving body*, i.e. vibrations of mass m_2 which are *proportional* to the maximum deflection amplitudes of spring k_3. In this optimization, the excitation of the *source body* $F_1(t)$ is assumed to have white noise spectral properties [38], i.e. unit loading amplitude $F_{01}(\Omega) = 1$ over all frequencies. The whole vibration system consists of discrete masses m_1 and m_2, ideally massless springs k_1, k_2 and k_3, viscous dampers c_1, c_2 and c_3 and an ideal inerter of inertance b_2. Isolator consists of spring k_2, damper c_2 and inerter b_2. The ideal inerter produces a force F_{inrt} proportional to the relative acceleration [2] between masses m_1 and m_2. Presented discrete parameter approximation may represent a system of a much more complex nature, including structures with distributed mass, stiffness and damping, as discussed in, for example, [39–41].

The equations of motion [1] for system in Fig. 1a can be written in the general matrix form as

$$\mathbf{M}\ddot{\mathbf{x}}(t) + \mathbf{C}\dot{\mathbf{x}}(t) + \mathbf{K}\mathbf{x}(t) = \mathbf{F}(t),\tag{1}$$

where $\mathbf{M}$ is the global mass matrix, $\mathbf{C}$ is the global damping matrix, $\mathbf{K}$ is the global stiffness matrix and $\mathbf{F}(t)$ is the excitation column force vector. Displacement of the masses m_1 and m_2 from their static equilibrium positions, velocity and acceleration vectors are denoted by $\mathbf{x}(t)$, $\dot{\mathbf{x}}(t)$ and $\ddot{\mathbf{x}}(t)$, respectively.

Global matrices and vectors from Eq. (1) can be written as

$$\mathbf{M} = \begin{bmatrix} m_1 + b_2 & -b_2 \\ -b_2 & m_2 + b_2 \end{bmatrix}, \quad \mathbf{C} = \begin{bmatrix} c_1 + c_2 & -c_2 \\ -c_2 & c_2 + c_3 \end{bmatrix}, \quad \mathbf{K} = \begin{bmatrix} k_1 + k_2 & -k_2 \\ -k_2 & k_2 + k_3 \end{bmatrix},\tag{2a, b, c}$$

$$\mathbf{x} = \begin{bmatrix} x_1(t) \\ x_2(t) \end{bmatrix}, \quad \mathbf{F} = \begin{bmatrix} F_1(t) \\ 0 \end{bmatrix},\tag{3a, b}$$

where the parameters and functions in the matrices and vectors are denoted in Fig. 1a.

As the damping of the source and receiving bodies is assumed to be fairly light, the effects of the source mass m_1 and the receiving mass m_2 dampers are further neglected, i.e. $c_1 \approx c_3 \approx 0$.

By assuming harmonic excitation and expressing the excitation and the steady-state response in the complex form $\mathbf{F}(t) = \mathbf{F}_0 e^{i\Omega t}$ and $\mathbf{x}(t) = \mathbf{x}_0 e^{i\Omega t}$, where $i = \sqrt{-1}$, the solution of Eq. (1) can be written as

$$\mathbf{x}_0(\Omega) = \left[-\Omega^2 \mathbf{M} + i\Omega \mathbf{C} + \mathbf{K}\right]^{-1} \mathbf{F},\tag{4}$$

where terms inside the square bracket denote dynamic stiffness matrix and $\mathbf{x}_0(\Omega)$ is the complex displacement amplitude. Differentiating Eq. (4) with respect to time t yields with complex velocity amplitude expression

$$\dot{\mathbf{x}}_0(\Omega) = \mathrm{i}\Omega\mathbf{x}_0(\Omega). \tag{5}$$

By considering $\mathbf{M}$, $\mathbf{C}$ and $\mathbf{K}$ matrices from Eq. (2a, b, c), the steady state, i.e. time-invariant complex response of mass m_2 can be expressed in simplified form as the following frequency response function (FRF)

$$\dot{x}_{02}(\Omega) = \frac{B_0 + (\mathrm{i}\Omega)\,B_1 + (\mathrm{i}\Omega)^2\,B_2 + (\mathrm{i}\Omega)^3\,B_3}{A_0 + (\mathrm{i}\Omega)\,A_1 + (\mathrm{i}\Omega)^2\,A_2 + (\mathrm{i}\Omega)^3\,A_3 + (\mathrm{i}\Omega)^4\,A_4}. \tag{6}$$

where coefficients $A_0 - A_4$ and $B_0 - B_3$ with respect to Eq. (6) are given by

$$\begin{aligned}
&A_0 = (k_2 + k_3)\,k_1 + k_2 k_3 &\quad& B_0 = 0 \\
&A_1 = c_2\,(k_1 + k_3) &\quad& B_1 = k_2 \\
&A_2 = (m_2 + b_2)\,k_1 + (m_1 + m_2)\,k_2 + (m_1 + b_2)\,k_3 &\quad& B_2 = c_2 \; . \\
&A_3 = c_2\,(m_1 + m_2) &\quad& B_3 = b_2 \\
&A_4 = (m_2 + b_2)\,m_1 + b_2 m_2
\end{aligned} \tag{7a–i}$$

The transfer mobility, i.e. FRF $\dot{x}_{02} \equiv v_{02}$, from Eq. (6) represents the complex velocity amplitude of the receiving body per unit forcing $F_{01} = 1$, of the source body. FRF from Eq. (6) is further used to assess the effectiveness of the vibration isolation.

Considering that the excitation force F_1 with unit power spectral density (PSD) is assumed, the specific kinetic energy of the receiving body I_k (per unit mass and per unit excitation force) can be calculated as

$$I_k = \int_{-\infty}^{\infty} \left| \frac{v_{02}(\Omega)}{F_{01}} \right|^2 \mathrm{d}\Omega, \tag{8}$$

according to [42]. The specific kinetic energy index I_k from Eq. (8) is used throughout this study as a quantitative measure of the broadband frequency vibration isolation performance. The objective is to minimize this quantity for all vibration isolation systems analysed in the scope of this paper. Vibration-based isolation optimization with the goal of vibration reduction by using the minimization of kinetic energy can be found in [38]. The specific kinetic energy index in Eq. (8) for I_k can according to [42] analytically be calculated with expression

$$I_k = \pi \frac{A_0 B_3^2 (A_0 A_3 - A_1 A_2) + A_0 A_1 A_4 \left(2 B_1 B_3 - B_2^2\right) - A_0 A_3 A_4 \left(B_1^2 - 2 B_0 B_2\right) + A_4 B_0^2 (A_1 A_4 - A_2 A_3)}{A_0 A_4 \left(A_0 A_3^2 + A_1^2 A_4 - A_1 A_2 A_3\right)}, \tag{9}$$

where substituting coefficients $A_0 - A_4$ and $B_0 - B_3$ from Eq. (7a–i) into Eq. (9) yields with final kinetic energy index I_k analytical expression, which is here omitted because of length.

In the next two subchapters of this study, two types of vibration transmission control are analysed with respect to potential opportunity of minimizing the specific kinetic energy index I_k: isolation control without inerter, i.e. $b_2 = 0$, and isolation control with optimized inertance b_{opt}. Optimized damping and inertance isolator parameters, for inerter excluded where $c_2 = c_{\mathrm{opt}}$, and inerter included where $c_2 = c_{\mathrm{opt2}}$ and $b_2 = b_{\mathrm{opt}}$, are obtained by minimizing the frequency averaged kinetic energy of the receiving body denoted symbolically in Eq. (9).

2.1 Isolation optimization without inerter

By setting the inertance $b_2 = 0$, and considering Eq. (7a–i), Eq. (9) now morphs into simpler form

$$I_k\,(b_2 = 0) = \pi \frac{k_2^2\,(m_1 + m_2) + c_2^2\,(k_1 + k_3)}{c_2\,(m_2 k_1 - m_1 k_3)^2}. \tag{10}$$

Differentiating Eq. (10) with respect to viscous damping coefficient c_2, equalling with zero and again solving for damping c_2 yields the single physically valid solution

$$c_{\mathrm{opt}} = k_2 \sqrt{\frac{m_1 + m_2}{k_1 + k_3}}, \tag{11}$$

which unambiguously represents the optimum damping coefficient $c_2 = c_{opt}$. Inserting Eq. (11) into Eq. (10) yields the value of optimum, i.e. minimum kinetic energy

$$I_{k\text{opt}} = 2\pi k_2 \frac{\sqrt{(m_1 + m_2)(k_1 + k_3)}}{(m_2 k_1 - m_1 k_3)^2}.$$

(12)

By inspecting Eq. (12) mathematical structure, two main conclusions can be drawn.

Firstly, optimum kinetic energy $I_{k\text{opt}}$ is directly proportional to value of isolator spring stiffness k_2, which strongly implies using soft/compliant spring for better isolation effect. Trivial solution is to incorporate zero stiffness spring k_2 which completely decouples the source and receiving bodies. In practical situations, static or stationary deflections impose true physical limits to spring compliance, therefore spring stiffness k_2 cannot be optimized arbitrarily and is further considered as fixed value.

Secondly, when values $m_2 k_1 \approx m_1 k_3$, denominator of Eq. (12) tends to zero and $I_{k\text{opt}}$ value tends to infinity; therefore, such vibration system should be accordingly detuned during design, i.e. $m_2 k_1 \neq m_1 k_3$.

2.2 Isolation optimization with inerter

When $b_2 \neq 0$, differentiating Eq. (9) with respect to damping c_2, equalling with zero and again solving for damping c_2 yields the single physically valid solution

$$c_2 (b_2 \neq 0) = \sqrt{\frac{m_1 + m_2}{k_1 + k_3} k_2^2 - 2b_2 k_2 + \frac{m_1 k_3^2 + m_2 k_1^2 + b_2 (k_1 + k_3)^2}{(k_1 + k_3)[m_1 (b_2 + m_2) + b_2 m_2]} b_2^2},$$

(13)

where c_2 now represents optimum damping $c_{opt}(b_2)$ for any given inertance b_2. For inertance $b_2 = 0$, Eq. (13) morphs into simple Eq. (11). By substituting Eq. (13) into Eq. (9), differentiating with respect to b_2, equalling with zero and solving for b_2, optimum inertance parameter b_{opt} is obtained. Inserting $b_2 = b_{opt}$ into Eq. (13) results with optimum damping c_{opt2}, which subsequently yields an expression for a minimum specific kinetic energy $I_{k\text{opt}2}$ from Eq. (9). Analytical expressions for b_{opt}, c_{opt2} and $I_{k\text{opt}2}$ are not explicitly shown in the scope of this paper because they are rather cumbersome and very lengthy. However, it is important to note that no numerical approximation is used in the process of optimization, thus all derived expressions are purely algebraic and exact, without any loss in accuracy.

3 Helical spring displacement and stress correction factors

In this chapter, spring stiffness and stress are discussed. A simple expression for determining the spring fatigue life is also derived, where HCF life [22–26] above 10^3 cycles is addressed and employed. Obtained displacement amplitudes in the frequency domain from previous chapter, i.e. Eq. (4), can now be tied to stress amplitudes below the yielding strength σ_Y, necessary for performing vibration fatigue analysis.

Cylindrical spring can for simplicity be viewed as a thin/slender, curved rod/beam subjected to torsion load exclusively. In such case [22], analytical expressions for spring stiffness, static displacement and shear stress can be denoted with

$$k_{\text{nom}} = \frac{F_0}{\delta_{\text{nom}}} = \frac{Gd^4}{8D^3 n} = \frac{Gd}{8C^3 n} \quad \Rightarrow \quad \delta_{\text{nom}} = \frac{8F_0 D^3 n}{Gd^4} = \frac{8F_0 C^3 n}{Gd}, \quad \tau_{\text{nom}} = \frac{8F_0 D}{\pi d^3} = \frac{8F_0 C}{\pi d^2},$$

(14a, b, c)

where k_{nom} is nominal spring stiffness, δ_{nom} is nominal spring deflection, τ_{nom} is nominal spring shear stress and $G = E/[2(1 + \nu)]$ is the shear modulus. As linear elastic/small deformation and deflection conditions are assumed, Eq. (14a, b, c) is valid for both tensile and compressive applied force amplitude $\pm F_0$. For simple harmonic loading conditions adopted, $F(t) = F_0 e^{i\Omega t}$. Helical spring geometry, parameters, loading and boundary conditions (BCs) are the same as schematically shown in Fig. 1b. For a more general approach in the scope of this paper, boundaries of spring index C are varied both inside and outside of recommended values $C = 4 - 12$, in order to parametrically test all physically obtainable solutions. As already noted, Eq. (14a, b, c) is obtained by simply considering spring as a thin beam/rod loaded with exclusively torsion shear, where direct shear, curvature and pitch angle effects are ignored and neglected for simplicity. Therefore,
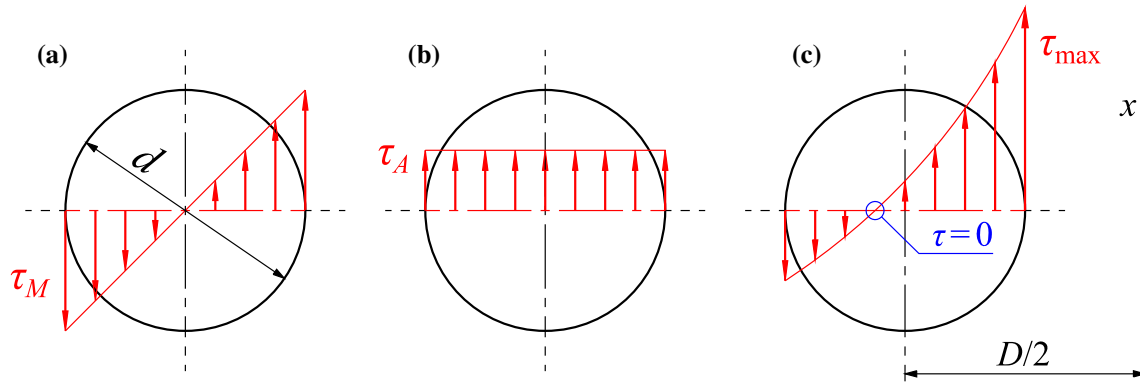
Fig. 2 Spring shear stresses: **a** torsion shear τ_M, **b** transverse/direct shear τ_A, **c** combined torsion and direct shear with additional curvature "c" and pitch angle α effects $\tau_{\max} = \tau_M + \tau_A + \tau_c + \tau_\alpha$ (colour figure online)

Table 1 Expressions for stress correction factors K_τ and deflection correction factors K_δ

Author/standard	Stress correction factor K_τ	Deflection correction factor K_δ
Strength of materials		
Wahl, DIN 13906	$\frac{4C-1}{4C-4} + \frac{k_W}{C} = \frac{4C-1}{4C-4} + \frac{1+2\nu}{2(1+\nu)C}$	–
Röver	$\cos(\alpha)\left[\frac{C}{C-\cos^2(\alpha)} + \frac{1+\sin^2(\alpha)}{4C}\right]$	–
Wood	$\frac{C}{C-1} + \frac{1}{2C}$	$\frac{2C^2+C-1}{2C^2}$
Honegger	$\cos(\alpha)\left[\frac{C}{C-\cos^2(\alpha)} + \frac{0.615}{C}\right]$	$\frac{2C^2-\cos^4(\alpha)}{2C^2\cos^5(\alpha)}$
Elasticity theory		
Göhner, DIN 2089	$1 + \frac{5}{4C} + \frac{7}{8C^2} + \frac{1}{C^3}$	$\cos(\alpha) + \frac{3\cos^5(\alpha)}{16(C^2-1)} + \frac{\sin(\alpha)\tan(\alpha)}{1+\nu}$
Ancker & Goodier	$1 + \frac{5}{4C} + \frac{7}{8C^2} + \frac{1}{2}\tan^2(\alpha)$	$1 - \frac{3}{16C^2} + \frac{3+\nu}{2(1+\nu)}\tan^2(\alpha)$
Approximate/empirical relation		
Bergsträsser, DIN 13906	$\frac{C+0.5+\sin^2(\alpha)}{C-0.75+1.51\sin^2(\alpha)}$	–
Sopwith, BS 1726	$\frac{C+0.2}{C-1}$	–
Strain energy (Castigliano's) method		
Shigley	–	$1 + \frac{1}{2C^2}$
Dym	–	$\left(1 + \frac{1}{2C^2}\right)\cos(\alpha) + \left(1 + \frac{1}{4C^2}\right)\frac{\tan(\alpha)\sin(\alpha)}{(1+\nu)}$

additional correction factors K_δ and K_τ need to be applied for displacement and shear stress, where relations $\delta_{\max} = K_\delta \delta_{\text{nom}}$ and $\tau_{\max} = K_\tau \tau_{\text{nom}}$ now hold [22,23]. Figure 2 schematically shows spring cumulative shear stress τ correction.

Shift of the helical spring neutral line towards outside of wire diameter d centre results with maximum shear stress $\tau_{\max}$ appearing at the point closest to spring axis x, as shown in Fig. 2c. As already pointed out in introduction, multiple expressions for correcting deflection and stress exist in the referent literature where authors sometimes present notably different correction factors depending on the theory they used for derivation [15]. Therefore, no unified solution can be found in the literature [14] or standards [8–11].

Table 1 sums up all the expressions from the referent literature used in the scope of this paper.

It is appropriate to recognize that important and thorough investigation regarding spring stress and deflection correction determination was conducted by the *Research Committee on the Analysis of Helical Spring* [14]

where authors parametrically compared influence of spring parameters on stress results based on the theory used. They used FEM for numerical part of the investigation. They obtained the best correlation for Bergsträsser and Göhner stress correction factors and found Wahl to be overly conservative; however, they neglected the influence of pitch angle α on stress correction where $\alpha = 0$ in their main FEM test model for stresses (see Table 5 and Fig. 20 in [14]).

Some data in Table 1 (most notably Wahl, Röver, Wood, Honegger, Göhner, Ancker & Goodier, Bergsträsser and Sopwith) are adopted from already mentioned *Research Committee* [14]. Wahl stress correction factor can also be found in current DIN 13906 (germ. *Deutsches Institut für Normung*) standard [10,11], and [6,7] among others. DIN 13906 [10,11], and [22] also include Bergsträsser stress correction factor, however without pitch angle α inclusion. Göhner stress correction factor, previously included in older, now defunct DIN 2089 [8,9] was later adopted by Ancker & Goodier [12] and rearranged in order to contain initial pitch angle α. By comparing it to original Göhner stress correction expression, it can be observed that the first three terms are identical; however, Göhner uses $1/C^3$, and Ancker & Goodier use $1/2 \cdot \tan^2(\alpha)$ as a last term instead, which takes into account the initial pitch angle α. Ancker & Goodier deflection correction factor from Table 1 can also be found in their original paper [12] and is considered to be one of the most accurate ones found in the literature [16]. Sopwith stress correction factor was used as a part of BS 1726 (British Standard) [16]. Both Shigley [22] and Dym [13] give similar solutions for deflection correction, based on strain energy (Castigliano) method, where Shigley solution is simpler; however, it neglects the influence of pitch angle α compared to Dym.

An additional comment is presented for Wahl stress correction factor, as shown in the first row of Table 1. Nominal expression for Wahl stress factor found in most literature, e.g. [6,7,16] is

$$K_{\tau,\text{Wahl}} = \frac{4C - 1}{4C - 4} + \frac{0.615}{C}. \tag{15}$$

Wahl in his textbook [7] cited Timoshenko [21] as an influence and main source for determining his often cited stress correction factor. It is interesting to observe the numerator of second term from Eq. (15), which is for the sake of this discussion temporarily denoted as $k_{\text{W}} = 0.615$. Wahl used Timoshenko solution which comes from setting a Poisson's ratio $\nu = 0.3$ in the equation derived for the shear stress at the horizontal edge of a cantilevered circular bar [21]. Using the dimensionless, Poisson's ratio ν dependent term found in Eq. (h), p. 321 from [21], one can write expression

$$K_{\tau,\text{Wahl}} = \frac{4C - 1}{4C - 4} + \frac{k_{\text{W}}}{C} \quad \Rightarrow \quad k_{\text{W}} = \frac{1 + 2\nu}{2(1 + \nu)}, \tag{16a,b}$$

and by setting the different values for Poisson's factor ν in Eq. (16b), values of k_{W} are obtained as

$$k_{\text{W}}(\nu = 0) = 0.5, \quad k_{\text{W}}(\nu = 0.3) = \frac{8}{13} \cong 0.615384615 \approx 0.615, \quad k_{\text{W}}(\nu = 0.5) = 0.\dot{6}, \tag{17a,b,c}$$

where it can be observed that if ν rises, k_{W} also rises, resulting in larger stress correction factor $K_{\tau,\text{Wahl}}$. By using fixed $k_{\text{W}} = 0.615$, one hard-codes universal, Poisson's ratio-independent stress correction solution. As stresses in helical spring are mostly shear governed [22,23], by adopting the von Mises energy criterion [19–22] with relation $\sigma_{\text{eqv(HMH),max}} = \sqrt{3}\tau_{\text{max}}$, stress correction factor K_{τ} can also be written as K_{σ}.

Two additional deflection correction factors are derived and presented as detailed below.

The first novel Timoshenko & Cowper deflection correction factor can be obtained as follows. Taking into the consideration nominal spring deflection from Eq. (14b) and introducing the additional deflection due to shear correction [19–21,36], maximum spring deflection can now be written as

$$\delta_{\text{Timoshenko}} = \delta_{\text{nom}} + \delta_k = \frac{8F_0 D^3 n}{G d^4} + \frac{F_0 L}{k A G}, \tag{18}$$

where k is the *shear correction factor* [19–21,36], L is the total length of the spring and A is spring cross-sectional area. By neglecting the pitch angle α, length L and cross-sectional area A are given by the following equations:

$$L(\alpha \approx 0) = nD\pi, \quad A = \frac{d^2 \pi}{4}. \tag{19a,b}$$

Improved shear correction factor k is adopted from Cowper [36] and can be expressed as

$$k = k_{\text{Cowper}} = \frac{6(1+\nu)}{7+6\nu}, \tag{20}$$

where it can be seen that shear correction k is solely Poisson's factor ν dependent, i.e. $k = k(\nu)$. Finally, after inserting Eqs. (20) and (19a,b) into Eq. (18) and dividing it with nominal deflection δ_{nom} from Eq. (14b), Timoshenko & Cowper (T/C) deflection correction, after considering $C = D/d$ and simplifying, is

$$K_{\delta,\text{T/C}} = \frac{\delta_{\text{Timoshenko}}}{\delta_{\text{nom}}} = 1 + \frac{7+6\nu}{12C^2(1+\nu)}, \tag{21}$$

where, as already noted, pitch angle α is for simplicity neglected in derivation.

The second explicit dimensionless deflection correction factor can also be derived by using Castigliano's energy theorem, as noted by Timoshenko [20]. Timoshenko's (Castigliano's) deflection expression is

$$\delta_{\text{Castigliano/Timoshenko}} = F_0 R^2 L \left[\frac{\sin^2(\alpha)}{EI} + \frac{\cos^2(\alpha)}{GI_p}\beta \right], \tag{22}$$

where $R = D/2$ is the mean spring radius, and I and I_p are spring axial and polar inertia moments, respectively,

$$I = \frac{d^4\pi}{64}, \quad I_p = 2I = \frac{d^4\pi}{32}. \tag{23a,b}$$

Interestingly, β from Eq. (22) is an additional deflection correction factor/parameter, for which Timoshenko cites Göhner. In case C is sufficiently small, factor β should be included and can be written as

$$\beta = 1 + 3\left(\frac{1}{C}\right)^2 \left\{ 16 \left[1 - \left(\frac{1}{C}\right)^2 \right] \right\}^{-1}, \tag{24}$$

where Timoshenko states that "torsional rigidity GI_p must be multiplied by the correction factor" [20] from Eq. (24). As initial pitch angle α is now fully taken into account in Eq. (22), total spring length L, with regard to Eq. (19a), can be calculated according to a more punctual and consistent general helix length expression

$$L(\alpha \neq 0) = \frac{nD\pi}{\cos(\alpha)}. \tag{25}$$

By using Eqs. (25), (24) and (23a,b), inserting them in Eq. (22), and dividing Eq. (22) with nominal deflection δ_{nom} from Eq. (14b), some mathematical simplifying results with Castigliano/Timoshenko (C/T) are as follows:

$$K_{\delta,\text{C/T}} = \frac{\delta_{\text{Castigliano/Timoshenko}}}{\delta_{\text{nom}}} = \frac{(16C^2 - 13)(1+\nu)\cos(\alpha) + 16(C^2 - 1)\sin(\alpha)\tan(\alpha)}{16(C^2 - 1)(1+\nu)}. \tag{26}$$

By inserting $\beta = 1$ in Eq. (22), Eq. (26) morphs into purely Castigliano governed expression

$$K_{\delta,\text{Cstg}} = \frac{(1+\nu)\cos(\alpha) + \sin(\alpha)\tan(\alpha)}{1+\nu}, \tag{27}$$

where spring index C influence is not taken into account; however, pitch angle α is considered. It can be shown that derived deflection correction from Eq. (26) and Göhner expression for deflection correction factor from Table 1 give almost identical results, as further shown in Fig. 3a, i.e. $K_{\delta,\text{C/T}} \approx K_{\delta,\text{Göhn}}$. It should be noted that as the pitch l is geometrically independent value of diameter d, pitch is for plotting purposes tied to wire diameter d through relation $l = 2 \cdot d$, as shown in Fig. 3 rectangular frame. Introduced expression $\alpha = \arctan[l/(\pi D)]$ is employed for calculating pitch angle α for arbitrary spring index C value. Values of $C = 2 - 25$ are considered for plotting. Conventional steel Poisson's ratio $\nu = 0.3$ is adopted for plotting correction factors. Wahl stress correction factor is for the purpose of plotting appropriately hard-coded with $k_W = 0.615$ value, according to Eq. (17b). All expressions from Table 1 are shown in Fig. 3, including newly derived Eqs. (21) and (26) in Fig. 3a.
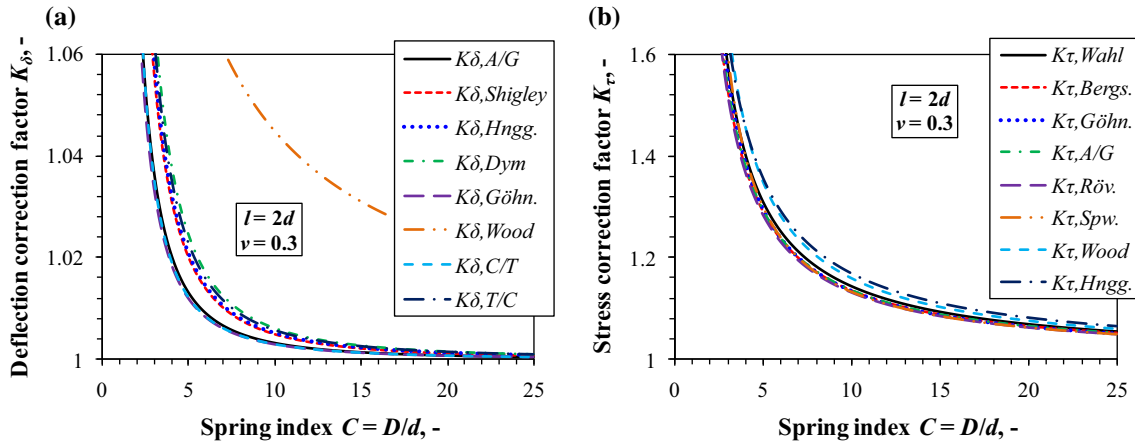
Fig. 3 Different correction factors for $\nu = 0.3$: **a** deflection correction K_δ, **b** stress correction K_τ (colour figure online)

It can be seen that all plot lines for both deflection and stress factors in Fig. 3 show good mutual correlation, except simple Wood deflection correction expression, which is thus disregarded and excluded from further analyses. It can also be noted that deflection correction factors K_δ contribution are almost one order of magnitude lower compared to stress correction factors K_τ. Neglecting Wood correction expression, Dym [13] presents the largest deflection correction factor. Derived Timoshenko & Cowper deflection correction factor $K_{\delta,\mathrm{T/C}}$ gives higher results compared to other deflection correction curves, however, still lower than Dym. Regarding stress correction, Wood and Honegger give the most conservative results for all values of spring index C.

Assumption that helical spring stress field is purely shear governed and therefore biaxial is employed in fatigue calculation. Adopted von Mises (HMH) $\sqrt{3}K_\tau\tau_{\mathrm{nom}}$ criterion with denoted stress correction factor K_τ is further used. Proportional fatigue stress state is assumed. Proportional stress/strain implies that ratio and/or line direction of principal stresses $\sigma_{1,2,3}$ does not change during fatigue load cycle [4,24], i.e. the orientation of the principal axes with respect to the loading axes remains fixed. For pure shear stress state, relations $\sigma_{1,3} = \pm\tau_{\mathrm{max}}$ and $\sigma_3/\sigma_1 = -1 = \mathrm{const.}$ are valid. By equalling the force amplitudes F_0 from Eq. (14a, b), and by using the defined deflection and stress correction factors, max von Mises equivalent stress amplitude is expressed as

$$\left|\sigma_{\mathrm{eqv(HMH), \, max}}\left(\delta_{\mathrm{max}}\right)\right| \equiv S_{\mathrm{a}} = \sqrt{3}\frac{K_\tau}{K_\delta}\frac{G}{C^2 n\pi d}\delta_{\mathrm{max}}, \tag{28}$$

where S_{a} denotes max fatigue stress amplitude as a function of max deflection amplitude δ_{max}. In order to tie fatigue nomenclature to vibrations, δ_{max} can be obtained from Eq. (4), i.e. relation $\delta_{\mathrm{max}} \equiv |x_{02}|$ holds. Classic HCF Basquin relation [24] for explicit number of cycles N_{f} can be written as

$$N_{\mathrm{f}} = \left(\frac{S_{\mathrm{a}}}{S_{\mathrm{f}}'}\right)^{\frac{1}{B}}, \tag{29}$$

By inserting Eq. (28) in Eq. (29) and using appropriate vibration terminology, i.e. obtained displacement amplitudes from Eq. (4), number of cycles to failure N_{f} can finally be explicitly written as

$$N_{\mathrm{f}} = \left[\sqrt{3}\frac{K_\tau}{K_\delta}\frac{G}{C^2 n\pi d}\frac{|x_{02}\left(\Omega\right)|}{S_{\mathrm{f}}'}\right]^{\frac{1}{B}}, \tag{30}$$

Advantage of employing simple Eq. (30) is that it is not necessary to explicitly know force amplitude F_0 acting on spring k_3, i.e. mass m_2; however, vibration displacement/deflection amplitudes should be determined before fatigue calculation. Also, it is necessary to know true deflection correction factor K_δ and stress correction factor K_τ, together with relevant fatigue parameters, i.e. fatigue strength coefficient S_{f}' and Basquin's exponent B. In addition, Shigley [22] recommends using factor k_c (*load modification factor*) and multiplying it with S_{f}' in Eq. (29), where $k_c = 0.59$ for torsion. Fatemi et al. [24] mention k_{L} (*empirical load factor*) where $k_{\mathrm{L}} = 0.58$ for torsion, while Bannantine et al. [26] introduce *loading effect* k_{T} which is the most conservative, and for

Table 2 Example 2-DOF vibration isolation system parameters

m_1, kg	m_2, kg	k_1, N/mm	k_2, N/mm	k_3, N/mm	F_0, kN
m_0	$2 \cdot m_0$	k_0	$k_0/10$	k_0	1

Table 3 Example helical spring of stiffness k_0 geometric and material properties

D, mm	d, mm	n, –	l, mm	E, MPa	ν, –	S_f', MPa	B, –
50	17	1	$2 \cdot d$	200,000	0.3	925	-0.1
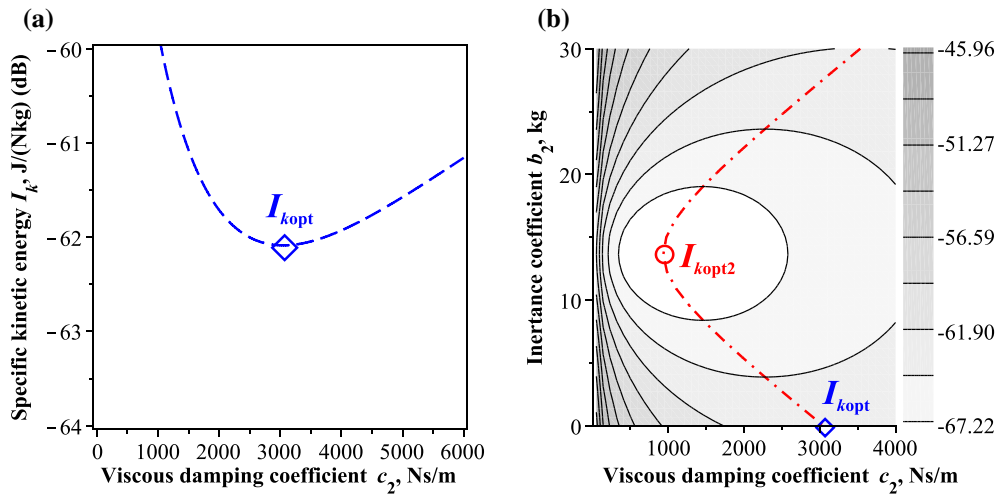
Fig. 4 Mass m_2 specific kinetic energy index I_k: **a** $c_2 = c_{\text{opt}}$ and $b_2 = 0$, **b** $c_2 = c_{\text{opt2}}$ and $b_2 = b_{\text{opt}}$ (colour figure online)

torsion $k_T = 0.577$. Bannantine explains all given values with energy effect theory, i.e. herein previously adopted *von Mises failure criterion* where $1/\sqrt{3} \approx 0.5774$.

In the next chapter, benchmark example is demonstrated for chosen deflection correction factor K_δ and stress correction factor K_τ. Based on information from the literature and this chapter, and by visually inspecting Fig. 3a, b for approximate median values, further adopted are *approximate* Ancker & Goodier deflection correction factor where $K_\delta = K_{\delta,\text{A/G}}$, and *approximate* Wahl stress correction factor where $K_\tau = K_{\tau,\text{Wahl}}$.

4 Example: inerter-based isolator helical spring vibration fatigue study

In this chapter, vibration fatigue analysis and optimization is performed on a general 2-DOF system, as shown in Fig. 1a. Table 2 shows example parameters used in this isolator optimization process. System is detuned, i.e. $m_2 k_1 \neq m_1 k_3$, and spring k_2 is notably compliant, compared to springs $k_{1,3}$.

General mass value is chosen as $m_0 = 100$ kg and spring stiffness k_0 is yet to be determined from helical spring parameters given in Table 3. Spring material parameters (E, ν, S_f' and B) are chosen in such way to represent physical elastic and fatigue properties of regular spring steel [24,25].

Diameters D and d are chosen so $C = D/d = 50/17 \approx 2.941$ which is a very small spring index. However, such small spring index C results with a relatively large stress correction factor which is a convenient fatigue benchmark. Ideal *massless* springs are considered for simplicity and straightforwardness. Spring stiffness is calculated according to relation $K_\delta F_0 = k_0 \delta_{\text{nom}}$. Figure 4 shows plotted numerical results of optimization process for given parameters from Tables 2 and 3. Minimum, i.e. optimum kinetic energy $I_{k\text{opt}}$ is determined for the cases without inerter (Fig. 4a—c_{opt}) which corresponds to $I_{k\text{opt}}$, and with inerter (Fig. 4b—c_{opt2} and b_{opt}) which corresponds to $I_{k\text{opt2}}$, by using the method described in Sects. 2.1 and 2.2. Diamond shape in the bottom of Fig. 4b corresponds to the case when $b_2 = 0$, i.e. Fig. 4a. Dash-dotted line in Fig. 4b which connects $I_{k\text{opt}}$ and $I_{k\text{opt2}}$ represents the implicit plot of function $c_{2(\text{opt})}(b_2 \neq 0)$, i.e. Eq. (13).

Obtained 2-DOF key values/factors and optimized parameters are further listed in Table 4.

Table 4 Example 2-DOF vibration isolation system referent values and optimized parameters

$C = D/d$, –	$K_{\delta,\text{A/G}}$, –	$K_{\tau,\text{Wahl}}$, –	k_0, N/mm	c_{opt}, Ns/m	b_{opt}, kg	c_{opt2}, Ns/m
2.941176471	1.037789623	1.595594406	6 190.746	3 047.31349	13.700475	934.329293
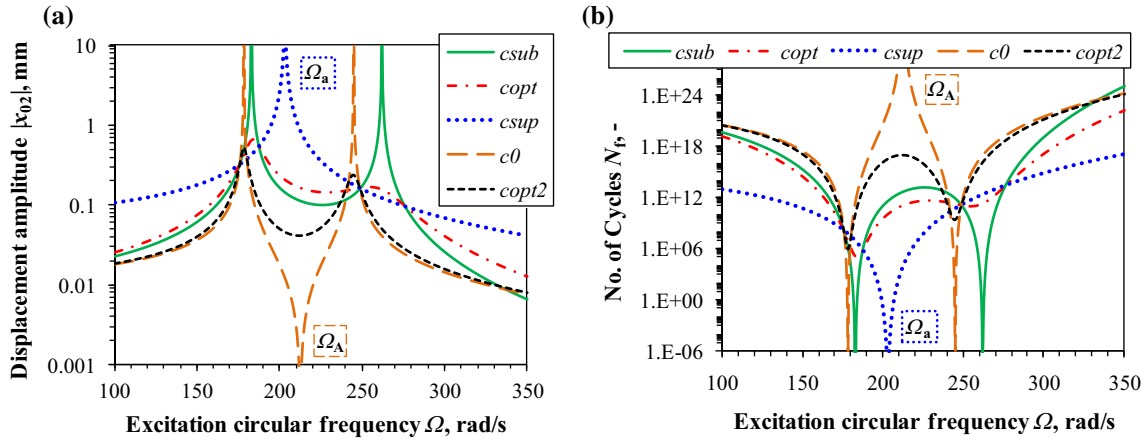
Fig. 5 The 2-DOF frequency response functions: **a** mass m_2 displacement amplitude $|x_{02}|$, **b** spring k_3 number of cycles to fatigue failure N_f (colour figure online)

Analytically obtained optimized parameters are used in the fatigue analysis of the spring k_3 which is considered next. Type of spring processing and manufacture, e.g. shot-peening described by SAE [15], Shigley [22], Ugural [23] and Fatemi [24], is not considered. Spring is for simplicity considered to be perfectly smooth and without any residual stresses. Also, spring fatigue notch sensitivity is presumed to be near unity, i.e. $K_{t(\tau)} \approx K_f$ which is a valid assumption according to Ugural [23]. Spring fatigue life N_f can now be calculated according to beforehand derived Eq. (30) where both displacement (A/G) and stress (Wahl) correction factors are taken into account. Analytical FRFs and vibration fatigue results for various cases are shown in Fig. 5.

By comparing FRFs, i.e. displacement amplitudes from Fig. 5a and number of cycles to fatigue from Fig. 5b, similitude of responses can be observed which arises from the fact that spring displacement is linearly proportional to stress, which is nonlinearly, i.e. exponentially proportional to number of cycles to failure, as shown in Eq. (30). Thus, observations for Fig. 5a are also valid for Fig. 5b. Sub-optimal and super-optimal damping are also considered for comparison where $c_{\text{sub}} = c_{\text{opt}}/100$ and $c_{\text{sup}} = 100 \cdot c_{\text{opt}}$. For additional reference, case with optimum inertance $b_2 = b_{\text{opt}}$ is also plotted for zero damping, i.e. $c_2 = c_0 = 0$. The improvement in the number of cycles to failure N_f is evident at most frequencies when using the optimum damping c_{opt} in comparison with low damping $c_{\text{sub}} = c_{\text{opt}}/100$, or high damping $c_{\text{sup}} = 100 \cdot c_{\text{opt}}$. Additionally, a significant further improvement in the fatigue life N_f is observed at most frequencies, in case where the optimum inerter b_{opt} is implemented in combination with the optimum damper c_{opt2}. Interesting anti-resonance phenomenon at frequency Ω_A is observed for the case with the optimum inerter b_{opt} and without damping ($c_2 = c_0 = 0$), which specifically demonstrates inerter b_2 influence that otherwise cannot be achieved on the receiving body by using only classic elements of MDS system [38]. Contrary to that, if using very large damping in the isolator, i.e. $c_{\text{sup}} = 100 \cdot c_{\text{opt}}$, new resonance Ω_a can be observed, as two masses m_1 and m_2 vibrate together in phase with equal displacements, velocities, and accelerations, acting as a quasi-rigid body. Same effect can be observed if a very large spring stiffness k_2 is used in the isolator, as isolator effectively locks and its proper functionality is consequently permanently compromised. Similar conclusion is already drawn based on $I_{k\text{opt}}$ structure of Eq. (12).

In summary, six characteristic circular frequencies denoted further in Fig. 6 are observed. These are: two circular natural frequencies for the case without inerter ($b_2 = 0$), i.e. ω_{n1b0} and ω_{n2b0} in Fig. 6a, two circular natural frequencies for the case with inerter ($b_2 = b_{\text{opt}}$), i.e. $\omega_{n1b\text{opt}}$ and $\omega_{n2b\text{opt}}$ in Fig. 6b, anti-resonant circular frequency $\Omega_A(b_2 = b_{\text{opt}})$ in Fig. 6b and isolator-locking resonant circular frequency $\Omega_a(c_2, k_2 \to \infty)$ in Fig. 6a. Circular natural frequencies can be obtained by solving the eigenvalue problem for the given 2-DOF as

$$\left[\mathbf{K} - (\omega_{n1,2})^2 \mathbf{M} \right] \mathbf{x}(t) = 0 \tag{31}$$
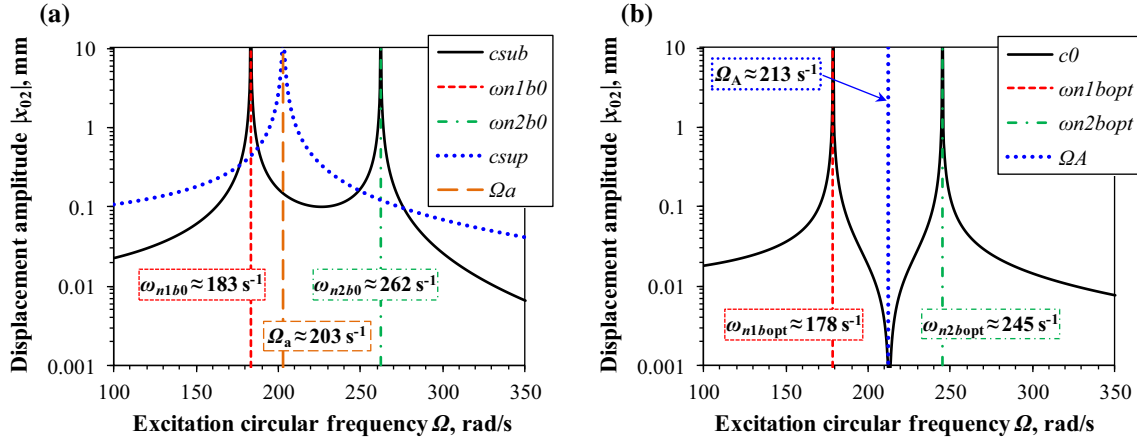
Fig. 6 Characteristic circular frequencies and accompanying FRFs: **a** $c_2 = c_{sub}$ and $c_2 = c_{sup}$, $b_2 = 0$, **b** $c_2 = 0$, $b_2 = b_{opt}$ (colour figure online)

Table 5 Characteristic circular frequencies: **a** without inerter ($b_2 = 0$), **b** with optimum inertance ($b_2 = b_{opt}$)

	ω_{n1b0}, rad/s	ω_{n2b0}, rad/s	Ω_a, rad/s		ω_{n1bopt}, rad/s	ω_{n2bopt}, rad/s	Ω_A, rad/s
(a)	183.017	262.015	203.154	**(b)**	178.373	244.852	212.571

Table 6 The 2-DOF isolator vibration fatigue optimization results

Isolator type	Ω, rad/s	$\lvert x_{02}(\Omega)\rvert$, mm	$N_f(\Omega)$, –
Sub-optimal damping ($c_2 = c_{opt}/100$, $b_2 = 0$)	ω_{n1b0}	47.583	$<< 1$
Super-optimal damping ($c_2 = 100 \cdot c_{opt}$, $b_2 = 0$)	Ω_a	14.539	< 1
Optimal damping ($c_2 = c_{opt}$, $b_2 = 0$)	ω_{n1b0}	0.640	134,539
Optimal damping and inertance ($c_2 = c_{opt2}$, $b_2 = b_{opt}$)	ω_{n1bopt}	0.524	1,002,948

where **M** and **K** matrices are denoted in Eq. (2a,c). Inserting data from Table 2 into Eq. (31) yields with

$$\left(\omega_{n1,2}\right)^2 = \frac{\frac{33}{10}m_0 k_0 + 2b_2 k_0 \mp \sqrt{\frac{129}{100}m_0^2 k_0^2 - \frac{6}{5}b_2 m_0 k_0^2 + 4k_0^2 b_2^2}}{2\left(2m_0^2 + 3m_0 b_2\right)}, \tag{32}$$

where inertance b_2 can be arbitrarily defined, or set to zero nevertheless. Following expressions

$$\Omega_A = \sqrt{\frac{k_2}{b_2}}, \quad \lim_{c_2, k_2 \to \infty} \Omega_a = \sqrt{\frac{k_1 + k_3}{m_1 + m_2}}, \tag{33a,b}$$

denote anti-resonance Ω_A and locking resonant circular frequency Ω_a, respectively. Table 5 shows Eqs. (32) and (33a,b) algebraic solutions by inserting data from Table 4 for the cases without, and with inerter where $b_2 = b_{opt}$.

Figure 6 presents characteristic frequencies data from Table 5 combined with belonging FRFs.

For small damping values, i.e. $c_2 \approx 0$, system response in wide frequency range is governed purely by natural frequencies vicinity where very large vibration amplitudes occur. For very large values of either damping c_2 and/or spring stiffness k_2, isolator effectively locks even with the inerter present, i.e. for c_2, $k_2 \to \infty$, $\Omega_a(b_2 = 0) = \Omega_a(b_2 = b_{opt})$. This is unfavourable setup and should be avoided, because if excited, locking frequency Ω_a vibration amplitudes tend to infinity, as demonstrated in Figs. 5a, b and 6a (c_{sup} curves, dotted line). In order to evaluate the quality of performed vibration isolation optimization, Table 6 is presented. Four characteristic system results are denoted where the most destructive excitation frequency Ω is solely considered.

For systems with sub- and super-optimal damping, violent spring rupture occurs for given loading immediately, without even considering fatigue failure. Optimized damping c_{opt} shifts the life of observed spring in

HCF range with over 10^5 expected life cycles. Finally, simultaneous optimization of damping and inertance shifts the expected life cycles over the 10^6 range, which can be considered as a significant improvement.

The present optimization is based on a vibration-related specific kinetic energy criterion. A future work could consider a type of optimization which would aim at directly maximizing fatigue life of the spring and compare it to the present results. Considering that pitch angle in the present study is defined through relation $l = 2 \cdot d$ and $\alpha = \arctan[l/(\pi D)]$, it would be beneficiary to further investigate the influence of arbitrary large pitch angle α on deflection and stress correction, as some of the expressions from Table 1 consider the pitch angle influence, and some do not. That most notably applies to further evaluation of Wahl's approximate stress correction factor in detail. Continuation of this work could also be the investigation of mean stress σ_m influence on the spring fatigue life optimization, as present calculations were performed for a simple harmonic fully reversed loading $R = -1$ where dead weight static load, or general pre-stress were not considered. In addition to a demonstrated analytical study, numerical method for verification purposes will be further employed as a continuation of this paper. Software packages which use FEM generated static/dynamic multi-axial complex stress fields for predicting fatigue life will be used.

5 Conclusion

A cylindrical spring fatigue optimization method for inerter-based vibration isolation system is presented in this paper. The method is demonstrated on a simple discrete two-degree-of-freedom system. A simplified model for calculating cylindrical spring high-cycle fatigue life is established by adopting von Mises energy criterion for shear governed biaxial proportional stress and relating it to spring displacement amplitudes in Basquin's equation. Most convenient deflection and stress correction factors are adopted for vibration fatigue study, namely Ancker & Goodier deflection correction and Wahl stress correction factor. Two additional displacement correction factors are derived and compared to other referent solutions.

Two main benchmark isolators are investigated; one with inerter of optimal inertance and optimal damping, and one with optimal damping but without the inerter. These two plain isolator systems are viewed as a simplified model of a possibly more complicated dynamic structure. Parameters of the inerter-based isolator are optimized to maximize the effect of vibration isolation, which also corresponds to significant reductions of the stresses in the considered receiving body spring and an increase of its fatigue life as a consequence. It is demonstrated that the vibration isolation effect of the isolator not containing the inerter can be substantially improved by employing the ideal inerter in parallel with the isolator spring and viscous damper. Hence, it can be concluded that minimizing the kinetic energy of the receiving body, by employing inerter of adequate, i.e. optimized inertance, can convincingly prolong the coupling helical spring fatigue life. Specifically inerter anti-resonance effects can also be potentially used to fine tune the system for one dominant excitation frequency, and significantly reduce vibration amplitudes on that particular frequency.

As a direct continuation of this work, finite element method will be employed for results verification purposes. Main challenges are to implement ideal inerter concept in the finite element model and to well correlate spring displacements and stresses obtained by the developed analytical model to the results obtained by the finite element analysis.

References

1. Rao, S.S.: Mechanical Vibrations, 5th edn. Prentice Hall, New York (2010)
2. Smith, M.C.: Synthesis of mechanical networks: the inerter. IEEE Trans. Autom. Control **47**(10), 1648–1662 (2002)
3. Steinberg, D.S.: Vibration Analysis for Electronic Equipment, Third edn. Wiley, New York (2000)
4. Bishop, N.W.M., Sherratt, F.: Finite Element Based Fatigue Calculations. NAFEMS, Farnham (2000)
5. Lee, Y., Barkey, M.E., Kang, H.: Metal Fatigue Analysis Handbook. Practical Problem-Solving Techniques for Computer-Aided Engineering. Elsevier, Waltham (2012)
6. Wahl, A.M.: Helical compression and tension springs. ASME paper A-38. J. Appl. Mech. **2**(1), A-35–A-37 (1935)
7. Wahl, A.M.: Mechanical Springs, 1st edn. Penton, Cleveland (1944)
8. DIN EN 2089-1-1963-01 (1963) Helical Springs Made From Round Wire and Rod—Calculation and Design of Compression Springs
9. DIN EN 2089-1-1963-02 (1963) Helical Springs Made From Round Wire and Rod—Calculation and Design of Tension Springs

10. Din EN 13906-1: Cylindrical Helical Springs Made From Round Wire and Bar—Calculation and Design—Part 1: Compression Springs. BeuthVerlag, Berlin (2002)
11. Din EN 13906-2: Cylindrical Helical Springs Made From Round Wire and Bar—Calculation and Design—Part 2: Extension Springs. BeuthVerlag, Berlin (2002)
12. Ancker Jr., C.J., Goodier, J.N.: Pitch and curvature correction for helical springs. ASME J. Appl. Mech. **25**(4), 466–470 (1958)
13. Dym, C.L.: Consistent derivations of spring rates for helical springs. ASME J. Mech. Des. **131**(7), 1–5 (2009)
14. Research Committee on the Analysis of Helical Spring: Report of research committee on the analysis of helical spring. Trans. Jpn. Soc. Spring Eng. **2004**(49), 35–75 (2004)
15. Society of Automotive Engineers (SAE): Spring Design Manual. Ae Series. Society of Automotive Engineers Inc., Warrendale (1990)
16. Hearn, E.J.: Mechanics of Materials, Volume 1, An Introduction to the Mechanics of Elastic and Plastic Deformation of Solids and Structural Materials, 3rd edn. Butterworth-Heinemann, Oxford (1997)
17. Meissner, M., Schorcht, H.-J., Kletzin, U.: Metallfedern: Grundlagen, Werkstoffe, Berechnung, Gestaltung und Rechnereinsatz, 3rd edn. Springer, Berlin (2015)
18. Shimoseki, M., Hamano, T., Imaizumi, T.: FEM for Springs. Springer, Berlin (2003)
19. Timoshenko, S.P.: Strength of Materials, Part I, Elementary Theory and Problems, 2nd edn. D. Van Nostrand, New York (1940)
20. Timoshenko, S.P.: Strength of Materials, Part II, Advanced Theory and Problems, 2nd edn. D. Van Nostrand, New York (1940)
21. Timoshenko, S.P., Goodier, J.N.: Theory of Elasticity, 2nd edn. McGraw-Hill, New York (1951)
22. Budynas, R.G., Nisbett, J.K.: Shigley's Mechanical Engineering Design, 10th edn. McGraw-Hill, New York (2015)
23. Ugural, A.C.: Mechanical Design of Machine Components, 2nd edn. CRC Press, Boca Raton (2015)
24. Stephens, R.I., Fatemi, A., Stephens, R.R., Fuchs, H.O.: Metal Fatigue in Engineering, 2nd edn. Wiley, New York (2005)
25. Roessle, M.L., Fatemi, A.: Strain-controlled fatigue properties of steels and some simple approximations. Int. J. Fatigue **22**(6), 495–511 (2000)
26. Bannantine, J.A., Comer, J.J., Handrock, J.L.: Fundamentals of Metal Fatigue Analysis. Prentice Hall, Englewood Cliffs (1990)
27. Romanowicz, P.: Numerical assessment of fatigue load capacity of cylindrical crane wheel using multiaxial high-cycle fatigue criteria. Arch. Appl. Mech. **87**, 1707–1726 (2017)
28. Berger, C., Kaiser, B.: Result of very high cycle fatigue tests on helical compression springs. Int. J. Fatigue **28**, 1658–1663 (2006)
29. Kaiser, B., Berger, C.: Fatigue behaviour of technical springs. Mater. Werkst. **36**(11), 685–696 (2005)
30. Del Llano-Vizcaya, L., Rubio-González, C., Mesmacque, G., Cervantes-Hernandez, T.: Multiaxial fatigue and failure analysis of helical compression springs. Eng. Fail. Anal. **13**(8), 1303–1313 (2006)
31. Pyttel, B., Ray, K.K., Brunner, I., Tiwari, A., Kaoua, S.A.: Investigation of probable failure position in helical compression springs used in fuel injection system of diesel engines. IOSR J. Mech. Civil Eng. **2**(3), 24–29 (2012)
32. Rivera, R., Chiminelli, A., Gómez, C., Núñez, J.L.: Fatigue failure analysis of a spring for elevator doors. Eng. Fail. Anal. **17**(4), 731–738 (2010)
33. Ružička, M., Doubrava, K.: Loading regimes and designing helical coiled springs for safe fatigue life. Res. Agr. Eng. **51**(2), 50–55 (2005)
34. Kamal, M., Rahman, M.M.: Finite element-based fatigue behaviour of springs in automobile suspension. Int. J. Autom. Mech. Eng. **10**, 1910–1919 (2014)
35. Kuznetsov, A., Mammadov, M., Sultan, I., Hajilarov, E.: Optimization of improved suspension system with inerter device of the quarter-car model in vibration analysis. Arch. Appl. Mech. **81**, 1427–1437 (2011)
36. Cowper, G.R.: The shear coefficients in Timoshenko's beam theory. ASME J. Appl. Mech. **33**(2), 335–340 (1966)
37. Mlikota, M., Schmauder, S., Božić, Ž., Hummel, M.: Modelling of overload effects on fatigue crack initiation in case of carbon steel. Fatigue Fract. Eng. Mater. Struct., Special Issue: 16th International Conference on New Trends in Fatigue and Fracture (NT2F16) 40(8):1182–1190 (2017)
38. Alujević, N., Čakmak, D., Wolf, H., Jokić, M.: Passive and active vibration isolation systems using inerter. J. Sound Vib. **418**, 163–183 (2018)
39. Alujević, N., Wolf, H., Gardonio, P., Tomac, I.: Stability and performance limits for active vibration isolation using blended velocity feedback. J. Sound Vib. **330**, 4981–4997 (2011)
40. Alujević, N., Gardonio, P., Frampton, K.D.: Smart double panel for the sound radiation control: blended velocity feedback. AIAA J. **49**(6), 1123–1134 (2011)
41. Caiazzo, A., Alujević, N., Pluymers, B., Desmet, W.: Active control of turbulent boundary layer-induced sound transmission through the cavity-backed double panels. J. Sound Vib. **422**, 161–188 (2018)
42. James, H.M., Nichols, N.B., Phillips, R.S.: Theory of Servomechanisms. MIT Radiation Laboratory Series, vol. 25, First edn. McGraw-Hill, New York (1947)

Paper 3, https://doi.org/10.1007/s00419-018-1495-2

CrossMark

ORIGINAL

D. Čakmak · Z. Tomičević · H. Wolf · Ž. Božić

$\mathcal{H}_2$ optimization and numerical study of inerter-based vibration isolation system helical spring fatigue life

Abstract This paper presents an optimization and numerical analysis of vibration-induced fatigue in a two degree-of-freedom inerter-based vibration isolation system. The system is comprised of a primary, e.g. source body, and a secondary, e.g. receiving body, mutually connected through an isolator. The isolator includes a spring, a dashpot and an inerter. Inerter is a mechanical device which produces a force proportional to relative acceleration between its terminals. A broadband frequency force excitation of the primary body is imposed throughout the study. The goal of the proposed optimization is to prolong the fatigue life of the ground connecting helical spring of the secondary body. The optimization is based on minimizing separately the displacement and velocity amplitudes. Both optimization criteria are compared with regard to spring fatigue life improvement for fair benchmark comparison. The inerter-based optimized systems, in which the $\mathcal{H}_2$ index of the receiving body is minimized, are also compared with the optimized systems without inerter. Notable improvements are observed in inerter-based systems due to the inclusion of an optimally tuned inerter in the isolator. The proposed analytical vibration fatigue method optimization results are compared with the finite element method results, and a very good agreement is observed. Most accurate helical spring deflection and stress correction factors are discussed and determined. Furthermore, the inerter concept is successfully implemented into finite element-based dynamic solution.

1 Introduction

The cylindrical helical coil spring is one of the fundamental and most important key mechanical components found in many industrial applications (e.g. vehicle suspension components, automotive valve springs, stamping presses, brakes). Springs are typically used to perform required mechanical functions (i.e. apply, transfer, indicate or maintain a force/torque, store energy and provide the system with the flexibility [1]).

Vibration isolation systems [2] (e.g. car suspension) are often subjected to high dynamic loading during service. These loadings can cause harmful vibrations and may result with premature failure from aggressive fatigue mechanisms which are especially prominent in case of resonant harmonic excitations [2,3]. Massive spring used in the suspension systems [3,4] is a common example where the crack may initiate at a high stress location and eventually propagate. This can lead to fatigue failure, especially due to vibration-induced fatigue effects [2,3,5]. In order to estimate the vibration fatigue, it is necessary to predetermine stiffness, strength and damping parameters of the system. In particular, all of the above-mentioned parameters should be taken into

D. Čakmak · Z. Tomičević (✉) · H. Wolf · Ž. Božić
Faculty of Mechanical Engineering and Naval Architecture, University of Zagreb, I. Lučića 5, 10 000 Zagreb, Croatia
E-mail: zvonimir.tomicevic@fsb.hr
Tel.: +00 385 1 6168 533

account while evaluating the helical spring fatigue life [2]. The springs as machine elements should withstand long exploitation period. Hence, they are commonly evaluated with appropriate high-cycle fatigue (HCF) calculation method (above 10^3 life cycles) [2]. Shear-governed life criterion is normally considered for spring fatigue calculation where highly stressed region is usually located at the inner side of the helix [1,2]. Contrary to that traditional concept, Todinov [6] in accordance with Del Llano-Vizcaya et al. [7] states that the highest stress region is reported at the outer surface of the helical compression springs with a large coil to wire radius ratio, rather than usual inside of the helix. Consequently, the fatigue crack origin will presumably also be located on the outer surface where the maximum amplitude of the principal tensile stress occurs. Furthermore, it is in accordance with the stress field obtained from numerical fatigue analysis via finite element method (FEM) [7]. As discussed in [2], the problem with unambiguous definition of the stress field and the corresponding fatigue life is noted in the literature since multiple stress correction factors for helical spring are proposed. One of the most often used and cited expressions originate from Wahl [8], Bergsträsser [2], Göhner [9–11] and Ancker and Goodier (A/G) [2,12–19]. The investigation conducted by Calder et al. [14] reported that A/G and Wahl stress correction factors differ only slightly for small spring pitch angles. Moreover, the Wahl correction factor matched with their experimental stress measurements of a helical coil automobile spring within less than $\pm 1\%$ difference. It is often discussed whether using aforementioned stress correction factors may result with highly conservative fatigue life prediction [1,2].

Numerically determining the vibration fatigue life is an increasingly evolving field. Various researchers use mostly FEM-based software for calculation depending on the availability, application and functionality [5,20–22]. Rahman et al. [23] used FEM for obtaining stress amplitudes of engine components and performing corresponding fatigue calculation. Authors employed a power spectral density (PSD) load and obtained fatigue results in the frequency domain. According to Halfpenny [24] and also reported by Mršnik et al. [25,26], operating with a PSD proves to be rather beneficial when working with complicated and computationally expensive FEM models. Hence, the calculation of the frequency response functions (FRFs) is convenient and much faster than a long-term transient dynamic analysis in the time domain [5]. When loading conditions are prescribed in the form of PSD which is defined in a frequency domain, structural response of systems can be computed by using the transfer function (TF), i.e. FRF of target systems and PSD of excitation loads [24]. Mršnik et al. also gave important scientific contribution to further understanding of the vibration-induced fatigue phenomena by studying multi-axial stress effects [25] and various frequency domain methods [26]. In [25], authors used both FEM and experimental approaches where similar numerical model was analysed as in [27]. Česnik and Slavič [27] investigated harmonic and random kinematic/base excitation load on the aluminium alloy "Y"-shaped specimen and used custom vibration fatigue plug-in developed for the commercial FEM package analysis environment. Furthermore, the numerically predicted fatigue life was compared to the experimental results. The results obtained via numerical analysis estimated substantially more conservative fatigue life compared to the actual fatigue life. Opposed to common unimodal (i.e. narrow-band PSD), Braccesi et al. [28] considered bimodal PSD for random stress process and created custom FE-based fatigue life calculation code valid for the frequency domain. Additionally, Bonte et al. [29] used combination of various FEM packages for the calculation of the vibration fatigue life. They developed a commercially used simulation method for the fatigue analysis of automotive and other products that are subjected to multiple random excitations by adopting PSD. Furthermore, Zhou et al. [30] used modal stress approach in random vibration fatigue assessment by employing FEM. The conducted investigations consisted of a two-step procedure. In the first step, modal stress analysis is conducted to locate the fatigue hotspots in a dynamic structure, while in the second step the frequency domain-based approach for random fatigue evaluation is performed at fatigue hotspots through PSD.

Vibration systems are commonly tuned (i.e. optimized) according to some optimization criterion. One of the metrics for vibrations of the dynamic structures is square vibration amplitude over the entire frequency range. Proposing the optimization of this quantity is first attributed to Warburton [31] and is generally referred to as $\mathcal{H}_2$ optimization [32–34]. $\mathcal{H}_2$ optimization has the objective function of minimizing the total vibration energy, i.e. mean square motion of the dynamic structure under the white noise of the PSD excitation [31]. Studies which incorporate this method usually employ the minimization of specific kinetic energy (i.e. vibration velocity amplitudes) [2,32,35]. However, alternate studies such as minimization of displacement amplitudes can also be applied [34]. Inerter is a novel mechanical element conceived and developed by Smith [4]. Inerter produces a force which is proportional to relative acceleration $(a_2 - a_1)$ between its terminals where equation $F_{\text{inerter}} = b(a_2 - a_1)$ holds. The coefficient of inerter resistance force F_{inerter} is called inertance. It is denoted by label "b" and is measured in kilograms, in SI units. Inerters are mathematically approximated in the same

sense as, for example, springs and dashpots. Consequently, it is assumed that inerter mass is rather small compared to inertance it provides [2,4,35].

In the preceding work [2], all the above presented concepts were implemented into an analytical solution. Although this problem is discussed in other studies [34–38], reference [2] is further suitably referred to, as this previously proposed approach addresses vibration isolation and fatigue life assessment simultaneously. The unit PSD load was applied on the dynamic system. The minimization of the specific kinetic energy of inerter-based system in the frequency domain yielded substantial reduction in vibration velocity amplitudes. Consequently, extension of the corresponding cylindrical spring fatigue life was reported. However, concerns were raised whether the exclusively fatigue-based optimization would prove more efficient with regard to the spring fatigue life when compared to solely kinetic energy-based optimization. The aim of this study is to revisit and address this question by employing alternate displacement-based criterion and utilizing linear FEM to assess the accuracy of the adopted expressions [2], especially with regard to before discussed approximate spring stress and displacement correction factors. Using FEM as control verification tool with a purpose of benchmark comparison is a common practice used in conjunction with complex analytical calculations [39].

In this study, which is a direct continuation leading the approach of the same problem from previous work [2], the goal is to model the fatigue load of a helical spring acting as a linear elastic element in a simplified two degree-of-freedom (2-DOF) inerter-based vibration isolation system. Analytical and numerical methods are employed by means of specialized software packages: FEM-based *Abaqus* [40] and *Fe-Safe* [41]. *Fe-Safe* can import and analyse FEM generated static/dynamic multi-axial complex stress fields with the aim of assessing the fatigue life. The paper is structured as follows. In Sect. 2, analytical mathematical 2-DOF inerter-based vibration isolation system model is established where optimized parameters for both viscous damper and inerter are determined. $\mathcal{H}_2$ optimization of the newly proposed displacement and referent velocity amplitudes [2] is used as a criterion. Novel displacement-based optimization parameters for inertance and damping are derived and explicitly given. In Sect. 3, various dimensionless spring deflection and stress correction factors from the referent literature are revisited from [2] and discussed. The accuracy of previously derived Timoshenko/Cowper (T/C)-based deflection factor [2,8] is determined. The most accurate spring correction factors are later used in the context of analytically calculating displacement and stress amplitudes under PSD force loading. In Sect. 4, previously established deflection and stress correction factors are further discussed by comparing analytically obtained results with FEM. Final Sect. 5 presents a benchmark example adopted from [2] by utilizing all before proposed methods and finally comparing analytical and numerical results of the vibration fatigue optimization study. Previously derived analytical expression [2] based on the von Mises energy criterion for shear-governed biaxial and proportional stress is verified. The proposed expression explicitly ties vibration displacement amplitudes with HCF life of the helical spring. Moreover, the ideal inerter concept is implemented in the commercial FEM code *Abaqus*.

2 2-DOF inerter-based vibration isolator mathematical model

In this chapter, the generalized analytical model for the discrete 2-DOF inerter-based vibration isolation system optimization process is established as a straightforward closed-form solution. The studied problem is fully adopted from [2] and represented by a simple model shown in Fig. 1a. It is assumed that the critical fatigue component is a helical spring k_3, shown in Fig. 1b. The material parameters of the spring are as follows: E is Young modulus, ν is Poisson's ratio, S_f' is fatigue strength coefficient and B is Basquin's exponent [2] denoted in capital letter in order not to be mistaken for inertance b. Number of active coils is designated as n ($n = 2$ in Fig. 1b), h is spring total length where $h = n \cdot l$ for $n =$ arbitrary integer ≥ 1, and l is the spring pitch. D and d are large and small spring diameters, respectively, while $C = D/d$ is defined as spring index [1,2]. Recommended values of spring index C for practical engineering purposes lie in between $C = 4-12$ [2]. Angle α represents the pitch angle which can be calculated according to usual geometric expression $\alpha = \arctan[l/(\pi D)]$ (Fig. 1b).

The goal of the vibration-based optimization is to minimize vibrations of the secondary or receiving body, i.e. vibrations of mass m_2 which are proportional to the maximum deflection amplitudes of the spring k_3. In this optimization, the excitation of the primary/source body $F_1(t)$ is assumed to contain white noise spectral properties [2,35], i.e. unit PSD loading amplitude $F_{01}(\Omega) = 1$ over the entire frequency range. The whole vibration system consists of discrete masses m_1 and m_2, ideally massless springs k_1, k_2 and k_3, viscous dampers c_1, c_2 and c_3 and an inerter of inertance b_2. Isolator consists of spring k_2, damper c_2 and inerter b_2. The ideal inerter produces a force F_{inerter} proportional to the relative acceleration [4] between masses m_1 and
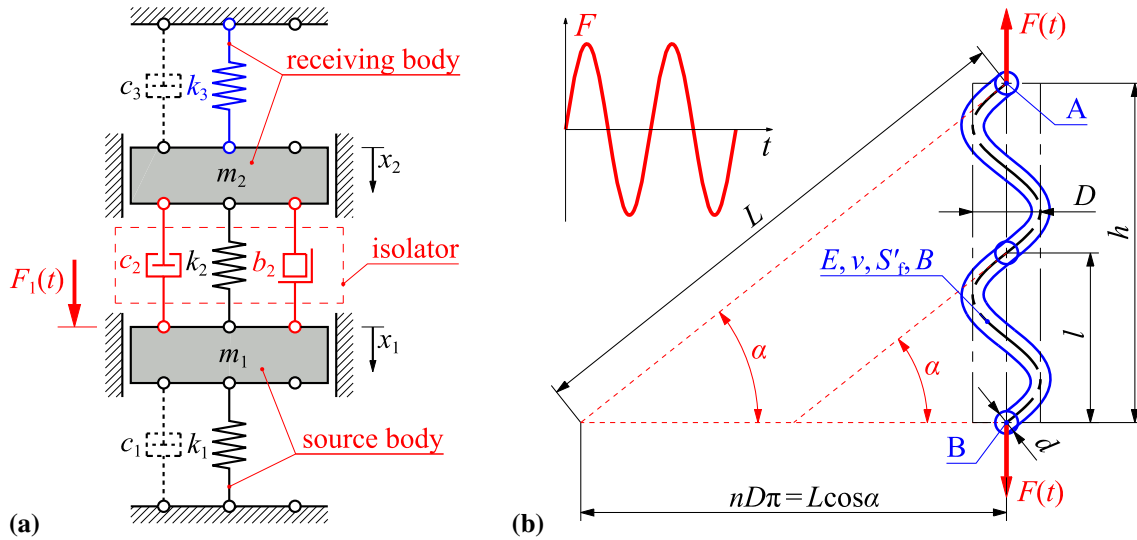
Fig. 1 **a** 2-DOF linear discrete vibration isolation system, **b** helical spring k_3 properties [2]

m_2. The described discrete parameter approximation may represent a reduced-order model [36] of a system of a more complex nature [37] which includes distributed mass, stiffness and damping parameters, as discussed in [35,38]. The damping of the source and receiving bodies is assumed to be negligible (i.e. $c_1 \approx c_3 \approx 0$) which provides for substantially more simple solution derivation. However, the relations are also approximately valid for the systems with small inherent damping [35].

The equations of motion [2,3,35] for system in Fig. 1a can be written in the general matrix form as

$$\mathbf{M}\ddot{\mathbf{x}}(t) + \mathbf{C}\dot{\mathbf{x}}(t) + \mathbf{K}\mathbf{x}(t) = \mathbf{F}(t), \tag{1}$$

where $\mathbf{M}$ is the global mass matrix, $\mathbf{C}$ is the global damping matrix, $\mathbf{K}$ is the global stiffness matrix and $\mathbf{F}(t)$ is the excitation column force vector. Displacement of the masses m_1 and m_2 from static equilibrium position, velocity and acceleration vectors are denoted by $\mathbf{x}(t)$, $\dot{\mathbf{x}}(t)$ and $\ddot{\mathbf{x}}(t)$, respectively.

Global matrices and vectors from Eq. (1), accounting for negligible damping c_1 and c_3, can be written as

$$\mathbf{M} = \begin{bmatrix} m_1 + b_2 & -b_2 \\ -b_2 & m_2 + b_2 \end{bmatrix}, \quad \mathbf{C} = \begin{bmatrix} c_2 & -c_2 \\ -c_2 & c_2 \end{bmatrix}, \quad \mathbf{K} = \begin{bmatrix} k_1 + k_2 & -k_2 \\ -k_2 & k_2 + k_3 \end{bmatrix}, \tag{2a, b, c}$$

$$\mathbf{x} = \begin{bmatrix} x_1(t) \\ x_2(t) \end{bmatrix}, \quad \mathbf{F} = \begin{bmatrix} F_1(t) \\ 0 \end{bmatrix}, \tag{3a, b}$$

where the parameters and functions in the matrices and vectors are denoted in Fig. 1a. Due to influence of inerter b_2, mass matrix $\mathbf{M}$ from Eq. (2a) is no longer diagonal [3]; however, it is still symmetric [2,35].

By assuming harmonic excitation and expressing the excitation and the steady-state response in the complex form $\mathbf{F}(t) = \mathbf{F}_0 e^{i\Omega t}$ and $\mathbf{x}(t) = \mathbf{x}_0 e^{i\Omega t}$, where $i = \sqrt{-1}$, the solution of Eq. (1) can be directly written as

$$\mathbf{x}_0(\Omega) = \begin{bmatrix} x_{01} & x_{02} \end{bmatrix}^T = \begin{bmatrix} (i\Omega)^2 \mathbf{M} + i\Omega \mathbf{C} + \mathbf{K} \end{bmatrix}^{-1} \mathbf{F}, \tag{4}$$

where terms inside the square bracket denote dynamic stiffness matrix and $\mathbf{x}_0(\Omega)$ is the complex displacement amplitude. Multiplying Eq. (4) with the term $i\Omega$ yields complex velocity amplitude $\mathbf{v}_0$ expression which can be written as

$$\dot{\mathbf{x}}_0(\Omega) \equiv \mathbf{v}_0(\Omega) = \begin{bmatrix} \dot{x}_{01} & \dot{x}_{02} \end{bmatrix}^T = i\Omega \mathbf{x}_0(\Omega). \tag{5}$$

By considering $\mathbf{M}$, $\mathbf{C}$ and $\mathbf{K}$ matrices from Eq. (2a–c), the steady-state (i.e. time-invariant) complex response of the mass m_2 can now be expressed in simplified form as the following FRFs

$$\frac{x_{02}(\Omega)}{F_{01}} = \frac{B_0 + (i\Omega) B_1 + (i\Omega)^2 B_2 + (i\Omega)^3 B_3}{A_0 + (i\Omega) A_1 + (i\Omega)^2 A_2 + (i\Omega)^3 A_3 + (i\Omega)^4 A_4}, \quad \frac{\dot{x}_{02}(\Omega)}{F_{01}} \equiv \frac{v_{02}(\Omega)}{F_{01}} = i\Omega \frac{x_{02}(\Omega)}{F_{01}}, \tag{6a, b}$$

where coefficients $A_0 - A_4$ and $B_0 - B_3$ with respect to Eq. (6a, b) are defined as

$$
\begin{aligned}
A_0 &= (k_2 + k_3)\, k_1 + k_2 k_3 & B_0\,(x_0) &= k_2 & B_0\,(v_0) &= 0 \\
A_1 &= c_2\,(k_1 + k_3) & B_1\,(x_0) &= c_2 & B_1\,(v_0) &= k_2 \\
A_2 &= (m_2 + b_2)\, k_1 + (m_1 + m_2)\, k_2 + (m_1 + b_2)\, k_3, & B_2\,(x_0) &= b_2, & B_2\,(v_0) &= c_2. \\
A_3 &= c_2\,(m_1 + m_2) & B_3\,(x_0) &= 0 & B_3\,(v_0) &= b_2 \\
A_4 &= (m_2 + b_2)\, m_1 + b_2 m_2
\end{aligned}
\tag{7a--m}
$$

The transfer admittance (i.e. FRF x_{02}/F_{01}) from Eq. (6a) represents the complex displacement amplitude of the receiving body per unit forcing $F_{01} = 1$ of the source body. The transfer mobility (i.e. FRF v_{02}/F_{01}) from Eq. (6b) represents the complex velocity amplitude of the receiving body per unit forcing $F_{01} = 1$ of the source body. Coefficients $B_0 - B_3$ from Eq. (7) are different with regard to variables of displacement x_{02} and velocity v_{02} amplitudes, respectively [i.e. Eqs. (4) and (5)]. FRFs from Eq. (6a, b) are further used to assess the effectiveness of the vibration isolation. Considering that the excitation force F_1 with the unit PSD is assumed, the $\mathcal{H}_2$ index of the receiving body $I_{\mathcal{H}2}$ per unit excitation force can be calculated with relations that write as

$$
I_{\mathcal{H}2}\,(x_0) = \int_{-\infty}^{\infty} \left| \frac{x_{02}\,(\Omega)}{F_{01}} \right|^2 \mathrm{d}\Omega, \quad I_{\mathcal{H}2}\,(v_0) = \int_{-\infty}^{\infty} \left| \frac{v_{02}\,(\Omega)}{F_{01}} \right|^2 \mathrm{d}\Omega,
\tag{8a, b}
$$

according to [31] and demonstrated in [2,32–35]. The $\mathcal{H}_2$ indices of the receiving body (i.e. $I_{\mathcal{H}2}$) from Eq. (8a, b) are used throughout this study as a quantitative measure of the broadband frequency vibration isolation performance quality. The objective is to minimize this quantity for all vibration isolation systems analysed in the scope of the conducted investigation. Vibration-based optimization with the goal of vibration reduction by using this particular method can be found in [2,32–35]. The $\mathcal{H}_2$ index in Eq. (8) for $I_{\mathcal{H}2} = I_4$ can according to [2,35] analytically be calculated with closed-form polynomial expression which can be written as

$$
I_{\mathcal{H}2(4)} = \pi \frac{A_0 B_3^2\,(A_0 A_3 - A_1 A_2) + A_0 A_1 A_4\,(2 B_1 B_3 - B_2^2) - A_0 A_3 A_4\,(B_1^2 - 2 B_0 B_2) + A_4 B_0^2\,(A_1 A_4 - A_2 A_3)}{A_0 A_4\,(A_0 A_3^2 + A_1^2 A_4 - A_1 A_2 A_3)},
\tag{9}
$$

where substituting coefficients $A_0 - A_4$ and $B_0 - B_3$ from Eq. (7) into Eq. (9) yields with the final $\mathcal{H}_2$ index $I_{\mathcal{H}2}$ analytical expression, which is herein omitted for substantial length [2]. In Eq. (9), index "4" denotes fourth-order polynomial of the denominator with regard to the term iΩ in Eq. (6).

Two fundamental circular natural frequencies $\omega_{n1,2}$ of the given 2-DOF vibration system can be analytically obtained by solving the classic eigenvalue problem [2,3] which readily writes as

$$
\left[\mathbf{K} - \left(\omega_{n1,2} \right)^2 \mathbf{M} \right] \mathbf{x}\,(t) = 0,
\tag{10}
$$

where influence of inertance b_2 on eigenvalues is demonstrated later on. The following expressions

$$
\Omega_A = \sqrt{\frac{k_2}{b_2}}, \quad \lim_{c_2, k_2 \to \infty} \Omega_a = \sqrt{\frac{k_1 + k_3}{m_1 + m_2}},
\tag{11a, b}
$$

denote anti-resonance Ω_A and isolator-locking circular frequency Ω_a, respectively, as reported in [2,35].

In the next subchapters of this study, two main types of the vibration transmission control are analysed with respect to minimizing the index $I_{\mathcal{H}2}$. The isolation control without inerter (i.e. $b_2 = 0$) and the isolation control with optimized inertance b_{opt} are considered. The optimized isolator damping and inertance parameters are obtained by minimizing the frequency averaged index $I_{\mathcal{H}2}$ of the receiving body denoted symbolically in Eq. (9). The displacement and velocity amplitudes criteria are used, respectively. As discussed in [2], due to this particular problem definition, spring k_2 cannot be optimized and is further considered as constrained/fixed value bound by physical limits [35].

2.1 Isolation optimization considering displacement amplitudes

The parameters from Eq. (7a–i) are considered. The procedure explained in [2] is applied. Differentiating Eq. (9) with respect to damping c_2, equalling with zero and again solving for damping c_2 yield with

$$c_{2(b_2 \neq 0)}\left[\mathcal{H}_2\left(x_0\right)\right] = \sqrt{\frac{\begin{array}{c}(m_1 + m_2)^2\, k_2^3 + \left[k_3 m_1^2 + m_2^2 k_1 - 2\,(m_1 + m_2)\,(k_3 + k_1)\,b_2\right]k_2^2 \\ + \left[(k_3 + k_1)^2\, b_2 - 2k_1 k_3\,(m_1 + m_2)\right]b_2 k_2 + (k_3 + k_1)\, b_2^2 k_1 k_3\end{array}}{\left[(k_2 + k_3)\, k_1 + k_2 k_3\right](m_1 + m_2)}}, \tag{12}$$

where c_2 now represents optimum damping $c_{opt}(b_2)$ for any given inertance b_2. By substituting Eq. (12) into Eq. (9), differentiating with respect to b_2, equalling with zero and solving for b_2, optimum inertance parameter b_{opt} is obtained. Inserting $b_2 = b_{opt}$ into Eq. (12) results with optimum damping c_{opt2}. These expressions write as

$$c_{opt2}\left[\mathcal{H}_2\left(x_0\right)\right] = \frac{k_2\,|k_1 m_2 - m_1 k_3|}{\sqrt{\left[(k_2 + k_3)\, k_1 + k_2 k_3\right](m_1 + m_2)\,(k_1 + k_3)}}, \quad b_{opt}\left[\mathcal{H}_2\left(x_0\right)\right] = \frac{k_2\,(m_1 + m_2)}{k_1 + k_3}. \tag{13a, b}$$

By setting the inertance $b_2 = 0$ in Eq. (12), the optimum damping c_{opt} for the case without inerter is

$$c_{opt(b_2=0)}\left[\mathcal{H}_2\left(x_0\right)\right] = k_2\,\frac{\sqrt{(m_1 + m_2)^2\, k_2 + k_1 m_2^2 + k_3 m_1^2}}{\sqrt{\left[(k_2 + k_3)\, k_1 + k_2 k_3\right](m_1 + m_2)}}. \tag{14}$$

Derived Eqs. (13, 14) unambiguously represent closed-form algebraic solutions for optimized damping and inertance parameters regarding displacement-based, i.e. consequently fatigue-based optimization.

2.2 Isolation optimization considering velocity amplitudes

The proposed procedure described in [2] is further utilized for optimization process. The parameters from Eq. (7a–e, j–m) are considered further. Differentiating Eq. (9) with respect to damping c_2, equalling with zero and again solving for damping c_2 yield with already known solution

$$c_{2(b_2 \neq 0)}\left[\mathcal{H}_2\left(v_0\right)\right] = \sqrt{\frac{m_1 + m_2}{k_1 + k_3}k_2^2 - 2b_2 k_2 + \frac{m_1 k_3^2 + m_2 k_1^2 + b_2\,(k_1 + k_3)^2}{(k_1 + k_3)\,[m_1\,(b_2 + m_2) + b_2 m_2]}b_2^2}, \tag{15}$$

where c_2 represents optimum damping $c_{opt}(b_2)$ for any given inertance b_2, but now in the context of velocity amplitudes, i.e. kinetic energy optimization. For inertance $b_2 = 0$, Eq. (15) morphs into simpler relation

$$c_{opt(b_2=0)}\left[\mathcal{H}_2\left(v_0\right)\right] = k_2\sqrt{\frac{m_1 + m_2}{k_1 + k_3}}, \tag{16}$$

which represents the optimum damping coefficient $c_2 = c_{opt}$. As reported in [2], explicit expressions for b_{opt} and c_{opt2} in the context of velocity-based optimization are not shown due to the fact that they are rather lengthy and cannot be expressed in the convenient algebraic form although they are purely analytical. Interestingly, displacement-based optimization yields with much simpler final expressions for optimized parameters. Albeit, initial Eq. (15) seems more straightforward for further manipulation when compared to Eq. (12).

3 Helical spring displacement and stress correction factors

In this chapter, spring stiffness and stress corrections from the literature are reviewed. A simple expression for determining the spring fatigue life is recapitulated from [2] where HCF life is addressed and employed. Obtained displacement amplitudes in the frequency domain from previous chapter [see Eq. (4)] can now be tied to stress amplitudes necessary for performing the vibration fatigue analysis. The cylindrical spring can for simplicity be viewed as a thin/slender and curved rod/beam subjected to torsion load [1]. In the case curvature,

Table 1 Expressions for stress correction factors K_τ and deflection correction factors K_δ

Author/standard	Stress correction factor K_τ	Deflection correction factor K_δ
Strength of materials		
Wahl, DIN 13906	$\frac{4C-1}{4C-4} + \frac{k_W}{C} = \frac{4C-1}{4C-4} + \frac{1+2\nu}{2(1+\nu)C}$	–
Röver	$\cos(\alpha)\left[\frac{C}{C-\cos^2(\alpha)} + \frac{1+\sin^2(\alpha)}{4C}\right]$	–
Wood	$\frac{C}{C-1} + \frac{1}{2C}$	$\frac{2C^2+C-1}{2C^2}$
Honegger	$\cos(\alpha)\left[\frac{C}{C-\cos^2(\alpha)} + \frac{0.615}{C}\right]$	$\frac{2C^2-\cos^4(\alpha)}{2C^2\cos^5(\alpha)}$
Timoshenko/Cowper	–	$1 + \frac{7+6\nu}{12C^2(1+\nu)}$
Elasticity theory		
Göhner, DIN 2089	$1 + \frac{5}{4C} + \frac{7}{8C^2} + \frac{1}{C^3}$	$\cos(\alpha) + \frac{3\cos^5(\alpha)}{16(C^2-1)} + \frac{\sin(\alpha)\tan(\alpha)}{1+\nu}$
Ancker and Goodier	$1 + \frac{5}{4C} + \frac{7}{8C^2} + \frac{1}{2}\tan^2(\alpha)$	$1 - \frac{3}{16C^2} + \frac{3+\nu}{2(1+\nu)}\tan^2(\alpha)$
Castigliano/Timoshenko	–	$\frac{(16C^2-13)\cos(\alpha)}{16(C^2-1)} + \frac{\sin(\alpha)\tan(\alpha)}{1+\nu}$
Approximate/empirical relation		
Bergsträsser, DIN 13906	$\frac{C+0.5+\sin^2(\alpha)}{C-0.75+1.51\sin^2(\alpha)}$	–
Sopwith, BS 1726	$\frac{C+0.2}{C-1}$	–
Strain energy (Castigliano's) method		
Shigley	–	$1 + \frac{1}{2C^2}$
Dym	–	$\left(1 + \frac{1}{2C^2}\right)\cos(\alpha) + \left(1 + \frac{1}{4C^2}\right)\frac{\tan(\alpha)\sin(\alpha)}{(1+\nu)}$

pitch and thickness effects are considered [2], and the analytical expressions for true spring stiffness k_{true} and maximum shear stress $\tau_{\max}$ are

$$k_{\text{true}} = \frac{1}{K_\delta}\frac{F_0}{\delta_{\text{nom}}} = \frac{1}{K_\delta}\frac{Gd}{8C^3n}, \quad \tau_{\max} = K_\tau\frac{8F_0C}{\pi d^2}, \qquad (17a, b)$$

where $\delta_{\text{nom}} = 8C^3n/(Gd)$ is nominal spring deflection, K_δ is displacement correction factor, K_τ is (shear) stress correction factor and $G = E/[2(1+\nu)]$ is the shear modulus. As linear elastic/small deformation and deflection conditions are assumed, Eq. (17) is valid for both tensile and compressive applied force amplitudes $\pm F_0$. For previously defined simple harmonic conditions, equation $F(t) = F_0 e^{i\Omega t}$ holds. The helical spring geometry, parameters, loading and boundary conditions (BCs) are the same as schematically shown in Fig. 1b. For a more general approach in the scope of this study, boundaries of spring index C are varied both inside and outside of the recommended values $C = 4-12$, in order to parametrically test all physically valid solutions. As already noted, additional correction factors K_δ and K_τ need to be applied for displacement and shear stress, where relations $\delta_{\max} = K_\delta\delta_{\text{nom}}$ and $\tau_{\max} = K_\tau\tau_{\text{nom}}$ now hold [2], while $\tau_{\text{nom}} = 8F_0C/(\pi d^2)$ is designated as nominal shear stress.

Table 1 is adopted from [2,13], expanded and fitly modified. It sums up all the expressions from the referent literature used in the scope of this paper. T/C deflection correction factor is proposed in [2] by adopting Timoshenko thick cantilevered shear-deformable beam analogy and Cowper's shear correction factor for circular cross-sectional area. Göhner-based Castigliano/Timoshenko (C/T) deflection correction factor is previously derived [2] in dimensionless form and denoted in Table 1 in a more convenient and simplified form.

Furthermore, additional stress correction factors can be found in the literature. The investigation conducted by Göhner [9] directly influenced Henrici [10] who derived similar approximate stress correction factor by using Legendre power series function which yielded with more complex expression

$$K_{\tau,\text{Henrici}} = 1 + \frac{5}{4C} + \frac{7}{8C^2} + \frac{155}{256C^3} + \frac{11911}{24576C^4} + \cdots. \qquad (18)$$

Berry [11], for instance, gives alternate Göhner stress correction equation compared to one denoted in Table 1.

$$K_{\tau,\text{Göhner}(alt)} = \left(\frac{C}{C-1} + \frac{1}{4C} + \frac{1}{16C^2}\right)\left(\frac{C^2-1}{C^2-0.8125}\right). \qquad (19)$$
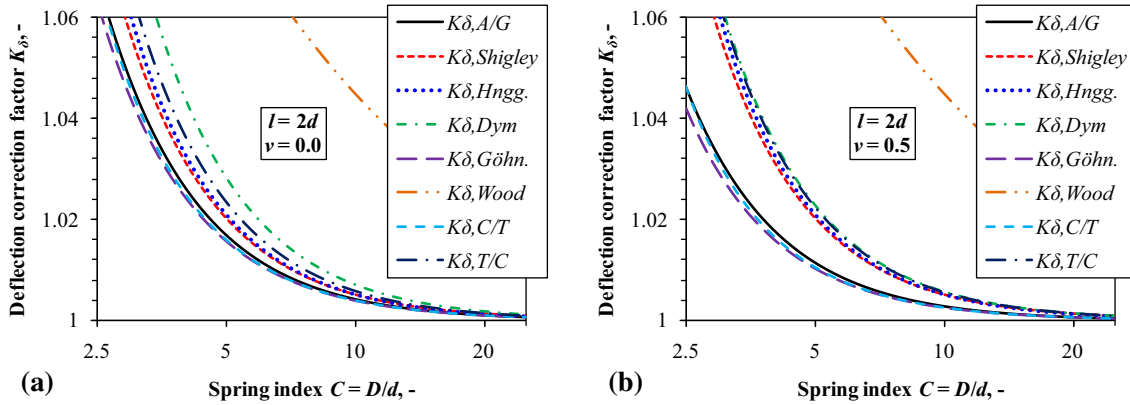
Fig. 2 Deflection correction factors, K_δ: **a** fully compressible material, $\nu = 0.0$, **b** incompressible material, $\nu = 0.5$

Interestingly, Eqs. (18), (19) and four-term Göhner equation from Table 1 give almost the same results for any physically acceptable value of spring index C. Moreover, Calder [14] gives alternate version of A/G correction

$$K_{\tau,\text{A/G}}(\text{Calder}) = 1 + \frac{5}{4C} + \frac{7}{8C^2} + \frac{1}{C}\tan^2(\alpha), \tag{20}$$

which differs from the expression in Table 1, by comparing the last term denominator. However, for small pitch angle the difference is negligible compared to original A/G relation, which is in return very similar to fundamental Göhner expression [2]. A/G deflection correction factor from Table 1 can also be found in their original paper [12], and it is considered to be one of the most accurate ones found in the literature [15,17,19]. A/G derived detailed equations for the stresses and deflections in a helical spring using the theory of elasticity approach and employing thin slice method. They used truncated, doubly infinite power series in the terms of spring index, coil curvature and spring's initial pitch angle or helix angle combined effects [12,15–17].

All deflection correction expressions from Table 1 are shown in Fig. 2. Fully compressible material (i.e. $\nu = 0$) and incompressible material (i.e. $\nu = 0.5$) are considered in Fig. 2a, b, respectively. Similar study was conducted by Burns [18] where dependency of Poisson's ratio on helical spring stiffness was evaluated.

Simple Wood deflection correction largely deviates from rest of the curves as reported in [2], although it is included here for the sake of completeness. It is interesting to note that for $\nu = 0.0$ curves are somewhat scattered for small spring indices C. However, for $\nu = 0.5$ the curves based on the theory of elasticity (A/G, C/T and Göhner) uniformly converge to lower values while the rest of the curves converge to higher values.

By using appropriate vibration terminology [i.e. obtained displacement amplitudes from Eq. (4)] and considering appropriate spring stress and displacement factors with embedded von Mises distortion energy criterion, Basquin's equation and number of cycles N_f can according to [2] finally be explicitly written as

$$N_\text{f} = \left(\frac{S_\text{a}}{S_\text{f}'}\right)^{\frac{1}{B}} \Rightarrow N_\text{f}(\Omega) = \left[\sqrt{3}\frac{K_\tau}{K_\delta}\frac{G}{C^2 n\pi d}\frac{|x_{02}(\Omega)|}{S_\text{f}'}\right]^{\frac{1}{B}}. \tag{21a, b}$$

The benefit of simple Eq. (21b) is that it is not obligatory to explicitly define force amplitude F_0 acting on spring k_3 (i.e. mass m_2). In the next chapter, FEM is employed for alternative K_δ and K_τ identification.

4 Finite element method helical spring displacement and stress analysis

In this chapter, spring stiffness and stress corrections are determined numerically by employing FEM-based software suite *Abaqus* [40]. Analytical/empirical solutions and referent relations for various deflection and stress correction factors from Table 1 are benchmarked and verified.

Table 2 shows example spring parameters used in this parametric evaluation. Mean coil diameter D is fixed at referent value $D = 50$ mm, and spring wire diameter d is varied in steps of $\Delta d = 3$ mm in order to obtain discrete numerical values for different spring indices C. For simplicity and computational efficiency, only one active coil is used (i.e. $n = 1$). Spring pitch l is parameterized with relation $l = 2 \cdot d$, analogue to the analytical

Table 2 Helical spring geometric and material parametric properties

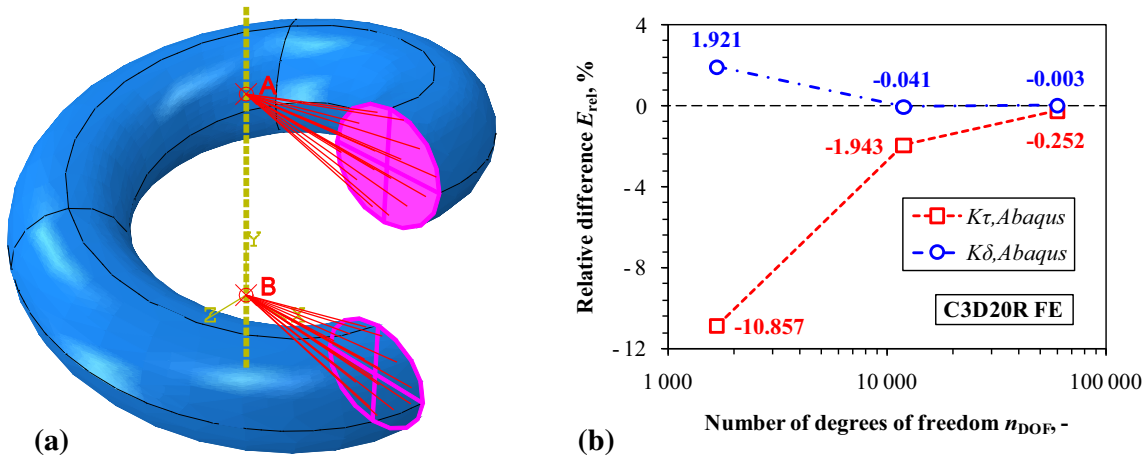| D (mm)	d (mm)	n (–)	l (mm)	E (GPa)	ν (–)
50	2–17	1	$2 \cdot d$	200	0–0.5

Fig. 3 *Abaqus* computational model, $n = 1$, $C = 50/17$, $\nu = 0.0$: **a** RPs (A, B) definition, **b** convergence study

model. Young's modulus denotes standard steel material properties. However, Poisson's ratio value is varied from $0 - 0.5$ in order to test the robustness and wide applicability of benchmarked displacement and stress correction factors.

Abaqus computational model consists of structured 3D second-order 20 node hexahedron continuum elements C3D20R FE mesh. The chosen mesh employs reduced integration and shows superior performance compared to first-order elements, due to additional nodes on mid-sides of finite element [40]. Structured mesh is enabled by partitioning 3D spring geometry accordingly. Preliminary analysis is defined as linear and quasi-static (i.e. time is dimensionless). Convergence study/mesh sensitivity check is performed beforehand, and it is found that eight second-order hexahedron elements per spring thickness (i.e. wire diameter d) give sufficiently accurate results for analysed linear deflection/stress class of problems.

Figure 3a shows the FEM model with the fully defined RPs A and B and kinematic couplings with highlighted surfaces. BCs are defined through two reference points (RPs) A and B, analogue to Fig. 1b. The moving-pinned and fixed-pinned conditions are assumed as they comply with open-coil analytical assumption where the pitch angle $\alpha \neq 0$ [1,2]. Full definition of BCs is: $B(u, v, w, \varphi_y = 0)$ and $A(u, w = 0)$. RPs A and B are coupled to belonging spring sides (i.e. outer highlighted surfaces) through kinematic attachment of type *distributing*. The imposed kinematic attachment allows for deformation of the connecting surfaces by using uniform weighting factors [40], i.e. surfaces coupled with RPs are still freely deformable. Special care is needed with employing such kinematic relations in the vicinity of high stress gradient locations since forcing additional rotational DOFs on otherwise 3-DOF per node continuum FE mesh can result with numerical anomalies and stress singularities in some cases.

Furthermore, referent FE model mesh convergence is reported in Fig. 3b. The convergence of model with zero Poisson's ratio (i.e. fully compressible material) is denoted herein. However, similar convergence behaviour is observed for arbitrary value of $\nu = 0-0.5$ which is hence not separately displayed.

As shown in Fig. 3a, relatively thick spring of small index $C = D/d = 50/17$ with sufficiently large pitch angle α is chosen as the representative model for convergence check. Arbitrary large force F_0 is acting on RP A. Displacement of RP A and maximum von Mises equivalent stress of the entire spring model are measured. Monotonous and quick convergence is observed in Fig. 3b. As expected, the deflections converge much quicker compared to calculated stresses. The relative error E_{rel} is defined as a difference between two successive meshes where every next mesh is considered as a referent solution and the previous mesh is a measured numerical solution, i.e. Equation $E_{rel} = (x_{(i+1)}/x_i - 1) \cdot 100\%$ holds. Since for this case analytical solution is unknown, more convenient term is still relative *difference* rather than relative *error*. Spring deflections and stresses are divided with nominal analytical deflection and stress solutions from Eq. (17) in order to obtain adequate
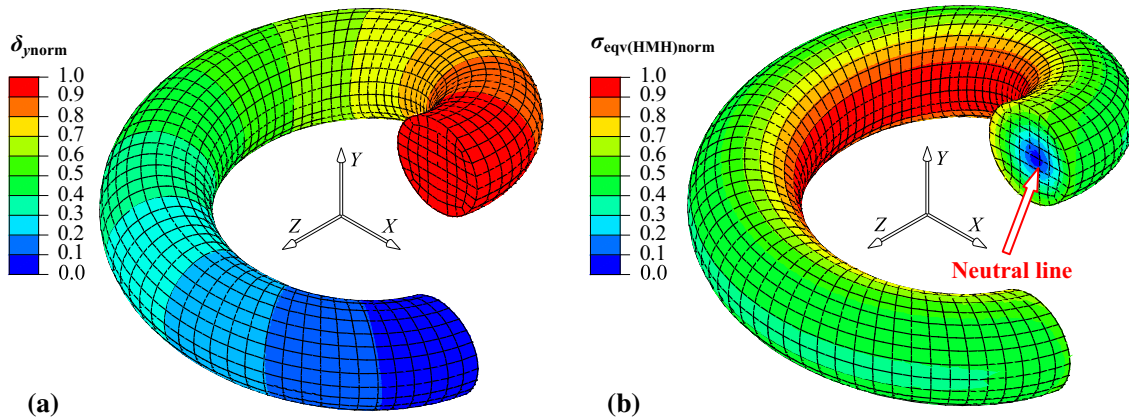
Fig. 4 *Abaqus* C3D20R normalized results: **a** deflection δ_{ynorm}, **b** equivalent stress $\sigma_{\text{eqv(HMH)norm}}$
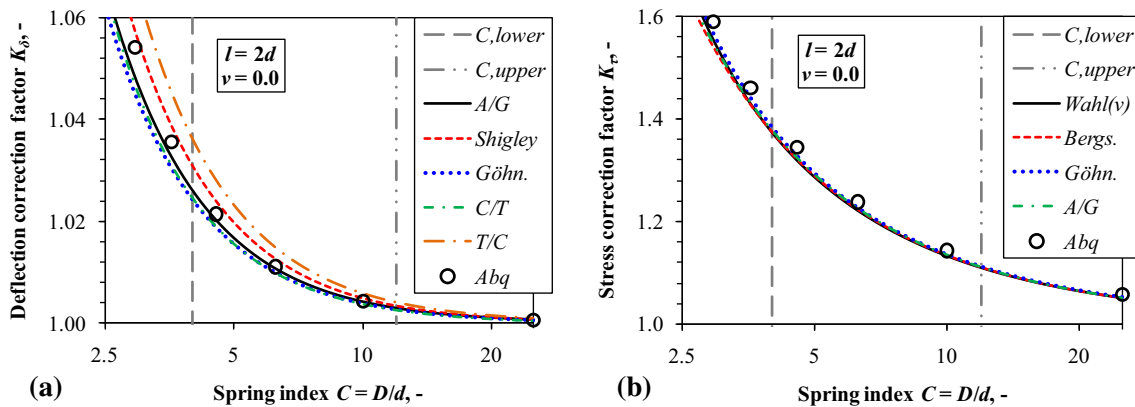

Fig. 5 Analytical and FEM correction factors, fully compressible, $\nu = 0.0$: **a** deflection correction K_δ, **b** stress correction K_τ

correction factors. Figure 4 shows *Abaqus* normalized deflection and stress results, respectively, for referent converged FE mesh.

Linear displacement field and relatively uniform, singularity-free stress field are observed through entire spring in Fig. 4. Homogeneity of the numerical stress field also implies that appropriate BCs are enforced in the model, and therefore, no stress singularities due to kinematic constraints or BCs occurred. It is also interesting to note the shift of the spring neutral line further away from the Y axis in Fig. 4b, also reported in [2]. As already observed by Timoshenko [8] and Wahl [1], maximum shear stress τ_{max} and corresponding equivalent von Mises stress $\sigma_{\text{eqv(HMH),max}}$ can be consequently observed at the inner side of the spring coil. That also agrees with *Abaqus* results in Fig. 4b. Thus, potential crack initiation location is uniformly identified nearest to the spring Y axis. As stress field is homogenous through entire isolated one coil numerical spring, the terminology of stress *correction* is favourable compared to stress *concentration*. The beneficiary effects of using relatively coarse and efficient but converged FE mesh needs to be highlighted.

Next, six parametric *Abaqus* models similar to one discussed beforehand are defined with regard to Table 2. The spring pitch $l = 2 \cdot d$ and incremental steps of $\Delta d = 3\,\text{mm}$ are applied. Eight FEs are used per spring thickness for obtaining accurate results according to Fig. 3b convergence guideline. Figures 5, 6 and 7 show comparison of selected best matching continuous analytical results and *Abaqus* results for six discrete C values ($C = 50/2; 50/5; 50/8; 50/11; 50/14; 50/17$) and three different values of Poisson's ratio ($\nu = 0; 0.3; 0.5$). Considered analytical expressions for deflection correction are: A/G, Shigley, Göhner, C/T and T/C. Furthermore, Wahl, Bergsträsser, Göhner and A/G stress correction analytical expressions are taken into account. Wahl stress correction is for this analysis considered to be Poisson's ratio ν dependent, i.e. Wahl = Wahl(ν) [2], as presented in Figs. 5, 6 and 7 legends. Vertical lines (C_{lower} and C_{upper}) denote practical spring index C limits. Circle markers represent *Abaqus* discrete results.

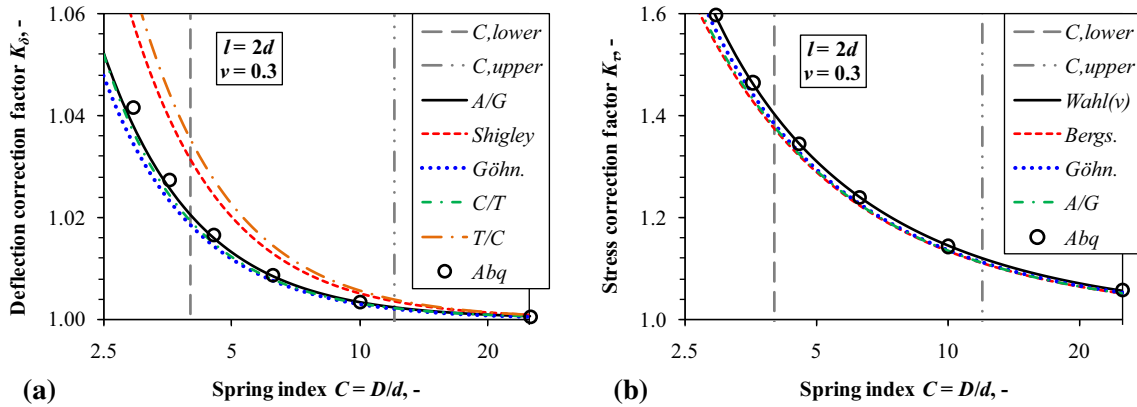**Fig. 6** Analytical and FEM correction factors, compressible, $\nu = 0.3$: **a** deflection correction K_δ, **b** stress correction K_τ
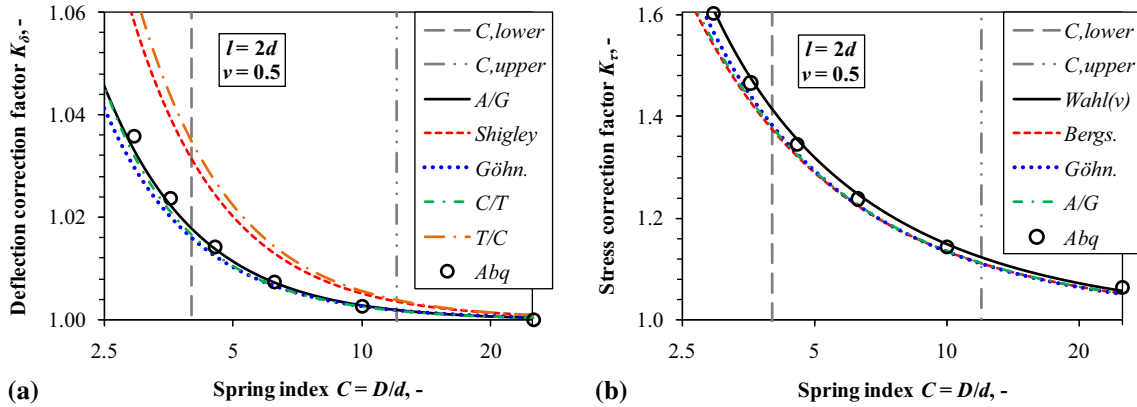

Fig. 7 Analytical and FEM correction factors, incompressible, $\nu = 0.5$: **a** deflection correction K_δ, **b** stress correction K_τ

For Poisson's ratio $\nu = 0$ (i.e. fully compressible material), the best correlation with FEM displacement is observed for A/G. Shigley and T/C overestimate while Göhner and C/T slightly underestimate FEM results. From the series of conducted analyses, it can be concluded that all authors show very similar results regarding obtained stress corrections and slightly underestimate FEM.

At the second test case, Poisson's ratio $\nu = 0.3$ (i.e. compressible material). The best agreement with displacements obtained via FEM is still observed for A/G. Shigley and T/C overestimate FEM even more compared to $\nu = 0.0$ test case. Considering the stress correction, Wahl now agrees rather closely with FEM. However, all the other authors still somewhat underestimate FEM.

Finally, for Poisson's ratio $\nu = 0.5$ (i.e. perfectly incompressible material) the best agreement with the FEM displacements is again reported for A/G. Shigley and T/C now overestimate FEM results much more compared to previous two cases. However, Göhner and C/T for all ν values constantly provide rather similar results compared to both A/G and FEM. Regarding stress correction factors, it is notable that for this test case Wahl somewhat overestimates FEM. Furthermore, all other authors continue to underestimate FEM, but Wahl is still closest to the FEM solution.

Considering this parametric analysis, A/G ($K_{\delta,\text{A/G}}$) deflection correction expression shows the best overall agreement with *Abaqus* model. Even though Göhner and C/T slightly underestimate the deflection, they can still be considered as a "reserve" or "backup" referent solution. Wahl ($K_{\tau,\text{Wahl}}$) stress correction expression agrees excellently with *Abaqus* model for $\nu = 0.3$ while Bergsträsser, Göhner and A/G constantly somewhat underestimate the stress field. However, they give almost identical mutual results. Based on the conducted numerical investigation, the currently adopted deflection and stress correction factors are

$$K_{\delta,\text{Ancker Goodier(A/G)}} = 1 - \frac{3}{16C^2} + \frac{3+\nu}{2(1+\nu)} \tan^2(\alpha), \quad K_{\tau,\text{Wahl}} = \frac{4C-1}{4C-4} + \frac{0.615}{C}. \quad (22a, b)$$
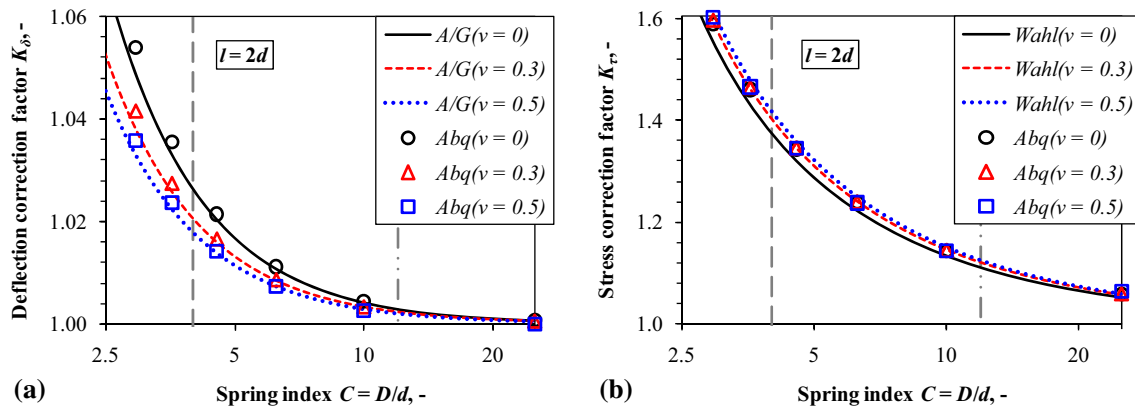
Fig. 8 Analytical and numerical correction factors, $\nu = 0-0.5$: **a** deflection correction K_δ, **b** stress correction K_τ
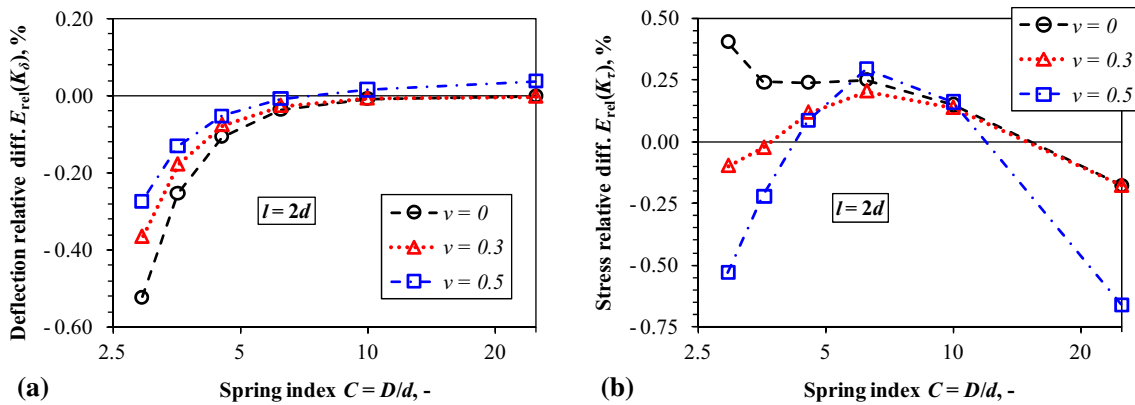

Fig. 9 Analytical and numerical correction factors relative difference E_{rel} comparison, $\nu = 0-0.5$: **a** deflection correction difference $E_{\text{rel}}(K_{\delta,A/G})$, **b** stress correction difference $E_{\text{rel}}(K_{\tau,\text{Wahl}})$

By inspecting Wahl expression from Eq. (22b), it should be noted that pitch angle α is not considered and $k_w = 0.615$ is hard-coded. Although, Wahl results still apparently show the all-around best agreement with FEM compared to solutions from other authors. Wahl correction is further examined. For comparison purpose, Poisson's ratio influence on deflection correction is summarized in Fig. 8a where differences are clearly visible, especially for lower spring indices C. Analytical A/G and numerical deflection correction solutions agree very well for all tested parametric cases. However, almost insignificant sensitivity of Poisson's ratio influence on *Abaqus* numerical stress correction can be detected by inspecting Fig. 8b. Thus, Eq. (22b) with fixed $k_w = 0.615$ (i.e. Wahl original solution) is adopted as approximate stress correction for further analyses.

In conclusion, both numerical and analytical (i.e. A/G) K_δ diminish with rising Poisson's ratio, even though numerical K_τ insignificantly rises with rising of Poisson's ratio for small α. That fact justifies excluding Poisson's ratio influence in further stress correction. Figure 9 correlates with Fig. 8 by denoting relative differences between analytical (A/G, Wahl) and numerical solutions for all given cases. Relative error/difference E_{rel} is well below $|1|\%$ for all shown parametric values. Largest differences in stress correction are observed for fully incompressible material (i.e. $\nu = 0.5$), especially for very high and low spring indices C presented in Fig. 9b.

Figure 10a shows relative difference between Wahl stress correction factors by varying Poisson's ratio ν. In order to check the relative differences for the other stress correction candidates (i.e. Bergsträsser, Göhner and A/G), they are contrasted to Wahl. The corresponding results are denoted in Fig. 10b. While comparing the obtained results (see Fig. 10b), the relative difference smaller than 2% is observed in most regions for practical C limits. Since much smaller relative difference $< |1|\%$ is achieved for FEM and Wahl comparison (see Fig. 9b), the selection of the Wahl stress correction factor is verified. The Wahl stress correction factor outperforms all the other authors based on the FEM results obtained herein.
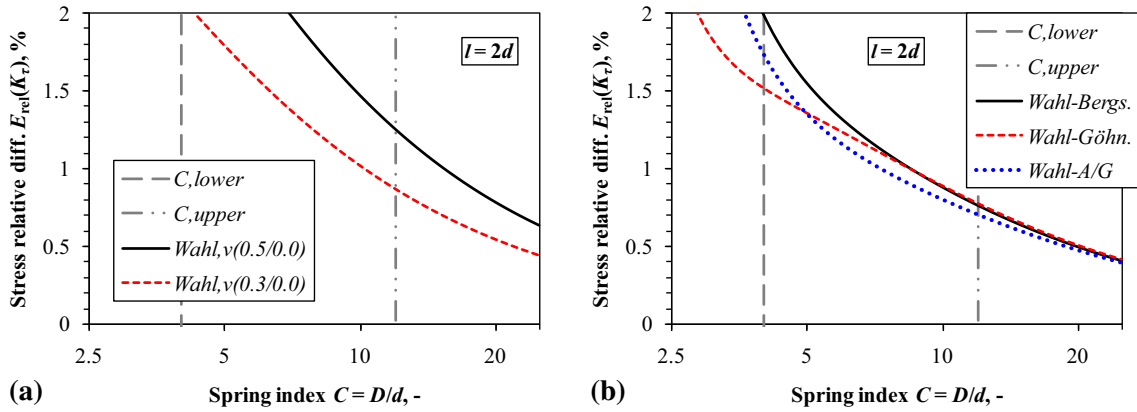
Fig. 10 Analytical stress correction factors relative difference $E_{\text{rel}}(K_\tau)$ comparison: **a** Wahl correction factor difference with respect to Poisson's ratio ν $E_{\text{rel}}(\nu)$, **b** Wahl correction factor difference with respect to Bergsträsser, Göhner and A/G
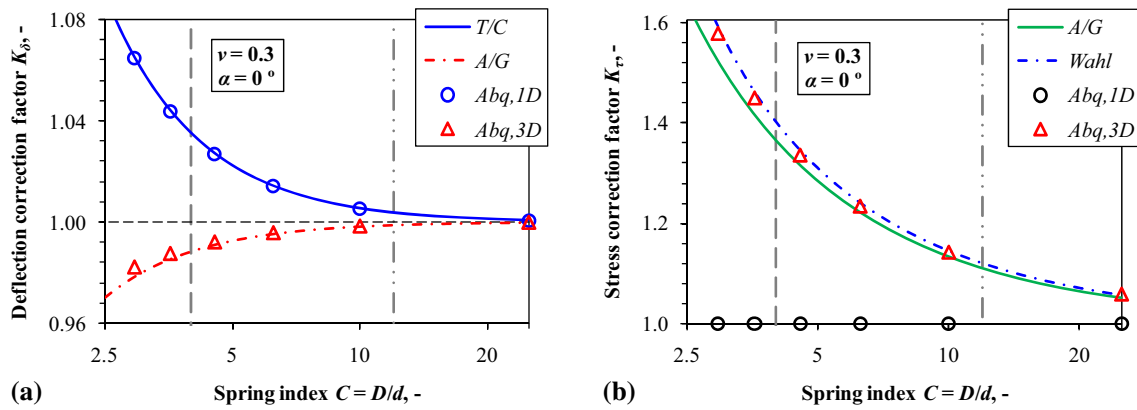

Fig. 11 Analytical and numerical 1D and 3D correction factors comparison, $\nu = 0.3$, $\alpha = 0$: **a** deflection correction K_δ, **b** stress correction K_τ

Finally, one specific case is used as a definitive benchmark for correction factors by setting the pitch angle $\alpha = 0$, analogue to the study conducted in [13]. Steel Poisson's ratio $\nu = 0.3$ is considered. A/G (i.e. Eq. (22a)) is again employed against *Abaqus* C3D20R solution. Derived T/C Eq. [2] is also evoked in order to contrast it with *Abaqus* B32 Timoshenko-based second-order beam elements. B32 FEs are formulated as shear flexible with quadratic interpolation [40]. It is interesting to compare these analytical and numerical solutions since *Abaqus* also uses Cowper [2] correction, according to [40]. From the analytical and numerical 1D and 3D correction factors, comparison (Fig. 11a) can be seen that A/G solution again follows *Abaqus* C3D20R (*Abq,3D* in legend) solution closely and that T/C derived solution matches *Abaqus* B32 (*Abq,1D* in legend) solution almost perfectly. For higher spring index C values, all analytical and numerical correction factors tend to unity. However, two concurrent solutions completely diverge for small spring indices C. Analytical and numerical 3D model even show concordant below unity trend. Analytical T/C solution is apparently correctly derived according to the thick beam theory [2] as it agrees with the corresponding Timoshenko beam FE element solution. However, T/C solution should not be used in the context of approximating real, thick cylindrical springs with small indices C because it overestimates the spring compliance. The trends reported in Fig. 2 already suggested aforementioned. Additionally, Fig. 11b demonstrates that beam elements (*Abq,1D* in legend) expectedly cannot capture stress correction because the value constantly remains at unity for any C value. Interestingly, numerical values for zero pitch angle (*Abq,3D* in legend, triangle symbol) now lie in between Wahl and A/G stress correction factors which implies that Wahl stress correction solution may be overly conservative when pitch angle $\alpha \approx 0$.

In summary, setting $\nu = 0$ underestimates the numerical stresses while setting $\nu = 0.5$ somewhat overestimates the numerical stresses considering generalized Wahl equation from Table 1. By setting $\nu = 0$, Wahl yields almost identical results to A/G, Göhner and Bergsträsser stress correction factors as demonstrated in

Fig. 5b. Keeping in mind that smaller spring index C results with larger stresses and deflections, the question of larger pitch angle α influence still remains unanswered.

A/G model is now firmly adopted for deflection correction. Furthermore, Wahl *approximate* model with fixed $k_w = 0.615$ is finally adopted for stress correction although it is a bit deficient according to performed parametric investigation. However, the advantage of the Wahl equation is that it best coincides with the current FEM solutions which embody relatively small, but nonzero pitch angle α. The main concern is whether the linear numerical solution should be considered as a referent one, compared to other available analytical/empirical/approximate models. In order to obtain objective/nonbiased numerical results, alternate linear FEM solver *Catia, Elfini* [42] is also employed for double checking of *Abaqus* computational accuracy, analogue to method used in [39]. *Catia Elfini* solver matches *Abaqus* numerical results rather closely for both 3D continuum solution and 1D Timoshenko beam-based solution. Thus, it is not separately shown, nor further discussed in detail. Moreover, it reassures about the accuracy of both adopted approximate correction factors and *Abaqus* detailed computational model. The implied correct choice of employing A/G for deflection correction and Wahl for stress correction used in previously published results [2] is confirmed.

5 Example: inerter-based isolator helical spring vibration fatigue optimization study

In this chapter, vibration optimization and fatigue analysis are performed on a general 2-DOF system shown in Fig. 1a. Table 3 shows parameters used in the isolator optimization process example. While following recommendations given in [2], the system is detuned (i.e. $m_2 k_1 \neq m_1 k_3$) and the spring k_2 is compliant compared to springs $k_{1,3}$.

The mass parameter value is chosen as $m_0 = 100$kg and spring stiffness k_0 is yet to be determined from helical spring parameters proposed in Table 4. Material parameters (E, ν, S'_f and B) of the spring in this example are chosen in such way to represent physical elastic and fatigue properties of regular, common steel, adopted from [2].

Diameters D and d are chosen so $C = D/d = 50/17 \approx 2.941$ in order to provide a very small spring index. However, such small spring index C results with a relatively large stress correction factor which makes it a convenient fatigue benchmark. The ideal *massless* springs are considered for simplicity and straightforwardness. Spring stiffness is calculated according to introduced Eq. (17a) where $K_\delta F_0 = k_0 \delta_{\text{nom}}$. Obtained 2-DOF key values/factors and optimized parameters are listed in Table 5. Equations (12–16) are used in the process of optimization. Velocity amplitude optimization results are taken from [2]. Some differences in obtained parameters with regard to optimization criterion are observed. Hence, it will be interesting to observe the impact of those differences to fatigue life assessment.

Figure 12 shows contour-plotted normalized results of the optimization process with regard to Table 5 for the prescribed parameters defined in Tables 3 and 4. The minimum (i.e. optimum $\mathcal{H}_2$) indices $I_{\mathcal{H}2norm}$ are represented as diamond markers. The contours of displacement-based optimization (Fig. 12a) and velocity-based optimization (Fig. 12b) are rather similar as expected from the results denoted in Table 5. Darker contours in both plots imply regions of higher $\mathcal{H}_2$ index (i.e. undesired effect). Dash-dotted curved lines denote implicit plots of function c_2 when $b_2 \neq 0$, i.e. Eqs. (12) and (15), respectively. Circles at the bottom of the both figures correspond to the optimized damping case c_{opt} when $b_2 = 0$, defined in Eqs. (14) and (16). Finally, diamond markers denote the position of both optimized damping c_{opt2} and inertance b_2 simultaneously from Eq. (13a, b) and previously omitted equations for the velocity-based optimization due to extensive length [2,35].

Table 3 Example 2-DOF vibration isolation system parameters [2]

m_1 (kg)	m_2 (kg)	k_1 (N/mm)	k_2 (N/mm)	k_3 (N/mm)	F_0 (kN)
m_0	$2 \cdot m_0$	k_0	$k_0/10$	k_0	1

Table 4 Example helical spring of stiffness k_0 geometric and material properties [2]

D (mm)	d (mm)	n (–)	l (mm)	E (GPa)	ν (–)	S'_f (MPa)	B (–)
50	17	1	$2 \cdot d$	200	0.3	925	-0.1

(a)

Damping coefficient c_2, Ns/m·10^3

(b)
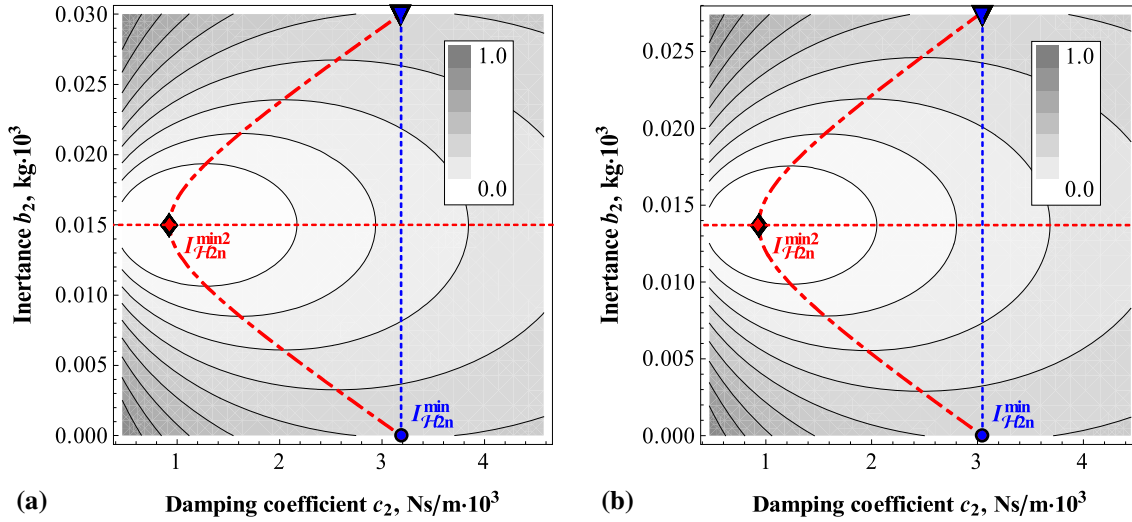
Damping coefficient c_2, Ns/m·10^3

Fig. 12 Mass m_2 normalized $\mathcal{H}_2$ index $I_{\mathcal{H}2\mathrm{norm}}$: **a** displacement index $I_{\mathcal{H}2\mathrm{norm}}(x_0)$, **b** velocity index $I_{\mathcal{H}2\mathrm{norm}}(v_0)$

Table 5 Example 2-DOF vibration isolation system referent values and optimized parameters

$C = D/d$ (–)	α (°)	k_0 (N/mm)	Displacement amplitude opt. $\mathcal{H}_2(x_0)$			Velocity amplitude opt. $\mathcal{H}_2(v_0)$		
			c_{opt} (Ns/m)	b_{opt} (kg)	$c_{\mathrm{opt}2}$ (Ns/m)	c_{opt} (Ns/m)	b_{opt} (kg)	$c_{\mathrm{opt}2}$ (Ns/m)
2.941	12.213	6 190.746	3 185.270	15.000	927.268	3 047.314	13.701	934.329

Table 6 Example 2-DOF vibration isolation system numerical values and relative difference comparison

Method	K_δ (–)	E_{rel} (%)	K_τ (–)	E_{rel} (%)
Analytical	1.037789623	−0.365	1.595594406	−0.097
Abaqus	1.04159154		1.597138873	

Consequently, diamond markers are located at the lightest region centre as they represent the global minimum of the displacement and velocity-based functions from Eq. (9).

The upper limit of the plots is defined as $b_{2\mathrm{max}} = 2b_{\mathrm{opt}}$. Furthermore, *bow and arrow*-like shapes outline the contours. Implicit functions from Eqs. (12) and (15) denote dashed-dotted *bow* while horizontal dashed lines $b_2 = b_{\mathrm{opt}}$ denote *arrow* and vertical dashed lines connecting circle with down-pointing triangle shown at the top with the corresponding coordinates $\nabla(c_{\mathrm{opt}}, 2b_{\mathrm{opt}})$ denote *string*. Similarly shaped contour optimization diagrams are reported in [2,35]. In conclusion, dash-dotted *bow* curve connects all three markers: circle, diamond and triangle.

Next, the analytical and numerical quasi-static results are compared for the displacement and stress correction. Results are shown in Table 6 with the corresponding maximum relative difference $E_{\mathrm{rel,max}} < 0.4\%$.

Although only minor discrepancies are observed for this static benchmark case, it should be noted that the vibration fatigue study conducted in the further investigation depends exponentially (Basquin) on both displacement and stress simultaneously as witnessed from structure of Eq. (21). Thus, special considerations are taken into account in the following.

With that in mind, two separate *Abaqus* vibration fatigue models are defined. First model is simplified and denotes closely Fig. 1a. Instead of *real* continuum helical spring k_3 analogue to Fig. 1b, a single 3D C3D8R first-order hexahedron continuum element with reduced integration is employed. It is acting as a simple truss/rod connector element which serves as both equivalent stiffness and fatigue stress concentrator. In order to approximate the *real* 3D spring presented in Fig. 1b, an equivalent *ideal* spring is defined by matching both stiffness k_0 and equivalent stress $\sigma_{\mathrm{eqv(HMH),max}}$ of the original spring which are prescribed as equal. This is performed in order to verify proposed dynamic procedure regardless of the chosen deflection and the stress correction accuracy. For pure normal axial load, stiffness and stress equations for truss can be, respectively, written as
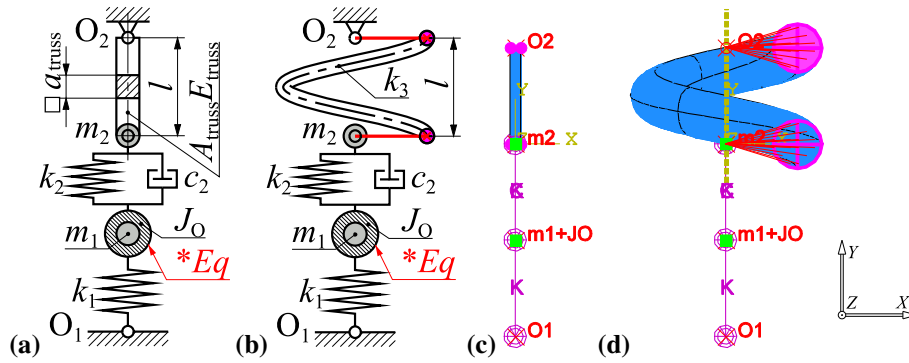
Fig. 13 2-DOF *Abaqus* isolator FE models: **a** *ideal* scheme, **b** *real* scheme, **c** *ideal* screenshot, **d** *real* screenshot

$$k_{\text{truss}} \equiv k_0 = \frac{A_{\text{truss}} E_{\text{truss}}}{l}, \quad \left|\sigma_{\text{eqv(HMH),max}}\right| \equiv |\sigma_{0\text{n}}| = \frac{k_0}{A_{\text{truss}}} |x_{02}|, \quad \text{(23a, b)}$$

where $A_{\text{truss}} = a_{\text{truss}}^2$ is truss axial quadratic surface area and E_{truss} is an equivalent Young's modulus of the truss. Since stress is uniaxial, equivalent stress amplitude $\sigma_{\text{eqv(HMH)}}$ according to von Mises is equal to normal stress amplitude $\sigma_{0\text{n}}$. Thus, the truss equivalent parameters follow from equalling Eqs. (23a, b) with previously established stiffness and stress relations for helical spring which consider both deflection and stress correction factors i.e.

$$k_{\text{true}} \equiv k_0 = \frac{1}{K_\delta} \frac{Gd}{8C^3 n}, \quad \left|\sigma_{\text{eqv(HMH),max}}\right| = \sqrt{3} K_\tau |\tau_{\text{nom}}| = \sqrt{3} \frac{K_\tau}{K_\delta} \frac{G}{C^2 n\pi d} |x_{02}|. \quad \text{(24a, b)}$$

Solving for the two unknowns from Eqs. (23–24) yields $E_{\text{truss}} \approx 15075.385$ MPa and $a_{\text{truss}} \approx 3.737$ mm. *Ideal* and *real Abaqus* isolator FE models are shown in Fig. 13. The model schematics are denoted in Fig. 13a, b, while Fig. 13c, d illustrates actual *Abaqus* FE model screenshots.

In *Abaqus*, springs $k_{1,2}$ and dashpot c_2 are utilized through *SpringA* and *DashpotA* FEs, respectively. They add axial spring/dashpot between the two nodes whose line of action is the line joining the two nodes [40]. *Abaqus* does not yet possess ideal inerter functionality which is similar to ideal spring/dashpot. Hence, analogue to Smith original rack and pinion inerter concept [4] the required optimum inertance b_{opt} is utilized alternatively by defining discrete dynamic inertia moment J_O and using embedded *Abaqus* *Equation* functionality. The imposed feature ties relative nodal displacement between masses m_1 and m_2 to rotation of inertia J_O through custom created relation

$$r_{\text{unit}} = 1\,m \Rightarrow r \cdot \underbrace{\varphi_z(J_O)}_{\text{DOF6}} - \underbrace{y_1(m_1)}_{\text{DOF2}} + \underbrace{y_2(m_2)}_{\text{DOF2}} = 0, \quad \text{(25)}$$

where nodal displacement y is measured in metres and nodal rotation φ_z is measured in radians. Equation (25) implies that if using SI units, one metre relative displacement between masses m_1 and m_2 yields one radian rotation of J_O. If the relative displacement between the two terminals (i.e. masses m_1 and m_2) is zero, no rotation occurs and inerter does not contribute to functionality of the isolator. Consequently, dynamic moment of inertia J_O in current configuration serves as an ideal inerter whose inertia characteristics can be calculated according to a simple expression

$$J_O = b_{\text{opt}} \cdot r_{\text{unit}}^2. \quad \text{(26)}$$

By adopting convenient unit radius $r_{\text{unit}} = 1$ m, dynamic moment of inertia for the displacement-based optimization is $J_O = 15$ kg m^2 and $J_O \approx 13.701$ kg m^2 for the velocity-based optimization (Table 5). Moreover, it can be concluded that $J_O \propto b_{\text{opt}}$ and stated that Eqs. (25, 26) are exact for both small and large rotation effects.

In *Abaqus*, *Lánczos* method is used as eigensolver. *Steady-state dynamics*, *Direct Step* is employed for obtaining linear response in frequency domain analogue to direct method Eq. (4). In order to obtain sufficient visual resolution of results, 500 equally spaced discrete frequency steps per analysis are requested. First, velocity-based optimization results from [2] and Sect. 2.1 are taken into account. Figure 14 denotes comparison
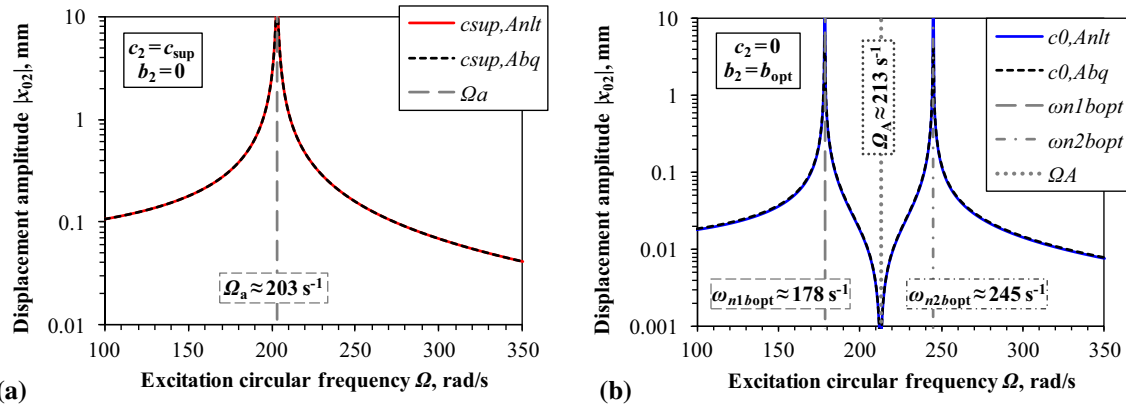
Fig. 14 Mass m_2 displacement amplitudes $|x_{02}|$ comparison: **a** super-optimal damping, **b** optimal inertance, no damping
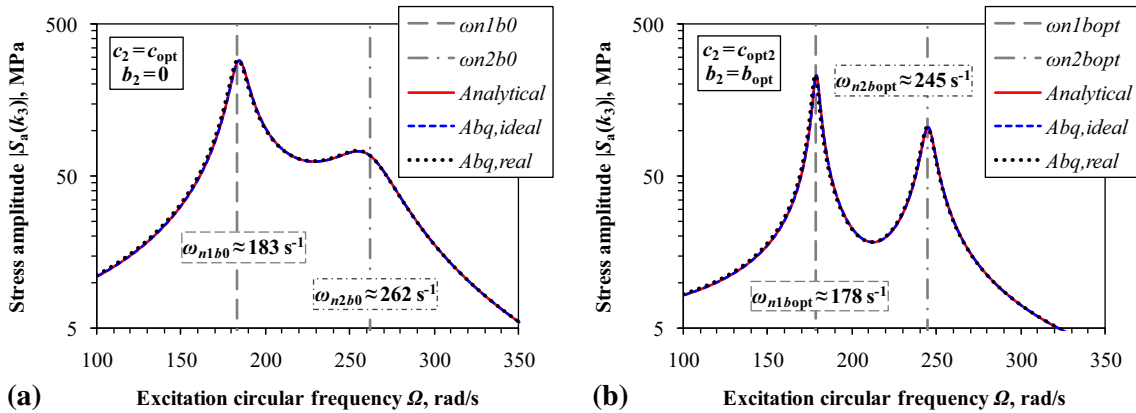

Fig. 15 Spring k_3 stress amplitudes $|S_a(k_3)|$ comparison: **a** optimal damping, **b** optimal damping and inertance

of the analytical and *Abaqus ideal* models from Eq. (23a, b) for mass m_2 displacement amplitudes. Two extreme cases are taken under consideration. The first case includes super-optimal extremely high damping $c_{\text{sup}} = 100 \cdot c_{\text{opt}}$. It effectively locks the isolator and produces new resonance Ω_a (Fig. 14a) from Eq. (11b). The second test case sets zero damping $c_2 = 0$ and considers optimal inertance $b_2 = b_{\text{opt}}$ which unveils anti-resonance Ω_A (Fig. 14b) from Eq. (11a). Since damping c_2 in Fig. 14b is prescribed to zero, responses at natural frequencies tend to infinity at eigenvalues obtained from Eq. (10). All desired effects, previously derived analytically [2,35], are successfully captured by FEM solutions. *Abaqus ideal* and *real* models yield almost the same displacement amplitudes results. Hence, they are purposely not distinguished here.

Figure 15 shows comparison of analytical, *Abaqus ideal* and *Abaqus real* models for spring k_3 stress amplitudes in fatigue nomenclature $|S_a(k_3)|$. Optimum damping c_{opt} and inertance b_{opt} parameters for the velocity-based optimization from Table 5 are considered. A very good agreement is observed between all models. Thus, the correct numerical inerter implementations and approximately correct displacement and stress correction factors adoption for analytical calculations is strongly implied. There is virtually no discrepancy noted between analytical and *Abaqus ideal* models.

Fe-Safe [41] software suite is further employed with *von Mises* criterion evoked for fatigue analysis. The converged FEM complex nodal stress amplitudes from *Abaqus* are taken into account for the most destructive frequency (*i.e.* first natural frequency where $\Omega = \omega_{n1}(b_{\text{opt}})$). Custom created *Fe-Safe* material $S - N$ (*i.e.* Stress amplitude–No. of cycles to fatigue) curve [2,41] is defined with respect to parameters S_f' and B (Basquin) from Table 4. The entire *ideal* and *real* FE spring models are analysed. Figure 16 shows the final results of performed HCF *real* spring analysis for the velocity-based optimization, analogue to [2]. Explicit Basquin's curve $S_a = S_f' \cdot (N_f)^B$ is superimposed and shown as inclined dashed line in Fig. 16. The presented curve is ranged from 10^3–10^7 fatigue life cycles.

Figure 16b shows particular vibration fatigue life results of *real* spring, post-processed in *Abaqus*. Analogue to analytical solution [1,2,8], the shortest fatigue life is expected on the inner-coil side of spring numerical
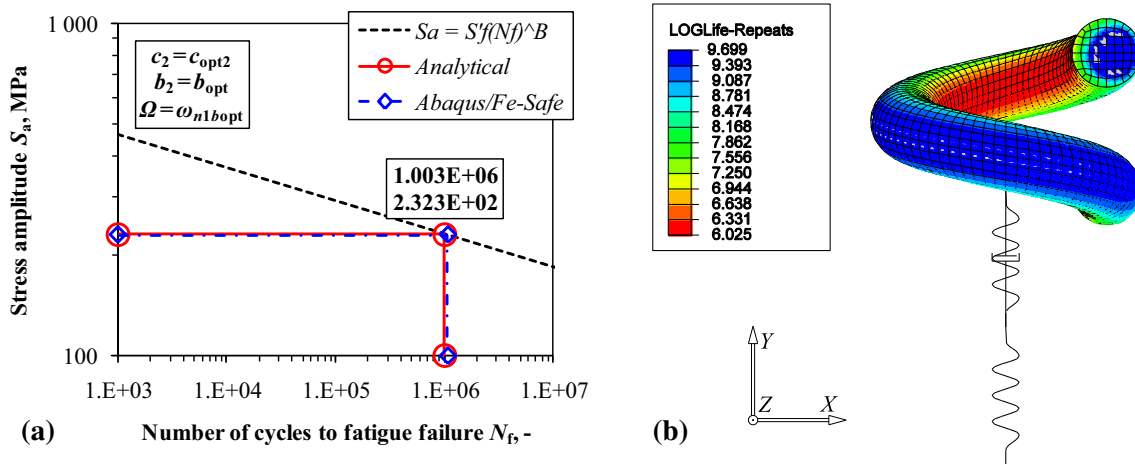
Fig. 16 *Real* spring k_3 fatigue life: **a** number of cycles to failure $N_f(k_3)$, **b** *Abaqus/Fe-Safe* $N_f(k_3)_{(log)}$

Table 7 Vibration fatigue optimization study analytical and numerical results comparison for $c_2 = c_{opt2}$ and $b_2 = b_{opt}$

Method	ω_{n1} (s^{-1})	E_{rel} (%)	ω_{n2} (s^{-1})	E_{rel} (%)	$|x_{02}(\omega_{n1})|$ (mm)	E_{rel} (%)	$S_a(\omega_{n1})$ (MPa)	E_{rel} (%)	$N_f(\omega_{n1})|$ (−)	E_{rel} (%)
Analytical	178.373	–	244.852	–	0.524	–	232.281	–	1,002,949	–
Abaqus/ideal	178.373	0.000	244.852	0.000	0.524	0.000	232.281	0.000	1,002,945	0.000
Abaqus/real	178.076	0.167	244.852	0.000	0.522	0.368	230.998	0.556	1,060,086	− 5.390

model. *Abaqus/Fe-Safe* LOGLife legend shows homogenous life field *scaled* according to expression [41]

$$(N_f)_{LOGLife-Repeats} = \log_{10}(N_f) \Leftrightarrow N_f = 10^{(N_f)_{LOGLife-Repeats}}, \qquad (27a, b)$$

where actual minimum number of cycles N_f compared to analytical results is shown in Table 7. These results correspond to the velocity-based optimization study conducted in [2]. Rigid benchmark method is adopted herein. All the results are compared for analytically calculated natural frequencies $\omega_{n1(Anlt)}$.

By comparing analytical and *Abaqus ideal* model, the difference $E_{rel} \approx 0.000\%$ can be observed for all quantities. With regard to number of cycles N_f, only negligible numerical rounding error occurred. However, some minor discrepancies can be observed while comparing analytical and *Abaqus real* model. It is necessary to emphasize that smaller differences are noted in Table 6 for the displacement and stress correction factors if compared to differences observed in Table 7 for displacement $|x_{02}(\omega_{n1})|$ and stress $|S_a(\omega_{n1})|$ amplitudes, respectively. In conclusion, it is important to point out that these are a cumulative consequence of mismatch between the fundamental natural frequency ω_{n1} obtained analytically and numerically.

The results for the stress amplitude $S_a(\omega_{n1})$ reported in Table 7 differ by only ~0.556%; however, difference is magnified in fatigue analysis to considerably larger $\sim |5.390|\%$. This is due to the fact that Eq. (21) presents exponential relation where small differences in stress yield with much larger dissipation for general fatigue analysis results. By taking into account stress amplitude $S_a(\omega_{n1}) \approx 230.998$ MPa computed by *Abaqus*, difference between hand calculated fatigue from Eq. (21a) and the one from FE complex nodal stress and *Fe-Safe* results now completely vanishes, i.e. falls to $E_{rel} \approx 0.000\%$. Hence, only analytical computational error lies in the helical spring adopted displacement and stress *approximate* correction factors (i.e. $K_{\delta,A/G}$ and $K_{\tau,Wahl}$). As a final consequence, analytical results are now on the safety side and provide more conservative approximate fatigue life assessment compared to FEM.

In the following, four specific optimized cases are considered regarding Table 5. The displacement-based optimization parameters with (b_{opt}) and without inerter (b_0), and the velocity-based optimization parameters with (b_{opt}) and without inerter (b_0) are taken into account. Comparison of analytical and FEM results is shown in Table 8. Influence of inerter on circular natural frequencies is presented, and it can be observed that due to the added apparent mass—frequencies diminish. Results are reported for the most destructive, e.g. first resonant excitation frequency where $\Omega = \omega_{n1(Anlt)}$.

Very good agreement is generally observed in Table 8. Analogue to results denoted in Table 7, *Abaqus ideal* spring results show almost no relative error compared to analytical solution with the exception of small

Table 8 Vibration fatigue displacement and velocity optimization study analytical and numerical result comparison

| Method	Displacement amplitude optimization $\mathcal{H}_2(x_0)$					Velocity amplitude optimization $\mathcal{H}_2(v_0)$				
	Ω (s^{-1})		E_{rel} (%)	$N_f(\Omega)$ (–)	E_{rel} (%)	Ω (s^{-1})		E_{rel} (%)	$N_f(\Omega)$ (–)	E_{rel} (%)
Analytical	ω_{n1b0}	183.017	–	170,956	–	ω_{n1b0}	183.017	–	134,540	–
Abaqus/ideal		183.017	0.000	170,963	− 0.004		183.017	0.000	134,544	− 0.003
Abaqus/real		182.714	0.166	160,733	6.361		182.714	0.166	126,690	6.196
Analytical	$\omega_{n1b\mathrm{opt}}$	177.885	–	3,669,242	–	$\omega_{n1b\mathrm{opt}}$	178.373	–	1,002,949	–
Abaqus/ideal		177.885	0.000	3,669,457	− 0.006		178.373	0.000	1,002,945	0.000
Abaqus/real		177.588	0.167	3,870,106	− 5.190		178.076	0.167	1,060,086	− 5.390
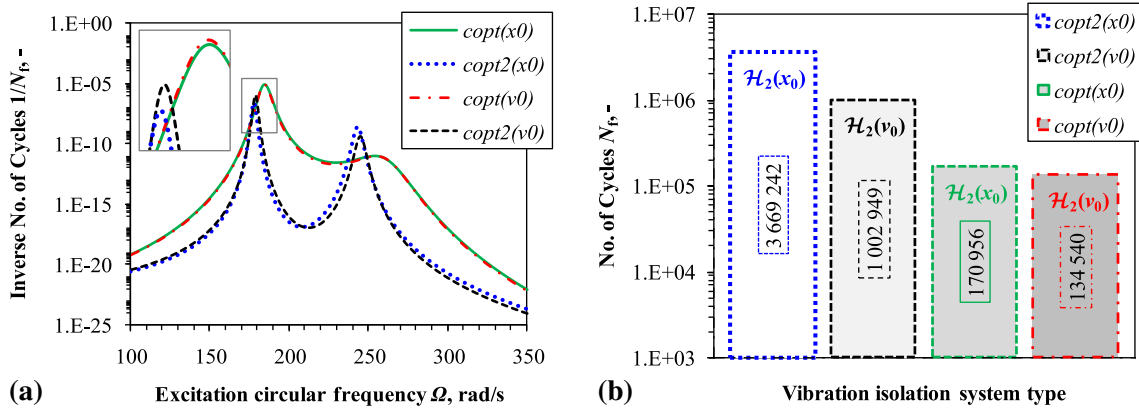
Fig. 17 Spring k_3 number of cycles to fatigue failure $N_f(k_3)$: **a** $1/N_f(\Omega)$ FRFs, **b** $N_f(\omega_n1(\mathrm{Anlt}))$

fatigue life assessment errors attributed to numerical rounding. Taking into account *Abaqus real* spring results, natural frequencies always seem to be a bit lower compared to analytical solution. Larger discrepancies are observed for fatigue calculation as a result of mismatch. If the inerter is present in the isolator, analytical results yield with more conservative fatigue life assessment compared to FEM. However, excluding the inerter from the isolator leads to less conservative analytical fatigue results compared to FEM.

Results are recapitulated and visually presented in Fig. 17. Inverse number of cycles to fatigue as a function of circular excitation frequency is shown in Fig. 17a for all four cases. The small rectangular detail represents range of response for near-resonant conditions. This detail also implies that the highest $1/N_f$ FRF peaks correspond to the lowest fatigue life. Labels c_{opt2} in legend imply both optimum damping and optimum inertance b_{opt}. Cases without inerter and with optimum damping (i.e. $c_{\mathrm{opt}}(x_0)$ and $c_{\mathrm{opt}}(v_0)$) almost cannot be visually distinguished, except near resonance conditions as shown in rectangular detail. Improvements are observed for optimum damping c_{opt2} and inertance b_{opt}, compared to only optimum damping c_{opt} on almost all frequencies, except in the vicinity of the second natural frequency $\omega_{n2b\mathrm{opt}}$. Bar chart shown in Fig. 17b denotes the most conservative criterion (i.e. number of cycles in resonant conditions) which corresponds to Table 8. It is organized as follows: bars are aligned so that the highest number of achieved life cycles is positioned far left and the lowest number of cycles is positioned right. The line dashing and colour definition of the FRFs (Fig. 17a) corresponds to line dashing and colour of bars (Fig. 17b).

As expected, displacement-based optimization criterion $\mathcal{H}_2(x_0)$ yields general further improvement compared to velocity-based criterion $\mathcal{H}_2(v_0)$ previously proposed in [2]. This is true for the test cases with and without inerter. Moreover, by inspecting results from Table 8 and Fig. 17b, improvements are much more pronounced for the displacement-based optimization compared to velocity-based optimization when utilizing combined optimum damping c_{opt2} and inertance b_{opt}. For the velocity-based optimization, over 1 million cycles are achieved [2]. However, for herein proposed displacement (i.e. fatigue)-based optimization, over 3.5 times more cycles are achieved. It can be considered as further substantial improvement. Thus, for shown family of vibration isolation systems it is justifiable to include inerter in the isolator and perform displacement-based optimization analysis if stress of coupling elastic components is of crucial importance.

It can finally be concluded that spring correction factors used in the context of this study and embedded in the analytical method provide sufficiently correct approximate solution compared to FEM. However, it should be noted that this direct dynamic stiffness analytical method provides for more transparent solution

and computationally inexpensive model. That is especially evident when compared to direct FEM solution. If the *real* spring model is considered for the range denoted in Fig. 15, computational process takes considerable amount of time on high-end PC desktop computer. At first glance, relatively simple FEM model is utilized. However, due to complex *real* spring geometry and many additional kinematic relations, the incremental numerical process in frequency domain tends to get saturated and rather slow. This only includes *Abaqus* complex stress direct computation, where *Fe-Safe* takes additional/considerable CPU time for PSD-based fatigue life calculation. Moreover, analytical expressions derived and used throughout this investigation are approximately true even for continuous systems with distributed mass across the spring with the assumption that ratios between spring mass to primary and secondary mass are small. This makes proposed analytical method more appealing and time effective for this class of systems.

Considering that pitch angle in this study is defined through relation $l = 2 \cdot d$ and $\alpha = \arctan[l/(\pi D)]$, it would be logical to further investigate the influence of arbitrary large pitch angle α on deflection and stress correction. The future study notably applies to further testing of Wahl approximate stress correction factor in detail as it does not contain the pitch angle in its formulation, compared to, for example, A/G. On the other hand, it is reassuring that Wahl currently demonstrates the highest accuracy compared to FEM for a wide variety of tested parameters. Additionally, the method proposed in this work could find its applicability on other types of springs used in suspension systems (e.g. leaf springs) [1,43]. Automobile leaf spring can act as both road shock absorber and carrier of lateral loads [1]. Thus, it could prove beneficiary to examine the effects of including both helical and leaf spring in conjunction with inerter in the isolator. Moreover, simplified analytical leaf spring vibration fatigue model analogue to one proposed in the scope of this investigation may be established.

6 Conclusion

A novel cylindrical helical spring solely displacement-based (i.e. vibration fatigue-based) $\mathcal{H}_2$ optimization method for inerter-based vibration isolation system is presented in this paper. The analysed spring couples receiving body (i.e. mass that needs to be isolated from vibrations) to the fixed ground. The optimization method is based on the previous findings which imply that the stresses in the spring are directly proportional to spring maximum displacement amplitudes. Power spectral density principle in the broadband frequency domain is employed for spring life assessment and complemented with the direct inversion of dynamic stiffness matrix method. The efficiency of the proposed method is studied on a two degree-of-freedom system which represents reduced-order model of a potentially much more complex general dynamic system. Results are compared to previous study which was based on broadband minimization of the specific kinetic energy as a vibration optimization criterion. Substantial improvement regarding prolonging spring high-cycle fatigue life is observed by utilizing currently proposed method.

Two types of referent isolators are studied throughout the paper. First referent isolator incorporates optimal inerter and optimal viscous damping, while the second one contains only the optimal damping (i.e. inerter is excluded). Based on the previous research, it is confirmed that simultaneous optimization of isolator damper and inerter connected in parallel convincingly outperforms any isolator configuration that contains only damper (i.e. system without inerter). Furthermore, in the scope of this work it is additionally reported that displacement-based optimization always outperforms kinetic energy (i.e. velocity-based) optimization if the ground-coupling spring fatigue life of the receiving body is a primary optimization criterion objective.

Spring deflection and stress correction factors from the referent literature are benchmarked versus finite element method. Previously derived approximate Timoshenko/Cowper displacement correction factor based on the strength of materials principles assumption, thick shear-deformable Timoshenko beam theory and enriched with Cowper shear correction is set to test against finite element method. It is found that proposed deflection correction factor matches excellently with the beam-based finite element solution. However, the obtained results are completely divergent compared to theory of elasticity based on approximate Ancker and Goodier solution and complementary continuum finite element method solution alike. Thus, it can be concluded that beam-based theory is not appropriate and should not be used for helical spring calculation, especially for small spring indices. The most convenient correction factors are adopted for further vibration fatigue study based on benchmark comparison results. Ancker and Goodier factor is confidently adopted for the spring displacement correction, while for the spring stress correction, Wahl factor is conditionally adopted. Despite the fact that some discrepancies and inconsistencies were found in the formulation of the Wahl stress correction factor, the parametric analyses and comparisons with numerical solutions have apparently shown the best agreement with adopted Wahl stress correction solution.

Previously introduced simplified analytical method for calculating cylindrical spring high-cycle fatigue life is verified herein by comparing the analytical and finite element method results. The proposed method employs von Mises energy criterion for shear-governed biaxial proportional stress and Basquin's relation. The only reported discrepancies between the analytical and numerical methods are related to adopted approximate displacement and stress correction factors. Otherwise excellent agreement is noted between the two employed methods.

Furthermore, the optimum inertance concept is integrated into finite element-based numerical solution by following the original rack and pinion analogy taken from Smith. Moreover, an excellent agreement with analytical solution is reported. The novel inerter-induced effects (e.g. anti-resonance of the receiving body and reduction in natural frequencies) are successfully reproduced within finite element-based solution.

The future work regarding investigation presented herein will be to further study the influence of much larger spring pitch angles on the displacement and stress fields. Consequently, a more general correction models could be developed with the aim to capture both small spring index and large pitch angle effects simultaneously. Finally, the alternate ways of implementing the both ideal inerter (e.g. massless) and real inerter into a more general and robust finite element-based solution will be investigated. In the future, possible benefits of additionally including the leaf spring in the inerter-based isolator with regard to absorbing shocks and carrying lateral load could be studied.

References

1. Wahl, A.M.: Mechanical Springs, 1st edn. Penton Pub. Co., Cleveland (1944)
2. Čakmak, D., Wolf, H., Božić, Ž., Jokić, M.: Optimization of an inerter-based vibration isolation system and helical spring fatigue life assessment. Arch. Appl. Mech. 1–14 (2018). https://doi.org/10.1007/s00419-018-1447-x
3. Rao, S.S.: Mechanical Vibrations, Sixth Edition in SI Units, Global Edition. Pearson, London (2017)
4. Smith, M.C.: Synthesis of mechanical networks: the inerter. IEEE Trans. Autom. Control **47**(10), 1648–1662 (2002)
5. Bishop, N.W.M., Sherratt, F.: Finite Element Based Fatigue Calculations. NAFEMS Ltd, Farnham (2000)
6. Todinov, M.T.: Maximum principal tensile stress and fatigue crack origin for compression springs. Int. J. Mech. Sci. **41**(3), 357–370 (1999)
7. Del Llano-Vizcaya, L., Rubio-González, C., Mesmacque, G., Cervantes-Hernandez, T.: Multiaxial fatigue and failure analysis of helical compression springs. Eng. Fail. Anal. **13**(8), 1303–1313 (2006)
8. Timoshenko, S.P.: Strength of Materials, Part I, Elementary Theory and Problems, 2nd edn. D. Van Nostrand. Company Inc, New York (1940)
9. Göhner, O.: Schubspannungsverteilung im Querschnitt einer Schraubenfeder. Ingenieur-Archiv **1**(5), 619–644 (1930)
10. Henrici, P.: On helical springs of finite thickness. Q. Appl. Math. **13**(1), 106–110 (1955)
11. Berry, W.R.: Practical problems in spring design. Proc. Inst. Mech. Eng. **139**(1), 431–524 (1938)
12. Ancker Jr., C.J., Goodier, J.N.: Pitch and curvature correction for helical springs. ASME J. Appl. Mech. **25**(4), 466–470 (1958)
13. Research Committee on the Analysis of Helical Spring: Report of Research Committee on the Analysis of Helical Spring. Trans. Jpn. Soc. Spring Eng. **2004**(49), 35–75 (2004)
14. Calder, G.A., Jenkins, C.: Stress analysis of a helical coil automobile spring using rosettes. Exp. Tech. **12**(2), 17–20 (1988)
15. Lin, Y., Pisano, A.P.: General dynamic equations of helical springs with static solution and experimental verification. ASME J. Appl. Mech. **54**(4), 910–917 (1987)
16. Yazdani Sarvestani, H., Akbarzadeh, A.H.: Thick isotropic curved tubes: three-dimensional stress analysis. Arch. Appl. Mech. **87**(6), 927–947 (2017)
17. Bockwoldt, T.S., Munsick, G.A.: Correction to design equation for spring diametral growth upon compression. Trans. ASME J. Mech. Des. **135**(12), 124503–124503-4 (2013)
18. Burns, S.J.: The relation between helical spring compliances with free and fixed end rotations. ASME J. Appl. Mech. **78**(6), 061005–061005-5 (2011)
19. Krużelecki, J.: Parametrical optimization of compression helical springs against instability. Struct. Multidiscip. Optim. **13**, 205–212 (1997)
20. Mlikota, M., Schmauder, S., Božić, Ž.: Calculation of the Wöhler (S–N) curve using a two-scale model. Int. J. Fatigue **14**, 289–297 (2018)
21. Mlikota, M., Schmauder, S., Božić, Ž., Hummel, M.: Modelling of overload effects on fatigue crack initiation in case of carbon steel. Fatigue Fract. Eng. Mater. Struct. **40**, 1182–1190 (2017)
22. Božić, Ž., Schmauder, S., Mlikota, M., Hummel, M.: Multiscale fatigue crack growth modelling for welded stiffened panels. Fatigue Fract. Eng. Mater. Struct. **37**, 1025–1033 (2014)
23. Rahman, M.M., Ariffin, A.K., Abdullah, S.: Finite element based vibration fatigue analysis of a new twostroke linear generator engine component. Int. J. Mech. Mater. Eng. **2**(1), 63–74 (2007)
24. Halfpenny, A.: A frequency domain approach for fatigue life estimation from finite element analysis. Key Eng. Mater. **167–168**, 401–410 (1999)
25. Mršnik, M., Slavič, J., Boltežar, M.: Multiaxial vibration fatigue: a theoretical and experimental comparison. Mech. Syst. Signal Process. **76–77**, 409–423 (2016)

26. Mršnik, M., Slavič, J., Boltežar, M.: Frequency-domain methods for a vibration-fatigue-life estimation: application to real data. Int. J. Fatigue **47**, 8–17 (2013)
27. Česnik, M., Slavič, J.: Vibrational fatigue and structural dynamics for harmonic and random loads. Strojniški vestnik J. Mech. Eng. **60**(5), 339–348 (2014)
28. Braccesi, C., Cianetti, F., Lori, G., Pioli, D.: A frequency method for fatigue life estimation of mechanical components under bimodal random stress process. Int. J. Struct. Integrity Durab. **1**(4), 277–290 (2005)
29. Bonte, M.H.A., de Boer, A., Liebregts, R.: Prediction of mechanical fatigue caused by multiple random excitations. Proc. ISMA **2004**, 697–708 (2004)
30. Zhou, Y., Fei, Q., Wu, S.: Utilization of modal stress approach in random-vibration fatigue evaluation. Proc. Inst. Mech. Eng. Part G J. Aerosp. Eng. **231**(14), 2603–2615 (2016)
31. Warburton, G.B.: Optimum absorber parameters for various combinations of response and excitation parameters. Earthq. Eng. Struct. Dyn. **10**(3), 381–401 (1982)
32. Alujević, N., Zhao, G., Depraetere, B., Sas, P., Pluymers, B., Desmet, W.: $\mathcal{H}_2$ optimal vibration control using inertial actuators and a comparison with tuned mass dampers. J. Sound Vib. **333**(18), 4073–4083 (2014)
33. Zhao, G., Alujević, N., Depraetere, B., Sas, P.: Dynamic analysis and $\mathcal{H}_2$ optimisation of a piezo-based tuned vibration absorber. J. Intell. Mater. Syst. Struct. **26**(15), 1995–2010 (2014)
34. Cheung, Y.L., Wong, W.O., Cheng, L.: Optimization of a hybrid vibration absorber for vibration control of structures under random force excitation. J. Sound Vib. **332**(3), 494–509 (2013)
35. Alujević, N., Čakmak, D., Wolf, H., Jokić, M.: Passive and active vibration isolation systems using inerter. J. Sound Vib. **418**, 163–183 (2018)
36. Alujević, N., Wolf, H., Gardonio, P., Tomac, I.: Stability and performance limits for active vibration isolation using blended velocity feedback. J. Sound Vib. **330**, 4981–4997 (2011)
37. Alujević, N., Gardonio, P., Frampton, K.D.: Smart double panel for the sound radiation control: blended velocity feedback. AIAA J. **49**(6), 1123–1134 (2011)
38. Caiazzo, A., Alujević, N., Pluymers, B., Desmet, W.: Active control of turbulent boundary layer-induced sound transmission through the cavity-backed double panels. J. Sound Vib. **422**, 161–188 (2018)
39. Senjanović, I., Alujević, N., Ćatipović, I., Čakmak, D., Vladimir, N.: Vibration analysis of rotating toroidal shell by the Rayleigh–Ritz method and Fourier series. Eng. Struct. **173**, 870–891 (2018)
40. Dassault Systèmes: Abaqus 6.9 User's Guide and Theoretical Manual. Hibbitt, Karlsson & Sorensen Inc., Providence (2009)
41. SafeTechnology, Fe-Safe 6 User Manual (2011)
42. Dassault Systèmes: Catia V5R19 Documentation: Finite Element Reference Guide (2007)
43. Kong, Y.S., Omar, M.Z., Chua, L.B., Abdullah, S.: Fatigue life prediction of parabolic leaf spring under various road conditions. Eng. Fail. Anal. **46**, 92–103 (2014)

Paper 4, https://doi.org/10.1016/j.engfailanal.2019.04.064

Vibration fatigue study of the helical spring in the base-excited inerter-based isolation system

D. Čakmak, Z. Tomičević[*], H. Wolf, Ž. Božić, D. Semenski, I. Trapić

University of Zagreb, Faculty of Mech. Eng. and Nav. Arch., I. Lučića 5, 10 000 Zagreb, Croatia

ABSTRACT

The aim of this study is to analytically and numerically model the vibration-induced helical spring fatigue in a generalized vibration isolation system. The system consists of a receiving body and a dynamically active base coupled through a passive isolator. The isolator consists of a coupling helical spring and an inerter. System inherent damping is considered through modal damping. Vibration isolation system is analysed parametrically by varying its corresponding dimensionless coefficients. The coupling helical spring fatigue life extension is used as the isolation quality criterion. Since isolator spring stress and related fatigue life directly correspond to relative displacement between spring terminals, the effect of inerter on relative displacement amplitudes is determined. Novel helical spring stress and deflection correction factors are proposed based on the theory of elasticity and finite element analysis results. The proposed helical spring correction factors are more accurate compared to correction factors available in the current literature, especially when considering very large pitch angles. Fatigue life improvement of considered helical spring is achieved due to introduction of inerter in the isolator system, which is especially evident in the resonant working conditions.

1. Introduction

Mechanical vibrations can span displacement amplitudes from nano-meters in precision engineering applications to meters in civil engineering practical situations. Vibrations detrimental effects on dynamic systems and structures may be of various natures, where failure is one of the most important ones [1]. Vibration-induced structural failure may occur due to excessive stress/strain during transient or steady-state events (e.g. building response to earthquake loading), by instability due to particular operating conditions (e.g. bridge flutter under wind excitation, reported in Tacoma Narrows bridge catastrophe during wind-induced vibration [2]), or simply by *fatigue* (e.g. flexible mechanical parts in operating machines) [1–3]. The engineering structure or machine component exposed to vibration can fail because of material fatigue resulting from the cyclic variation of the induced stress/strain [2,3]. Isolation implies preventing the propagation of disturbance forces to sensitive parts of the systems, where the system (i.e. receiving body [4,5]) is protected against the motion of its foundation or base [1,2], or from any type of disturbance force [6]. Inerter is a relatively new element in the theory of mechanical networks. It is a device which produces a force which is proportional to relative acceleration between its terminals [7] and it has been extensively used in research of the structural vibration suppression. Various types of the inerter-based isolator systems were considered [4–6] with special emphasis on the suspension systems [8]. Moreover, beneficial influence of inerter in the vibration fatigue optimization studies is reported in the literature [4,5]. In these studies, particular accent is given on coupling helical spring fatigue life extension due to the optimally tuned inerter in the isolator [4]. Proposed optimization

method and analytical results reported in [4] were further verified via extensive parametric finite element method (FEM) analysis [5] where very good agreement with the analytical method was observed. Exploiting FEM as an established control verification procedure is usual practice employed in parallel with complicated analytical computations [9]. In addition, FEM is also commonly used for advanced inverse identification of material parameters [10–12].

A spring is a type of mechanical link, which is in most applications ideally assumed to possess negligible mass and damping [2]. It is one of the most important fundamental mechanical components found in many practical applications [5]. Springs in the vibration isolation systems are subjected to random dynamic loads during service. The crack may initiate and eventually propagate at a stress concentration location of the spring, leading to a potentially catastrophic fatigue failure [4], especially evident in case of resonant conditions [5]. In order to evaluate the vibration induced fatigue in the spring, it is necessary to designate stiffness, stress and damping parameters of the dynamic system [4]. The springs must expectedly withstand relatively long exploitation period. Thus, appropriate high-cycle fatigue (HCF) [13] calculation method (above $\sim 10^3$ life-cycles) is usually used for evaluating fatigue life [5]. Biaxial shear-governed fatigue life criterion is commonly utilized for spring fatigue estimation where most stressed region is normally located at the inner side of the helix [4,14–19]. Multiple stress correction factors for helical spring are proposed in the literature which account for influence of this highly stressed region [5,15]. In parametric numerical study conducted in [5], it was reported that Wahl stress correction [14–16] best coincides with the results obtained via FEM. Moreover, an unresolved discussion is noted in the literature [4,5,15] whether using the aforementioned stress correction factor may yield with overly conservative fatigue life estimation.

Due to complex geometries used in the modern machine components, analytical fatigue life estimation is commonly omitted and is almost exclusively conducted via FEM-based software [5,16,19–24]. If considering dynamic (i.e. vibration) effects, operating with a power spectral density (PSD) load and obtaining vibration fatigue results in the frequency domain can prove much less time consuming when employing complicated, computationally expensive FEM models [25]. Consequently, the calculation of the broadband frequency response functions (FRFs) [26] is much faster than a detailed transient dynamic analysis in the time domain [27]. When excitation is given in the form of PSD in a frequency domain, the response of the systems is commonly obtained by using the transfer function (TF), i.e. FRF of target systems and PSD of excitation loads [5,26,27].

In literature [5,16], doubts were raised whether approximate Wahl's helical spring stress correction factor can capture large pitch angle effects accurately enough due to simplifications made in derivation of governing equations. In [4], an attempt was made to model the analytical spring deflection correction by using thick Timoshenko beam theory [28] enriched with Cowper shear correction [29]. The obtained results [5] match almost perfectly with FEM based [29,30] beam solution. Nevertheless, it is additionally reported that these beam-based results are completely divergent when compared to theory of elasticity based Ancker and Goodier deflection correction [17] and the corresponding 3D FEM results [29,30]. Consequently, it was implied that the beam-based solution should not be used in the context of (relatively thick) helical springs. Furthermore, the question of large pitch angle influence on helical spring deflection correction still remains unanswered.

In this study the vibration fatigue induced effects in a cylindrical helical spring acting as an elastic element in an inerter-based isolation system are considered. The contribution of this study is divided into two main parts. The first part focuses on contrasting the performance of isolator with and without inerter and emphasizes the novel beneficial inerter-induced effects. The second part focuses on determining the spring stress and deflection factors and embedding these proposed correction factors into analytical expression for HC vibration fatigue assessment by incorporating previously established TF. The paper is structured as follows. In section 2, the theoretical background for inerter-based vibration isolation system model is established. In section 3, novel spring deflection and stress correction factors are derived and discussed. Final section 4 establishes a benchmark example incorporating all previous concepts by comparing analytical and FEM results of the vibration fatigue study. Moreover, the ideal inerter concept is further implemented in the FEM code *Abaqus* by additionally employing modal superposition method [26,29].

2. Inerter-based isolator model

In this chapter, general analytical expressions for vibration amplitudes of the inerter-based vibration isolation system are derived. Stress amplitudes of the isolator spring are linearly proportional to relative displacement of its terminals [27], thus influence of inerter on relative displacement is studied. The goal of the conducted vibration isolation-based parametric analysis is to lower the stresses of the isolator coupling spring.

The proposed simplified discrete inerter-based isolator vibration fatigue model is shown in Fig. 1a). The whole vibration system consists of discrete mass m (i.e. "receiving body") coupled to a dynamically active base/ground by a spring of stiffness k, a viscous
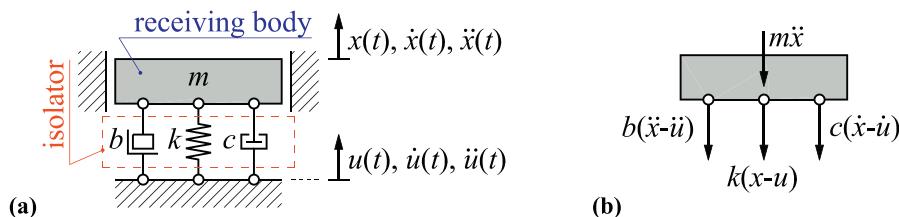

Fig. 1. 1-DOF vibration isolation system: a) load and displacement scheme, b) free-body scheme, assumption: $x > u$.

damper with damping coefficient c and an inerter of inertance b. Isolator consists of all three connecting elements coupled in parallel; i.e. spring k, damper c and inerter b. Connecting elements are commonly assumed to be ideally massless for calculation simplicity reasons, as their mass is usually rather small compared to primary mass m in engineering applications [2,6]. The inerter produces a force proportional to the relative acceleration between mass m and ground/base. For the analysed case, the excitation is provided by the imposed motion of the supporting base. The displacement of the base about a neutral position is denoted by $u(t)$ and the response of the mass from its static equilibrium position is represented by $x(t)$. At any given time, the relative displacement of the helical spring is $x - u$, the relative velocity between the two ends/terminals of the damper is $\dot{x} - \dot{u}$ and the relative acceleration between the two terminals of the inerter is $\ddot{x} - \ddot{u}$.

The equation of motion [1–6] for the free-body scheme in Fig. 1b) can be written as

$$m\ddot{x} + b(\ddot{x} - \ddot{u}) + c(\dot{x} - \dot{u}) + k(x - u) = 0 \tag{1}$$

Base/ground complex broadband excitation is assumed in the form $u(t) = u_0 e^{i\Omega t}$, where u_0 is the ground displacement complex amplitude, "e" is the base of the natural logarithm, imaginary number $i = \sqrt{-1}$, Ω is the excitation circular frequency and t is the time. Furthermore, the solution of Eq. (1) is assumed as $x(t) = x_0 e^{i\Omega t}$ where x_0 is the complex displacement amplitude of mass m. Separating the response and excitation variables yields with the dynamic forces equilibrium, and consequent absolute (i.e. x_0/u_0) and relative (i.e. $x_{0,\mathrm{rel}}/u_0$) steady-state complex solutions of Eq. (1), which can respectively be written as

$$(m + b)\ddot{x} + c\dot{x} + kx = b\ddot{u} + c\dot{u} + ku \quad \Rightarrow \quad \frac{x_0}{u_0} = \frac{(i\Omega)^2 b + i\Omega c + k}{(i\Omega)^2(m + b) + i\Omega c + k}, \quad \frac{x_{0,\mathrm{rel}}}{u_0} = \frac{x_0 - u_0}{u_0}. \tag{2a-c}$$

It is implied from Eq. (2c) that relative displacement complex amplitude $x_{0,\mathrm{rel}} = x_0 - u_0$ directly corresponds to spring k stress [27]. In return, spring stress is inversely and non-linearly proportional to number of cycles to fatigue failure N_f, analogue to results reported in [4,5] and further discussed in chapter 3.

For a more general approach in the scope of this study, the following parameters are introduced

$$m_{\mathrm{eqv}} = m + b, \quad \omega_n = \sqrt{\frac{k}{m_{\mathrm{eqv}}}} \quad \Rightarrow \quad \eta = \frac{\Omega}{\omega_n}, \quad \zeta = \frac{c}{c_{\mathrm{cr}}} = \frac{c}{2\sqrt{m_{\mathrm{eqv}} k}}, \quad \mu = \frac{b}{m}, \tag{3a-e}$$

where $\eta = \Omega/\omega_n$ is dimensionless excitation frequency, Ω is circular excitation frequency and $\omega_n = (k/m_{\mathrm{eqv}})^{1/2}$ is a fundamental natural frequency of the system, conveniently scaled with respect to system equivalent mass $m_{\mathrm{eqv}} = m + b$. Since inertance b algebraically contributes to equivalent, i.e. apparent mass m_{eqv}, this effect yields with diminishing of fundamental natural frequency ω_n. Furthermore, $\zeta = c/[2(m_{\mathrm{eqv}} k)^{1/2}]$ is dimensionless damping ratio, i.e. proportional [2] or modal [1,3,29,30] damping as a fraction of critical damping, and $c_{\mathrm{cr}} = 2(m_{\mathrm{eqv}} k)^{1/2}$ is critical damping. Finally, dimensionless inertance ratio is designated as $\mu = b/m$. Relative displacement amplitude $|x_{0,\mathrm{rel}}| = |x_0 - u_0|$ is further shown through convenient relative magnification factor $M_{0,\mathrm{rel}}$ with respect to Eqs. (2–3). Absolute magnification factor $M_0 = |x_0/u_0|$ from Eq. (2b) and its corresponding relative magnification factor $M_{0,\mathrm{rel}} = |x_0/u_0 - 1|$ from Eq. (2c) can now be written as dimensionless frequency η-dependent scalars

$$M_0(\eta) = \left| \frac{x_0}{u_0} \right| = \left| 1 + \frac{\eta^2}{(1 + 2i\eta\zeta - \eta^2)(1 + \mu)} \right|, \quad M_{0,\mathrm{rel}}(\eta) = \left| \frac{x_{0,\mathrm{rel}}}{u_0} \right| = \left| \frac{x_0 - u_0}{u_0} \right| = \left| \frac{\eta^2}{(1 + 2i\eta\zeta - \eta^2)(1 + \mu)} \right|. \tag{4a,b}$$

Parametric plots for relative magnification factor $M_{0,\mathrm{rel}}$ from Eq. (4b) are shown in Fig. 2 for various combinations of ζ and μ. In Fig. 2a), inertance μ is kept as constant value while damping ζ is varied. Two main phenomena can be observed from Fig. 2. Firstly, damping beneficially influences relative response only near the resonant frequency (i.e. $\eta \approx 1$), see Fig. 2a). Otherwise, response is not significantly influenced by damping ζ. Secondly, when $\eta \to \infty$ and $\mu \neq 0$, then $M_{0,\mathrm{rel}\infty}$ tends to value lower than unity, i.e. $M_{0,\mathrm{rel}\infty} < 1$, see Fig. 2a) and b). Unity is otherwise common limit value for relative magnification factor $M_{0,\mathrm{rel}\infty}$ in standard base-
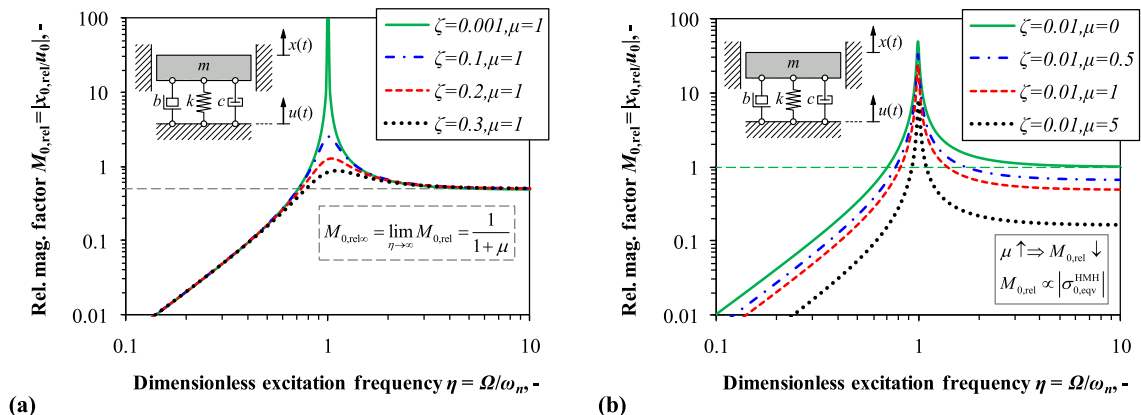

Fig. 2. Relative magnification factor $M_{0,\mathrm{rel}}$ by varying: a) damping ratio ζ ($\mu = 1$), b) inertance ratio μ ($\zeta = 0.01$).

excited 1-DOF isolators [2] without inerter, i.e. when dimensionless inertance $\mu = 0$. Since equivalent spring stress directly corresponds to relative magnification factor $M_{0,\text{rel}}$, this is considered to be a broadband improvement.

By performing limit analysis on Eq. (4b), the limit value $M_{0,\text{rel}\infty}$ is obtained. Furthermore, relative magnification factor in resonant excitation conditions $M_{0,\text{rel,res}}$ is determined by setting $\eta = 1$ in Eq. (4b). These relations can be respectively written as

$$M_{0,\text{rel}\infty} = \lim_{\eta \to \infty} M_{0,\text{rel}} = \frac{1}{1+\mu}, \qquad M_{0,\text{rel,res}}(\eta = 1) = \frac{1}{2\zeta(1+\mu)}, \tag{5a,b}$$

which implies that any positive isolator inertance value, i.e. $\mu > 0$, always corresponds to lowering relative magnification factor $M_{0,\text{rel}}$ in broadband frequency range, including resonant conditions $\eta \approx 1$. Moreover, isolator spring stress amplitudes σ_0 are directly proportional to $M_{0,\text{rel}}$ [4]. Thus, it can be concluded that higher the inertance ratio μ is set – lower the stress amplitudes in the spring become for the entire broadband excitation range. Further adopting equivalent complex biaxial stress in the spring according to von Mises distortion energy criterion [5] yields with general relation $M_{0,\text{rel}} \propto |\sigma_{0,\text{ eqv}}^{\text{HMH}}|$. The improvements are evident for relative magnification factor $M_{0,\text{rel}}$ at all frequencies $0 < \eta \leq \infty$ due to addition of an inerter. This generalized finding of this section is summarized through following relation

$$\mu \uparrow \ \Rightarrow M_{0,\text{rel}}(\eta \in \langle 0,\infty]) \downarrow. \tag{6}$$

In conclusion, for this class of isolation systems the goal of minimizing coupling spring stress amplitudes can be achieved by simply setting large enough dimensionless inertance μ.

3. Helical spring correction factors and fatigue assessment

In this chapter, helical spring stiffness and stress are discussed. Novel displacement and stress correction factors are proposed. A simple expression for determining the spring fatigue life is also recapitulated from [4,5], where HCF life above 10^3 cycles is utilized and novel stress and displacement correction factors are included. Obtained relative displacement amplitudes in the frequency domain from previous chapter, i.e. Eq. (2c) and Eq. (4b), are tied to fatigue life stress amplitudes S_a.

The studied helical spring analytical model is represented in Fig. 3a). Spring parameters are as follows; E is (Young) modulus of elasticity, ν is Poisson's factor/ratio, S'_f is fatigue strength coefficient, and "B" is dimensionless Basquin's exponent, i.e. fatigue strength exponent [4,5,31] presented herein in capital letter in order not to be mixed up with inertance "b". Diameters D and d are mean coil and spring wire diameters respectively, and $C = D/d$ is defined as spring index. Angle α is the helix pitch angle $\alpha = \text{arc tan}[l/(\pi D)]$, and l is the pitch of the spring. Number of active coils is designated as integer n ($n = 2$ in Fig. 3a) and h is spring total height where $h = n \cdot l$. Material of the spring is considered to be homogenous and isotropic. Small displacements/rotations and small/engineering strains are assumed. Corresponding engineering stresses are considered to be linearly proportional to strain and below yield stress σ_Y. The geometry of one isolated helical spring coil (i.e. $n = 1$) modelled in *Abaqus* [5,29] is shown in Fig. 3b).

Cylindrical spring is usually considered as thin/slender, curved rod/beam subjected to torsion load exclusively [4]. In that case, classical strength of materials expressions are employed [4,18]. Analytical expressions for nominal spring stiffness k_{nom}, nominal static displacement δ_{nom} and nominal shear stress τ_{nom} thus respectively write as

$$k_{\text{nom}} = \frac{F_0}{\delta_{\text{nom}}} = \frac{Gd}{8C^3 n}, \qquad \delta_{\text{nom}} = \frac{8F_0 C^3 n}{Gd}, \qquad \tau_{\text{nom}} = \frac{8F_0 C}{\pi d^2}, \tag{7a-c}$$

where $G = E/[2(1+\nu)]$ is the shear modulus. Eq. (7) holds for tensile and compressive applied force $\pm F_0$, in case linear assumptions
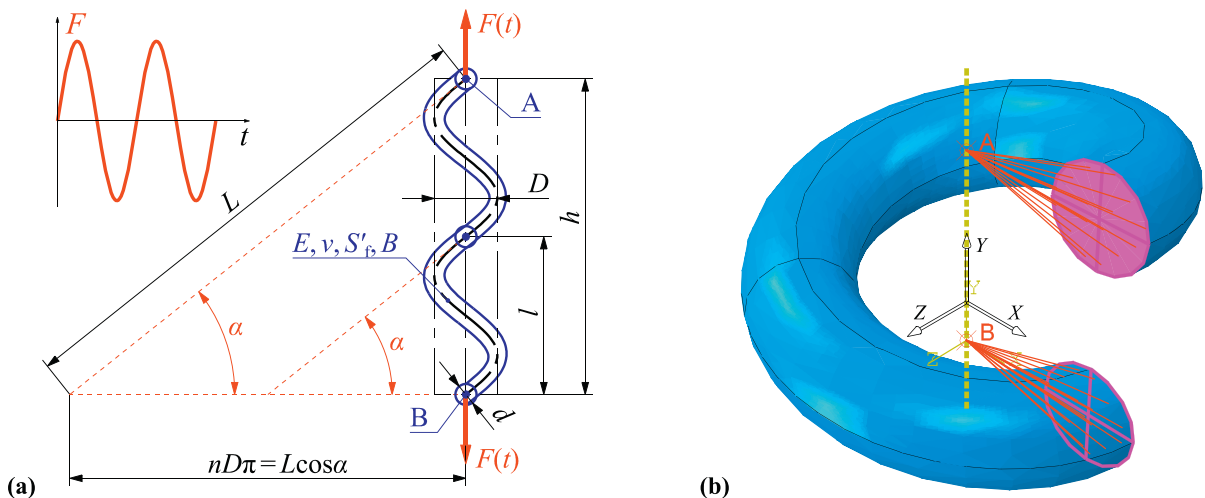

Fig. 3. Helical spring k properties: a) analytical model [4], b) *Abaqus* geometric model, $n = 1$, $C = 50/17$, $l = 2d$ [5].

Table 1

Expressions for stress correction factors K_σ and deflection correction factors K_δ.

Author/standard	Stress correction factor K_σ	Deflection correction factor K_δ
Wahl, DIN 13906 (Strength of Materials)	$k_{W/T} = \frac{1+2\nu}{2(1+\nu)} \quad \Rightarrow \quad \frac{4C-1}{4C-4} + \frac{k_{W/T}}{C}$	–
Ancker and Goodier (Theory of Elasticity)	$1 + \frac{5}{4C} + \frac{7}{8C^2} + \frac{1}{2}\tan^2(\alpha)$	$1 - \frac{3}{16C^2} + \frac{3+\nu}{2(1+\nu)}\tan^2(\alpha)$

are valid. If direct shear, curvature and pitch angle effects are included in the spring model, additional correction factors K_δ and K_σ need to be applied for displacement and shear stress, where relations $\delta_{max} = K_\delta \delta_{nom}$ and $\tau_{max} = K_\sigma \tau_{nom}$ now hold [4]. Multiple proposed correction factors are observed in literature [5,14–18]. By considering these correction factors and employing von Mises energy stress criterion [4,5], corrected spring stiffness and max (i.e. corrected) spring equivalent stress can be respectively written as

$$k_{corr} = \frac{F_0}{\delta_{max}} = \frac{F_0}{K_\delta \delta_{nom}} = \frac{Gd}{K_\delta 8C^3 n}, \qquad \sigma_{eqv,max}^{HMH} = K_\sigma \sqrt{3}\, \tau_{nom} = K_\sigma \sqrt{3}\, \frac{8F_0 C}{\pi d^2}. \tag{8a,b}$$

Based on findings of parametric investigation conducted in [5], A/G correction best describes FEM displacement field, while Wahl correction best coincides with FEM stress field. Moreover, Wahl correction is currently part of DIN 13906 standard [4], and A/G correction is considered to be one of the most accurate displacement correction factors in literature [5]. Table 1 sums up these expressions, and additionally includes original A/G stress correction which is derived according to theory of elasticity assumptions [17,18].

Supplementary observations are presented for Wahl stress correction factor. Nominal expression for Wahl stress correction factor [14,15] can be written as

$$K_{\sigma,Wahl} = \frac{4C-1}{4C-4} + \frac{0.615}{C}. \tag{9}$$

Wahl was partially influenced by Timoshenko [28] in derivation of this correction factor. The numerator of second term from Eq. (9) is for now denoted as $k_{W/T} = 0.615$, where index "W/T" denotes Wahl/Timoshenko. Wahl readily used Timoshenko solution which comes from setting a Poisson's ratio $\nu = 0.3$ in the equation derived for the shear stress at the horizontal edge of a cantilevered circular bar with circular cross-section [28]. Such circular bar can be considered as a simplified isolated coil of cylindrical helical spring [15]. By setting the different values for Poisson's factor ν, values of $k_{W/T}$ from second row of Table 1 are obtained as

$$k_{W/T} = \frac{1+2\nu}{2(1+\nu)} \quad \Rightarrow \quad k_{W/T}(\nu = 0) = 0.5, \quad k_{W/T}(\nu = 0.3) = \frac{8}{13} \approx 0.615, \quad k_{W/T}(\nu = 0.5) = 0.\dot{6}, \tag{10a-d}$$

where it can be observed that ν and $k_{W/T}$ are proportional. By using fixed $k_{W/T} = 0.615$ as denoted in Eq. (9), Poisson's ratio-independent stress correction solution is hard-coded. Findings from [5] and comparison with FEM results justified excluding Poisson's ratio influence and using Eq. (9) as-is. Interestingly, by considering $\nu = 0$ in W/T shear correction from Eq. (10b) and taking into account small pitch angles ($\alpha \approx 0$) for A/G stress correction factor from Table 1, almost the same results are obtained for any C value. This effect is also reported in [5]. However, for larger pitch angles, these two approximate correction factors completely diverge. Thus, detailed parametric FEM analysis is employed herein for further evaluation. Larger pitch angles and Poisson's ratio influence on both stress and deflection fields are considered simultaneously.

In order to assess the sensitivity of the analysed spring model, C, α and ν parameters are independently varied. Six discrete values used in the FEM analyses for spring index C are: $D/d = 50/2, 50/5, 50/8, 50/11, 50/14$ and $50/17$. Furthermore, six independent pitch angles α, i.e. spring lengths/pitches $l = \tan(\alpha)\pi D$, see Fig. 3a), are: $l = 2d, 3d, 4d, 5d, 6d$ and $7d$. Three values of Poisson's ratio ν are also considered: $\nu = 0.0, 0.3$ and 0.49. Fully incompressible material (i.e. $\nu = 0.5$) is omitted in the scope of this work in order to avoid possible shear/general locking effects due to consequent singularities in FE numerical formulation [29]. By considering all three varied parameters (i.e. C, α and ν), $6 \times 6 \times 3 = 108$ FEM analyses in total are performed in *Abaqus* and *Catia* control models separately, in order to obtain objective and impartial numerical results.

Abaqus parametric computational model is defined according to Fig. 3a) and analogue to Fig. 3b). Guidelines from [5] are employed for FE modelling. Structured hexahedron continuum C3D20R FE mesh is used. Analysis is defined as linear and quasi-static. Eight 2nd order hexahedron elements per spring thickness provide sufficiently accurate results according to herein performed mesh sensitivity check, also available in [5]. Boundary conditions (BCs) are prescribed through two reference points (RPs) A and B. The moving-pinned and fixed-pinned conditions are employed in RPs A and B respectively. Full BCs are: $A(u,w = 0)$ and $B(u,v,w,\varphi_y = 0)$. RPs A and B are coupled to corresponding spring sides (i.e. outer highlighted surfaces in Fig. 3b) through flexible kinematic coupling of type "*Distributing*". In analogue *Catia* FE model, "*Smooth*" kinematic coupling is used which corresponds to MSC *Nastran* RBE3 [32] flexible connection. In *Catia*, general unstructured tetrahedral mesh is employed which consists of 2nd order TE10 elements.

General observations of performed FE analyses are as follows. Due to familiar nature of tetra elements limited shape functions [29,30], more scatter in *Catia* tetra results is observed compared to superior *Abaqus* hex elements. Nevertheless, same trends are reported regardless of the used FEs (hex/tetra) or solver (*Abaqus*/*Catia*). The increase of the pitch angle corresponds to higher values of stress and displacement factors respectively. Furthermore, rising pitch angle α introduces more prominent influence of Poisson's ratio ν on stress and displacement factors respectively. Hence, optimization and fitting process is performed on existing correction
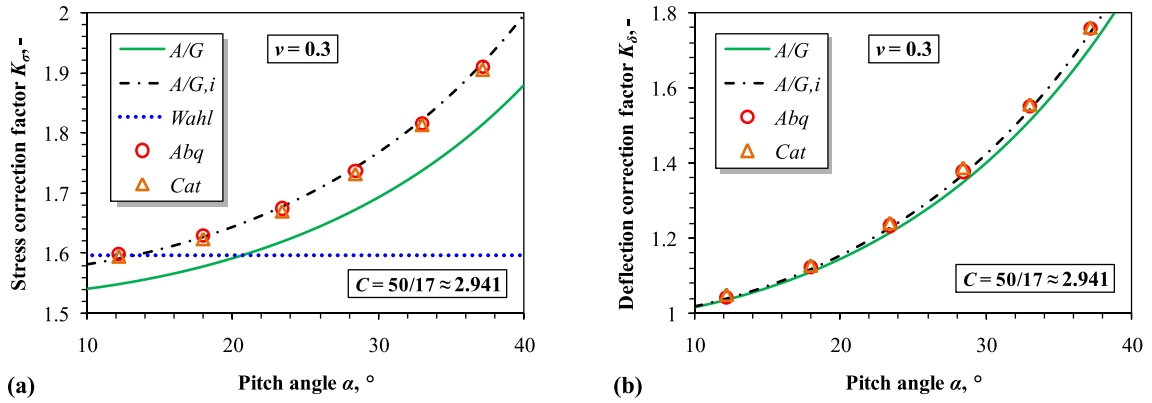
Fig. 4. Spring correction factors comparison, $\nu = 0.3$, $C = 50/17$, $\alpha = 10 - 40°$: a) $K_\sigma(\alpha)$, b) $K_\delta(\alpha)$.

factors from Table 1 based on beforehand conducted numerical parametric analyses. The proposed *improved* (index "i") expressions based on original A/G theory of elasticity relations [17] and additional *W/T* shear correction [28] can be written as

$$K_{\sigma,A/G,i} = \overbrace{1.005}^{\text{emp. corr.}} + \frac{5}{4C} + \overbrace{\frac{8}{7C^2}}^{\text{math. corr.}} + \overbrace{\frac{1+2\nu}{2(1+\nu)}}^{\text{Wahl/Timo. corr.}} \tan^2(\alpha), \qquad K_{\delta,A/G,i} = 1 - \frac{3}{16C^2} + \frac{\overbrace{3.185}^{\text{emp.corr.}} + \nu}{2(1+\nu)}\tan^2(\alpha). \tag{11a,b}$$

Rounded, most rational optimized results are proposed and presented in Eq. (11). Fig. 4a) shows the improved stress correction factor $K_{\sigma,A/G,i}$ from Eq. (11a), Wahl, and original A/G Eqs. from Table 1 compared to FE (*Abq/Cat*) results. Fig. 4b) denotes improved displacement correction factor $K_{\delta,A/G,i}$ from Eq. (11b) contrasted to original A/G Eq. from Table 1 and FE results. The results reported in Fig. 4 are obtained for fixed values of small spring index $C = 50/17$ (which implies thick spring) and Poisson's ratio $\nu = 0.3$, while α is varied.

In Fig. 4a), it can be seen that *Wahl* predicts stress correction well for small pitch angle α which corresponds to spring pitch value $l \approx 2d$, i.e. when pitch is approximately equal to two spring wire diameters. However, it fails to capture larger pitch angle effect. Elementary A/G stress correction [17] follows the numerical results trend closely, but constantly underestimates the FE correction. Finally, improved A/G,i stress correction consistently predicts numerical stress correction results very well. The first term in Eq. (11a) represents empirical correction and shifts the entire curve up by 0.5%. The third term, i.e. 8/7, introduces the mathematical correction and influences the stress correction curvature. It is in fact the inverse of original 7/8 found in the authentic A/G correction. The last term in Eq. (11a) denotes analytical *W/T* shear stress correction influenced by Poisson's factor ν, which is now tied to pitch angle α. This makes improved Eq. (11a) compliant with previously published results [5] where it was reported that Poisson's effect was negligible for small pitch angles. Also, relative numerical difference between *Abaqus* and *Catia* FEM results is far < 1% for all given cases.

Furthermore, it is evident in Fig. 4b) that initial A/G deflection correction factor underestimates FE solutions for very large pitch α values. Thus, additional empirical correction factor "3.185" shown in the last term numerator of Eq. (b) is used, instead of authentic "3" from [4,5,17,18] and Table 1. Otherwise, original A/G displacement correction factor is left intact as it coincides with the FE solution rather well.

Moreover, Fig. 5 presents superimposed results from Eqs. (11a,b) and *Abaqus* results where Poisson's ratio influence is clearly
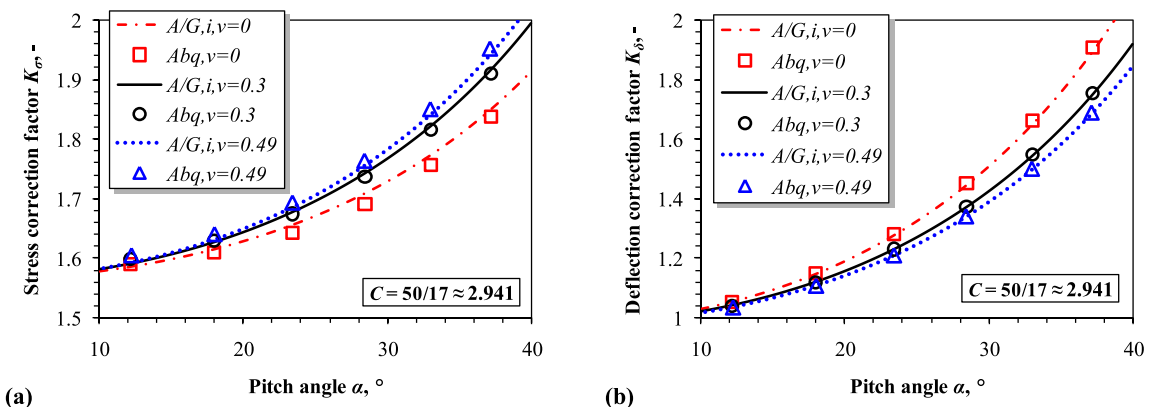

Fig. 5. Spring correction factors comparison by varying Poisson's ratio ν, $C = 50/17$, $\alpha = 10 - 40°$: a) $K_\sigma(\alpha)$, b) $K_\delta(\alpha)$.
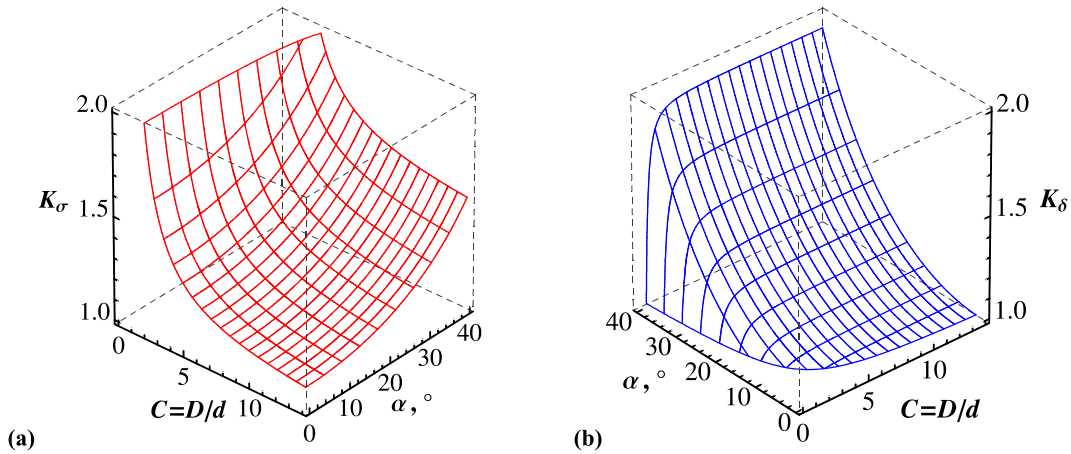
Fig. 6. Improved spring correction factors, $\nu = 0.3$, $C = 1 - 14$, $\alpha = 10 - 40°$: a) $K_{\sigma,A/G,i}(C,\alpha)$, b) $K_{\delta,A/G,i}(C,\alpha)$.

demonstrated. Very good agreement between analytical and FEM solutions is observed for stress and displacement curves respectively. In Fig. 5a), it is reported that increase of the Poisson's ratio yields with higher stress correction, which is especially prominent for larger pitch angles. That fact further justifies including W/T shear correction tied to pitch angle α. Opposed to stress correction, in Fig. 5b) it is noted that higher values of Poisson's ratio correspond to lower displacement correction. Although displacement correction is negligible for small pitch angles, for larger pitch angles it becomes almost as prominent as stress correction. Thus, by neglecting displacement correction K_δ, erroneous results could be produced when pitch of the spring helix becomes large enough. The results and trends for larger spring indices C are qualitatively very similar to ones denoted in Fig. 5. Hence, they are neither separately presented, nor further discussed.

Fig. 6a) and b) denote 3D plot trends of improved stress and deflection correction factors from Eqs. (11a,b) respectively, as functions of spring index C and pitch angle α simultaneously. Poisson's ratio is set to $\nu = 0.3$. Plots are cut below unity and above two, with regard to correction value K. In both plots is observed that singularity occurs when $C \to 1$, since this is neither physically, nor geometrically achievable combination.

Improved semi-analytical optimized correction models from Eq. (11) capture FEM results and trends very well. Maximum relative error $E_{rel} = (K_{A/G,i}/K_{Abq} - 1) \cdot 100\%$ is below 1% for all compared values, i.e. $6 \times 6 \times 3$ FE analyses for stress and displacement correction respectively. Moreover, inconsistent influence of C, α and ν is reported throughout parametric analyses (see Fig. 5 and Fig. 6). Thus, the trends of these findings are recapitulated and summarized in Table 2. It needs to be emphasized that although displacement correction seems to be dependent upon C (i.e. for lower C, displacement correction gets smaller, see Fig. 6b trends), that effect is not so prominent when compared to e.g. rising pitch angle α consequences.

It seems that large pitch angles α correspond to higher K_δ and K_σ correction factors. Hence, pitch angle effects should not be neglected if all structural effects need to be captured in the model while cylindrical spring deforms under loading. By adopting convenient fatigue nomenclature, stress amplitudes $|\sigma_0|$ now write as S_a [4]. Basquin's equation $S_a = S'_f(N_f)^B$ [5] is considered next. Previously obtained expressions for assessment of spring fatigue life in the frequency domain $N_f(\Omega)$ from [4] are recapitulated. Instead of absolute displacement, relative displacement amplitudes from Eq. (2c) are considered. Novel correction factors from Eq. (11) are employed. Expressions for spring stress amplitudes S_a, Basquin's mathematical approximation, and corresponding fatigue life in the frequency domain $N_f(\Omega)$ can respectively be written as

$$S_a \equiv |\sigma_{0,eqv}^{HMH}(\Omega)| = \sqrt{3}\frac{K_\sigma}{K_\delta}\frac{G}{C^2 n\pi d}\,|x_{0,rel}(\Omega)|, \qquad N_f = \left(\frac{S_a}{S'_f}\right)^{\frac{1}{B}} \quad \Rightarrow \quad N_f(\Omega) = \left[\sqrt{3}\frac{K_\sigma}{K_\delta}\frac{G}{C^2 n\pi d}\frac{|x_{0,rel}(\Omega)|}{S'_f}\right]^{\frac{1}{B}}. \tag{12a-c}$$

Simplified Eq. (12c) is valid for HCF beyond 10^3 life-cycles; and for biaxial and proportional stress/strain cycle [4] where von Mises distortion energy criterion is assumed. As already implied when defining spring correction factors, material must be linear and homogenous, and equivalent stresses shouldn't surpass yield strength. Type of spring processing and manufacture (e.g. shot-peening [4,21]) is for simplicity not considered herein. Spring is also assumed to be perfectly smooth and without any residual stresses. Moreover, spring fatigue notch sensitivity is presumed to be near unity, i.e. $K_t \approx K_f$, which is rather common for spring steel [4]. Nevertheless, these effects can readily be incorporated into Eq. (12c) when more complex model is considered. The same applies for mean stress S_m effects which are not considered in the scope of this work.

Table 2
Trends of stress correction factors $K_\sigma(C,\alpha,\nu)$ and deflection correction factors $K_\delta(C,\alpha,\nu)$.

K_σ	$\Rightarrow$	$C\downarrow$	$\alpha\uparrow$	$\nu\uparrow$	K_δ	$\Rightarrow$	$C\downarrow$	$\alpha\uparrow$	$\nu\uparrow$
		$K_\sigma\uparrow$	$K_\sigma\uparrow$	$K_\sigma\uparrow$			$K_\delta\downarrow$	$K_\delta\uparrow$	$K_\delta\downarrow$

Table 3

1-DOF inerter-based isolator model example parameters.

m, kg	μ, −	ζ, −	$|u_0|$, mm	D, mm	d, mm	n, −	l, mm	E, GPa	ν, −	S'_f, MPa	B, −
100	5	0.01	0.1	50	17	1	$7d$	200	0.3	925	− 0.1

4. Inerter-based isolator helical spring vibration fatigue analysis

In this chapter, an illustrative example is solved in detail. Benchmark example embodies all previously shown principles. FEM is extensively utilized for proposed method verification. Vibration system example parameters are given in Table 3.

Quantities m, μ, ζ and $|u_0|$ describe vibration system parameters, while D, d, n and l denote helical spring geometric parameters, and E and ν denote linear material parameters. Fatigue parameters are depicted by S'_f and B. Material and fatigue parameters are adopted from [4,5] and represent spring steel. Small modal damping $\zeta = 1\%$ is assumed for lightly damped steel mechanical system [3] in order to demonstrate relatively large inertance effect ($\mu = 5$). Ideal one coil spring segment ($n = 1$) is defined to depict the fatigue calculation procedure on computationally fairly light model. For real engineering applications, $n \approx 5$ active coils or more are commonly used [15]. Also, very large pitch $l = 7d$ is employed in conjunction with very small spring index $C = 50/17$ in order to test the robustness of Eq. (11) embedded in Eq. (12c). The analysed vibration fatigue problem is represented by a discrete/lumped parameter model as shown in Fig. 7, where $u(t) = u_0 e^{i\Omega t}$.

The whole system consists of a mass m, a spring k and an *implicitly given* inerter of inertance b through dynamic inertia moment J_A. This simple system represents the scheme for possible physical realization of real inerter by using Smith initial *rack and pinion* inerter analogy [7]. Levers $\overline{CO}$ and $\overline{OA}$ are assumed to be ideally rigid and massless. It is assumed that the critical component regarding fatigue failure is a helical spring of stiffness k (Fig. 7a). Moreover, the equivalent truss (Fig. 7b) stiffness is defined as $k_{ideal} = AE/l$, while the helical spring stiffness can be obtained from Eqs. (8a) and (11b) with the data from Table 3. Furthermore, A is designated as truss spring quadratic cross-section area with dimensions $a \times a$. Analogue, the truss equivalent stress is denoted by relation $\sigma_{eqv,ideal} = F_0/A$, while the spring equivalent stress can be obtained from Eqs. (8b) and (11a) with respect to Table 3. In order to make the two proposed systems in Fig. 7a) and b) equivalent, truss and helical spring stiffness and stress are prescribed as equal. This is done in order to verify the entire dynamic procedure, regardless of accuracy of the proposed correction factors from Eq. (11).

Small vibration rotation amplitudes are assumed where $\sin(\varphi) \approx \varphi$, and $\cos(\varphi) \approx 1$. Free-body scheme from Fig. 7c) is considered. System implicit equivalent viscous damping c is related to modal damping ratio ζ through Eq. (3d). The sum of moments ΣM_O with respect to vertically moving hinge "O" yields with differential equation of motion which can readily be expressed as

$$\sum M_O = 0 \quad \Rightarrow \quad m\ddot{x}r + J_A\ddot{\varphi} + c(\dot{x} - \dot{u})r + k(x - u)r = 0. \tag{13}$$

By further considering relations $J_A = r^2 b$ and $(x - u) \equiv x_{rel} = r\varphi$, and dividing by rotation radius r, Eq. (13) morphs into dynamic force equilibrium from Eq. (1). Hence, this simple rotational/translational system exhibits inerter-like behaviour through explicit relation $b = J_A/r^2$. Before performing detailed dynamic analysis, stress and displacement correction factors for given parameters from Table 3 are obtained analytically and numerically. Correction factors with regard to different assumptions and theories are shown in Table 4 with the corresponding relative errors. At this stage of investigation, *Abaqus* solution is considered as a referent one.

Abaqus/Catia FEM solutions mutually vary only slightly. If no correction is used, correction factors for both stress and displacement are grossly underestimated. Furthermore, by considering previously adopted A/G correction [4,5], relatively small ~3% error is introduced for displacement. This is already implied in Fig. 4b). However, large stress error of ~20% is observed when considering *Wahl* correction. Finally, the proposed improved $A/G,i$ stress correction factor from Eq. (11a) gives very good correlation with *Abaqus*, with less than ~0.3% E_{rel}. Additionally, improved $A/G,i$ deflection correction from Eq. (11b) shows ~0.53% error for given very large pitch angle α. Hence, proposed correction factors outperform the most accurate ones from referent literature [4,5,14,15,17]. Nevertheless, even newly proposed improved $A/G,i$ correction factors could yield erroneous results for resonant conditions $\Omega = \omega_n$ (i.e. $\eta = 1$) with small damping $\zeta = 1\%$ assumed; due to steep characteristics of magnification factor near
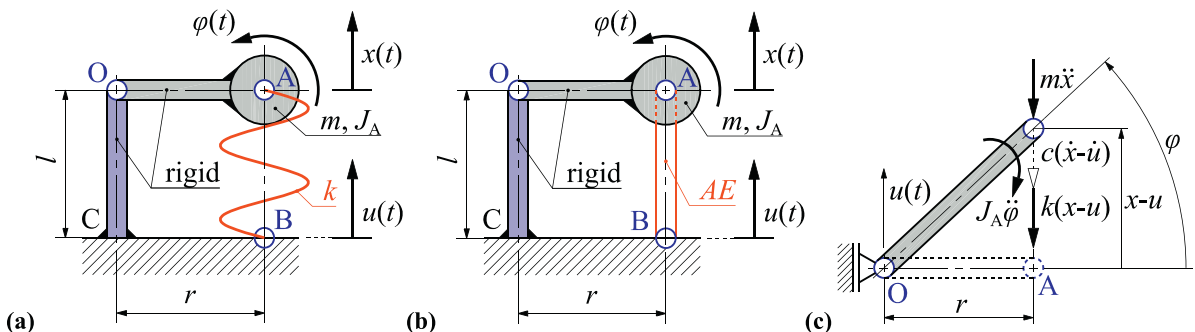

Fig. 7. 1-DOF inerter-based vibration isolator model: a) helical spring, b) truss spring, c) free-body scheme, $x > u$.

Table 4

Analytical and numerical results for helical spring correction factors K_σ and K_δ.

Method	$C = D/d$, −	α, °	k_{nom}, N/mm	K_σ, −	E_{rel}, %	K_δ, −	E_{rel}, %
Abaqus	2.941	37.147	6 424.692	1.910	–	1.757	–
Catia				1.906	0.196	1.761	− 0.236
No corr.				1.000	90.973	1.000	75.686
Wahl-A/G				1.596	19.688	1.707	2.935
A/G,i				1.915	− 0.291	1.748	0.530

resonance, see Fig. 2. Linear dynamic analysis which employs modal damping is considered next.

Modal analysis [1,26] embedded into commercial FEM codes [29,30,32] is utilized in *Abaqus*. Fundamental natural frequency ω_n (i.e. *eigenvalue*) and corresponding mode shape (i.e. *eigenvector*) for system in Fig. 7 is obtained via FEM. Kinematic excitation cannot be imposed directly through BCs due to known limits of the standard FEM analysis when employing modal superposition method. Alternative "Big mass method" (BMM) model [29] analogue to Fig. 8 is hence introduced and exploited.

If a very *large* [32,33] (i.e. *big* [29]) mass M, which is several orders of magnitude larger than the mass of the entire structure (m_{eqv}) is connected to a DOF and a dynamic load $F(t)$ is applied to the same DOF, then the corresponding acceleration can be approximated using 2nd Newton's law by $\ddot{u}(t) \approx F(t)/M$ [32]. The accuracy of this approximation increases as M is made larger in comparison to the equivalent mass m_{eqv} of the structure. The only limit for the size of mass M is the possible numeric overflow in the computer. General recommendations are that the value of equivalent big mass should be approximately 10^6 times the mass of the entire structure for an enforced translational DOF and 10^6 times the dynamic moment of inertia of the entire structure for a rotational DOF [29,32]. The factor $\sim10^6$ is a safe limit that should produce approximately six digits of numerical accuracy [32]. With regard to Fig. 8a) and b), following expressions are used to recapitulate the BMM:

$$\ddot{u}(t) = (i\Omega)^2 u(t), \qquad M = {\sim}10^6 \cdot \sum_{i=1}^{n} m_i = 10^6(m + b), \qquad F(t) \approx M\ddot{u}(t).$$

(14a-c)

Furthermore, both truss (i.e. *ideal*) spring and helical (i.e. *real*) spring systems (Fig. 7a,b) are employed in *Abaqus*. The ideal system spring is denoted by one C3D8R hexahedral FE for which dimensions are $a \times a \times l$. Inertance b is employed through native *Equation* functionality which is defined in order to tie dynamic inertia moment J_A rotation with relative displacement between mass and ground, analogue to the procedure described in [5]. Equivalent Young's modulus $E_{eqv} \approx 37.611$ GPa and equivalent truss dimension $a \approx 3.411$ mm for *ideal* spring are obtained by equalling $k_{real} \equiv k_{ideal}$ and $\sigma_{real} \equiv \sigma_{ideal}$. By setting unit rotation radius $r = 1$ m with regard to Fig. 7, inertia is obtained as $J_A = m\mu r^2 = 500$ kg·m², where inertance $b = m\mu = 500$ kg, from Eq. (3e). For even more detailed clarification of the given procedure, reference [5] is recommended. Following the guidelines and obtained results from chapter 3 and [5], *real* spring is meshed in *Abaqus* with C3D20R 2nd order hexahedral elements where 8 FEs are used per spring thickness, i.e. spring wire diameter d.

First benchmark test case excludes inerter from the model, i.e. $\mu = 0$. In *Abaqus*, previously described BMM in *Steady state-dynamics, Modal* step is employed. Eq. (14c) is used for obtaining equivalent excitation force $F(t)$ in order to mimic PSD kinematic excitation. *Ideal* and *real* springs are analysed in the $\Omega_{min} = 0$ and $\Omega_{max} \approx 2\omega_n$ frequency range. FRFs for analytical correction models from Table 4, including *Abaqus* as a referent solution, are shown in Fig. 9 for 500 discrete frequency steps. Ideal spring FEM model is not denoted at this stage. At first glance it can be observed that large offset error is introduced if no correction (*No corr.*, dashed line) is introduced in the computational model with regard to both displacement and stress amplitudes. "*No corr.*" model is thus completely disregarded as no objective correlation can be found. Framed rectangle in Fig. 9a) represents the detail of mass m displacement amplitudes for near-resonant conditions. When *Wahl-A/G* correction is considered, offset of resonant response can be observed, which is already implied by $\sim3\%$ error in Table 4. Regarding *A/G,i* correction, very good agreement is observed, although small offset is still present when compared to *Abaqus* results. Considering stress amplitudes in Fig. 9b), *Wahl-A/G* correction now reveals both offset error and response error which is a cumulative consequence of $\sim3\%$ displacement error and $\sim20\%$ stress error from Table 4. Finally, the results acquired by *A/G,i* stress correction agree very well with FEM, even though inherent small offset is still present.
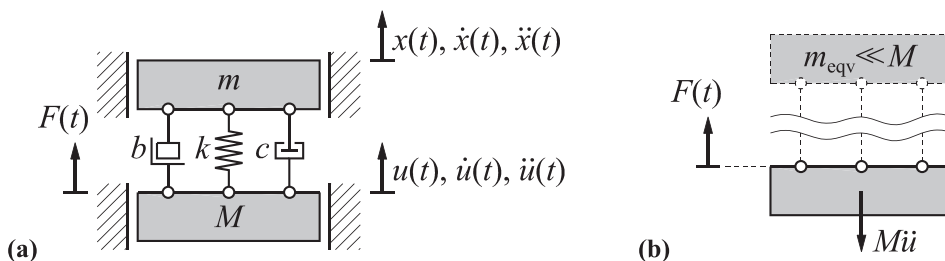

Fig. 8. Big mass method model: a) 2-DOF vibration isolation system, b) free-body scheme, $m_{eqv} \ll M$.
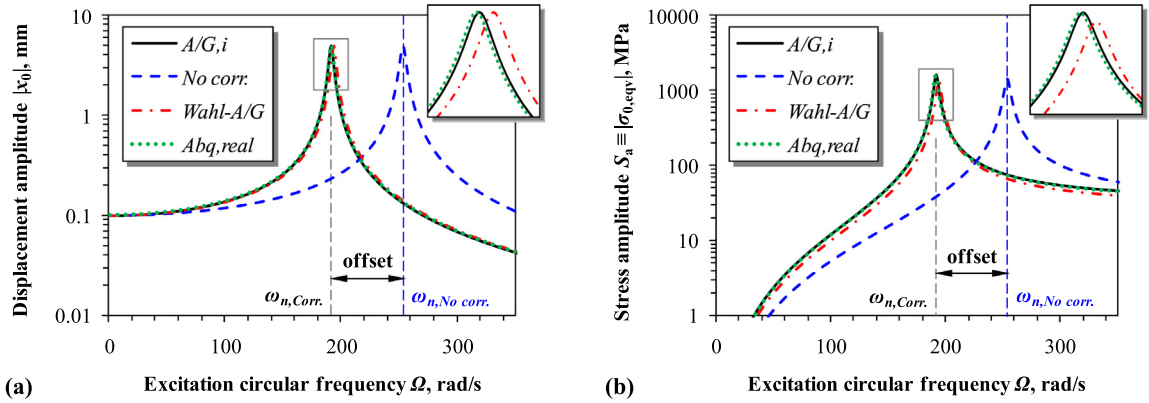
Fig. 9. FRFs comparison, $\mu = 0$: a) displacement amplitude $|x_0|$, b) stress amplitude $S_a \equiv |\sigma_{0,\text{eqv}}|$.

In order to quantify the differences between the FE simulation and analytical results in the broadband frequency range, discrepancies of the FRFs reported in Fig. 9 are plotted with respect to relative error (see Fig. 10). *Abaqus* is considered as a referent solution, while approximate analytical solutions are benchmarked and measured for error E_{rel}. It is evident that $A/G,i$ outperforms *Wahl-A/G* combined correction by far when extremely large pitch angle α effect is considered. Moreover, it is necessary to emphasize that the relative error for both newly proposed $A/G,i$ displacement and stress correction is almost constantly one order of magnitude lower compared to established *Wahl-A/G* correction [4,5].

Next, inerter is fully considered and employed in analytical and numerical solutions. Vibration study results are shown in Fig. 11. By observing the response curves, an excellent visual agreement is reported between all models. Impeccable correlation is noted for *ideal* spring and very good correlation is noted for *real* spring with regard to both displacement and stress amplitudes in Fig. 11a) and b) respectively. Resonance ω_n and anti-resonance $\Omega_A = (k/b)^{1/2}$ [4–6] respectively are outlined by two vertical dashed lines in Fig. 11a).

Furthermore, both *ideal* and *real* springs *Abaqus* output databases are imported and analysed in *Fe-Safe* software suite. Converged complex nodal spring stresses from modal dynamic *Abaqus* step are considered. The *von Mises* energy criterion in the context of Basquin's curve $S_a = S'_f(N_f)^B$ is used within *Fe-Safe* algorithm, where inverse number of cycles $1/N_f$ is non-linearly proportional to Fig. 11b) [5]. Same fatigue material parameters are used as in Table 3. Since this 1-DOF lightly damped system expectedly acts as a band-pass filter, only the most destructive, i.e. system fundamental resonant frequency ω_n, is taken into account.

Fig. 12 shows *real* spring vibration study results with $\mu = 5$ and for most conservative case when $\eta = 1$, i.e. resonant conditions. Spring resonant displacement amplitudes are reported in Fig. 12a), in mm. Node-averaged, converged equivalent stress amplitudes are presented in Fig. 12b), in MPa.

By considering relative magnification factor $M_{0,\text{rel}}$ from Eq. (5b) (i.e. resonant conditions) and modifying the Eq. (12c) accordingly, the following relation is obtained for assessing the spring fatigue life in resonance

$$N_{f,\text{res}}(\Omega = \omega_n) = \left[\sqrt{3} \frac{K_\sigma}{K_\delta} \frac{G}{C^2 n \pi d} \frac{|u_0|}{2\zeta(1+\mu)S'_f} \right]^{\frac{1}{B}}. \tag{15}$$
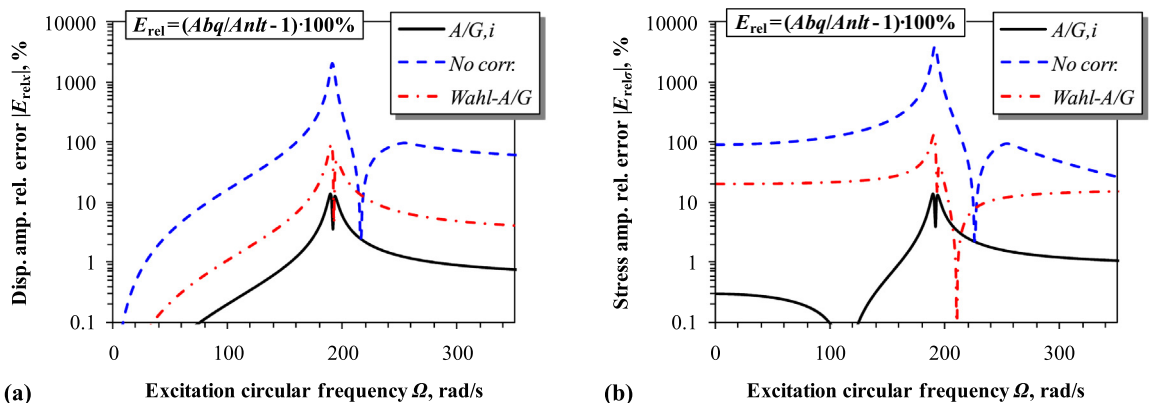

Fig. 10. FRFs relative error comparison, $\mu = 0$: a) displacement error $|E_{\text{rel}x}|$, b) stress error $|E_{\text{rel}\sigma}|$.
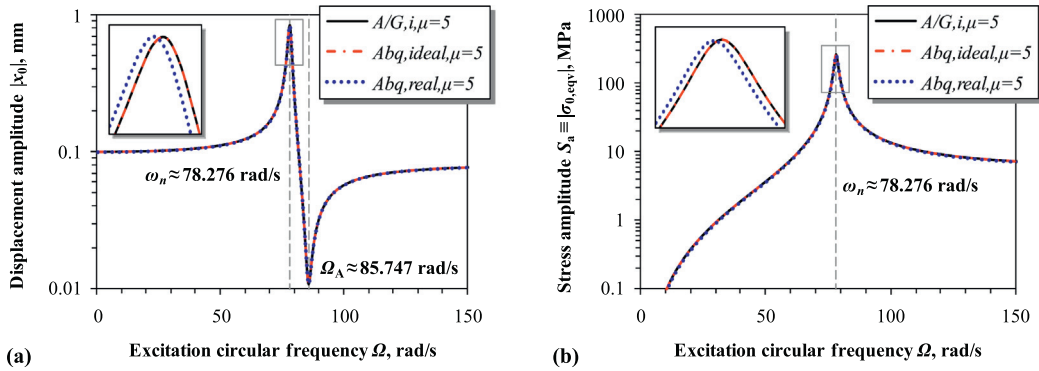
Fig. 11. FRFs comparison, inertance ratio $\mu = 5$: a) displacement amplitude $|x_0|$, b) stress amplitude $S_a \equiv |\sigma_{0,eqv}|$.
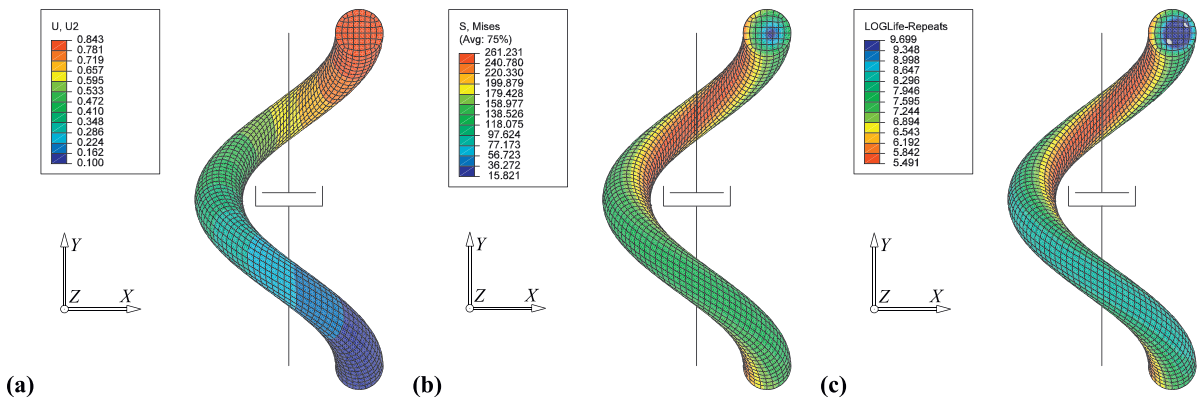

Fig. 12. Abaqus/Fe-Safe results, $\eta = 1$, $\mu = 5$: a) displacement amplitude $|\delta_{0,y}|$, mm, b) equivalent stress amplitude $|\sigma_{0,eqv}|$, MPa, c) fatigue life N_{flog}.

From two extreme cases in Table 5, i.e. when $\mu = 0$ and $\mu = 5$, the following observations can be made. In case large enough dimensionless inertance $\mu \gg 0$ is implemented in the isolator, a significant improvement in the fatigue life can be observed. However, if no inerter is used in the isolator, violent spring rupture occurs for given parameters without even considering fatigue failure, since reported $N_f(\mu = 0) < 1$.

By comparing results from Table 5, an excellent agreement between analytical A/G,i and Abaqus/ideal model is reported in all cases. Negligible relative differences E_{rel} are a consequence of rounding error due to combined influence of approximate BMM and discrete numerical fatigue calculation errors.

For Abaqus/real model, situation is a bit different. First, K_δ error noted in Table 4 is reduced to ~0.264% as a result of squaring, i.e. $\omega_n = (k/m_{eqv})^{1/2}$. Second, as a result of small mismatch between ω_n and K_δ, stress amplitude results S_a now show more prominent error compared to $K_\sigma(A/G,i)$ from Table 4. This yields with ~0.82% relative error as a function of both ω_n and modal damping ζ. Finally, since HCF Eq. (15) describes an exponential curve, the accumulated difference is further accentuated to significant ~|7.877|%. When considering Abaqus stress amplitude $S_{a,Abq} \approx 261.231$ MPa and recalculating fatigue life by hand using Eq. (12b), one obtains exactly the same number of life-cycles from Table 5 where $N_{f,Fe-Safe} \approx 309\,860$ and error completely vanishes.

From the proposed benchmark example, it can be concluded that only computational error is made through adopting novel stress and deflection correction factors K_σ and K_δ, based on improved, although still approximate Ancker and Goodier elasticity theory based correction. The benchmarked spring geometry parameters from Table 3 are chosen in such way to provide a very low spring

Table 5
Analytical and numerical results for helical spring resonant vibration fatigue comparison ($\zeta = 0.01$).

Method	ω_n, rad/s	E_{rel}, %	$|x_0(\omega_n)|$, mm	E_{rel}, %	$S_a(\omega_n)$, MPa	E_{rel}, %	$N_f(\omega_n)$, −	E_{rel}, %
A/G,i, μ = 0	191.736	–	5.000	–	1 580.301	–	< 1	–
Abq/ideal, μ = 0	191.737	0.000	5.001	– 0.020	1 580.301	0.000	< 1	–
Abq/real, μ = 0	191.231	0.264	5.001	– 0.020	1 567.413	0.822	< 1	–
A/G,i, μ = 5	78.276	–	0.839312	–	263 383	–	285 451	–
Abq/ideal, μ = 5	78.276	0.000	0.839336	– 0.003	263 383	0.000	285 453	– 0.001
Abq/real, μ = 5	78.070	0.264	0.839439	– 0.015	261 231	0.824	309 860	– 7.877

index C and a very high pitch angle α in order to firmly test the robustness of the improved correction factors. In practice, such combination of spring parameters is rarely used for the reason of resulting high stresses and low spring stiffness. Furthermore, the influence of higher frequencies and mode shapes is omitted in this investigation, as only fundamental system frequency ω_n is considered.

As a final note, this simplified vibration fatigue analysis aims to contribute in providing better understanding of yet unexplored inerter capabilities. Transparent analytical method is presented herein where proposed expressions match very well with more accurate FEM calculations. It can be used as a starting point for much more complicated analyses which include isolation systems with multiple DOFs. Moreover, expressions derived in the scope of this work are approximately true even for continuous systems with distributed masses if the ratio between the primary mass and other components mass is large enough. Proposed method could be potentially used for assessing the influence of vibrations and corresponding durability of suspension systems. It may also be expanded from helical springs to leaf springs which are commonly used in suspension systems [5,15,22].

5. Conclusion

The vibration fatigue parametric analysis of an inerter-based isolator helical spring is presented. The broadband frequency base excitation is considered. The analysis method is demonstrated on a simple discrete one degree-of-freedom isolator system. Dimensionless parameters for the inerter-based isolator system are derived and parametrically evaluated. Relative displacements, which are proportional to coupling helical spring stress and its corresponding fatigue life, are analysed. In order to more accurately model the system, the improved stress and deflection correction factors for isolator spring are proposed herein. Based on the conducted study, the following major conclusions are drawn:

- Extended high-cycle fatigue life of isolator helical spring is achieved due to beneficiary inerter related effects. Corresponding improvements in fatigue life are noted in broadband frequency excitation range, and are especially evident in most destructive, i.e. resonant working conditions.
- Based on finite element analysis, more accurate helical spring correction factors are determined, compared to the correction factors available in the current literature. This accuracy improvement is especially evident when large spring pitch angle effects are addressed in conjunction with small spring index.
- The proposed procedure demonstrated on a simplified dynamic model could be used for computationally efficient analytical vibration fatigue assessment of a more complex isolation system, e.g. helical springs in the suspension systems.

References

[1] A. Preumont, Vibration control of active structures, an introduction, Solid Mechanics and its Applications, Fourth edition, vol. 246, Springer International Publishing, AG, 2018.
[2] S.S. Rao, Mechanical Vibrations, Sixth Edition in SI Units, Global Edition Pearson, London, 2017.
[3] V. Adams, A. Askenazi, Building Better Products with Finite Element Analysis, OnWord Press, Santa Fe, N.M, 1999.
[4] D. Čakmak, H. Wolf, Ž. Božić, M. Jokić, Optimization of an inerter-based vibration isolation system and helical spring fatigue life assessment, Arch. Appl. Mech. (2018) 1–14, https://doi.org/10.1007/s00419-018-1447-x.
[5] D. Čakmak, Z. Tomičević, H. Wolf, Ž. Božić, H₂ optimization and numerical study of inerter-based vibration isolation system helical spring fatigue life, Arch. Appl. Mech. (2018) 1–22, https://doi.org/10.1007/s00419-018-1495-2.
[6] N. Alujević, D. Čakmak, H. Wolf, M. Jokić, Passive and active vibration isolation systems using inerter, J. Sound Vib. 418 (2018) 163–183.
[7] M.C. Smith, Synthesis of mechanical networks: the inerter, IEEE Trans. Autom. Control 47 (10) (2002) 1648–1662.
[8] M.C. Smith, F.-C. Wang, Performance benefits in passive vehicle suspensions employing Inerters, Veh. Syst. Dyn. 42 (4) (2004) 235–257.
[9] I. Senjanović, N. Alujević, I. Ćatipović, D. Čakmak, N. Vladimir, Vibration analysis of rotating toroidal shell by the Rayleigh-Ritz method and Fourier series, Eng. Struct. 173 (2018) 870–891.
[10] Z. Tomičević, J. Kodvanj, F. Hild, Characterization of the nonlinear behavior of nodular graphite cast iron via inverse identification: analysis of uniaxial tests, Eur. J. Mech. A/Solids 59 (2016) 140–154.
[11] Z. Tomičević, J. Kodvanj, F. Hild, Characterization of the nonlinear behavior of nodular graphite cast iron via inverse identification: analysis of biaxial tests, Eur. J. Mech A/Solids 59 (2016) 195–209.
[12] F. Hild, A. Bouterf, L. Chamoin, H. Leclerc, F. Mathieu, J. Neggers, F. Pled, Z. Tomičević, S. Roux, Toward 4D mechanical correlation, Adv. Model. Simul. Eng. Sci. 3 (17) (2016) 1–26.
[13] M. Mlikota, S. Schmauder, Ž. Božić, Calculation of the Wöhler (S-N) curve using a two-scale model, Int. J. Fatigue 14 (2018) 289–297.
[14] Wahl, A.M., Helical compression and tension springs, ASME Paper A-38, J. Appl. Mech. 2(1) (1935) A-35–A-37.
[15] A.M. Wahl, Mechanical Springs, First edition, Penton Pub. Co., Cleveland, 1944.
[16] Y. Prawoto, M. Ikeda, S.K. Manville, A. Nishikawa, Design and failure modes of automotive suspension springs, Eng. Fail. Anal. 15 (8) (2008) 1155–1174.
[17] C.J. Ancker Jr., J.N. Goodier, Pitch and curvature correction for Helical Springs, ASME J. Appl. Mech. 25 (4) (1958) 466–470.
[18] Research Committee on the Analysis of Helical Spring, Report of research committee on the analysis of helical spring, Trans. Jpn. Soc. Spring Eng. 2004 (49) (2004) 35–75.
[19] L. Del Llano-Vizcaya, C. Rubio-González, G. Mesmacque, T. Cervantes-Hernandez, Multiaxial fatigue and failure analysis of helical compression springs, Eng. Fail. Anal. 13 (8) (2006) 1303–1313.
[20] Ž. Božić, S. Schmauder, H. Wolf, The effect of residual stresses on fatigue crack propagation in welded stiffened panels, Eng. Fail. Anal. 84 (2018) 346–357.
[21] S.K. Das, N.K. Mukhopadhyay, B. Ravi Kumar, D.K. Bhattacharya, Failure analysis of a passenger car coil spring, Eng. Fail. Anal. 14 (1) (2007) 158–163.
[22] Y.S. Kong, M.Z. Omar, L.B. Chua, S. Abdullah, Fatigue life prediction of parabolic leaf spring under various road conditions, Eng. Fail. Anal. 46 (2014) 92–103.
[23] A. Kulkarni, S.A. Ranjha, A. Kapoor, Fatigue analysis of a suspension for an in-wheel electric vehicle, Eng. Fail. Anal. 68 (2016) 150–158.
[24] R.K. Luo, W.J. Mortel, X.P. Wu, Fatigue failure investigation on anti-vibration springs, Eng. Fail. Anal. 16 (5) (2009) 1366–1378.
[25] M. Mršnik, J. Slavič, M. Boltežar, Frequency-domain methods for a vibration-fatigue-life estimation - application to real data, Int. J. Fatigue 47 (2013) 8–17.
[26] M. Mršnik, J. Slavič, M. Boltežar, Vibration fatigue using modal decomposition, Mech. Syst. Signal Process. 98 (1) (2018) 548–556.
[27] X. Song, S. Wang, A novel spectral moments equivalence based lumping block method for efficient estimation of offshore structural fatigue damage, Int. J. Fatigue 118 (2019) 162–175.

[28] S.P. Timoshenko, J.N. Goodier, Theory of Elasticity, Second edition, McGraw-Hill Book Co, New York, 1951.
[29] Dassault Systèmes, Abaqus 6.9 User's Guide and Theoretical Manual, Hibbitt, Karlsson & Sorensen, Inc, 2009.
[30] Dassault Systèmes, Catia V5R19 Documentation: Finite Element Reference Guide, (2007).
[31] Safe Technology, Fe-Safe 6 User Manual, (2011).
[32] MSC. Software Corporation, MSC Nastran 2016 Dynamic Analysis User's Guide, Newport Beach, CA, U.S.A, (2016).
[33] Y.-W. Kim, M.J. Jhung, A study on large mass method for dynamic problem of multiple degree-of-freedom system excited by ground acceleration time history, J. Mech. Sci. Technol. 28 (1) (2014) 25–41.